AMERICAN UNIVERSITY OF BEIRUT

THE EFFECT OF LAMIN A/C LOSS OR MUTATION ON NUCLEAR ENVELOPE PROTEOMICS AND SPLICING FACTOR DEREGULATION IN EMERY-DREIFUSS MUSCULAR DYSTROPHY AND DILATED CARDIOMYOPATHY

by
HIND CAMILLE ZAHR

A dissertation
submitted in partial fulfillment of the requirements
for the degree of Doctor of Philosophy
to the Department of Biology
of the Faculty of Arts and Sciences
at the American University of Beirut

Beirut, Lebanon
September 2019

AMERICAN UNIVERSITY OF BEIRUT

THE EFFECT OF LAMIN A/C LOSS OR MUTATION ON NUCLEAR ENVELOPE PROTEOMICS AND SPLICING FACTOR DEREGULATION IN EMERY-DREIFUSS MUSCULAR DYSTROPHY AND DILATED CARDIOMYOPATHY

by

HIND CAMILLE ZAHR

Approved by:

Dr. Diana Elias Jaalouk, Associate Professor — Advisor
Biology Department
Faculty of Arts and Sciences, American University of Beirut

Dr. Georges Nemer, Professor — Co-Advisor
Department of Biochemistry & Molecular Genetics
Faculty of Medicine, American University of Beirut

Dr. Rabih Talhouk, Professor — Chair of Committee
Biology Department
Faculty of Arts and Sciences, American University of Beirut

Dr. Marwan Refaat, Associate Professor — Member of Committee
Department of Biochemistry & Molecular Genetics
Faculty of Medicine, American University of Beirut

On behalf of Dr. Jan Lammerding Diana Jaalouk

Dr. Jan Lammerding, Associate Professor — Member of Committee
Meinig School of Biomedical Engineering
Weill Institute for Cell and Molecular Biology, Cornell

Dr. Elias Akoury, Assistant Professor — Member of Committee
Department of Natural Sciences
School of Arts and Sciences, Lebanese American University

Date of dissertation defense: September 13, 2019

AMERICAN UNIVERSITY OF BEIRUT

THESIS, DISSERTATION, PROJECT RELEASE FORM

Student Name: Zahr Hind Camille
Last First Middle

○ Master's Thesis ○ Master's Project ● Doctoral Dissertation

☐ I authorize the American University of Beirut to: (a) reproduce hard or electronic copies of my thesis, dissertation, or project; (b) include such copies in the archives and digital repositories of the University; and (c) make freely available such copies to third parties for research or educational purposes.

☑ I authorize the American University of Beirut, to: (a) reproduce hard or electronic copies of it; (b) include such copies in the archives and digital repositories of the University; and (c) make freely available such copies to third parties for research or educational purposes after:

One ---- year from the date of submission of my thesis, dissertation, or project.
Two ---- years from the date of submission of my thesis, dissertation, or project.
Three ---- years from the date of submission of my thesis, dissertation, or project.

Hind Sep. 19, 2019

Signature Date

ACKNOWLEDGMENTS

First and foremost, I would like to express my deepest gratitude to my advisor Dr. Diana Jaalouk. This work would not have been possible without your invaluable guidance and support. Your sincerity and enthusiasm for scientific research have greatly inspired me. I am extremely grateful for your empathy, encouragement and commitment to my professional advancement throughout my PhD. I would also like to thank you for being available for discussions and advice, not only at the professional level but also at the personal level. Besides by advisor, I would like to extend my heartful thanks to my thesis committee members, Dr. Rabih Talhouk, Dr. Georges Nemer, Dr. Marwan Refaat, Dr. Jan Lammerding and Dr. Elias Akoury for investing time and effort by serving on my thesis committee and for their contribution through their knowledge, experience, insightful comments and suggestions. I specifically would like to thank Dr. Jan Lammerding for welcoming me at his laboratory. It was a great privilege and honor to work under your guidance and alongside your amazing team.

I also would like to thank my friends, colleagues, research labs and staff in the Biology Department. I could not have wished for a more cooperative and supportive environment that has made the department more like a home to me. Throughout these years, I've had the chance to work with different members of the DJ lab from master's students to graduate and undergraduate tutorial and volunteer students. It was a pleasure working with each one of you. I am especially grateful for the truthful friendship of Lara Kamand, Ingrid Younes, Ranim Daw, Sara Assi, Mike Kareh and Rachad Ghazal. You have made my time at AUB more positive and enjoyable. As for the new DJ lab members, Rahme Hilal, Marie Thereze Bou Younes and Houda Tantawi, it was a pleasure meeting you and working with you even for a short period of time. I wish you all the success in your studies and research.

Finally, and most importantly, I would like to thank my family for their unconditional love and support. You have all contributed differently and in your own special way to my success and have stood by my side throughout all the ups and downs of this journey. I love you all from all my heart. My PhD would not have been possible without you.

AN ABSTRACT OF THE DISSERTATION OF

Hind Camille Zahr for Doctor of Philosophy
Major: Cell & Molecular Biology

Title: The Effect of Lamin A/C Loss or Mutation on Nuclear Envelope Proteomics and Splicing Factor Deregulation in Emery-Dreifuss Muscular Dystrophy and Dilated Cardiomyopathy

Mutations in the *LMNA* gene, which encodes for lamins A and C (lamin A/C) of the nuclear lamina, cause a wide array of tissue-specific pathologies, mostly affecting cardiac and skeletal muscle tissues. How mutations in a single ubiquitously expressed gene lead to a broad spectrum of phenotypes has long been a dazzling question. Lamin A/C interacts with chromatin and proteins both at the nuclear envelope (NE) and in the nuclear interior, thus serving many functions ranging from structural support of the nucleus to gene regulation. Many *LMNA* mutations cause Emery-Dreifuss muscular Dystrophy (EDMD), a progressive muscle weakening and wasting disorder with conduction system malfunction and dilated cardiomyopathy (DCM), as well as DCM with conduction defects in the absence of skeletal muscle involvement. To date the pathological mechanisms underlying EDMD and DCM remain incompletely understood, particularly the incurable cardiac phenotype that leads to premature sudden death.

In this study, we investigated two non-mutually exclusive hypotheses that could explain the disease phenotypes of EDMD and DCM: 1) Disrupted structural integrity of the nuclear lamina, caused by lamin A/C deficiency, alters the composition of tissue-specific proteins that interact with the NE; 2) Lamin A/C loss or mutation causes deregulation in RBM20, a muscle-specific RNA binding protein that has recently been identified to be highly implicated in familial cardiomyopathies. We also sought to get a better understanding of the pathophysiological role of RBM20 in the heart by identifying novel interacting partners. Using a phage display-based approach, we identified panels of peptides and protein mimics with preferential binding to WT and lamin A/C deficient nuclei. Among the novel proteins revealed by our assay, we showed that HuR interacts with lamin A/C and has altered cleavage and subcellular localization in the absence of lamin A/C. Using the same phage display screening method in combination with co-immunoprecipitation and proximity ligation assays, we identified novel RBM20-interacting partners including lamin A/C, lamin B1 and nesprin-1. Using *in vitro* and *in vivo* models of EDMD and DCM, we showed that Rbm20 and the different isoforms of its splicing target titin are deregulated in lamin A/C-related cardiomyopathies. The downregulation in Rbm20 expression was not restored by insulin treatment despite AKT activation, suggesting a defect in the PI3K-AKT-mTOR pathway downstream of AKT phosphorylation. Our

findings provide mechanistic insights into the tissue-specific phenotypes of lamin A/C cardiomyopathies and highlight the implication of Rbm20 proposing RNA splicing as a novel area for potential pharmacological intervention.

CONTENTS

ILLUSTRATIONS

Figure Page

TABLES

CHAPTER I

LITERATURE REVIEW

A. Overview of Nuclear Structure and Organization

As the most prominent compartment in eukaryotic cells and encompassing the majority of the genome and the transcription machinery, the nucleus is widely viewed as the "mastermind" of the cell. The nucleus controls fundamental processes including maintenance of the genome, chromatin organization and regulation of gene transcription. Moreover, owing to the presence of the nuclear envelope (NE) that physically separates nuclear components from the rest of the cytoplasm, the nucleus provides protection to the genome[1]. Inside the nucleus, chromatin, formed from winding of DNA around histone proteins, broadly exists in two states: euchromatin and heterochromatin. While euchromatin has an open organization that allows it to be transcriptionally active, heterochromatin is more condensed and thus transcriptionally inactive. The two chromatin states also differ in their typical nuclear localization, with euchromatin usually residing in the nuclear interior and heterochromatin in the nuclear periphery and around the nucleolus. Chromosomes are arranged into chromosome territories with active genes occupying the outside of dynamic territories[2]. Another level of organization is achieved by the presence of nuclear domains or sub-compartments that store and concentrate regulatory proteins and RNA. Chromosome territories and regulatory complexes are thought to be held and organized by nucleoskeletal scaffolds. The most prominent nucleoskeletal proteins are lamins that impart nuclear organization both at the periphery and in the nuclear interior. In addition, many cytoskeletal

proteins are recently being recognized to play roles in the nucleus. Of these are spectrin II-α, titin, 4.1R, actin and myosin[3].

1. The Nuclear Envelope

The NE is more than just a physical barrier as it relays biochemical and mechanical stimuli from the cytoplasm and extracellular environment into the nuclear interior, where processing of these signals occurs. At the same time, it controls transport of mRNA into and out of the nucleus, thus allowing for an additional layer of gene regulation[4]. The NE consists of two distinct phospholipid membranes, namely the outer nuclear membrane (ONM) and inner nuclear membrane (INM), and the underlying nuclear lamina. The ONM is separated from the INM by the perinuclear space, a 30-50 nm thick lumen that is continuous with the lumen of the endoplasmic reticulum (ER). The nuclear lamina is 10-30 nm thick meshwork that is closely associated with the INM and mainly composed of lamin proteins. The NE harbors integral and associated proteins and connects the nucleus to the cytoskeleton through the linker of nucleoskeleton and cytoskeleton (LINC) complex. Interspersed across the NE, at sites where the two membranes connect, are nuclear pore complexes (NPCs). NPCs regulate exchange of large molecules (> 30 kDa) across the NE and interact with the cytoskeleton, the nucleoskeleton and chromatin[5]. Given the structural and functional complexity of the NE, integrity of nuclear envelope proteins is essential for nuclear homeostasis.

2. The LINC Complex

Spanning both the inner and outer nuclear membranes, the LINC complex acts as a molecular bridge between the nucleoskeleton and cytoskeleton (Figure 1). Such physical coupling is achieved through the interaction of KASH domain proteins at the outer nuclear membrane with SUN domain proteins at the inner nuclear membrane, in association with lamin A/C and emerin[6]. KASH domain proteins include nesprins-1, -2, -3, -4, KASH5 and lymphoid-restricted membrane protein (LRMP). In mammals, KASH5 is germ cell specific whereas LRMP is restricted to a group of taste receptor cells[7-9]. The four nesprins (nuclear envelope spectrin repeat proteins) are encoded by different genes, each giving rise to multiple isoforms by alternative splicing and alternative initiation[10]. Nesprin-1 and -2 are ubiquitously expressed and particularly abundant in striated muscle tissue[11]. Nesprin-3 is also widely expressed; whereas nesprin-4 is mainly present in epithelial cells[10,12]. Nesprin-1 and -2 are the second and third largest known human proteins following the giant sarcomeric protein titin. The full length isoforms of nesprin-1/2 share a common structural organization consisting of three domains: A C-terminal KASH domain that integrates into the NE and into the perinuclear space, a central spectrin repeat (SR) rod domain that associates with other proteins in the cytoplasm, and an N-terminal Calponin Homology (CH) domain that mediates the link with cytoskeletal elements[13] (Figure 1). While larger isoforms of nesprin-1/2 localize to the ONM and interact on the cytoplasmic side with the actin cytoskeleton through their CH domain[14], short isoforms like nesprin-1α and nesprin-2β localize to the INM where they interact through their SRs with SUN1/2, emerin and lamin A/C[15]. Nesprin-1/2 have been primarily known to interact with the actin cytoskeleton[14]; however, recent findings have shown that they are also capable of interacting with microtubules through microtubule-associated proteins such as

dynein/dynactin, kinesin light chain-1/2 (KLC-1/2) and Akap450[16-18]. As for the other nesprin types, nesprin-4 also interacts with the microtubule motor proteins, dynein/dynactin and KLC-1/2[19], while nesprin-3 mainly interacts with intermediate filaments through the linker protein plectin[20,21]. Thus, nesprins form various connections with the cytoskeleton through the LINC complex.

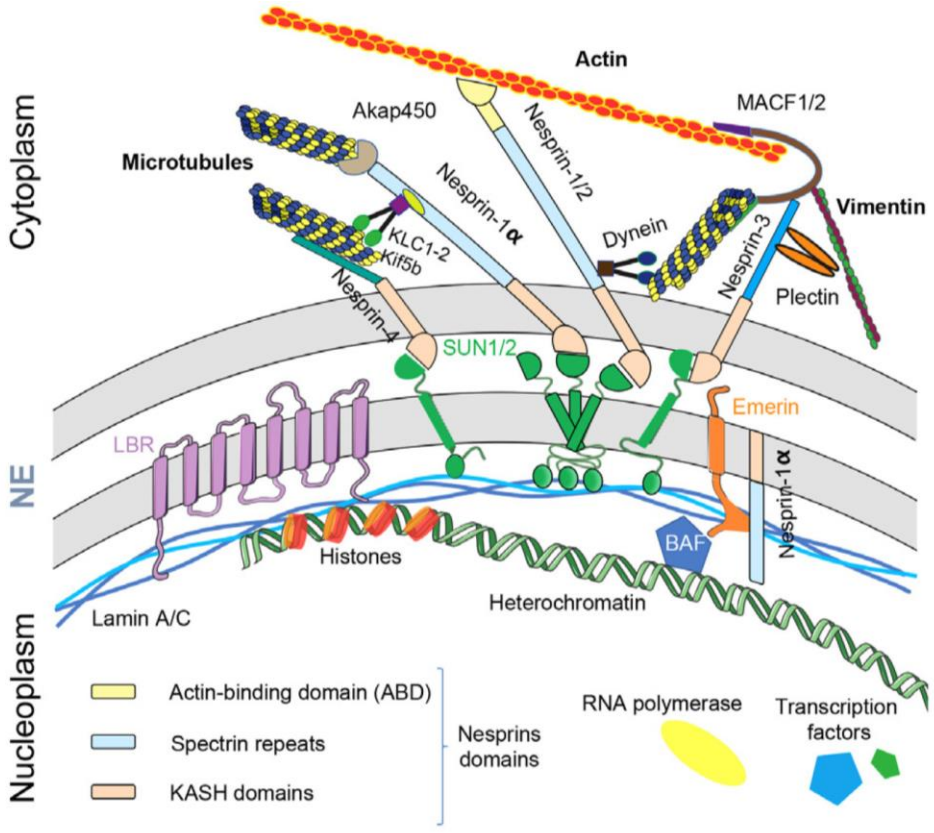

Figure 1. The LINC Complex.
Lamins interact with SUN and nesprin proteins to form the LINC complex that links the nucleoskeleton to the cytoskeleton. Different nesprin proteins interact with different cytoskeletal elements either directly or through anchor and motor proteins. Some nesprin isoforms, such as nesprin1α, are also localized to the INM where they interact with emerin and lamins. NE, nuclear envelope; LINC, linker of nucleoskeleton to cytoskeleton; ONM, outer nuclear membrane; INM, inner nuclear membrane; KASH domain, Klarsicht/ANC-1/Syne homology; SUN, Sad1p/UNC84; BAF, barrier to auto-integration factor. (Janin & Gache, 2018).

SUN proteins constitute the second component of the LINC complex. There are five SUN proteins in mammalian cells. SUN 1 and 2 are expressed in somatic cells and SUN 3, 4, 5 are specific to male germ cells[22]. All SUN proteins consist of an N-terminal domain that interacts with the lamina in the nucleoplasm, a transmembrane domain, a coiled-coil rod domain holding a C-terminal trimeric SUN domain in the perinuclear space. The SUN domain binds up to three KASH domain proteins through interactions with the luminal portions of their KASH domains[23].

The LINC complex allows physical and mechanical coupling of the nucleoskeleton and the cytoskeleton, maintains nuclear morphology, controls nuclear positioning and regulates gene expression[10]. As such, loss of LINC complex integrity has been shown to compromise force transmission across the NE and cause both nuclear and cytoskeletal defects[24]. For instance, LINC complex disruption results in altered nuclear morphology and distribution of actin and vimentin cytoskeletal filaments[25] as well as defects in myonuclear positioning[26] and mechanosensitive gene expression[27].

3. Lamins at the Nuclear Envelope:

Lamins are type V intermediate filaments, exclusively localized to the nucleus of most differentiated cells and mesenchymal stem cells[28-30]. Mammalian cells express two types of lamins: A-type lamins, encoded by the *LMNA* gene which generates by alternative splicing lamins A and C (lamin A/C) and other less common isoforms; and B-type lamins, encoded by *LMNB1* and *LMNB2* genes which give rise to lamin B1 and lamin B2/B3 respectively[29]. While lamin A/C and lamin B1 and B2 are expressed in most somatic cells, lamin B3 is germ cell specific. In addition, while B-type lamins are expressed in both

embryonic and adult cells[31], lamin A/C is developmentally regulated with low expression in embryonic stem cells and significantly higher expression in most adult cells[30,32,33]. B-type lamins have been thought to be essential for cell viability, as at least one kind of B-type lamins is expressed in all cells; however, recent findings have shown that both stem and adult cells remain viable and capable of proliferating and differentiating even in the absence of B-type lamins[34,35].

In humans, the *LMNA* gene is composed of 12 exons[36]. Lamins A and C are produced by alternative splicing of exon 10 of the *LMNA* gene[36,37]. Both isoforms are identical in their first 566 amino acids after which they become different in both length and amino acid composition. While lamin C is 572 amino acids long, mature lamin A is composed of 646 amino acids (Figure 2). Another difference is the presence of CAAX motif at the C-terminal end of pre-lamin A which acts as a site for sequential posttranslational modifications, including farnesylation and carboxymethylation, that result in cleavage of prelamin A into mature lamin A[38]. B-type lamins also contain the CAAX motif, but instead of undergoing the final cleavage step as lamin A, which removes the farnesyl and carboxymethyl groups, they remain farnesylated and carboxymethylated and thus permanently attached to the nuclear envelope throughout the cell cycle[39]. On the other hand, the absence of the farnesyl and carboxymethyl groups from mature lamin A and lamin C renders them more soluble and available at both the nuclear envelope and in the nucleoplasm[40].

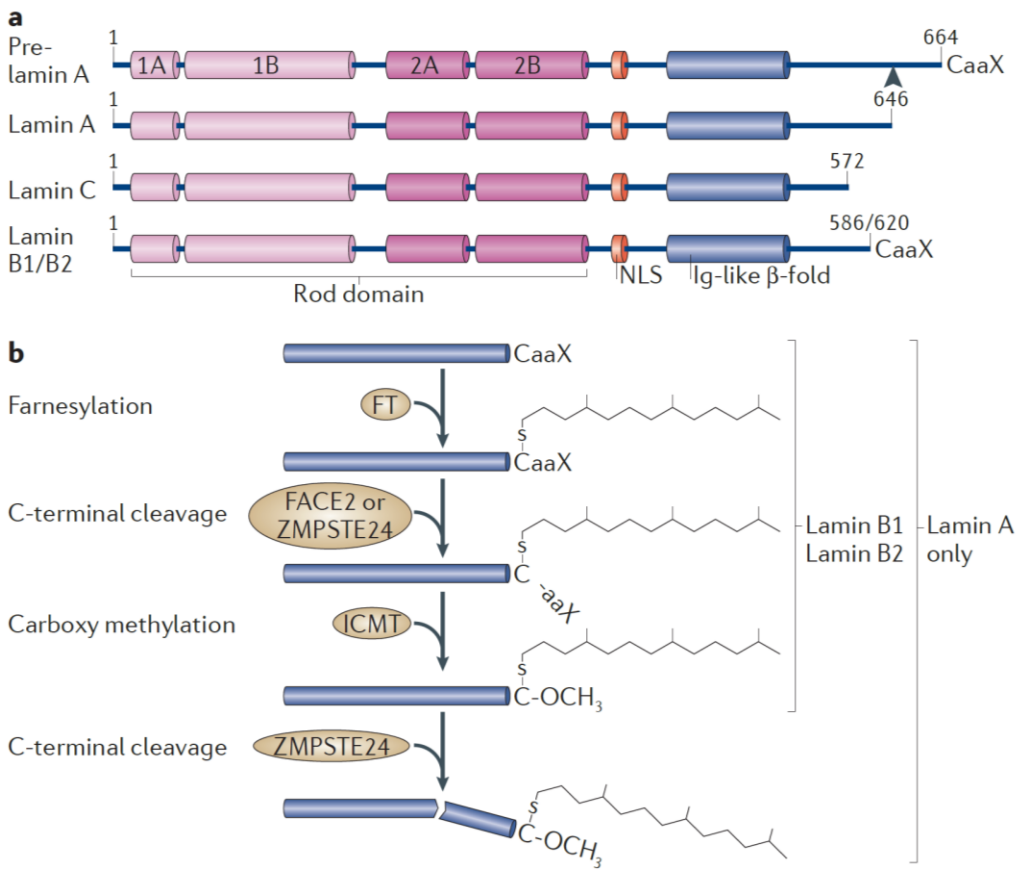

Figure 2. Structural Organization and Post-Translational Modifications of Lamins. a) Lamins share a common structure composed of a small head domain, a central rod domain featuring four regions (1A, 1B, 2A and 2B) and a tail domain containing a nuclear localization signal (NLS) and an immunoglobulin (Ig) fold. The black arrowhead denotes the site of proteolytic cleavage of prelamin A. b) Processing of the CaaX motif of lamin A and B-type lamins begins with farnesylation of the Cysteine of the CaaX motif by farnesyltransferase (FT), followed by proteolysis of the aaX residues by farnesylated proteins-converting enzyme 2 (FACE2) or ZMPSTE24, and finally by carboxy methylation of the Cysteine by ICMT (isoprenylcysteine carboxylmethyltransferase). After incorporation into the nuclear lamina, lamin A, but not B-type lamins, undergoes an additional cleavage step by ZMPSTE24 (black arrowhead in a) which removes the farnesylated Cysteine and an additional 15 amino acids giving rise to mature lamin A. (Burke & Stewart, 2013).

All lamins have a similar structural organization consisting of a short globular N-terminal head domain, a central coiled-coil rod domain and a long globular C-terminal tail domain[36]. The rod domain is highly conserved and is implicated in lamin dimerization. An

immunoglobulin-like domain is also present in the tail of lamin A/C where various posttranslational modifications occur[29,41]. Lamins assemble first by dimerizing into coiled-coiled dimers, then by forming polar polymers, through head-to-tail dimer arrangement, and finally by forming antiparallel nonpolar filaments[42-44]. Although different lamin isoforms form heteropolymers *in vitro*, they characteristically polymerize into independent yet interacting networks *in vivo*[45-47].

Lamins constitute the main components of the nuclear lamina and interact with proteins and DNA. Through their architectural attachment to the inner nuclear membrane, lamins provide mechanical and structural support to the nucleus. Furthermore, by acting as a platform for diverse protein interactions, they play a role in anchoring and positioning nuclear membrane proteins, regulating various signaling pathways, recruiting and sequestering transcription and DNA replication and repair factors, coupling the nucleoskeleton to the cytoskeleton and mechanotransduction. In addition, lamins bind DNA both directly and indirectly and hence play a role in chromatin organization, gene silencing and transcription[29].

a. Lamin Binding Partners at the Nuclear Envelope

Lamins at the nuclear lamina interact with hundreds of proteins both directly and indirectly. Lamin binding partners include integral membrane proteins, LINC complex components, nuclear pore complex proteins and lamina-associated proteins and transcription factors (Figure 3). Lamins also interact with chromatin, both directly and through DNA-binding proteins. While the list of lamin binding proteins continues to expand, the evolutionary conserved LEM-domain proteins were among the first to be

identified[48]. The LEM (LAP2-Emerin-MAN) domain allows LEM-domain proteins to bind to Barrier to Autointegration Factor (BAF), a chromatin binding protein that anchors heterochromatin to the nuclear lamina[49]. Nonetheless, both lamins and LEM-domain proteins can directly bind chromatin through DNA and histones[50]. The regions of the genome that bind lamins, termed lamina associated domains (LADs), are mainly heterochromatin regions enriched for repressive epigenetic marks[51]. In addition to its roles in nuclear organization and heterochromatin maintenance, BAF is involved in assembling lamins and emerin into the NE[52,53]. LBR is another lamin binding protein that tethers chromatin to the NE and regulates epigenetic gene repression[54]. Lamins associate with many transcription factors, thereby regulating gene expression by sequestering them at the NE. c-Fos, pRb and SREBP1, among others are transcripton factors that interact with lamin A/C[50]. Lamin A/C-dependent regulation of transcription factors works in tandem with upstream signaling pathways. For instance, lamin A/C sequesters c-Fos at the NE; and ERK1/2 activation by MAPK signaling releases c-Fos and promotes cell proliferation[55]. Many of the lamina associated proteins vary between different tissues and depend on lamins for their nuclear envelope localization[56]. As such, in the absence of lamins or in the presence of lamin mutations, some of these interacting partners become mislocalized, thus affecting downstream signaling pathways in a tissue-specific manner.

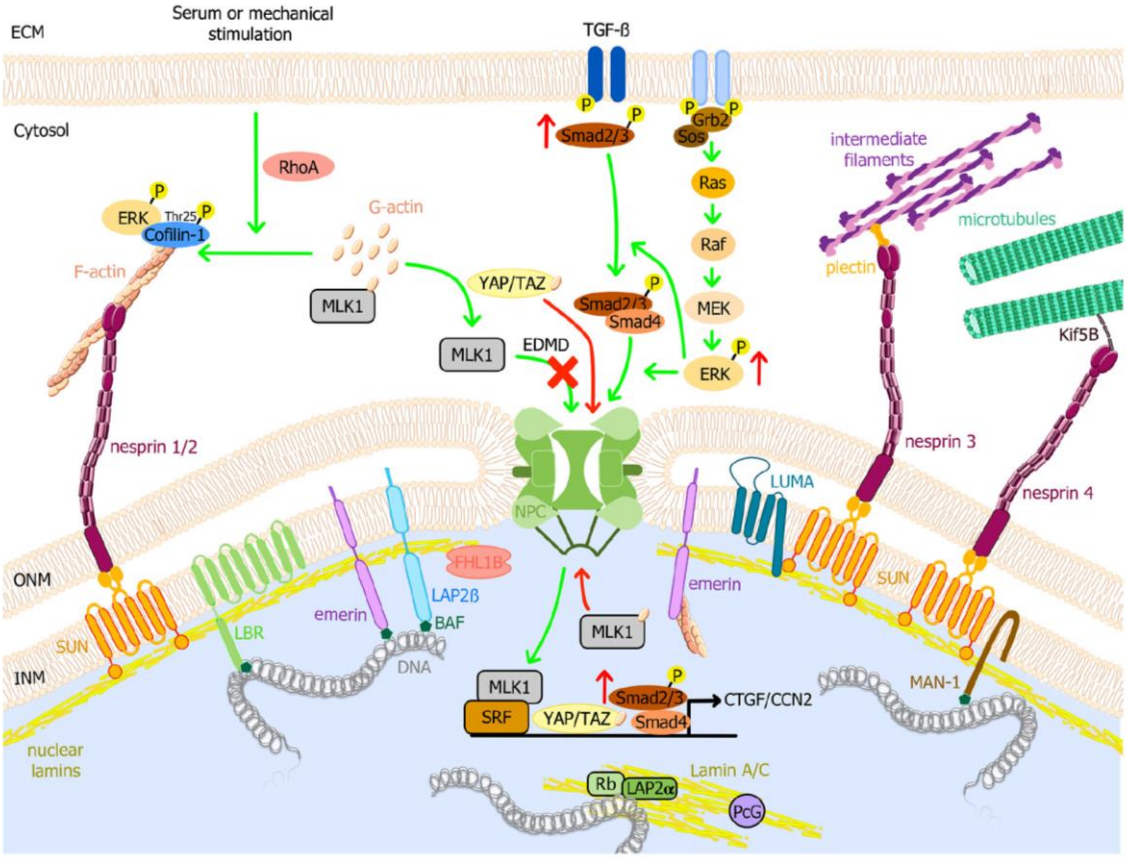

Figure 3. Nuclear Envelope Proteins and Some Signaling Pathways Altered in EDMD. Lamins interact with NE proteins (LBR, LAP2, SUN1/2, MAN1, LUMA, emerin), transcription factors (Rb), and cytoskeletal elements (actin, intermediate filaments and microtubules) through the LINC complex and motor proteins. Several signaling pathways are deregulated in the presence of EDMD-associated LMNA mutations such as hyperactivation of ERK, JNK, and p38α cascades which in turn activate TGF-β/Smad signaling pathway and cofilin-1. TGF-β/Smad signaling activates CTGF/CCN2 transcription. Cofilin-1 activation leads to actin depolymerization which opposes RhoA-dependent actin polymerization that releases MKL1 from cytoplasmic G-actin and facilitates its nuclear import upon serum or mechanical stimulation. Lamin mutations mislocalize emerin, thereby affecting its ability to polymerize nuclear actin. Nuclear G-actin then binds to MKL1 and increases its nuclear export thus preventing the transcription of SRF target genes. LMNA mutations lead to activation of YAP/TAZ transcription factors and their nuclear accumulation, which promotes cell proliferation and opposes differentiation. Green arrows represent normal signaling while red arrows indicate disrupted pathways in EDMD. BAF, barrier-to-autointegration factor; ECM, Extracellular matrix; EDMD, Emery-Dreifuss muscular dystrophy; ERK, extracellular signal-regulated kinase; F-actin, actin filament; G-actin, globular actin; Grb2, growth factor receptor-bound protein 2; INM, inner nuclear membrane; Kif5B, kinesin family member 5B; LAP, lamin associated protein; LBR, lamin B receptor; MAPK, mitogen-activated protein kinase;

MKL1, megakaryoblastic leukemia 1; NPC, nuclear pore complex; ONM, outer nuclear membrane; Raf, proto-oncogen serine/threonine-protein kinase; Rb, retinoblastoma protein; RhoA, ras homolog family member A; Sos, son of sevenless homolog 1; SRF, serum response factor; TGF-ß, transforming growth factor ß; YAP, yes-associated protein 1; TAZ, transcriptional coactivator with PDZ-binding motif. (Brull et al., 2018).

4. Nuclear Domains

Studies have demonstrated that the nucleus is much more organized than what has previously been thought. Nuclear organization is endowed by the presence of various nonmembrane-bound subnuclear organelles or domains that concentrate specific components and carry on specialized functions[57]. It is widely accepted that these domains are dynamic, in that they constantly exchange contents with the nucleoplasm[58]. However, a better understanding of the assembly and direct function of these domains is still awaited. Nuclear domains or bodies include but are not limited to: the nucleolus, Cajal bodies, nuclear speckles, PML bodies, and PcG bodies[59]. The nucleolus functions in rRNA biogenesis, processing and assembly of ribosomal subunits[57]. Cajal bodies play a role in the biogenesis of snRNP and snoRNP, storage of splicing factors and short non-coding RNA, and trafficking of snRNP and snoRNP to nuclear speckles and nucleoli respectively. Cajal bodies also associate with snRNA gene clusters but the implication of this association is not yet clear[59]. Nuclear speckles are storage sites for splicing factors that are constantly recruited by transcription sites on perichromatin fibrils[57,60]. PML bodies gain their name from the presence of the PML protein among other proteins; and are suggested to play a role in regulating gene transcription[61]. PcG bodies are storage compartments for polycomb group proteins. PcG bodies are suspected to be involved in gene silencing as PcG target

genes shuttle between PcG bodies in their repressed state and transcription factories in their active state[62].

5. Lamins in the Nuclear Interior

In addition to being integral components of the nuclear lamina, A-type lamins are also present in the nucleoplasm. However, the regulation and specific functions of lamins in the nuclear interior are poorly understood. Unlike B-type lamins which retain their farnesyl and carboxy-methyl groups and remain tightly associated with the NE[39], mature lamin A and lamin C lack these groups, rendering them more soluble during different stages of the cell cycle[40]. Nonetheless, a few studies reported the presence of nuclear B-type lamin pools[63,64]. Nucleoplasmic A-type lamins are thought to be more mobile and less structured than lamins at the nuclear envelope[65]. Although the current view is that they mainly form foci and short fibrous structures, the assembly state of nuclear lamins remains to be elucidated[63]. Nuclear A-type lamins probably originate from the disassembly of nuclear lamina during mitosis, prompted by kinase-dependent phosphorylation. Upon lamina reassembly in G1 phase, a pool of lamins is sequestered into the nucleoplasm by mechanisms that may involve binding to LAP2α or post-translational modifications. Moreover, pre-lamin A may transiently contribute to this nucleoplasmic pool prior to its post-translational processing and association with the NE. Although not very likely, dynamic exchange between A-type lamins at the NE and nucleoplasmic pool cannot be ruled out[66]. Like A-type lamins at the NE, nucleoplasmic lamins tether heterchromatic lamina-associated domains (LADs) that reside in the nuclear interior and have been suggested to regulate the proportion of lamina-associated LADs at the nuclear periphery[67].

In addition, nucleoplasmic A-type lamins have been found to associate with euchromatin regions enriched for LAP2α[68]. Whether the LAP2α-lamin A/C complex drives chromatin accessibility or maintains the accessible state is not known; nonetheless, nucleoplasmic A-type lamins have reported roles in epigenetic pathways. For instance, they are required for assembly of Polycomb group (PcG) proteins involved in epigenetic transcriptional repression[69]. Another possible mechanism of gene regulation by nuclear lamins is through direct binding to gene promoters[70]. Moreover, nuclear A-type lamins play a role in spatial chromatin organization by restricting chromatin mobility, with indirect effects on the mechanical properties of the nucleus[65]. Reorganization of lamins between the lamina and the nuclear interior has been shown to occur in response to mechanical strain[71]. Although most previous studies did not examine each lamin pool separately, lamins at the nuclear interior might be more directly involved in regulating gene expression through binding to "open" chromatin regions, with evidence pointing to roles in mechanosensitive gene regulation. Defining the specific functions of NE-associated versus nucleoplasmic lamins will help translate the effects of mutations shifting the balance between the two pools, such as the DCM-causing lamin N195K mutation that shows increased nucleoplasmic localization in DCM patient cells[72].

a. Lamin A/C Speckles and Splicing Factor Compartments

Several reports identified an association between lamin A/C and splicing factor compartments (SFCs). SFCs are 1-2 μm diameter speckles in which RNA splicing factors are concentrated. Acting as storage sites for transcription factors, SFCs are dynamic in that

splicing factors are constantly recruited into and out of these compartments from and to transcription sites[73]. As such, their size changes depending on the level of transcription and mRNA splicing[74-76]. Splicing of most nascent transcripts is simultaneous with transcription[77] and occurs on perichromatin fibrils that, in addition to being localized at the borders of SFCs, are also found throughout the nucleoplasm away from SFCs[78-80]. In accordance with the previously proposed role of intranuclear lamins in nuclear organization, the finding that intranuclear lamin foci or speckles colocalize with RNA splicing factors in SFCs was suggestive of a structural role of lamins in SFCs[81]. The findings of other studies that followed were as well implicative of a role of lamin A/C in SFC organization. For instance, the expression of terminally tagged lamin A/C resulted in depletion of lamin speckles and SFCs, which was associated with reduction in RNA polymerase II (pol II) transcription. Furthermore, lamin speckles and SFCs concomitantly became larger upon pol II transcriptional inhibition and reversibly attained their normal size upon withdrawal of inhibition[82]. In another study published the same year, the authors showed that disruption of the nuclear organization of lamin A/C, by means of a dominant-negative mutant that lacks the N-terminal domain, also reorganizes SFCs and inhibits pol II transcription[83]. Contradicting these studies, Vecerova *et al.* tested *Lmna*$^{-/-}$ cells and showed that lamin A/C is non-essential for the formation and maintenance of SFCs[84]. Nonetheless, this discrepancy between the different studies might be due to the different protein factors used to label SFCs. In addition, the expression of a truncated fragment of lamin A in *Lmna*$^{-/-}$ cells might be sufficient to preserve lamin speckles, despite its failure to preserve the nuclear lamina[85].

b. Interaction Between Lamin A/C and Splicing Factors/RNA-Binding Proteins

As mentioned earlier, disruption of lamin speckles was associated with down-regulation of pol II transcription[82,83]. This could be a direct effect of the loss of the putative interaction between lamin A/C and SFC components such as SC-35. Indeed, it has been shown that SC-35 supports pol II-dependent elongation through its interaction with cyclin-dependent kinase 9 (CDK9), a component of the positive transcription elongation factor b (P-TEFb). CDK9 phosphorylates the C-terminal domain (CTD) of pol II and results in transcriptional elongation[86]. In addition to its interaction with CDK9, an interaction between SC-35 and the CTD of pol II has also been reported[87]. Interestingly, cardiac-specific deletion of SC-35 causes DCM[88], which is also well-known to be caused by *LMNA* gene mutations[89]. ASF/SF2 is another splicing factor which interacts with lamin A/C[90, 91]. ASF/SF2 is a splicing regulator of several genes that encode for cardiac proteins, such as CamkIIδ[92]. Dysregulated CamkIIδ isoforms are associated with cardiomyopathy and heart failure[93,94] and loss of ASF/SF2 in the heart tissue is responsible for DCM as well as perturbed excitation-contraction coupling[92]. Therefore, the loss of association between lamin A/C and each of ASF/SF2 and SC-35 might affect their functions pertaining to striated muscle tissue which might explain the skeletal and cardiac muscle effects of most *LMNA* mutations.

A recent study identified 130 proteins that repeatedly associate with lamin A tail in C2C12 myoblasts differentiated to form myotubes. Upon functional classification of these proteins, enrichment of proteins involved in RNA splicing was noted. Furthermore, binding partners belonging to this functional category were solely found to differ between wild type lamin A and two lamin A mutants associated with EDMD[90]. Of the identified proteins in

this study, 15 proteins are localized in nuclear speckles (CDC5L, DDX3X, EFTUD2, LUC7L3, NPM1, PRPF19, RNPS1, SFRS1, SFRS3, SFRS4, SRSF10, SRRM1, SRRM2, THOC4 and U2AF2) and 30 proteins in the spliceosomal complex. Furthermore, some of the identified proteins, such as ASF/SF2 (or SFRS1) and SRSF10 are localized to both compartments (Figure 4). Both alternative splicing factors have heart-specific effects despite their ubiquitous expression and their knockout in mice is embryonically lethal due to impaired cardiac development[95]. Accordingly, dysregulated interaction between lamin A/C and these splicing factors or lack thereof might account for the tissue-specific effects of lamin A/C mutations.

Driven by the importance of protein interactions in core cellular processes, large-scale biochemical, proteomic and bioinformatic approaches were employed to characterize the composition of cellular protein complexes in cultured human cells[96]. This study identified new proteins that associate with lamin A/C. Although none of the identified putative lamin A/C partners are localized to nuclear speckles, three play a role in splicing (NONO, SF3B3 and hnRNP-M). hnRNP-M belongs to the heterogeneous nuclear ribonucleoprotein (hnRNP) family of proteins. Members of this family are implicated in pre-mRNA transcription, translation, processing and transport, all of which might affect gene expression[97]. They exert their effects on the fate of pre-mRNA by alternative splicing, manipulating the structure of pre-mRNA and affecting accessibility to other RNA processing factors[98]. Remarkably, hnRNP-M has been shown to interact with cell division cycle 5-like (CDC5L) and pleiotropic regulator 1 (PLRG1)[99], two core components of the CDC5L complex which is crucial for spliceosome assembly and function[100,101]. The interaction domain in hnRNP-M was shown to be essential for its role in constitutive and

alternative splicing. In addition to its presence in the spliceosome, CDC5L is also present in nuclear speckles and have been shown to interact with lamin A/C[90,99]. Other CDC5L-associated proteins that are localized to nuclear speckles and putatively interact with lamin A/C are SC-35 and ASF/SF2[100].

As such, lamin A/C might regulate the pre-assembly and targeting of sub-complexes such as the CDC5L complex to the emerging spliceosomal complex, such that loss of interaction between sub-complex components and lamin A/C might influence the function of the spliceosome and gene expression. Other hnRNPs were identified by a novel approach that assesses proximity or binding to lamin A in a quite natural cellular context. This approach utilizes a biotin ligase fusion of lamin A followed by mass spectrometry of biotinylated proteins. The biotinylated hnRNPs by this procedure were hnRNP-E1, hnRNPA1, hnRNPA2B1, hnRNPA0 and hnRNPR. In addition to hnRNPs, other splicing factors that interact with and/or are proximal to lamin A, such as SF1, U2SURP, GPATCH1, DGCR14, RBM10, SUGP1, PAPOLA, TFIP11 and GTF2F2, were identified[102]. Interestingly, hnRNP-E1 was shown by another study to retain its interaction with progerin, a truncated form of lamin A that causes Hutchinson-Gilford progeria syndrome[103]. This implies that the interaction domain might be preserved in progerin and that loss of interaction between lamin A and its interacting partners is mutation dependent, thus providing further insight into the diverse tissue-specific phenotypes associated with *LMNA* mutations[103].

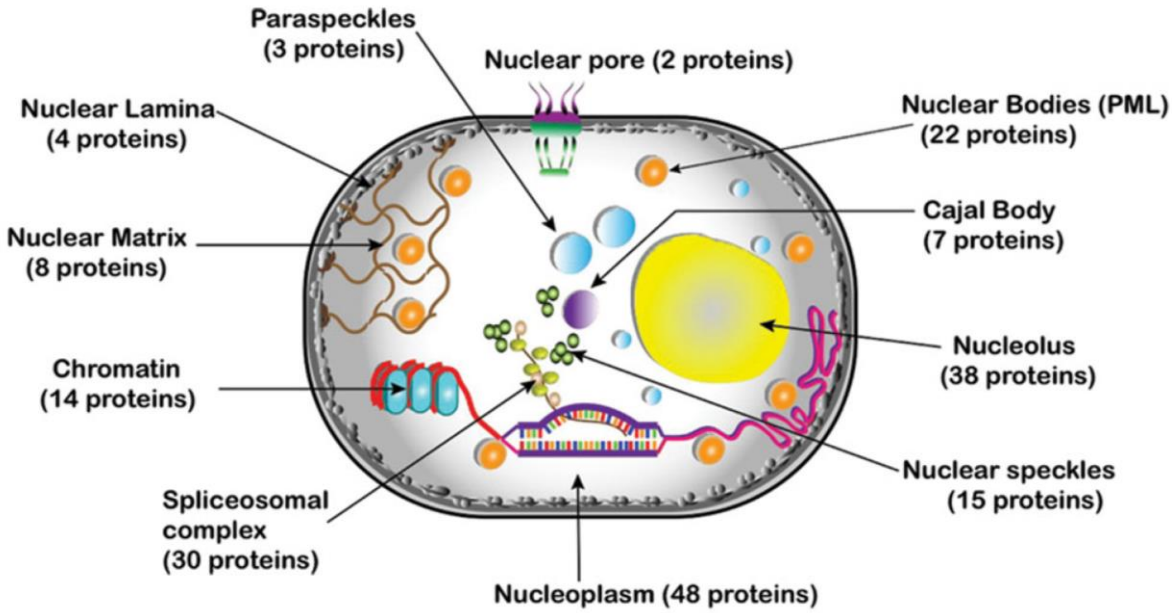

Figure 4. Lamin A Tail Interacting Proteins and Their Distribution Across Nuclear Domains.
The nuclear localization of 130 proteins that associate with lamin A tail was determined by gene ontology. The number of proteins corresponding to each compartment is indicated with some proteins having more than one localization. (Depreux et al., 2015).

B. *LMNA* Gene Mutations in Laminopathies, EDMD and DCM

The first mutation in the *LMNA* gene was identified in 1999 to be causative of Emery-Dreifuss muscular Dystrophy (EDMD), a progressive muscle weakening and wasting disorder with conduction system malfunction and dilated cardiomyopathy[104,105]. *LMNA* gene mutations were also shown, in the same year, to be causative of DCM and conduction system disease in the absence of skeletal muscle involvement[106]. Since then, more than 450 mutations in the *LMNA* gene have been reported (http://www.umd.be/LMNA/). The different mutations are associated with diverse diseases collectively called Laminopathies that are either manifested as tissue-specific disorders or multisystem disease[107,108]. While tissue-specific effects are seen in striated muscle tissue,

adipose tissue or peripheral nervous tissue, multisystem effects incorporate multiple tissues and are seen in premature aging syndrome or overlapping syndromes [107,109-111]. Most *LMNA* mutations (79.1%) affect striated muscle tissue, followed by adipose tissue (8.6%) and peripheral nervous tissue (0.3%). Furthermore, the percentage of *LMNA* mutations causing progeroid and overlapping syndromes is 9.3% and 10.9% respectively[112].

DCM caused by *LMNA* mutations has the worst prognosis, and the highest rate of heart transplantation [113]due to congestive heart failure and considerable risk of sudden cardiac death[114-117]. Affected individuals frequently suffer from progressive conduction system disease such as atrioventricular block, bradyarrhythmias and tachyarrhythmias and have a high chance of developing thromboembolic disorder[106,118-121]. Males have a worse prognosis than females, owing to frequent ventricular arrhythmias and end stage heart failure[122]. Altogether, *LMNA* mutation carriers have high disease penetrance, often presenting symptoms at an early age and having high mortality rate[117]. Furthermore, most *LMNA* mutation carriers exhibit an age-dependent penetrance, with the percentage of carriers showing a cardiac phenotype increasing from 7% under the age of 20 years to 100% above the age of 60 years[123].

In 2014, 165 DCM-associated mutations, based on four different databases, were identified in the *LMNA* gene[124] (see Ref. for a detailed table of all 165 mutations). Most of these pathogenic variants were missense/nonsense mutations, some were splicing mutations, small deletions or small insertions and very few were small indel, gross deletions or gross insertions[125-132]. Since then more DCM-associated mutations were identified in the *LMNA* gene[116,133-138]. Remarkably, a recent study performed on a multicenter cohort of 77 subjects from 45 different families identified 24 novel mutations in

the *LMNA* gene[139]. Of these mutations, 18 were associated with DCM and were considered pathogenic[139]. Most DCM-causing mutations in the *LMNA* gene occur in the head and rod domains, which comprise more than half of lamin A and two thirds of lamin C, but rarely in the tail domain. Unlike DCM, mutations linked to other laminopathies such as EDMD, familial partial lipodystrophy and Hutchinson-Gilford progeria syndrome (HGPS) commonly affect the tail domain and thus overlap with the various phosphorylation sites that are abundant in that region of the protein[108]. In addition, although hot spots have been identified for some laminopathies including HGPS, mandibuloacral dysplasia and adipose tissue-specific disorders, hot spots for DCM or disorders affecting striated muscle tissue have not been recognized [112].

1. Signaling Defects in Lamin A/C-Related Cardiomyopathies

Lamins interact with a plethora of NE proteins and transcription factors at the nuclear lamina. As such, it is not surprising that laminopathies are associated with multiple deregulated signaling pathways that may account for different pathophysiological mechanisms underlying the broad spectrum of clinical phenotypes caused by *LMNA* mutations[140] (Figure 3). However, most of the information regarding deregulated signaling in laminopathies has been inferred from the $Lmna^{H222P/H222P}$ mouse model, generated by a knock-in mutation (H222P) in the *Lmna* gene. These mice manifest EDMD and DCM, with a relatively late disease onset and prolonged survival, thus resembling human disease phenotype[141]. Currently, there is no available treatment for striated muscle laminopathies, and all therapeutic interventions are preventive, symptomatic or supportive. Nonetheless, several treatment options focusing on altered signaling pathways are under investigation[142].

In addition, more novel gene therapy approaches that use antisense oligonucleotides (ASO) and trans-splicing to attenuate the dominant-negative effects of *LMNA* transcripts are currently under development (Figure 5)[143-145].

a. MAPK Signaling Pathway

The mitogen activated protein kinase (MAPK) signaling cascade regulates processes such as cell proliferation, differentiation and apoptosis in response to extracellular growth factors and cytokines[146]. There are multiple branches to this pathway depending on the MAPK, the most common being ERK1/2, JNK and p38α[147]. All three branches of the MAPK pathway were observed to be deregulated in EDMD and DCM. For instance, hyperactivation of ERK1/2, JNK and p38α was observed in the hearts of *Lmna*$^{H222P/\ H222P}$ mutant mice[148]. In addition, phosphorylation and nuclear sequestration of both ERK and JNK were observed in hearts of cardiomyopathy patients with different lamin A/C mutations[148]. The mechanism by which lamin A/C mutations affect MAPK signaling are not fully understood but could be attributed to the interaction between lamin A/C and each of ERK1/2 and its downstream transcription factor c-Fos[55]. Anyhow, one possible mechanism by which hyperactivated MAPK signaling could contribute to lamin A/C-related cardiomyopathies is through increased expression of MAPK target genes[149]. Nonetheless, attenuated gene expression of mechanosensitive genes downstream MAPK pathway has also been observed in lamin A/C-deficient fibroblasts subjected to cyclic strain[150]. A recent study has demonstrated the role of increased actin depolymerization, induced by direct ERK1/2 phosphorylation of the actin-depolymerizing factor Cofilin-1, thus explaining the defects in actin organization and force generation in lamin A/C-related

cardiomyopathies[151]. ERK1/2 activation has a spill-over effect on other signaling pathways, such as TGFβ/Smad and MKL1/SRF signaling pathways which have also been shown to be activated in lamin A/C-related EDMD and DCM (Figure 3). Pharmacological inhibitors of different targets in the MAPK pathway are currently under investigation. Many have proven effective in improving the phenotype of lamin A/C mutant mice and prolonging survival, hence leading to the testing of a p38α inhibitor in clinical trials (Figure 5)[149,152-154].

b. PI3K/AKT/mTORC1 Signaling Pathway

The mTOR signaling pathway links nutrient and energy status of the cell to metabolic control. In this pathway, mTOR is a central serine/threonine kinase and the main catalytic subunit of two distinct complexes: mTORC1 and mTORC2. Activation of mTORC1 by cytokines and growth factors typically occurs through the PI3K/AKT pathway. Nonetheless, mTORC1 is also activated by the Ras/Raf/MEK/ERK1/2 pathway and both mTORC1 and mTORC2 are activated by the Wnt and LKB1/AMPK signaling pathways[155]. mTORC1 activation drives mitochondrial, ribosomal and lysosomal biogenesis, protein, lipid and nucleotide syntheses, and downregulates autophagy. mTORC2 stimulates lipid and glucose metabolism, cell proliferation and survival. Hyperactivation of both AKT and mTORC1 has been noted in *Lmna*$^{H222P/\ H222P}$ mice and correlated with reduced autophagy. Interestingly, mTORC1 inhibition has been shown to restore autophagy and ameliorate cardiac defects in *Lmna*$^{H222P/\ H222P}$ mice[156] (Figure 5). Its inhibition has also been shown to attenuate defects in fibroblasts from patients with different *LMNA* mutations[157].

c. TGFβ/Smad Signaling Pathway

The TGFβ/Smad signaling pathway regulates cell proliferation, fibrosis and extracellular matrix deposition. Activation and nuclear translocation of Smad transcription factors is induced by binding of TGFβ to its receptor. Smads enter the nucleus as a transcriptionally active complex made of R-Smads (Regulatory Smads) and Co-Smads. The TGFβ/Smad Signaling pathway has been shown to be regulated by NE proteins[158]. For instance, the inner NE protein MAN1 opposes TGFβ-induced transcription by binding to R-Smads, thus breaking its association with Co-Smads and inducing their nuclear export[159]. In addition, PP2 a phosphatase that binds lamin A/C has been shown to regulate Smad phosphorylation levels[160]. Thus, disruption of nuclear envelope proteins might affect TGFβ/Smad signaling, which is particularly relevant to muscle regeneration, as TGFβ has been shown to induce satellite cell differentiation. Moreover, elevated TGFβ/Smad signaling has been observed in the hearts of *Lmna*$^{H222P/H222P}$ mice and has been shown to induce ERK1/2 activation[161,162]. Owing to the role of TGFβ in cardiac fibrosis and hypertrophy, it has been suggested to contribute to cardiomyopathy-associated cardiac remodeling.

d. Wnt/β-catenin Signaling

The Wnt/β-catenin signaling pathway, involved in cellular processes including proliferation, differentiation and apoptosis, has been shown to be downregulated in *Lmna*$^{H222P/H222P}$ mice[163]. The transcriptional co-activator β-catenin has different effects on connexin 43 (CX43) expression as well as stability within intercalated discs. β-catenin induces the transcription of CX43 and physically associates with CX43, thus stabilizing

CX43 complexes at intercalated discs. As such, reduced CX43 expression was observed in *Lmna*$^{H222P/H222P}$ mice and was rescued upon restoring β-catenin levels through pharmacological inhibition of GSK-3β, a kinase that targets β-catenin for proteasomal degradation[163]. While reduced CX43 expression was also noted in *Lmna* null mice, *Lmna*$^{N195K/N195K}$ mice showed altered expression and distribution of both CX40 and CX43[164]. These results correlated with the conduction defects seen in *Lmna* knockout or mutant mice. Reduced stability of microtubules is another factor contributing to abnormal distribution of CX43 in *Lmna*$^{H222P/H222P}$ mice. Accordingly, treatment with paclitaxel restored the correct CX43 distribution and attenuated the conduction defects in these mice[165] (Figure 5). Several NE proteins interact with β-catenin and regulate its nuclear import and export. For instance, emerin mediates β-catenin nuclear export, which explains the nuclear accumulation of β-catenin in emerin or lamin A/C deficient cells characterized by enhanced growth and proliferation[166]. In addition, β-catenin has been shown to interact with a complex composed of α-catenin, emerin and nesprin-2 at the NE. This complex has been suggested to recruit β-catenin, which lacks a nuclear localization sequence, thus enabling its nuclear import[167,168]. This is in line with the reduction in β-catenin nuclear levels upon nesprin-2 depletion[168].

Other signaling pathways have also been reported to be deregulated in striated muscle laminopathies. Hyperactivation of forkhead box O transcription factors (FoxO TFs) has been noted in the hearts of *Lmna*$^{-/-}$ mice[169]. FoxO TFs transcribe apoptotic target genes and are inhibited by AKT-dependent phosphorylation[170]. Inhibition of FoxO TFs by shRNA reduced the expression of apoptotic genes in *Lmna*$^{-/-}$ mice. Moreover, FoxO TFs knockout *Lmna*$^{-/-}$ mice showed ameliorated cardiac phenotypes[169]. In addition, the MKL1/SRF

signaling pathway and the YAP/TAZ pathway have also been reported to be deregulated in laminopathies[171,172] (Figure 3).

C. Genetic Basis of Dilated Cardiomyopathy

Nearly 35% of idiopathic DCM cases are familial and are therefore due to a genetic cause[173,174]. Familial DCM gene mutations mainly follow an autosomal dominant mode of inheritance. Nonetheless, autosomal recessive, X-linked and mitochondrial patterns of inheritance also occur but less frequently[175]. The most commonly mutated gene in DCM is *TTN*, being altered in ~25% of familial DCM cases and in 18% of sporadic cases[134,176]. *TTN* encodes titin, the largest known human protein and a key component of the sarcomeres which, through its interaction with thin and thick filaments, plays a role in sarcomere assembly, passive force generation during diastole and elasticity during systole. The majority of *TTN* variants are truncating mutations[176].

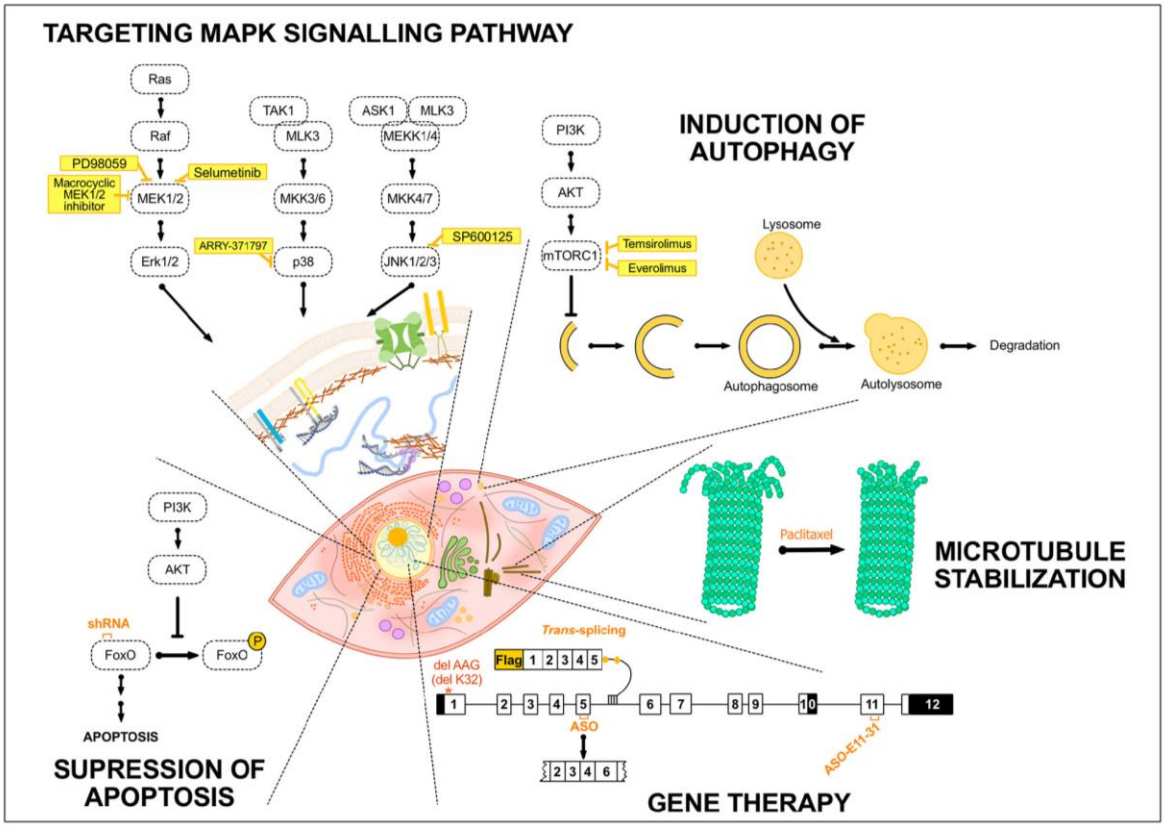

Figure 5. Summary of Potential Therapies for EDMD.
Treatment strategies that have been tested target different components of the MAPK pathway, the PI3K pathway, the apoptotic pathway or exclude mutated exons through exon skipping and trans-splicing based gene therapy. AKT, protein kinase B; ASK1, apoptosis signal-regulating kinase 1; ASO, antisense oligonucleotide; ERK, extracellular signal-regulated kinase; FoxO, forkhead box O; MEK1/2, MAPK/ERK kinase 1/2; MEKK1/4, mitogen-activated protein kinase kinase kinase 1/4; MKK3/6, mitogen-activated protein kinase kinase 3/6; MLK3, mitogen-activated protein kinase kinase kinase 11; mTORC1, mammalian target of rapamycin complex 1; PI3K, Phosphoinositide 3-kinase; Raf, proto-oncogen serine/threonine-protein kinase; TAK1, mitogen-activated protein kinase kinase kinase 7. (Brull et al., 2018).

A study employing human induced pluripotent stem cell-derived cardiac tissue showed that certain *TTN* truncating mutations exert their pathogenicity by improper interaction with other proteins during sarcomere assembly, attenuated contractility and impaired response to stress and growth signals[177]. The *LMNA* gene, which encodes A-type

lamins, is the second most commonly mutated gene in DCM, accounting for ~6% of cases[178]. Mutations in sarcomeric genes such as *MYH7*, *MYH6*, *MYBPC3*, *ACTC1*, *TNNT2* and *TPM1* have also been associated with DCM, collectively being responsible for ~5% of all cases[179]. DCM-causing mutations in *RBM20* gene, which encodes the splicing regulator RNA binding motif protein 20 (RBM20), were first identified in 2009[180]. The studies that followed showed that *RBM20* gene mutations occur at a rate of 3% of all DCM cases[181]. Other pathogenic variants, causing a predominant cardiac DCM phenotype, have been reported in Z-disk, desmosomal and ion channel genes[182-186] (Figure 6).

DCM-associated mutations in the above genes include missense/nonsense mutations, insertions, deletions and splicing mutations[175]. Variants that arise from the different mutations exert their pathogenicity via dominant negative or haploinsufficient effects of abnormal, normal-sized, or truncated proteins respectively. Mechanistically, the diversity of the genes involved in DCM underscore the complexity of the underlying mechanisms. Various mechanistic insights have illustrated abnormalities in protein degradation, transcriptional activity, Ca^{2+}-handling and homeostasis, metabolic activity, nuclear integrity and force generation and transmission[175]. Adding to the mechanistic complexity of DCM, only 30-35% of familial DCM cases follow a Mendelian mode of inheritance, suggesting a more complex mutli-variant or oligogenic basis of inheritance for the remaining cases[178]. In support of this notion, genetic screening methods have revealed the presence of nonrare variants in multiple genes for several DCM cases[187]. Another complicating aspect is the variability of expression of the same mutation in different carriers within the same family. Variability also occurs in terms of onset, severity, progression and phenotype of disease. For instance, the 960delT mutation in the *LMNA*

gene may be manifested as primary DCM, or DCM associated with either EDMD-like or limb girdle muscular dystrophy (LGMD)-like phenotype[188].

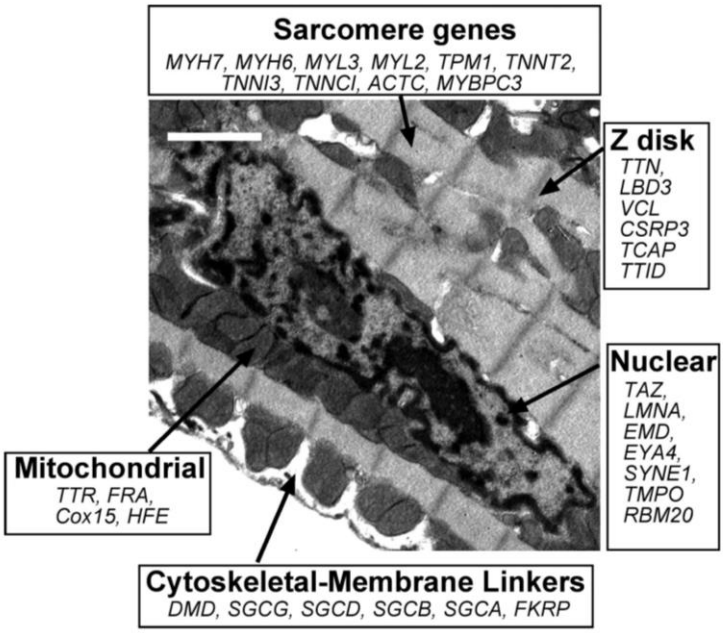

Figure 6. DCM-Associated Genes.
An electron micrograph of a cardiomyocyte depicting some of the most commonly mutated genes in DCM, grouped according to subcellular localization and function. Error bar = 2μm. (Dellefave & McNally, 2010).

D. Splicing Alterations in DCM

Several splicing factors have been associated with heart diseases including DCM[189]. Splicing alterations in DCM arise from splicing factor deletion or downregulation, deregulation in expression of alternative splicing isoforms and splice-site mutations.

1. Splicing Factor Deletion or Downregulation

Embryonic lethality of mouse knockout models of essential splicing factors narrowed the list of splicing regulators described to cause human cardiac pathologies. Nonetheless, many of these splicing factors were shown to be embryonically lethal due to aberrant cardiogenesis. For instance, RNA binding motif protein 24 (RBM24) knockout mice die of many cardiac abnormalities and show hindered sarcomere formation. Further analysis showed that RBM24 is responsible for splicing of 64 genes many of which are important for cardiac development and sarcomere function, which goes in line with its preferential expression in striated muscle tissue[190]. By generating Rbm24 conditional knockout mice, a recent study showed that postnatal homozygous deletion of RBM24 in the heart causes DCM that rapidly progresses into lethal heart failure. RBM24 deletion was associated with prevalent missplicing of cardiac genes including titin[191]. This recent finding has raised the first speculations of whether RBM24 is a novel but rare DCM gene[192]. In addition, loss of SRSF10 (or SRp38), a ubiquitously expressed splicing factor belonging to the conserved SR (serine/arginine) protein family, leads to embryonic lethality due to impaired cardiogenesis. Particularly, its loss has been shown to be associated with altered expression and splicing of Ca^{2+} handling genes[95].

Another example is the ubiquitously expressed SR protein ASF/SF2 (or SFRS1), which plays a role in both constitutive and alternative splicing. As it is embryonically lethal, conditional cardiac-specific ablation of ASF/SF2 has been shown to result in DCM due to aberrant Ca^{2+} handling and excitation-contraction coupling. These effects were attributed to missplicing of several genes including Ca^{2+}/calmodulin-dependent protein kinase II delta (*CamkIIδ*), troponin T2 (*TNNT2*), and LIM domain binding 3 (*LDB3*)[92].

SC35 (or SRSF2) is another ubiquitously expressed SR protein whose heart-specific loss results in DCM. Although a missplicing effect of SC35 was not confirmed, downregulation of ryanodine receptor 2 (RyR2) was observed in SC35-deficient hearts. This downregulation is speculated to be an effect of the nonsense-mediated decay pathway of misspliced RyR2 mRNA. In addition to its heart-specific effects, SC35 appears to be essential for embryogenesis as knockout mice die at a very early stage even before the beginning of cardiogenesis[88]. In addition to SR proteins, a heterogeneous nuclear ribonuclear protein (hnRNP) family member, hnRNP U that acts both as a constitutive and alternative splicing factor, has been associated with cardiac disease. Heart specific deletion of hnRNP U was shown to be lethal during early postnatal life due to the development of severe DCM. The DCM phenotype was associated with altered alternative splicing of the Ca^{2+} handling gene *CamkIIδ*[193].

Dysregulation in the expression of certain splicing factors has also been shown to be associated with cardiac disease. For instance, Rbfox2 which belongs to the FOX-protein family of splicing regulators is down-regulated in heart disease. Rbfox2 regulates the alternative splicing of many genes that are related to cardiac function and its heart-specific deletion in mice develops DCM and heart failure[194].

Despite the associations of several splicing factors with cardiac pathologies, mutations in a single splicing factor, RBM20, have thus far been confirmed to cause heart disease[180,195,196]. Mutations in the *RBM20* gene have recently been shown to cause DCM[180,195,196], putting it forward as one of the most commonly affected genes in DCM[181]. In addition to being prevalent among DCM patients, *RBM20* mutations rank first for the youngest mean age of heart transplantation and are correlated with advanced disease[137,180].

2. Deregulation in Alternative Splicing Isoform Expression

Many studies revealed, by deep sequencing and microarray analysis, sets of genes that show differential splicing between control and diseased heart; yet the mechanisms behind these alterations were not identified. In humans, splicing alterations of the sarcomeric genes, *TNNT2* (troponin T2), *TNNI3* (troponin I3), *MYH7* (myosin heavy chain 7), and *FLNC* (filamin C gamma) were observed in both DCM and hypertrophied myocardium. Interestingly, the ratio of the different splice-isoforms of each of *TNNT2*, *MYH7*, and *FLNC* served as markers that distinguished failing from non-failing heart[197]. Down-regulation of the L-type voltage gated Ca^{2+} channel Cav1.2 has previously been associated with cardiac hypertrophy and heart failure[198,199]. Recently, a novel neonatal splice variant of Cav1.2 has been identified and was shown to be aberrantly re-expressed in adult rodent heart, upon pressure overload-induced cardiac hypertrophy, as well as in left ventricles of DCM patients. Re-expression of the identified isoform by missplicing of the Cav1.2 gene, *Cacna1c*, promoted proteasomal degradation of wild-type Cav1.2, thus explaining the reported decreased expression and activity of Cav1.2 in cardiac hypertrophy[200].

3. Splice-Site Mutations

In addition to loss or dysregulation of splicing factors, splice site mutations also cause splicing alterations and disease[189]. DCM has also been associated with splice-site mutations in its most commonly mutated gene, *TTN*. One fourth of idiopathic familial DCM cases harbor truncated titin proteins and almost 31% of mutations that generate a

truncated titin protein are splice-site mutations[201]. Splice site mutations in *TTN* are also thought to be responsible for HCM through the generation of a truncated titin protein which results in a reduced myocardial passive stiffness[201]. However, while *TTN* truncating mutations frequently occur in DCM, they are rare in HCM[201]. In addition, splice site mutations in other genes such as those encoding for lamin A/C (*LMNA*)[202], desmoplakin (*DSP*)[203] and dystrophin (*DMD*)[204] have been reported in DCM. For instance, an A > G substitution at the 3'splice site of exon 4 of *LMNA* gene leads to an in-frame addition of 3 amino acids to lamin A/C protein thus causing DCM[205].

E. RBM20 and Cardiac Function

1. RBM20 Expression During Development

RBM20 is an RNA-binding protein (RBP) that regulates alternative mRNA splicing. RBPs have been shown to be involved in almost every stage of heart development[206]. Based on the importance of RBM20 in regulating myofibril formation and function, its role was suggested to coincide with heart tube development[206]. Supporting this hypothesis, RBM20 expression was first detected between E7.5 and E8.5 of *in vivo* mouse cardiogenesis, coincident with the appearance of the cardiac crescent and the primitive heart tube respectively. Moreover, RBM20 expression occurred in a timely manner with the induction of known pre-cardiac genes and continued steadily throughout cardiac maturation[207]. In addition, RBM20 expression in differentiating C2C12 myoblasts was shown to correlate with sarcomere assembly, with lowest levels in undifferentiated cells, intermediate levels before and after sarcomere assembly and highest levels midway during sarcomere assembly[208].

2. RBM20 Structure and mRNA Binding Motif

RBM20 belongs to the SR family of RBPs characterized by an arginine-serine rich (RS) domain that mediates interactions with other proteins and at least one RNA recognition motif (RRM) that binds RNA. RBM20 has one RRM domain in exons 6 and 7, an RS domain in exon 9, and two zinc finger domains of the U1 type[208,209] (Figure 7). Besides their RNA splicing role, SR proteins are usually implicated in mRNA nuclear export, stability and translation[209]. The subcellular localization and, hence, function of SR proteins is determined by their phosphorylation state. Phosphorylation of SR proteins at their RS domain drives their nuclear localization. In the nucleus, they mediate the assembly of the spliceosomal complex and recruitment to pre-mRNA through interactions of their RRM and RS domains with pre-mRNA and regulatory proteins respectively. Finally, dephosphorylation of SR proteins causes their nuclear export[210,211].

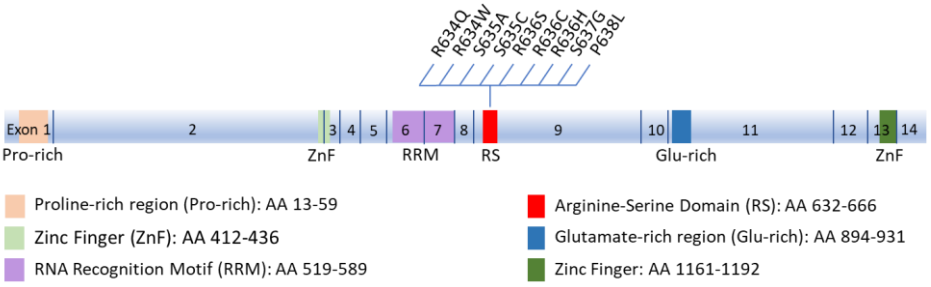

Figure 7. Schematic Diagram of Rbm20 Structure.
The 14 exons and the corresponding functional domains of the protein are indicated, along with the amino acid residues spanned by each domain. All known mutations in the RS region that cluster in a five-amino acid mutation hotspot (residues 634-638) are also shown. (Zahr & Jaalouk, 2018).

RBM20 has been shown to bind to a distinct UCUU-containing RNA recognition element that is conserved between rats and humans. This binding motif is enriched within introns, such that binding of RBM20 to intronic regions flanking 3′ and 5′ splice sites represses exon splicing[212]. Many cardiac-expressed transcripts containing the UCUU motif have been shown to directly bind RBM20. The most prominent of these targets is *TTN* which encodes the protein titin[212]. In addition to *TTN*, transcripts of 17 genes (*CamkIIδ*, *DST*, *ENAH*, *IMMT*, *LDB3*, *LMO7*, *MLIP*, *LRRFIP1*, *MYH7*, *MYOM1*, *NEXN*, *OBSCN*, *PDLIM3*, *RTN4*, *RyR2*, *SORBS1*, *TNNT2*) were shown to be directly regulated by RBM20, mainly by mutually exclusive splicing[212]. Splicing regulation of mutually exclusive exons is often related to the expression of tissue-specific splice variants[213]. This regulation mechanism is in accord with the tissue-specific expression of RBM20, being chiefly expressed in striated muscle with the highest amounts in cardiac muscle[208]. Supporting this idea is the enrichment of the identified RBM20 targets for tissue-specific diseases associated with RBM20 mutations (DCM, hypertrophic cardiomyopathy and heart failure) according to NCBI Medical Subject Heading (MeSH)[29].

3. RBM20 Splicing Targets

To date RBM20 has been shown to regulate the alternative splicing of 31 genes, many of which are associated with cardiomyopathies and cardiac cell biology[208]. RBM20 regulates several sarcomeric and calcium-regulating genes, thus influencing sarcomere structure and function. The most prominent targets of Rbm20 are discussed below.

a. Titin

The genuine splicing target of RBM20 is titin[196,208,214], an enormously large elastic protein that spans half the length of the sarcomere[215].Titin maintains the structural integrity of the sarcomere and restores it to normal length following extension and contraction[216]. Alternative splicing of titin results in many protein isoforms, the most common are N2B and N2BA isoforms[217]. N2B isoform is short and rigid while N2BA isoforms are longer and more compliant[218]. The relative ratio of short to long titin isoforms is developmentally regulated and is a determining factor of myocardial passive stiffness[218,219]. Cardiac N2BA is predominantly expressed during fetal life; however, N2B isoform becomes mainly expressed after birth[218,220,221]. This shift in titin isoforms is essential for proper diastolic function[220,222] as N2B-enhanced passive stiffness prevents ventricular overfilling during diastole[220]. In addition, titin isoform switch is important for systolic function as N2B-increased Ca^{2+} sensitivity improves contractility during systole[222].

b. Myomesin 1

Another direct target of RBM20 is myomesin1, a structural component of the sarcomeric M-line. Interaction of myomesin with myosin and titin is responsible for structural organization of these contractile proteins and sarcomere integrity during contraction[223]. In addition, the presence of a phosphorylation site in myomesin suggests that it responds to stretch-dependent signaling[224]. Myomesin 1 undergoes an isoform switch in a timely manner with titin[225]. After birth, myomesin 1 isoforms that lack a molecular spring domain (EH domain) become upregulated[225]. The myomesin1 switch has been suggested to

enhance alignment of contractile filaments and contraction efficiency[226]. Remarkably, re-expression of fetal isoforms of both titin and myomesin has been observed in DCM[227-229].

c. Tropomyosin 1

Tropomyosin 1 (TPM1), a component of thin filaments, is yet another target of RBM20[208]. Tropomyosin binds actin and mediates contraction in response to Ca^{2+} binding to troponin. Alternative splicing of TPM1 results in two striated muscle specific isoforms (TPM1α and TPM1κ) and a smooth muscle specific isoform (TBM1β). The specific role of RBM20 in these splicing events is not known. However; overexpression of the TBM1κ isoform has been observed in DCM patients and has been shown to cause systolic and diastolic dysfunction in transgenic mice[230].

d. Lim domain binding 3

RBM20 regulates the tissue-specific splicing of Lim domain binding 3 (LDB3), a Z-line structural protein important for maintaining sarcomere integrity during contraction[208,212,231]. RBM20 controls the inclusion of mutually exclusive exons of LDB3 that are either present in its cardiac-specific isoform (exon 4) or skeletal muscle-specific isoform (exons 5 and 6). Loss of RBM20 results in the inclusion of exons 5 and 6 rather than exon 4[208]. Moreover, mutations in exon 4 as well as in another cardiac-specific exon (exon 10) of LDB3 were identified in DCM patients[232]. Thus, loss of exon 4 due to loss of RBM20 might contribute to the development of the DCM phenotype in *Rbm20* null mice[208,232].

e. CamkIIδ

RBM20 is also a splicing regulator of CamkIIδ, a crucial enzyme in the heart[208]. Four of the eleven isoforms described for CamkIIδ are expressed in the heart[233]. CamkIIδ isoforms phosphorylate proteins of the sarcomere and the sarcoplasmic reticulum, calcium channels and transcription factors thus affecting cell signaling, Ca^{2+} handling and gene expression[93,94,234,235]. As such, splicing regulation of CamkIIδ by RBM20 can greatly affect cardiac function by modulating these processes. This is further elucidated by the association of dysregulated CamkIIδ isoforms with DCM and heart failure[93,94].

4. Regulation of Rbm20

Both insulin and triiothyrodine (T3), a thyroid hormone, have been shown to trigger titin isoform switching in an RBM20 dependent manner, thus favoring the expression of the short N2B isoform[236-238]. Mechanistically, RBM20 has been shown to be activated through the PI3K/AKT pathway, possibly by AKT-mediated phosphorylation which goes in line with the observed AKT activation upon insulin or T3 treatment. Phosphorylation of RBM20 might also be mediated by SR protein kinases (SRPK) which regulate the activity of SR proteins by phosphorylation at an evolutionary conserved motif within the RS domain[239,240]. In fact, it has been shown that the activation of PI3K/AKT/SRPK axis plays a major role in EGF-induced alternative splicing[211,239,241]. Moreover, both insulin and T3 treatments induced upregulation of RBM20 at both the transcript and protein levels[236,238]. This increase in RBM20 gene expression could result from the activation of mTOR via the PI3K/AKT pathway[242]. In addition to insulin and T3, angiotensin II was shown to

upregulate RBM20 expression levels in neonatal cardiomyocytes, thus mediating the expression of the short N2B titin isoform[243]. More studies are needed to decipher the complete upstream regulation of RBM20. Nonetheless, another level of regulation of RBM20 is mediated through its interactions with other splicing regulators that might bestow an inhibitory, excitatory or synergistic effect. For instance, both RBM20 and RBM24 were shown to cooperatively regulate the alternative splicing of *Enh* gene, which encodes a PDZ-LIM domain scaffold protein. Although each of RBM20 and RBM24 poorly regulated *Enh* splicing; association of both splicing factors promoted the expression of the short isoform, ENH3, and repressed the expression of the long isoform, ENH1[244]. Both RBM20 and RBM24 mRNA were downregulated in response to neurohumoral factors such as endothelin-I, phenylephrine and aldosterone[244]. Moreover, RBM20 splicing activity of titin was shown to be counteracted by PTB4, a novel splicing regulator of titin[245].

F. RBM20 Gene Mutations in DCM

In an attempt to find a novel pre-clinical biomarker for DCM, genome-wide analysis of 8 families with DCM uncovered distinct heterozygous missense mutations in exon 9 of *RBM20*. These mutations segregated with the DCM phenotype, which led to the recognition of *RBM20* as a DCM-causing gene[180]. Genotype-phenotype associations linked *RBM20* mutations with aggressive DCM characterized by variable symptoms that include arrhythmias, heart failure and sudden death. Patient-derived tissues also showed variable involvement of cardiac hypertrophy and interstitial fibrosis[180]. Multiple *RBM20* mutations were identified by subsequent studies[195,196]. The role of *RBM20* in DCM was revealed in rats harboring a loss of function mutation that removes the RRM, RS and zinc finger

domains (exons 2-14) of *RBM20*[208]. This spontaneously occurring mutation resulted in altered titin mRNA splicing. In addition to titin, alternative splicing of 30 other transcripts was shown to be altered in both rats and a DCM-patient carrying an S635A missense mutation in the RS region of RBM20. The identified RBM20-dependant genes were enriched for genes related to ion-handling, sarcomere function and cardiomyopathy[208]. As most of the identified genes are key determinants of cardiac cell function and as some of them have been associated with cardiomyopathy, their missplicing is thought to be a key determinant of the DCM phenotype. This is illustrated by impairment of the Frank-Starling mechanism (FSM) as a result of expression of longer and more compliant titin isoforms in Rbm20-deficient mice[214]. In addition to titin, missplicing of other sarcomeric proteins, such as myomesin 1, might affect their contractile function. On the other hand, splicing alterations in other RBM20 targets such as *CamkIIδ*, *RyR2*, and *Cacna1c* might affect Ca^{2+} homeostasis. Indeed, Rbm20 deficiency induces a switch into larger cardiac-specific isoforms of CamkIIδ, which might compromise its normal function[212].

In addition to altered expression of adult/fetal protein isoforms, RBM20 loss or mutation is also manifested in deregulation of tissue-specific protein isoforms or mislocalization of misspliced proteins. For instance, RyR2 and CamkIIδ aberrant splicing caused by RBM20 mutation results in the expression of mislocalized protein isoforms. RyR2 constitutes the key calcium release channel in the sarcoplasmic reticulum membrane that plays a role in excitation-contraction coupling. A 24-bp exon inclusion in RyR2 transcript causes a translocation of the corresponding protein from the ER to the intranuclear cisternae, thus deeply affecting calcium signaling[246]. Interestingly, RyR2 transcripts containing this exon are upregulated in *Rbm20*-null rats as well as in

cardiomyopathy patients[212]. Moreover, mutations affecting RyR2 function have been associated with cardiomyopathies[247]. Remarkably, DCM-associated RBM20 mutation reversed the splicing of mutually exclusive exons in CamkIIδ, resulting in an isoform switch from CamkIIδB into CamkIIδA. Although both isoforms are expressed in the heart, CamkIIδB is predominantly found in the nucleus where it regulates gene expression[93], while CamkIIδA lacks the nuclear localization signal and is mainly located in T-tubules where it plays a role in facilitation of the L-type calcium channel (LTCC)[234]. This isoform switch has been shown, under other circumstances, to cause excitation-contraction coupling defects and proneness to tachyarrhythmia, symptoms that are also seen in DCM caused by RBM20 mutations[92]

RBM20 has also been shown to repress splicing of different targets (such as LMO7, RTN4, PDLIM3 and LDB3) in favor of their heart specific isoforms. LMO7 is a transcription factor that regulates both skeletal and cardiac muscle-related genes[248]. RBM20 represses the inclusion of exons 9 and 10 which characterize the brain specific isoform of LMO7[212,249]. Although LMO7 has not been associated with DCM, expression of its brain specific isoform in the absence of RBM20 might be an important disease mechanism. Similarly, RBM20 suppresses the neuronal-specific isoform of RTN4 in favor of the heart-specific isoform[212]. RTN4 is a neurite growth inhibitor with unknown role in the heart[250]. Brain-specific RTN4 isoform is weakly detected in the heart; however, it is upregulated in cases of ischemia and DCM and has also been suggested as a marker of heart failure[251-253].

Most reported cardiomyopathy-related mutations in the *RBM20* gene arise in the RS region which includes a five-amino acid mutation "hotspot" within exon 9[127,180,195,196,208,254-257] (Figure 7). The RS region is thought to mediate protein-protein

interactions[209]. Indeed, quantitative proteomic analysis revealed that RBM20 interacts with many protein components of the U1 and U2 small nuclear ribonucleoproteins (snRNPs), which associate with pre-mRNA to form spliceosomal complex A of the spliceosome. Moreover, the RNA recognition element of RBM20 is proximal to U1 and U2 snRNP binding sites. Association of RBM20 with early-stage spliceosomal assembly but not with the catalytically active spliceosome has been suggested to stall further spliceosomal assembly beyond complex A formation, thus causing splicing repression[212]. As such, mutations in the RS region of RBM20 are expected to abrogate protein-protein interactions essential for RBM20 function as a splicing repressor. Indeed, the DCM-associated S635A mutation in the RS region of RBM20[208] has been shown to considerably reduce interactions with 38 alternative spliceosomal factors with no effect on interactions with fundamental spliceosomal proteins. One possible explanation of this outcome is that association of RBM20 with these alternative splicing factors might be needed for the suggested spliceosomal stalling mechanism and splicing repression[212].

In addition to protein-protein interactions, binding of RBM20 to nascent transcripts is important for its function. Indeed, mutations in exon 6 of *RBM20* were identified in idiopathic DCM patients. As these mutations localize to the RRM domain of RBM20, they are expected to disrupt its binding to mRNA[196]. Mice lacking the RRM domain of RBM20, by deletion of exons 6 and 7, exhibit altered titin splicing with a favored expression of more compliant titin isoforms that increased in length from heterozygous to homozygous RBM20 mutant mice (Figure 8). Increased titin compliance was associated with a decrease in passive stiffness and FSM which also correlated with the number of affected alleles[214]. Along the same line, mutations in the RBM20 binding site

also influence its splicing activity[212]. Although many other missense and nonsense mutations of RBM20 have been identified in DCM patients, their functional consequences have not been explored[181,195,258,259]. Yet, many of these mutations localized to novel exons of *RBM20*, including exons 2, 4, 11 12, 13 and 14[195,258,260].

Recently, a novel familial DCM-causing mutation (E913K) in a glutamate-rich region of RBM20, encoded by exon 11, has been studied. Although the region of the mutation is not characterized, its conservation across distinct species suggests its functional significance. This mutation was shown to cause a strong reduction in RBM20 protein levels in human cardiomyocytes, which was suggestive of compromised RBM20 protein stability. One possible mechanism that could affect protein stability is the generation of misfolded proteins and their subsequent proteasomal degradation. The outcome of reduced RBM20 protein levels was manifested in the aberrant inclusion of several exons in the spring region of titin. Missplicing of titin caused a dramatic shift from the stiff N2B isoform to the highly compliant N2BA isoform and resulted in an attenuated FSM[260]. Notably, similar effects on titin splicing and the FSM were previously reported in a mouse model of RRM-deficient RBM20 as well as in mice lacking RBM20[214].

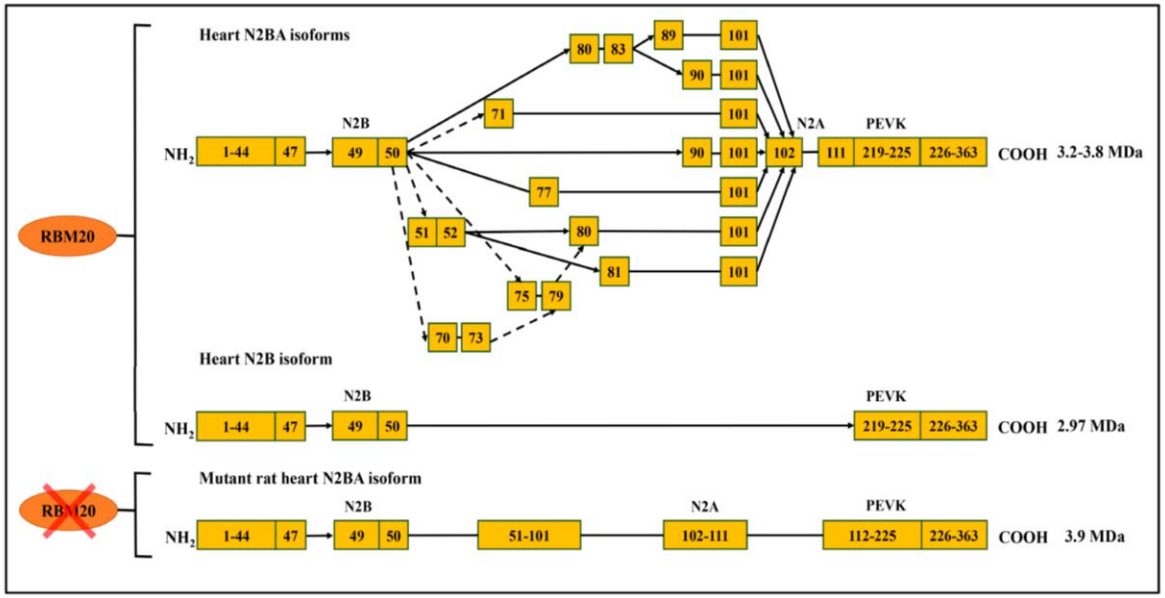

Figure 8. Regulation of Titin Alternative Splicing by RBM20 in the Heart.
In the presence of Rbm20 the ratio of N2B to N2BA titin isoforms is developmentally regulated with predominant N2B expression in the adult heart. Rbm20 loss or mutation causes a switch in the expression of titin isoforms, in favor of the longer and more compliant N2BA isoforms. The figure only shows splicing events that occur in the immunoglobulin (Ig) region, but more complex splicing also occurs in the PEVK (Proline (P), Glutamate (E), Valine (V), Lysine (K)) region. Arrows indicate spliced exons while lines denote consecutive exons. (Rexiati et al., 2018).

G. Synopsis

The structural and functional interactions between different DCM-causing genes (Figure 9) suggest common or overlapping disease mechanisms. The interaction of lamin A/C with several splicing factors and the emerging role of splicing factor mutations and splicing deregulation in DCM suggests that lamin A/C plays more than a mere scaffolding role at splicing factor compartments. Moreover, *LMNA* mutations affect important cellular signaling pathways that might be involved in splicing regulation. For instance, the PI3K/AKT/mTOR signaling pathway is deregulated in *LMNA* mutations; and the same pathway is thought to regulate both the expression and splicing function of RBM20.

RBM20 and the newly identified Rbm24 are currently the most prominent DCM-associated splicing factors that are characterized by tissue-specific expression with highest amounts in striated muscle. As such, studying the role of DCM-associated splicing factors in lamin A/C related EDMD and DCM would offer new insights into the mechanisms of tissue-specific effects of these debilitating diseases.

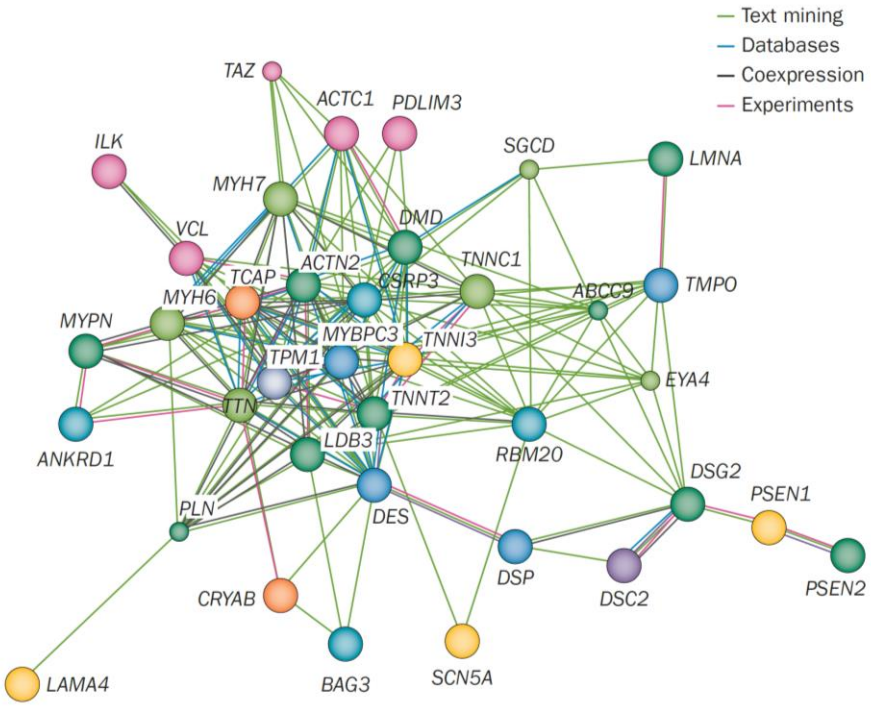

Figure 9. STRING Database Gene-Gene Interactions of DCM-Associated Genes. The colored lines represent the indication that led to the depicted association, with text mining being the weakest and experimental evidence being the strongest. (Hershberger et al., 2013).

CHAPTER II

PROFILING OF NUCLEI FROM WILD-TYPE AND LAMIN A/C-DEFICIENT MOUSE EMBRYO FIBROBLAST CELLS USING DIRECT AND DIFFERENTIAL PHAGE DISPLAY BIOPANNING

Authors[1]: Hind C. Zahr, Heinrich zu Dohna, Jan Lammerding, and Diana E. Jaalouk

A. Abstract

Laminopathies are versatile disorders including skeletal and cardiac muscular dystrophy. They are caused by mutations in the *LMNA* gene, which encodes for lamins A and C that anchor other proteins to the nuclear envelope. The mechanisms underlying the phenotypic diversity in laminopathies have not been fully deciphered. We employed a phage display-based approach termed Biopanning and Rapid Analysis of Selective Interactive Ligands for profiling of nuclei from $Lmna^{+/+}$ and $Lmna^{-/-}$ mouse embryo fibroblasts. Direct biopanning resulted in significant enrichment in phage binding to both

[1] Zahr C. H., zu Dohna H., Lammerding J., Jaalouk E. D. Profiling of Nuclei from Wild-type and Lamin A/C-Deficient Mouse Embryo Fibroblast Cells Using Direct and Differential Phage Display Biopanning. Manuscript in revision. D.E.J. and J.L. conceived and designed the overall project. H.C.Z. and D.E.J. performed the experiments and data acquisition. H.C.Z., H.D., and D.E.J. contributed to the data analysis and interpretation. H.C.Z. and D.E.J. wrote the paper. H.D. and J.L. revised the paper.

types of nuclei whereas differential biopanning resulted in significant enrichment in phage binding to *Lmna*$^{+/+}$ nuclei, but not to *Lmna*$^{-/-}$ nuclei. Sequencing the inserts in phage plaques, we identified panels of peptides with preferential binding to either type of nuclei. Bioinformatic analysis indicates differential clustering of the derived peptides and uncovers proteins they mimic. In addition to identifying previously reported A-type lamin interactors, the assay also found several novel proteins including HuR, an RNA-binding protein that is also implicated in splicing regulation. By text mining the GeneCard and UniProt databases, we mapped the functional distribution of the protein panels identified in the three screens and noted overlapping and distinct functional patterns. Herein, we show that Lamin A/C and HuR co-immunoprecipitate, and that the presence of A-type lamins in the nucleus influences the subcellular localization of HuR. The proteomic profiles reported in this study unveil novel players that warrant further investigation, potentially providing mechanistic insights into the tissue-specific phenotypes in laminopathies.

B. Introduction

Lamins are type-V intermediate filaments exclusively found in the nucleus. Mammalian cells express two types of lamins, the A-type and the B-type. Both share a common structural organization and form parallel coiled-coil dimers, which in turn assemble into stable strings and higher-order networks [261]. Their ability to polymerize allows them to form the nuclear lamina, a dense protein meshwork underlying the inner nuclear membrane (INM). The nuclear lamina also consists of associated nuclear envelope (NE) proteins. In addition, lamins are also found to a lesser extent in the nucleoplasm [112].

A-type lamins are encoded by the *LMNA* gene, which gives rise by alternative splicing to four isoforms, with lamins A and C (lamin A/C) being the most common in somatic cells. The first *LMNA* mutation was reported by Bonne *et al.* in 1999 as a non-sense mutation that causes autosomal dominant Emery–Dreifuss muscular dystrophy (EDMD) [104]. Since then, a torrent of publications linked different mutations in the *LMNA* gene to phenotypically different diseases, commonly called laminopathies, which affect diverse tissues in the body [107,112]. More than 400 *LMNA* mutations have been identified to date, the majority of which are linked to muscular dystrophies and cardiac disease [262]. With the increased identification of *LMNA* mutations, the number of functions associated with A-type lamins has also expanded. These functions range from providing structural and mechanical support to the nucleus to influencing chromatin organization, transcriptional regulation, and DNA replication and repair [29]. These pleiotropic functions make laminopathies particularly important, especially since the associated cardiac symptoms result in high incidence (> 40%) of sudden cardiac death in affected patients [263-266].

The mechanisms underlying the pathogenesis of laminopathies—particularly how mutations in a single, nearly ubiquitously expressed gene can result in diverse tissue-specific phenotypes—are inadequately understood. Two rationales, that are not mutually exclusive, have emerged to explain how mutations in lamin proteins could cause the disease phenotypes of laminopathies. The "gene regulation" rationale proposes that disrupted gene regulation may underlie the development of different disease phenotypes, while the "structural fragility" rationale proposes that mutations in the lamin proteins render the nucleus more fragile, causing cell death and eventually disease in mechanically stressed tissues [267-269]. The creation of the first *Lmna* deletion mouse model allowed studying the

effect of complete loss of lamin A/C function [270]. The homozygous (*Lmna*$^{-/-}$) mice display the EDMD phenotype characterized by skeletal muscle dystrophy and dilated cardiomyopathy with conduction defects [270]. Although they appear similar to their wild-type (WT) littermates at birth, they soon suffer from retarded growth and die by eight weeks of age [270]. Mouse embryonic fibroblast (MEF) cells derived from the *Lmna*$^{-/-}$ mouse model have irregular nuclear morphology and compromised nuclear integrity, accompanied by the mislocalization of emerin from the NE [24,270,271]. Moreover, cells deficient in lamin A/C have decreased nuclear stiffness, increased nuclear fragility, and impaired mechanotransduction signaling [272-274], which could contribute to the gradual loss of muscle cells in laminopathies. However, direct nuclear damage alone is insufficient to explain the different and severe myopathy phenotypes found in many of these diseases [275,276].

The discovery of two NE protein families, nesprins and SUN proteins, provided new insights into the muscle specific effects of *Lmna* mutations. SUN proteins, located on the INM, interact across the perinuclear space with nesprins on the outer nuclear membrane (ONM) to form the Linker of Nucleoskeleton and Cytoskeleton (LINC) complex, thereby linking the nucleus to the cytoskeleton [277,278]. Lamins A/C can directly bind to nesprins and SUN proteins and contribute to their correct localization at the NE [279-281]. Loss of lamin A/C or *Lmna* mutations could thus disrupt the LINC complex function [72,282]. Hence, it is conceivable that in addition to the nesprins and the SUN proteins, a number of other NE and/or NE interacting proteins implicated in nuclear-cytoskeletal coupling and/or other biological processes are similarly affected by complete lamin A/C loss or by distinct mutant forms in a tissue-specific manner. Recent findings regarding the tissue specificity of the NE

proteome provide strong support for this viewpoint [283]. We therefore hypothesize that there are differential panels of proteins that may home to and/or interact with the NE bearing an intact nuclear lamina, and that these proteins are lost from the NE in cells lacking A-type lamins. The loss of these proteins could differentially influence biological processes and pathways that would convey tissue-specific phenotypes in the diverse laminopathies.

To address this hypothesis, we employed a phage display-based technology termed Biopanning and Rapid Analysis of Selective Interactive Ligands (BRASIL) to profile the nuclear proteomic differences in *Lmna*$^{+/+}$ versus *Lmna*$^{-/-}$ MEF cells. Advancements made to peptide phage display technology in the past two decades have rendered it a powerful modality for high-throughput screening of protein interactions with versatile applications in biomedical science [284]. In line with these advances, the BRASIL method of phage display was developed by the Arap-Pasqualini Laboratory for single-cell targeting with genetically-modified phage libraries [285]. It allows cell-phage complexes to be separated from the remaining unbound phage while reducing nonspecific binding and artifacts obtained with the standard phage washing methods. Here, we present the first application of this method of phage display for nuclear biopanning to characterize lamin A/C-dependent differences in the NE proteome. A major advantage of using this approach is that protein-protein interactions are assessed in an unbiased functional assay, without any pre-conceived notion about the type or the nature of the uncovered proteins. Thus, nuclear panning with differential phage display using the BRASIL method provides an ideal tool for the identification of changes in the proteome, particularly at the NE, in the context of A-type lamin loss. In contrast to yeast two-hybrid screens or in vitro pull-down assays, this method

also maintains the in situ organization of the NE, including specific protein localization to the INM or ONM. Using this approach, we uncovered panels of peptides with preferential binding to either type of nuclei and identified the putative proteins they mimic. A number of these proteins were previously reported as A-type lamin interactors or altered in laminopathies, but the nuclear BRAZIL method also pointed to several novel proteins that are plausibly lost from the NE in *Lmna*$^{-/-}$ cells. By virtue of their bio-functional relevance, these novel hits warrant further investigation into their implication in the tissue–specific pathogenesis in laminopathies.

C. Materials and Methods

1. Cell Culture

WT and lamin A/C-deficient immortalized MEF cell lines were obtained from Lammerding Laboratory (Cornell, NY). Lamin A/C-deficient MEF cells were derived from *Lmna*$^{-/-}$ mice and WT MEFs were derived from *Lmna*$^{+/+}$ littermates[286]. Cells were maintained in Dulbecco's Modified Eagle's Medium DMEM-AQ media (D0819, Sigma-Aldrich), supplemented with 1% penicillin-streptomycin (DE17-602E, Lonza), 10% fetal bovine Serum (F9665, Sigma-Aldrich) and 1% sodium pyruvate (S8636, Sigma-Aldrich). 1x phosphate buffered saline (PBS) without calcium and magnesium (17-517Q, Lonza) and 1x trypsin (BE17-160E, Lonza) were used for washing and detaching cells. Trypan blue vital exclusion stain was used to determine the number of viable cells. A hemacytometer was used for counting both viable cells and intact nuclei. Cells and nuclei were visualized using a standard phase-contrast microscope (Olympus microscope, Axiovert 200, Zeiss).

2. Nuclear Isolation

When cells reached 80% confluence, nuclear isolation was performed using the Nuclei EZ Prep Nuclei Isolation Kit (NUC-101, Sigma) based on the manufacturer's instructions. Cells were washed with 10ml ice-cold PBS, detached with trypsin and neutralized with DMEM-AQ media. Following centrifugation at 600xg, 4°C for 5min, the cell pellet was resuspended in PBS and counted. Another centrifugation step was done to separate and remove the PBS. Ice cold Nuclei EZ lysis buffer was then added to the pellet; 4ml per $5x10^6$ cells, mixed and left on ice for 5min. Nuclei were collected by centrifugation at 500xg, 4°C for 5min. The pellet was vortexed briefly, resuspended in Nuclei EZ lysis buffer and set on ice for 5min. Nuclei were then collected by centrifugation, supernatant removed and the pellet was re-suspended in 200µl ice-cold Nuclei EZ storage buffer. Nuclei were microscopically checked for integrity and stored at -80°C in Nuclei EZ storage buffer. On the day of phage display screening, nuclei were counted and bio-panning was performed on $50x10^3$ nuclei in 50µl Nuclei EZ storage buffer.

3. Nuclear Integrity Assay

Nuclei from WT and Lamin A/C deficient MEF cell lines were stained for Lamin B1, a marker of nuclear integrity, following isolation and storage in nuclei EZ storage buffer at -80°C. Briefly, cover slips were coated with 150µl of a 1:10 dilution of Sta-On liquid adhesive (3803105, Leica Biosystems) using a slide spinner at 1500rpm for 2min. Nuclei were counted by Trypan blue vital exclusion stain and 10-500,000 nuclei were

smeared on the coated coverslips, placed in 6-well plates. Nuclei were then fixed with methanol for 10min at -20°C and permeabilized with acetone for 1min at -20°C. Nuclei were stained with Lamin B1 primary antibody (sc-374015, SANTA CRUZ BIOTECHNOLOGY) at a dilution of 1:50 and Alexa Fluor-conjugated secondary antibody (ab150113, abcam) at a dilution of 1:500. Coverslips were mounted on slides using ultraCruz Hard-set mounting medium (sc-359850, SANTA CRUZ BIOTECHNOLOGY). Images were acquired with the ZEN 2009 Light Edition confocal microscope, using the 60x oil objective. Images were analyzed by the ZEN 2009 Light Edition software.

4. Host Bacterial Strain Maintenance

The F+ recA+ *E. coli* host strain ER2738 was used for M13KE insert-less phage (N0316S, NEB) propagation. Supplied as a non-competent 50% glycerol culture as part of the Ph.D.–C7C Phage Display Peptide Library Kit (E8120S, NEB), ER2738 colonies or lawns were grown on 100mm LB-Agar (M1151, HiMedia) plates supplemented with Tet (T3383, Sigma-Aldrich). Plates were incubated at 37°C overnight and stored wrapped with parafilm at 4°C in the dark. ER2738 was propagated weekly and new cultures were streaked from glycerol stock once per month. ER2738 cultures were grown in LB Broth (J106, AMRESO) and bulk amplified in LB Broth + Tet.

5. Phage Display Bio-panning on Nuclei

The Ph.D.–C7C Phage Display Peptide Library Kit (E8120S, NEB) was used. The library has filamentous phage particles displaying random peptides with the cyclic

arrangement CX7C (C, Cysteine; X, any amino acid residue) at a diversity of 10^9 transducing units (TU). This library was used along with the control M13KE insert-less phage to pan on nuclei from either WT or lamin A/C null MEFs, with and without pre-clearing. Phage display bio-panning was performed using the Bio-panning and Rapid Analysis of Selective Interactive Ligands (BRASIL) method. M13KE phage or the library phage was diluted in PBS supplemented with protease inhibitors to a concentration of $1x10^9$TU/μl. Pre-clearing was performed by mixing 1μl of diluted phage with $50x10^3$ nuclei in a microfuge tube and incubating on ice for 30min. The nuclei-bound phage was then pelleted by spinning at 500xg, 4°C for 5min. Phage binding was performed by mixing the unbound phage-containing supernatant with $50x10^3$ nuclei in a microfuge tube and incubating on ice for 1h with brief vortex step every 15min. After the binding step, the phage/nuclei mixture was carefully overlaid on top of 100μl of BRASIL Oil [dibutyl phthalate:cyclohexane 9:1 (v/v)] contained in BRASIL tubes and spun at 10,000rpm, 4°C, for 10min. BRASIL tubes were frozen by overnight storage at -80°C. The following day, host bacterial strain ER2738 was grown to mid-log phase (OD_{600} ~ 0.5). When the bacterial culture was ready, the bottom of each frozen BRASIL tube was clipped into a clean microfuge tube and 400μl of bacterial culture was added to the clipped pellet to rescue the bound phage. Infection was allowed for 1h at room temperature with a brief vortex step every 15min. After 1h, the phage-infected bacterial culture was serially diluted in LB Broth + Tet and different dilutions were mixed with top agarose and overlaid on top of LB agar/IPTG/X-Gal plates. The plates were left to dry in the dark and incubated at 37°C for 14h. Plaques from the different dilutions were counted. Well-separated plaques were picked

and stored in 30% glycerol (E520, AMRESCO) in 96-well plates at -20°C. The eluted phage was bulk amplified, isolated, and titer tested (see below) prior to its use in the following round of bio-panning. Three successive rounds of bio-panning were performed whereby the amplified eluted phage pool from one round was used as input in the successive round. The eluted phage was used at a concentration of $1x10^{9}$TU/µl. Dilution was done based on the calculated phage titer. In differential phage display screens, pre-clearing was done before each successive round of bio-panning.

6. Bulk Amplification and Isolation of Eluted Phage

Phage-infected bacterial culture (mid-log phase) was diluted 1:10 in LB Broth + Tet, bulk amplified at 37°C, 180rpm shaker for 5h, then transferred into a clean round bottom tube and bacterial sedimentation was performed by centrifugation at 6000rpm, 4°C for 15min. The phage-containing supernatant was transferred into a fresh tube, re-spun and phage particles precipitation was performed by transferring the supernatant into a clean tube and adding PEG-NaCl (1:5) (PEG 8000 Powder, V3011, Promega; NaCl, 0241, AMRESCO). The tube was mixed gently by tilting upside down and incubated on ice in the cold room overnight. Subsequently, the round bottom tube was centrifuged at 14000rpm, 4°C for 15min. The supernatant was discarded; the phage pellet was suspended in 1ml cold PBS (without calcium and magnesium), transferred into a clean microfuge tube and re-spun for 5min. The supernatant was mixed with 200µl of PEG-NaCl in a clean tube and incubated on ice for at least 1h. After centrifugation at 14000rpm, 4°C for 10min, the supernatant was discarded and the phage pellet was re-suspended in 250µl cold PBS, re-

spun for 1min and transferred into a clean microfuge tube. The bulk amplified phage suspension was stored at 4°C for 2 weeks or at -20°C for long term storage.

7. Phage Titer Determination

ER2738 was inoculated from a fresh plate into 20ml LB broth and incubated at 37°C, 180rpm shaker until it reached mid-log growth (OD_{600} ~ 0.5). Phage serial dilutions were prepared in PBS and 1µl of each dilution was used to infect 100µl of ER2738 culture at room temperature for 30min (performed in triplicates per dilution). 50mm LB-Agar plates supplemented with IPTG/X-Gal (R0391/R0401, Fermentas) were pre-warmed at room temperature. Top agar consisting of LB Broth and agarose (A9593, Sigma) was molten in microwave and kept at 48°C in water bath. Then, 1.5ml top agar was mixed with 100µl of each infection and overlaid on LB agar/IPTG/X-Gal plates. Allowed to solidify at room temperature for 5-10min, the plates were incubated at 37°C for 14h. Subsequently, the dilution that gave non-overlapping plaques (less than 100 plaques) was chosen for determining the titer. The average count was determined by counting plaques on triplicate plates corresponding to that dilution. Then, phage titer in transducing units (TU) was obtained by multiplying the average count by the dilution factor for those plates.

8. PCR Amplification of Phage Inserts and Agarose Gel Electrophoresis

A 326bp stretch of the phage genome, surrounding the random peptide inserts, was amplified by performing PCR directly on the phage plaques using the Phusion Flash High-Fidelity PCR Master Mix (F-548L, Thermo Scientific) and the PTC-200 DNA Engine

Peltier Thermal Cycler (ALS 1296, Bio-Rad). The forward primer: 5′-TGTCGGCGCAACTATCGGTATCAA-3′, and reverse primer: 5′-TAGCATTCCACAGACAGCCCTCTA-3′ (Sigma) were used. Each PCR reaction consisted of 7µl DNase/RNase free water (W4502, Sigma), 10µl Phusion Flash High-Fidelity PCR Master Mix, 1µl of each primer (8µM), and 1µl of each phage clone pre-stored in glycerol stock. PCR was performed in 0.2ml thin-walled PCR tubes with flat caps (AB-0620, Thermo Scientific) and the protocol consisted of: 94°C step for 3min to break bacterial cell walls followed by 50 cycles of denaturation at 94°C for 10s, annealing at 60°C for 30s, and extension at 72°C for 30s. PCR products were stored at –20°C. To check for the presence of insert, PCR amplicons were run on 2% agarose gels in 1xTBE buffer (0658, AMRESCO) in an electric field alongside Direct Load DNA Step Ladder (D3812, Sigma). Samples were prepared for loading by mixing 2µl of PCR-amplified clones with 1µl of 6x DNA Loading Dye (R0611, Thermo Scientific) and 3µl of DNase/RNase free water. Samples were run at 100V and the bands were visualized using the Molecular Imager Chemidoc XRS System (170-8070, Bio-Rad) using the Quantity One 1-D Analysis Software (170-9600).

9. Purification of PCR Amplicons and Sequencing

Purification of PCR amplicons was performed using the GenElute PCR Clean-Up Kit (NA1020, Sigma-Aldrich). GenElute plasmid mini spin columns were prepared for DNA binding by adding 0.5ml of the column preparation solution to each column and spinning at 12,000xg for 1min. After discarding the eluate, the PCR reaction was mixed

with binding solution (1:5 v/v), transferred into the mini spin column and centrifuged at 16000x g for 1min. The eluate was discarded, and the column was washed by 0.5ml of diluted wash solution. This was followed by centrifugation and discarding the eluate. Another centrifugation step was done to remove excess ethanol. The column was then transferred into a fresh collection tube and incubated with 30µl DNase/RNase free water at room temperature for 5min. Purified DNA was eluted by centrifugation at 16000xg for 2min. The purified PCR amplification products were stored at -20°C. Sequencing was performed at Macrogen Inc. (South Korea) such that 30µl of each PCR reaction, corresponding to a single phage clone, along with 5µM of the sequencing primer M13F: 5′-TGTCGGCGCAACTATCGGTATCAA-3′ (Sigma) were placed in Hard-Shell PCR plates with 96-wells (HSP9601, Bio-Rad) and sealed with Optical Flat Cap Strips (TCS0803, Bio-Rad), then sent for sequencing.

10. Processing of Sequencing Reads and Clustering Analysis of Derived Peptides

The statistical programming language R was used to write a script that processes the sequencing reads [287]. This script reads fasta files generated by sequencing of phage clones, identifies nucleotide sequences surrounding the heptapeptide insert in the phage amplicon, cuts out the nucleotide sequence corresponding to the insert, and translates it into an amino acid sequence. The program also identifies and excludes amplicons with no insert or with inserts longer than 7 amino acids. The final list of different peptide sequences were clustered (R function *hclust*) based on the amino acid scoring matrix PAM30.

11. Bioinformatic Analysis of Peptide Sequences

To identify proteins that are mimicked by the uncovered peptides, protein-protein BLAST analysis of the peptide sequences was performed. The search was set to non-redundant protein sequence in the mouse taxid (http://blast.ncbi.nlm.nih.gov). Multiple protein mimics were determined for each sequence and were selected from the full BLAST list of hits based on the Max score, E-value and Identity. Furthermore, mimics were selected based on their nuclear expression score, tissue expression profile, and biofunctional relevance particularly to A-type lamins, muscle tissue, heart function, myopathies, and cardiomyopathies as determined by the Gene Cards (http://www.genecards.org/) and UniProt (http://www.uniprot.org) databases, and PubMed (http://www.ncbi.nlm.nih.gov/pubmed) search of the biomedical literature.

12. Sub-cellular Fractionation

Nuclear and cytosolic fractions from WT and Lamin A/C deficient MEF cell lines were separated using the Qproteome Cell Compartment Kit (37502, QIAGEN) according to the manufacturer's instructions. Briefly, 8 x 10^6 cells were lysed with 1ml ice-cold extraction buffer (CE1) and incubated for 10min at 4°C on an end-over-end shaker. The cytosolic fraction was separated from the pellet by centrifugation at 1000x g for 10min at 4°C. Membrane proteins were separated by incubating the pellet with 1ml of ice-cold extraction buffer (CE2) for 30min at 4°C on an end-over-end shaker and centrifugation at 6000x g for 10min at 4°C. The remaining pellet was resuspended in Benzonase Nuclease and incubated for 15min at room temperature. This was followed by incubation with 500µl of ice-cold extraction buffer (CE3) for 10min at 4°C on an end-over-end shaker. The

supernatant, containing the nuclear fraction was separated from the pellet by centrifugation at 6800x g for 10min at 4°C. All extraction buffers were supplemented with protease inhibitor solution before use. Both cytosolic and nuclear fractions were stored at -80°C.

13. Protein Extraction and Immunoblotting

Total proteins were extracted from a confluent cell culture plate using 250µl of RIPA lysis buffer (R0278, SIGMA) supplemented with protease inhibitors (22020009-1, Bioworld). Protein concentrations of total, cytoplasmic and nuclear fractions were determined by Bradford protein assay. 20µg protein lysates from the different sub-cellular fractions were resolved by SDS-PAGE and immunoblotted using HuR antibody (sc-20694, SANTA CRUZ BIOTECHNOLOGY) at 1:500 dilution, Lamin B1 antibody (sc-374015, SANTA CRUZ BIOTECHNOLOGY) at 1:200 dilution and GAPDH antibody (sc-25778, SANTA CRUZ BIOTECHNOLOGY) at 1:500 dilution. HRP-conjugated secondary antibodies (ab97023, ab97110, abcam; 111-035-144, Jackson Immunoresearch) were used at a dilution of 1:5000. Bands were detected using ECL western blotting substrate kit (ab65628, abcam) and quantified using ImageJ software.

14. Immunofluorescence Staining

Cells were seeded on coverslips in 6-well plates, fixed with 4% formaldehyde in PBS and permeabilized with 0.5% TritonX-100 in PBS. HuR protein was visualized by immunostaining using HuR antibody (sc-20694, SANTA CRUZ BIOTECHNOLOGY) at 1:50 dilution and Alexa Fluor-conjugated secondary antibody (ab150113, abcam) at 1:500 dilution. Coverslips were mounted on slides using the UltraCruz Hard-set mounting

medium (sc-359850, SANTA CRUZ BIOTECHNOLOGY). Images were acquired with the ZEN 2009 Light Edition confocal microscope, using the 60x oil objective. Images were analyzed by the ZEN 2009 Light Edition software.

15. Co-immunoprecipitation

The Dynabeads Co-Immunoprecipitation Kit (14321D, Novex) was used according to the manufacturer's instructions. Briefly, 1.5mg of Dynabeads M-270 Epoxy were coupled to 10µg of either HuR (sc-20694, SANTA CRUZ BIOTECHNOLOGY) or Lamin A/C (sc-6215, SANTA CRUZ BIOTECHNOLOGY) antibody, through an overnight incubation on a roller at 37°C. The beads were then washed and blocked with 0.1% BSA in PBS before incubation with 0.07g cell sample on a roller at 4°C for 1hour. Finally, the beads were washed and the purified protein complex was eluted and used directly for Western Blot analysis using both HuR and Lamin A/C antibodies at 1:500 and 1:200 dilutions respectively.

D. Results

1. Nuclear Shape is Maintained Following Nuclear Isolation and Storage

Lamin B1 staining was performed on nuclei isolated from *Lmna*$^{+/+}$ and *Lmna*$^{-/-}$ MEF cell lines to assess nuclear shape following nuclear isolation and storage at -80°C. Immunofluorescence staining of both *Lmna*$^{+/+}$ and *Lmna*$^{-/-}$ MEFs showed continuous Lamin B1 staining at the nuclear rim. This was assessed short-term within 48hr-to-1 week post nuclear isolation and freezing (Figure 10b) and also when evaluated long-term up-to-1

year storage of nuclei at -80°C (Supplementary Figure 1). Notably, Lamin B1 intensity was reduced in *Lmna*$^{-/-}$ nuclei in comparison to *Lmna*$^{+/+}$ nuclei.

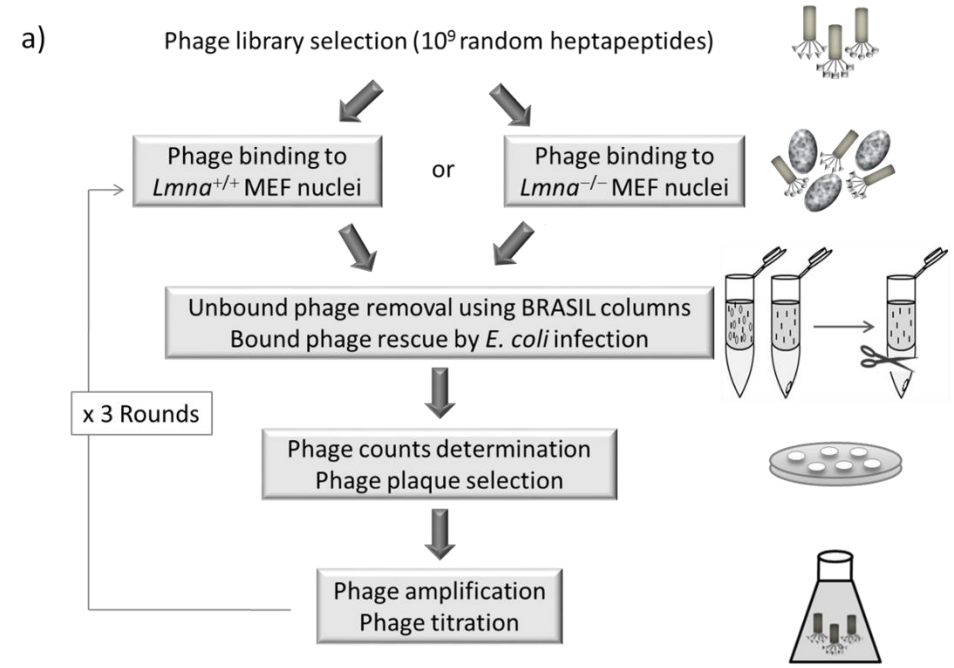

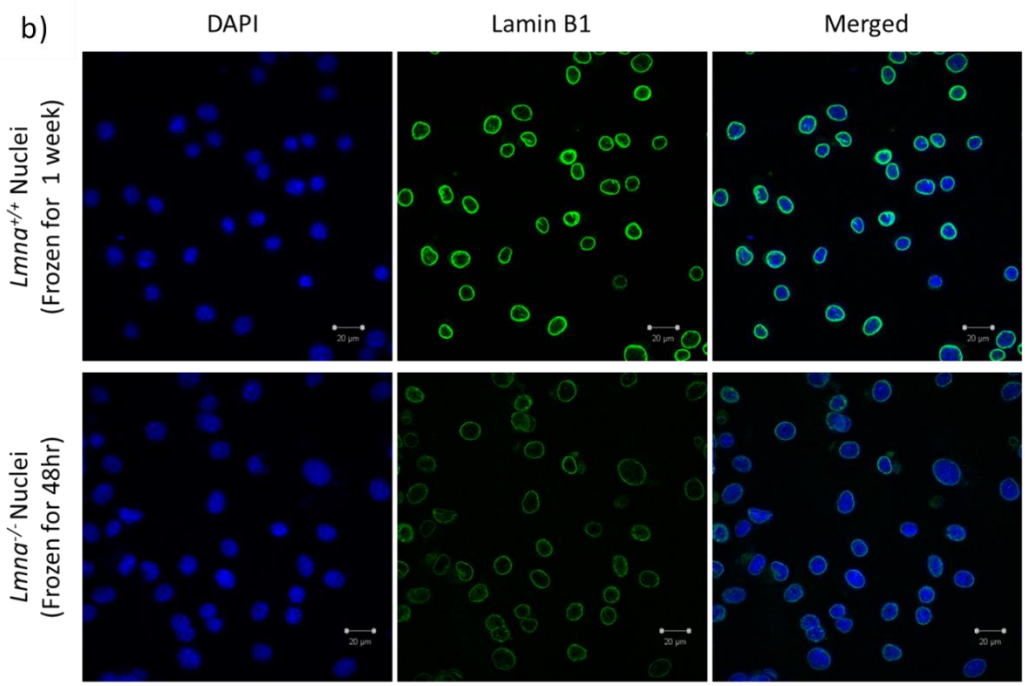

Figure 10. A Schematic Diagram Showing the Experimental Strategy for Direct Phage Display Bio-Panning on Intact Nuclei Using the BRASIL Method.
(*a*) The Ph.D.–C7C library with a diversity of $1x10^9$ heptapeptides per μl was used for direct bio-panning on either *Lmna*$^{+/+}$ or *Lmna*$^{-/-}$ MEF nuclei. Post incubation and binding step on ice, BRASIL method of separation was applied and bound phage was rescued by *E. coli* infection. Serial dilutions were then streaked on tetracycline supplemented IPTG-X-Gal plates with agarose top to count the phage transducing (plaque forming) units post overnight incubation. Colonies were picked and the phage output post amplification and titration in bacteria was used as input for the subsequent bio-panning round to enrich for phage particles that bind to either type of nuclei. In total, three rounds of bio-panning were performed. (*b*) Representative confocal microscope images showing immunofluorescence staining of Lamin B1 protein in nuclei isolated from *Lmna*$^{+/+}$ and *Lmna*$^{-/-}$ MEF cell lines, and stored at -80°C. The first row shows *Lmna*$^{+/+}$ nuclei that were stored at -80°C for a week before performing Lamin B1 staining. The second panel shows *Lmna*$^{-/-}$ nuclei that were stored at -80°C for 48hr before performing Lamin B1 staining. Nuclei were counterstained with 4′,6-diamidino-2-phenylindole (DAPI).

2. Direct Phage Display Biopanning on MEF Nuclei Using the BRASIL Method (Screen 1)

The Ph.D.–C7C library was applied, without pre-clearing, and phage particles displaying random heptapeptides were allowed to bind to nuclei from either MEF cells expressing WT lamin A/C or cells deficient in A-type lamins (*Lmna*$^{-/-}$). Using BRASIL, phage particles displaying peptides with preferential binding abilities to either type of nuclei were separated from unbound phage and rescued by infection of competent *E. coli* cells (Figure 10a). Serial dilutions were plated on agarose top on IPTG-X-Gal plates supplemented with tetracycline (Tet) and bacteriophage plaques were counted post overnight incubation to determine the phage transducing unit (TU) counts. Three successive rounds of biopanning were performed such that the output from each round for each type of nuclei was amplified, titered, and used as input for similar type of nuclei in the subsequent round. The ratio of TUs of phage binding to *Lmna*$^{+/+}$ MEF nuclei relative to TUs of the

insert-less control phage M13KE, increased significantly from Round I (0.45 ± 0.19) to Round II (1.00 ± 0.07) and stayed in Round III (1.02 ± 0.22) higher than in Round I; *p=0.02* and *p=0.05* for the difference between Round I and II and between Round I and III, respectively in unpaired one-tailed t-test (Figure 11a). The results represent the mean ratio of phage TU counts (phage library/M13KE per sample) ± SEM of 4 independent repeats. Accordingly, a 2.2- and a 2.3-fold increase in relative phage binding to $Lmna^{+/+}$ MEF nuclei was observed in Round II and Round III respectively in comparison to Round I. Notably, significant enrichment in phage binding to $Lmna^{-/-}$ MEF nuclei was not obtained until Round III of biopanning whereby the mean ratio of phage TU counts (1.39 ± 0.21) was significantly higher than that obtained in Round I (0.68 ± 0.26) or Round II (0.71 ± 0.09); *p=0.04* and *p=0.01* respectively in unpaired one-tailed t-test (Figure 11a), hence indicating a 2-fold increase in relative phage binding to $Lmna^{-/-}$ MEF nuclei in Round III in comparison to Round I.

3. Sequence Determination of the Phage Inserts & Clustering Analysis for Clones Selected from Screen

As no further increase in relative phage binding to $Lmna^{+/+}$ MEF nuclei was observed between Round II and Round III in Screen 1, we sequenced phage inserts in clones picked from only Round I and Round II in order to identify peptides that bind with high frequency to $Lmna^{+/+}$ MEF nuclei. In total, 40 and 49 phage clones were sequenced and analyzed from Round I and Round II respectively. To process and analyze the sequencing reads, we developed a program using the statistical programming language R to identify the heptapeptide insert in the sequenced phage amplicon, and to perform clustering

analysis of the recovered peptides using the scoring matrix Point Accepted Mutation 30 (PAM30). Amino acid substitution matrices describe the rate at which one amino acid in a

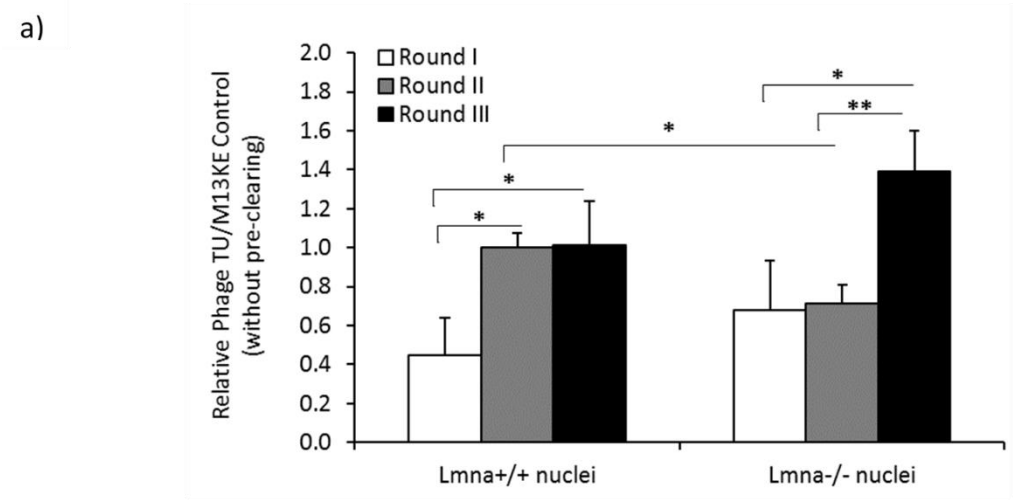

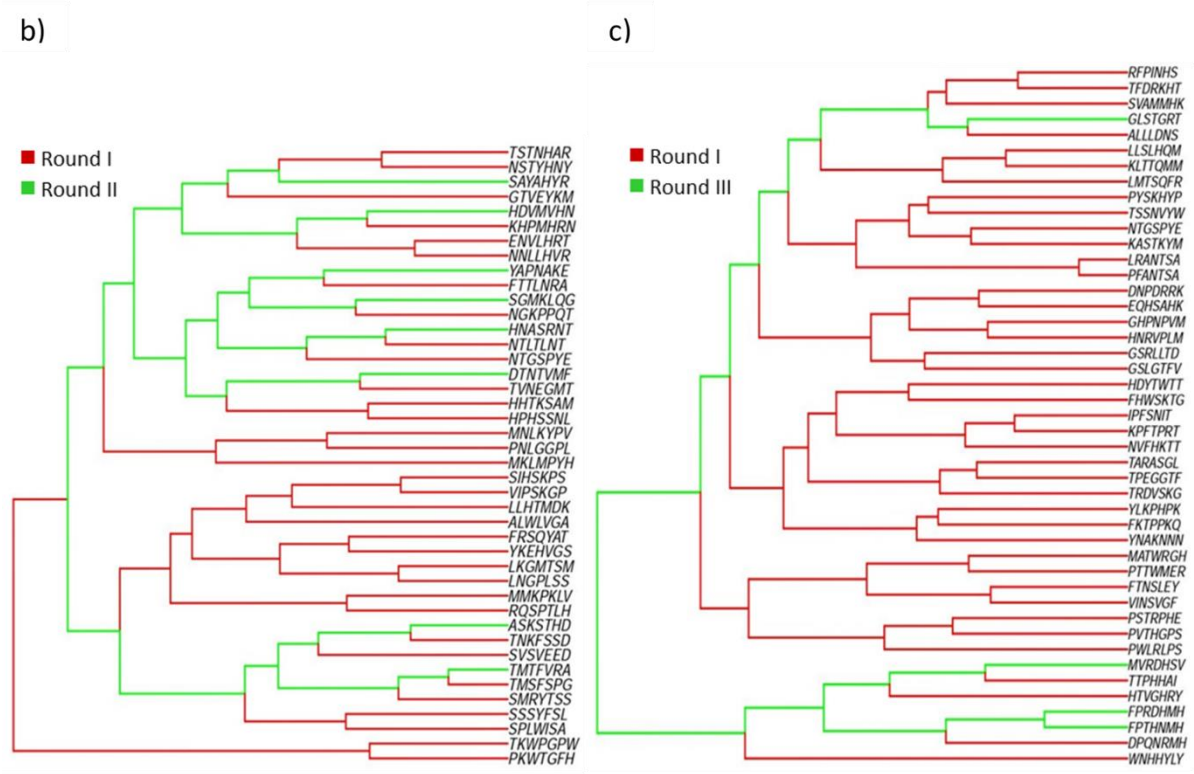

Figure 11. Direct Phage Display Bio-panning on MEF Nuclei Using the BRASIL Method (Screen 1).
(*a*) Phage binding was performed, without pre-clearing the Ph.D.–C7C library, directly on nuclei from either MEF cells expressing WT *Lmna* or deficient in A-type lamins. Normalized to M13KE control insert-less phage, significant enrichment in phage binding to $Lmna^{+/+}$ nuclei was achieved by Round II and to $Lmna^{-/-}$ nuclei by Round III. Results represent the mean ratio of phage TU counts ± SEM of 4 independent repeats (*$p \leq 0.05$; ** $p \leq 0.01$; unpaired one-tailed t-test). (*b*) Clustering analysis of peptides derived from $Lmna^{+/+}$ nuclei; 40 and 49 peptides were analyzed from Round I and Round II respectively. (*c*) Clustering analysis of peptides derived from $Lmna^{-/-}$ nuclei; 43 and 50 peptides were analyzed from Round I and Round III respectively.

sequence changes to another amino acid over time. The substitution rates given by such matrices can be used to determine the similarity between amino acid sequences [288]. Hence, we employed the PAM30 amino acid substitution matrix to determine the amino acid similarity between the recovered peptides. Clustering analysis of the recovered peptides from $Lmna^{+/+}$ MEF nuclei showed a decrease in the diversity of peptide sequences obtained in Round II in comparison to Round I (Figure 11b). The 8 peptide sequences recovered from Round II segregate into 2 different clusters on the dendrogram in that 2 peptide sequences are located close to each other while the other 6 peptides form one cluster reflecting their biochemical similarity (Figure 11b). Similarly, based on the enrichment profile from direct phage display biopanning on $Lmna^{-/-}$ MEF nuclei, we sequenced phage inserts in clones picked from only Round I and Round III to identify peptides that bind with high frequency to $Lmna^{-/-}$ MEF nuclei. Accordingly, 43 and 50 phage clones were sequenced and analyzed from Round I and Round III respectively. Moreover, clustering analysis of recovered peptides from $Lmna^{-/-}$ nuclei showed a decrease in the diversity of peptide sequences obtained in Round III in comparison to Round I in that only 4 peptide

sequences dominated the profile in Round III (Figure 11c). While 3 of these peptides formed a cluster in the dendrogram, the fourth peptide identified was unrelated.

4. High Frequency Peptides Recovered from Screen 1 & The Proteins They Mimic

The percent frequency of occurrence of a given peptide was calculated based on the number of times it appeared in the total number of sequenced clones from each round. Peptides with frequency of occurrence ≥ 2% are listed in Table 1, along with the matching motifs in the putative proteins mimicked by the recovered peptides, which were obtained by protein-protein BLAST analysis based on the Max score, E-value, and Identity (see Methods). By exploring the proteome of *Lmna*$^{+/+}$ MEF nuclei using direct phage display biopanning with BRASIL and BLAST analysis, we uncovered a panel of 26 proteins that may potentially interact with the NE that has an intact nuclear lamina (Table 1). A number of these proteins are known A-type lamin interactors (see Discussion). The identified proteins have overlapping as well as distinct molecular functions and are implicated in diverse biological processes and pathways (Figure 12a) as determined by text mining of the gene and protein databases GeneCards (http://www.genecards.org/) and UniProt (http://www.uniprot.org/). On the other hand, direct phage display biopanning using BRASIL on *Lmna*$^{-/-}$ MEF nuclei yielded less peptides (Table 1). None of these peptides was also obtained by the direct phage display biopanning that was performed on *Lmna*$^{+/+}$ MEF nuclei. Moreover, BLAST analysis of these peptides resulted in the identification of 16 proteins that are functionally less diverse (Figure 12b) as determined from text mining

of the GeneCards and UniProt databases. Two of the uncovered proteins, CPED1 and F136A, have no annotated function.

Table 1. A list of peptides recovered from direct phage display biopanning on *Lmna*$^{+/+}$ or *Lmna*$^{-/-}$ MEF nuclei using the Ph.D.–C7C library and the BRASIL method (Screen 1).

Matching motifs in candidate proteins (bold) mimicked by the phage inserts were obtained by protein-protein BLAST analysis based on the Max score, E-value, and Identity.

Sample (Round)	Peptide (% Frequency)	Matching Motif	Protein Mimic (Gene)	UniProtKB Accession
***Lmna*$^{+/+}$ MEF nuclei (R II)**	HDVMVHN	338-D**IMVH**-342	Cullin-4A: CUL4A (*Cul4a*)	Q3TCH7
	(23)	1020-**HDIMV**-1024	Epidermal growth factor: EGF (*Egf*)	P01132
		3229-**HD**Q**MVH**-3234	Cardiomyopathy-associated protein 5: CMYA5 (*Cmya5*)	E9QLJ0
		912-**VMVH**D-916	Nuclear pore membrane glycoprotein 210: PO210 (*Nup210*)	Q9QY81
	HNASRNT	1399-D**ASRNT**-1404	Nuclear receptor coactivator 2: NCOA2 (*Ncoa2*)	Q61026
	(18)	1590-**N**G**SRNT**-1595	Lysine-specific demethylase 6B: KDM6B (*Kdm6b*)	Q5NCY0
		2118-**ASRNT**-2122	AT-hook-containing transcription factor 1: ELYS: MEL28 (*Ahctf1*)	Q8CJF7
	SAYAHYR	123-**SAY**QSI**AHYR**-132	Emerin: EMD (*Emd*)	O08579
	(18)	120-**SAYA**VQ**YR**-127	Amyloid beta A4 protein-binding family A-1: APBA1 (*Apba1*)	B2RUJ5
		220-**SAY**M**HY**-225	Tensin-2: TNS2 (*Tns2*)	Q8CGB6
	DTNTVMF	931-D**SNTVM**-936	Desmoplakin: DESP (*Dsp*)	E9Q557
	(18)	77-**DTNTV**L-82	Endoribonuclease deubiquitinase ZC3H12A (*Zc3h12a*)	Q5D1E7
		187-**DTNTV**-191	E3 ubiquitin-protein ligase RNF146 (*Rnf146*)	Q9CZW6
	SGMKLQG	361-**SGMKLQ**-366	Mitogen-activated protein kinase 13: MK13 (*Mapk13*)	Q9Z1B7
	(14)	171-**GMKL**E**G**-176	Nuclear receptor subfamily 5 group A-2: NR5A2 (*Nr5a2*)	P45448
		432-**SGMKL**E-437	Nuclear RNA export factor 1: NXF1 (*Nxf1*)	Q99JX7
	ASKSTHD	110-**ASCKSTHD**-117	Regulator of G-protein-signaling 3: RGS3 (*Rgs3*)	I7HPB2
	(4)	2-**ASKS**Q**HD**-8	7-dehydrocholesterol reductase: DHCR7 (*Dhcr7*)	O88455
		658-**ASK**P**TH**-663	E3 SUMO-protein ligase RanBP2: RBP2 (*Ranbp2*)	Q9ERU9
		65-**ASKST**-69	Prelamin-A/C: LMNA (*Lmna*)	P48678
	TMTFVRA	27-**TM**V**FVR**-32	Myosin light chain kinase 2: MLCK2: MYLK2 (*Mylk2*)	Q8VCR8
	(2)	1130-**TMT**LGLPE**FIRA**-1141	Nebulin-related-anchoring protein: NRAP (*Nrap*)	Q80XB4
	YAPNAKE	256-**PNAKE**-260	Transducer of erbB-2 2: TOB2 (*Tob2*)	Q9JM55
	(2)	286-**PNAKE**-290	Transducer of erbB-2 1: TOB1 (*Tob1*)	Q61471
		676-**PNAKE**-680	Ataxin-2: ATX2 (*Atxn2*)	O70305
		33-**YAPN**C**AK**-39	PDZ and LIM domain protein 7: PDLI7 (*Pdlim7*)	Q3TJD7
***Lmna*$^{-/-}$ MEF nuclei (R III)**	FPTHNMH	84-**FPTH**D**M**-89	Pantothenate kinase 2: PANK2 (*Pank2*)	Q7M753
	(64)	99 -**PTHN**L**H**-104	Ephrin-A3: EFNA3 (*Efna3*)	O08545
		440-**FP**PVC**THNM**-448	Muscle glycogen synthase: GYS1 (*Gys1*)	Q9Z1E4
	MVRDHSV	1050-**MVRDH**-1054	Nesprin-1: SYNE1 (*Syne1*)	Q6ZWR6
	(32)	104-**VRDHS**-108	Zinc finger protein 394: ZN394 (*Znf394*)	Q9Z1D9
		134-**RDHSV**-138	Zinc finger protein RFP: TRI27 (*Trim27*)	Q62158

	157-**VRDHS**-161	Apaf1 protein: APAF1 (*Apaf1*)	Q80VR5
	1535-**MVRD**QDV-1541	Fat 1 cadherin: CDHF7 (*Fat1*)	Q9QXA3
GLSTGRT	422-**GLS**LL**TGRT**-430	Putative E3 ubiquitin-protein ligase SH3RF2: SH3R2 (*Sh3rf2*)	Q8BZT2
(2)	17-**STGRT**-21	Exosome complex component RRP41: EXOSC4 (*Exosc4*)	Q921I9
	26-**LSTGR**-30	Proteasome subunit beta type-10: PSB10 (*Psmb10*)	O35955
	114-**GL**A**TGR**-119	DDB1- and CUL4-associated factor 11: DCA11 (*Dcaf11*)	Q91VU6
FPRDHMH	2-**PR**NQ**MH**-7	Carboxylesterase 2: CES2 (*Ces2c*)	Q8K033
(2)	168-**PR**E**HM**-172	Cadherin like PC-esterase domain containing 1: CPED1 (*Cped1*)	E9Q7L8
	117-**DHMH**-120	Protein FAM136A: F136A (*Fam136a*)	Q9CR98
	95-**DHMH**-98	Wnt-3: WNT3 (*Wnt3*)	P17553

5. Differential Phage Display Biopanning on Lmna+/+ MEF Nuclei Using the BRASIL Method (Screen 2)

In the second screen, the Ph.D.–C7C library was pre-cleared on *Lmna*$^{-/-}$ MEF nuclei, and the pool of unbound phage particles was incubated with nuclei from either *Lmna*$^{+/+}$ or *Lmna*$^{-/-}$ MEF cells. Three successive rounds of biopanning were performed such that the output from each round for *Lmna*$^{+/+}$ MEF nuclei was amplified, titered, and used as input for the subsequent round, with a pre-clearing step on *Lmna*$^{-/-}$ MEF nuclei done in each round. We expect that phage particles displaying peptides which can interact with the NE of the *Lmna*$^{-/-}$ MEF nuclei get cleared. As such, the ones enriched post binding to *Lmna*$^{+/+}$ MEF nuclei are presumably those displaying peptides with preferential binding to nuclei with A-type lamins likely because their interacting partners are still retained there. Relative to the M13KE control phage, significant enrichment in phage binding to *Lmna*$^{+/+}$ MEF nuclei was achieved by Round III, with a mean ratio of phage TU counts (0.91 ± 0.24) that was significantly higher than that for Round I (0.38 ± 0.13; p =

a)

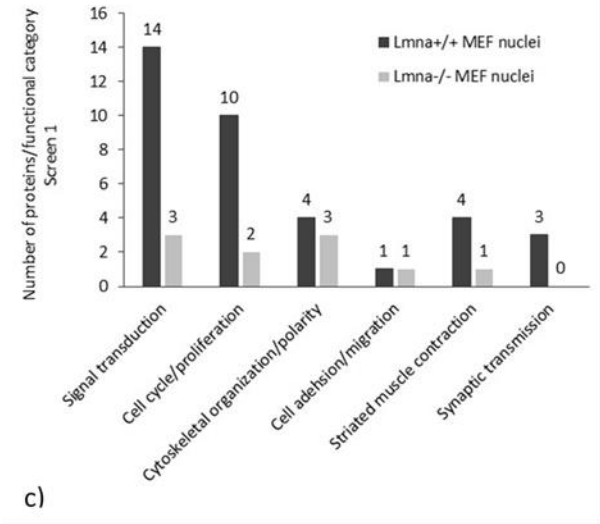

b)

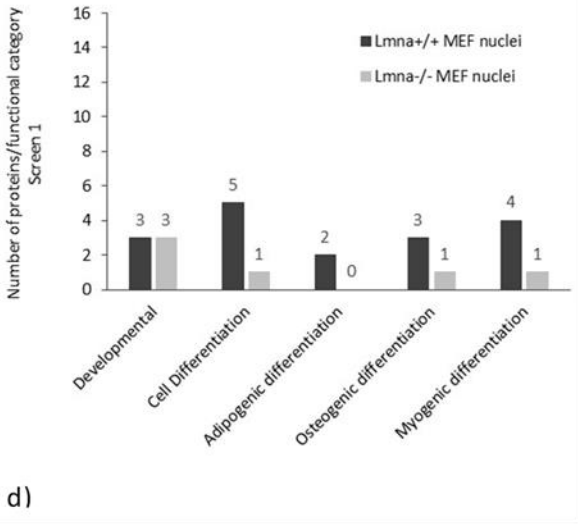

c)

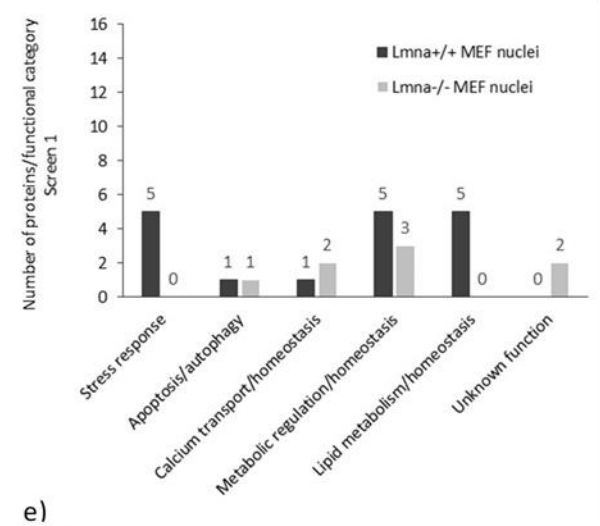

d)

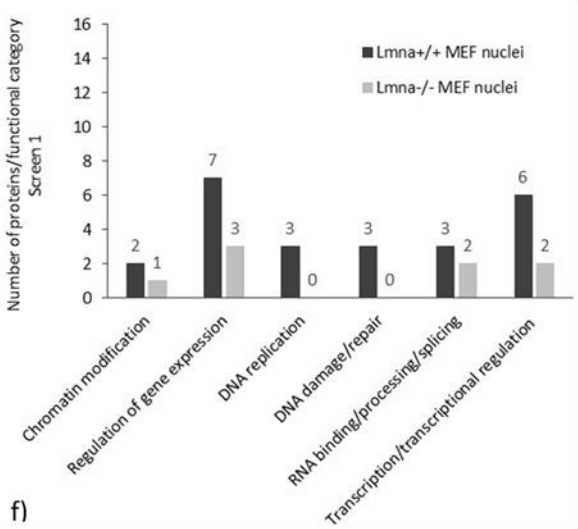

e)

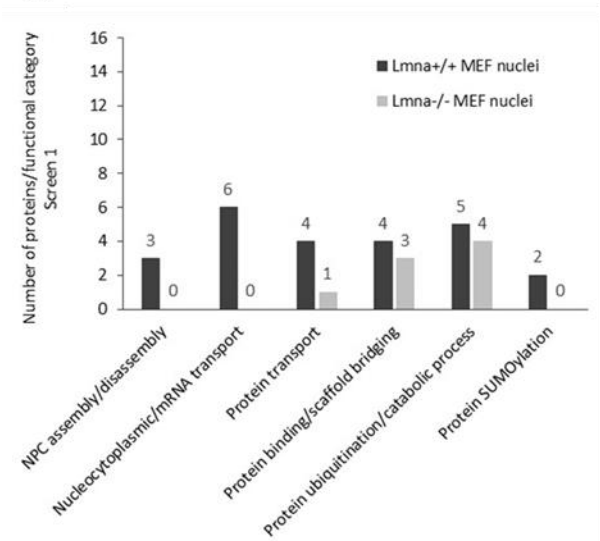

f)

Screen 1	Round	No. of peptides	No. of protein mimics
Lmna$^{+/+}$ MEF nuclei	II	8	26
Lmna$^{-/-}$ MEF nuclei	III	4	16

Figure 12. Functional Stratification of the Proteins Mimicked by the Peptides Uncovered by Direct Phage Display Bio-Panning on *Lmna*$^{+/+}$ and *Lmna*$^{-/-}$MEF Nuclei in Screen 1.

(*a*-*e*) Bar graph labels indicate the number of proteins per functional category. (*f*) The chart shows the total number of selected peptides and their protein mimics derived from BLAST analysis for each type of nuclei per bio-panning round.

0.05 in unpaired one-tailed t-test (Figure 13a). The results represent the mean ratio of phage TU counts (pre-cleared library/M13KE) ± STDEV of 2 independent repeats; each done in duplicates. Accordingly, a 2.4-fold increase in relative phage binding to *Lmna*$^{+/+}$ MEF nuclei was observed in Round III in comparison to Round I. However, there was no significant difference in relative phage binding to *Lmna*$^{+/+}$ MEF nuclei between Round II and Round III ($p = 0.40$), which indicates that enrichment was practically attained by Round II. This goes in line with the clustering analysis of peptide sequences obtained from this differential phage display screen for lamin A/C WT nuclei, whereby the diversity of peptides did not decrease from Round II to Round III (see below). Despite pre-clearing the Ph.D.–C7C library on *Lmna*$^{-/-}$ MEF nuclei, we still noted significant subsequent enrichment in phage binding to *Lmna*$^{-/-}$ MEF nuclei in Rounds II and III (plausible reasons discussed later). The mean ratio of phage TU counts in Round II (0.70 ± 0.06) and in Round III (0.82 ± 0.14) was significantly higher than that obtained in Round I (0.49 ± 0.00); $p=0.02$ and $p=0.04$ respectively in unpaired one-tailed *t*-test, thus showing a 1.4- and a 1.7-fold increase in relative phage binding to *Lmna*$^{-/-}$ MEF nuclei in Rounds II and III respectively in comparison to Round I even after pre-clearing the library on *Lmna*$^{-/-}$ MEF nuclei (Figure 13a).

a)

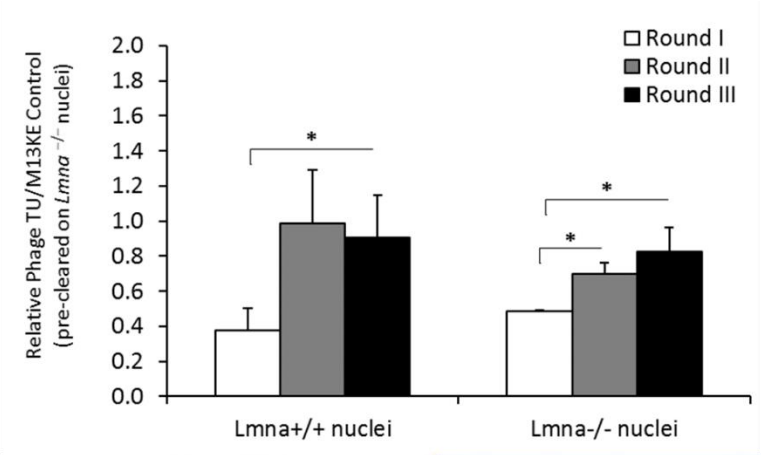
Round I
Round II
Round III
Relative Phage TU/M13KE Control
(pre-cleared on Lmna −/− nuclei)
2.0
1.8
1.6
1.4
1.2
1.0
0.8
0.6
0.4
0.2
0.0
*
*
*
Lmna+/+ nuclei
Lmna-/- nuclei

b)

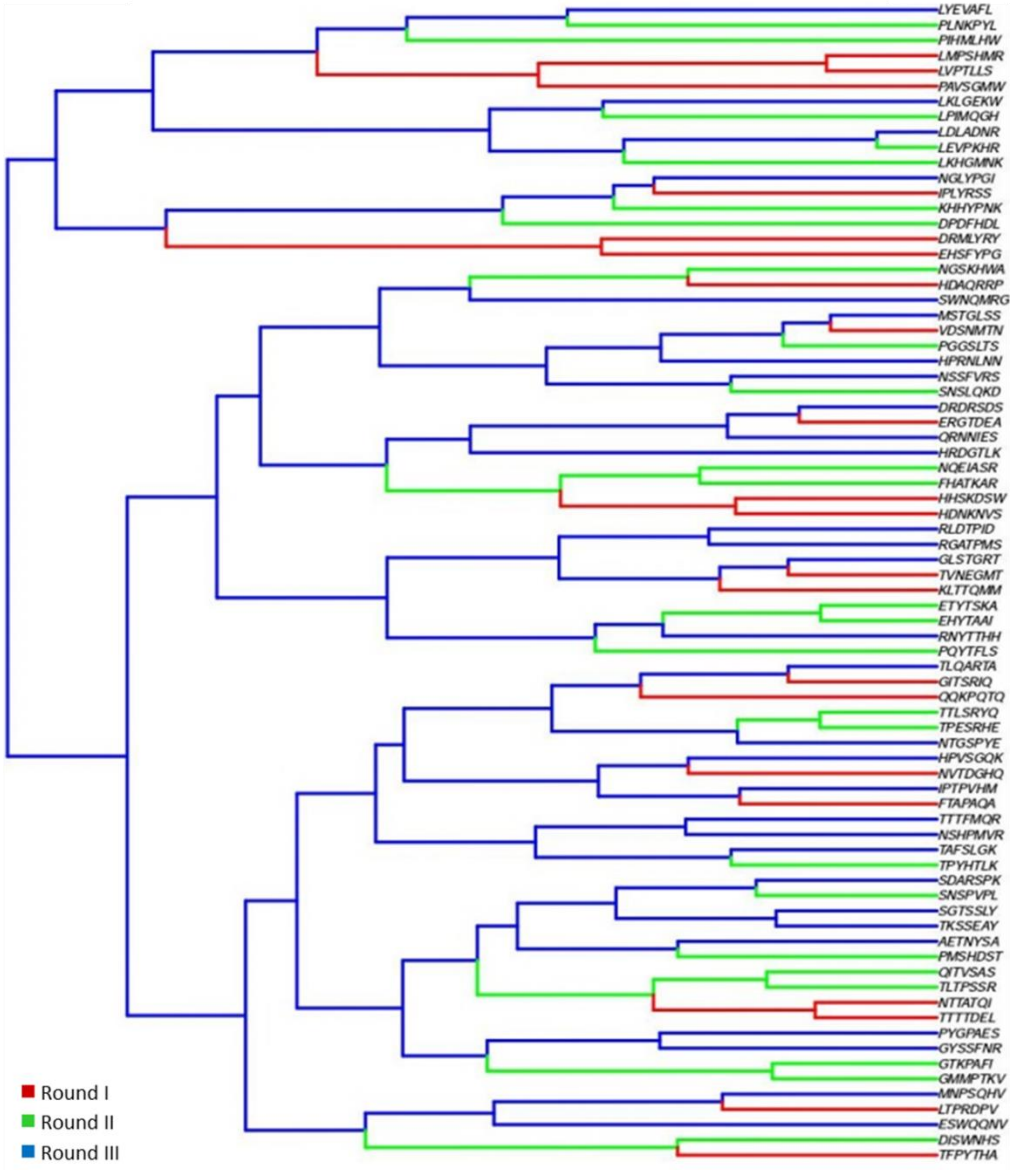
LYEVAFL
PLNKPYL
PIHMLHW
LMPSHMR
LVPTLLS
PAVSGMW
LKLGEKW
LPIMQGH
LDLADNR
LEVPKHR
LKHGMNK
NGLYPGI
IPLYRSS
KHHYPNK
DPDFHDL
DRMLYRY
EHSFYPG
NGSKHWA
HDAQRRP
SWNQMRG
MSTGLSS
VDSNMTN
PGGSLTS
HPRNLNN
NSSFVRS
SNSLQKD
DRDRSDS
ERGTDEA
QRNNIES
HRDGTLK
NQEIASR
FHATKAR
HHSKDSW
HDNKNVS
RLDTPID
RGATPMS
GLSTGRT
TVNEGMT
KLTTQMM
ETYTSKA
EHYTAAI
RNYTTHH
PQYTFLS
TLQARTA
GITSRIQ
QQKPQTQ
TTLSRYQ
TPESRHE
NTGSPYE
HPVSGQK
NVTDGHQ
IPTPVHM
FTAPAQA
TTTFMQR
NSHPMVR
TAFSLGK
TPYHTLK
SDARSPK
SNSPVPL
SGTSSLY
TKSSEAY
AETNYSA
PMSHDST
QITVSAS
TLTPSSR
NTTATQI
TTTTDEL
PYGPAES
GYSSFNR
GTKPAFI
GMMPTKV
MNPSQHV
LTPRDPV
ESWQQNV
DISWNHS
TFPYTHA
Round I
Round II
Round III

Figure 13. Differential phage display bio-panning on MEF nuclei using the BRASIL method post pre-clearing the Ph.D.–C7C library on *Lmna*$^{-/-}$ MEF nuclei (Screen 2). (*a*) Phage binding was performed on nuclei from either MEF cells expressing WT *Lmna* or deficient in A-type lamins. Significant enrichment in phage binding to *Lmna*$^{+/+}$ nuclei was achieved by Round III and to *Lmna*$^{-/-}$ nuclei by Round II. Results represent the mean ratio of phage TU counts ± STDEV of 2 independent repeats; each done in duplicates (*$p \leq 0.05$; unpaired one-tailed t-test). (*b*) Clustering analysis of identified peptides with preferential binding to *Lmna*$^{+/+}$ nuclei was performed using the statistical programming language R and the scoring matrix PAM30. A panel of 21, 52, and 46 peptides were analyzed from Rounds I, II, and III respectively.

6. Sequence Determination of the Phage Inserts & Clustering Analysis for Clones Selected from Screen 2

To identify peptides that preferentially bind to *Lmna*$^{+/+}$ MEF nuclei, the phage inserts for a panel of 21, 52, and 46 phage clones from Rounds I, II, and III respectively, that were selected from the output for the *Lmna*$^{+/+}$ MEF nuclei, were PCR amplified, sequenced, and analyzed. Performed in a similar manner as that for Screen 1, clustering analysis of the recovered peptides shows considerable diversity in the different peptides recovered from all three rounds of biopanning. The sequenced clones from Round I did not show any repeated peptide sequences (data not shown) whereas Round II yielded 25 different peptides, and 30 different peptides were recovered from Round III (Figure 13b). Some of the peptides from Round II localize to both narrow and wide clusters, a feature that was also observed for most peptides from Round III. In addition, overlap between peptides from Rounds II and III was clearly seen by the clustering of red, blue and green colors in the dendrogram, thus indicating that these peptide sequences have similar characteristics which likely underlie their binding to lamin A/C WT nuclei and ensure their

appearance in both biopanning rounds. On the other hand, 10 peptide sequences from Round II and 7 peptide sequences from Round III appeared more than once per round.

7. High Frequency Peptides Recovered from Screen 2 & The Proteins They Mimic

Peptides recovered from Screen 2 with a frequency of occurrence ≥ 2% are listed in Table 2. Matching motifs in proteins mimicked by these peptides, which were obtained by protein-protein BLAST analysis are listed in

Table 2 and Supplementary Table 1. Profiling the proteome of *Lmna*$^{+/+}$ MEF nuclei using differential phage display biopanning with BRASIL followed by protein-protein BLAST analysis, we uncovered a large panel of proteins that preferentially interact with the nucleus of *Lmna*$^{-/-}$ cells (

Table 2 and Supplementary Table 1). Some of these proteins have been previously reported as A-type lamin interactors (see Discussion). As in the case with direct phage

display biopanning performed on *Lmna*$^{+/+}$ MEF nuclei (Screen 1), the uncovered proteins from Screen 2 have overlapping as well as distinct pleiotropic functions (Figure 15a).

Table 2. A list of peptides recovered from differential phage display biopanning on *Lmna*$^{+/+}$ (Screen 2) or *Lmna*$^{-/-}$ (Screen 3) MEF nuclei using pre-cleared Ph.D.-C7C library and the BRASIL method.

Matching motifs in candidate proteins (bold) mimicked by the phage inserts were obtained by BLAST analysis based on the Max score, E-value, and Identity. Supplementary Tables S1 and S2 show expanded lists of the protein mimics for the peptides derived from Screens 2 and 3 respectively.

Sample (Screen/Round)	Peptide (% Frequency)	Matching Motif	Protein Mimic (Gene)	UniProtKB Accession
***Lmna*$^{+/+}$ MEF nuclei (S2/R II)**	FHATKAR (11)	97-**HATKA**-101	Cleavage & polyadenylation specificity factor subunit 3: CPSF3 (*Cpsf3*)	Q9QXK7
	ETYTSKA (11)	20-**TYTSK**-24	Fibroblast growth factor 1: FGF1 (*Fgf1*)	P61148
	TPYHTLK (9)	96-**YHTLK**-100	Gamma-enolase: Enolase 2: ENOG (*Eno2*)	P17183
	LPIMQGH (8)	80-**LPIMQ**-84	Peroxisomal biogenesis factor 19: PEX19 (*Pex19*)	Q8VCI5
		227-**PIMQG**-231	Cyclin-dependent kinase 9: CDK9 (*Cdk9*)	Q99J95
		1658-M**PIMQ**-1662	Protein PRR14L (*Prr14l*)	E9Q7C4
	EHYTAAI (8)	376-**HY**S**AAI**-381	Protein SMG5 (*Smg5*)	Q6ZPY2
		38-**E**NF**TAAI**-44	Protein Slc22a29: Solute carrier family 22. member 29 (*Slc22a29*)	Q8BWG6
		170-**YTAAI**-174	Cyclin-dependent kinase 11B: CD11B: p58 CDK11 (*Cdk11b, Cdc2l1*)	P24788
		170-**YTAAI**-174	DnaJ homolog subfamily C member 3: DNJC3 (*Dnajc3*)	Q91YW3
	LKHGMNK (8)	862-**KHGMN**-866	Mediator of RNA polymerase II transcription subunit 12:MED12 (*Med12*)	A2AGH6
	GMMPTKV (6)	1282-**GMMP**S**K**-1287	Vascular endothelial growth factor receptor 2: VEGFR2: KDR (*Kdr*)	P35918
			Eukaryotic translation initiation factor 4E transporter: 4ET (*Eif4enif1*)	Q9EST3
		969-**MPTKV**-973	Ubiquitin carboxyl-terminal hydrolase 7: USP7 (*Usp7*)	E9PXY8
		32-**MMPT**-35		
	TPESRHE (6)	373-**ESRHE**-377	Double-stranded RNA-specific adenosine deaminase: DSRAD (*Adar*)	Q99MU3
	NQEIASR (4)	24-**NQEIA**-28	Nucleoplasmin-3: Nucleophosmin-3: NPM3 (*Npm3*)	Q9CPP0
	PLNKPYL (4)	747-LH**KPYL**-752	Tubulin polyglutamylase TTLL4 (*Ttll4*)	Q80UG8
***Lmna*$^{+/+}$ MEF nuclei (S2/R III)**	MSTGLSS (14)	1-**MSTGL**-5	Septin-5: SEPT5 (*Sept5*)	Q9Z2Q6
		477-**MSTGL**-481	Lipoxygenase-3: ALOXE3: LOXE3 (*Aloxe3*)	Q9WV07
	NSSFVRS (11)	426-**NSSFV**P**S**-432	Pericentriolar material 1 protein: PCM1 (*Pcm1*)	Q9R0L6
		82-**SSFVR**-86	Nuclear envelope pore membrane protein POM 121: PO121 (*Pom121*)	Q8K3Z9
	RGATPMS (11)	267-**RGATP**K**S**-273	Protocadherin 1: Cadherin-Like Protein 1: PCDH1 (*Pcdh1*)	Q8CFX3
		629-**RG**-**TPMS**-634	Nuclear pore complex protein Nup133: NU133 (*Nup133*)	Q8R0G9

	HPVSGQK (7)	2249-**HPV**T**GQ**-2254	Chromodomain-helicase-DNA-binding protein 6: CHD6 (*Chd6*)	A3KFM7
	LKLGEKW (7)	276-**LGEKW**-280	Syntaxin-4: STX4 (*Stx4*)	P70452
		88-K**I**G**EKW**-93	Fibronectin: FN1 (*Fn1*)	Q4KL80
		128-**KLGE**M**W**-133	High mobility group protein B1: HMGB1 (*Hmgb1*)	P63158
		1752-**LKLGE-W**-1757	Serine/threonine-protein kinase mTOR (*Mtor*)	Q9JLN9
	SWNQMRG (5)	342-**SW**R**QMR**-347	Calpain-13: CAN13 (*Capn13*)	Q3UW68
	SDARSPK (5)	187-**DAR**N**PK**-192	Global transcription activator SNF2L2: Smarca2: SMCA2 (*Smarca2*)	Q6DIC0
		26-E**ARSPK**-31	Proline-rich protein 14: PRR14 (*Prr14*)	Q7TPN9
		633-**DARSP**-637	Protein kinase C gamma type: KPCG (*Prkcg*)	P63318
***Lmna*$^{-/-}$ MEF nuclei (S3/R II)**	SGGRMHQ (14)	252-**GRMH**-255	Aurora kinase B: AURKB (*Aurkb*)	O70126
		43-**GRM**N**Q**-47	Matrin-3: MATR3 (*Matr3*)	Q8K310
	QNPNQKF (12)	111-**NPNQ**- 114	Myogenin: MYOG (*Myog*)	P12979
		113-**NPNQ**- 116	Myogenic factor 5: MYF5 (*Myf5*)	P24699
		139-**NPNQ**-142	Myoblast determination protein 1: MYOD1 (*Myod1*)	P10085
		186-**NPNQ**-189	ELAV-like protein 1: ELAV1: ELAV1: Hu-antigen R: HuR (*Elavl1*)	P70372
	HPVSGQK (4)	2249-**HPV**T**GQ**-2254	Chromodomain-helicase-DNA-binding protein 6: CHD6 (*Chd6*)	A3KFM7
	SISSLTH (4)	489-**SISSLT**-494	Runt-related transcription factor 2: RUNX2 (*Runx2*)	Q08775
		185-**SISSLT**-190	E3 ubiquitin-protein ligase RBBP6 (*Rbbp6*)	P97868
	HQSSTST (4)	43-**QSSTST**-48	Phosphatase 2A 56 kDa regulatory subunit γ isoform: 2A5G (*Ppp2r5c*)	Q60996
		61-**HQS**N**TS**-66	Alpha-1-antiproteinase: A1AT: Serpin A1 (*Serpina1*)	Q63969
***Lmna*$^{-/-}$ MEF nuclei (S3/R III)**	PTNQHHL (44)	155-**P**GS**QHHL**-161	Protein Wnt-7b: WNT7B (*Wnt7b*)	P28047
		513-**PT**Y**QHHL**-519	NACHT, LRR & PYD domains-containing protein1b allele2:NL1B2 (*Nlrp1b*)	A1Z198
	NAFMKWA (16)	110-**NAFM**V**WA**-116	Transcription factor SOX-9 (*Sox9*)	Q04887
		223-**FMKW**-226	Inositol 1,4,5-trisphosphate receptor type 1: ITPR1 (*Itpr1*)	P11881
	PTVKQKW (10)	56-**PE**V**KQKW**-62	Nuclear factor 1 A-type: NFIA (*Nfia*)	Q02780
		85-**TV**Q**QKW**-90	Synaptotagmin-7: SYT7 (*Syt7*)	Q9R0N7
	GLKLGAL (8)	568-**GLKLG**L**L**-574	Catenin alpha-like protein 1: Alpha-catulin: CTNL1 (*Ctnnal1*)	O88327
	HGSSLLK (6)	489-**HGSSLL**-494	Probable ATP-dependent RNA helicase DDX31 (*Ddx31*)	Q6NZQ2
	GGGPLYM (4)	362-**GGG**E**LYM**-368	Obscurin: OBSCN (*Obscn*)	A2AAJ9

8. Differential Phage Display Biopanning on Lmna$^{-/-}$ MEF Nuclei Using the BRASIL Method (Screen 3)

In the third screen, the Ph.D.–C7C library was pre-cleared on *Lmna*$^{+/+}$ MEF nuclei, and the pool of unbound phage particles was incubated with nuclei from either *Lmna*$^{+/+}$ or *Lmna*$^{-/-}$ MEF cells. We expect that phage particles displaying peptides that interact with the NE of the *Lmna*$^{+/+}$ MEF nuclei are cleared, resulting in peptides enriched post binding to *Lmna*$^{-/-}$ MEF nuclei that preferentially bind to *Lmna*$^{-/-}$ nuclei. This could be caused by their interacting partners being enriched or become more accessible in *Lmna*$^{-/-}$ nuclei. Three successive rounds of biopanning were performed such that the output from each round for *Lmna*$^{-/-}$ MEF nuclei was amplified, titered, and used as input for the subsequent

round with a pre-clearing step on *Lmna*$^{+/+}$ MEF nuclei done in each round. Remarkably, pre-clearing the phage library on *Lmna*$^{+/+}$ MEF nuclei resulted in no subsequent enrichment in phage binding to either type of nuclei by Round II or Round III (plausible reasons discussed later). Relative to the M13KE control phage, the mean ratio of phage TU counts obtained for *Lmna*$^{-/-}$ MEF nuclei in Round II (1.28 ± 0.55) or in Round III (0.82 ± 0.11) was not statistically significantly different from that for Round I (0.73 ± 0.20); *p=0.16* and *p=0.33* respectively in unpaired one-tailed t-test (Figure 14a). The results represent the mean ratio of phage TU counts (pre-cleared library/M13KE) ± STDEV of 2 independent repeats; each done in duplicates. Likewise, the mean ratio of phage TU counts obtained for *Lmna*$^{+/+}$ MEF nuclei in Round II (0.90 ± 0.29) or in Round III (0.86 ± 0.05) was not statistically significantly different from that for Round I (0.84 ± 0.15); *p=0.40* and *p=0.44* respectively in unpaired one-tailed t-test (Figure 14a).

a)

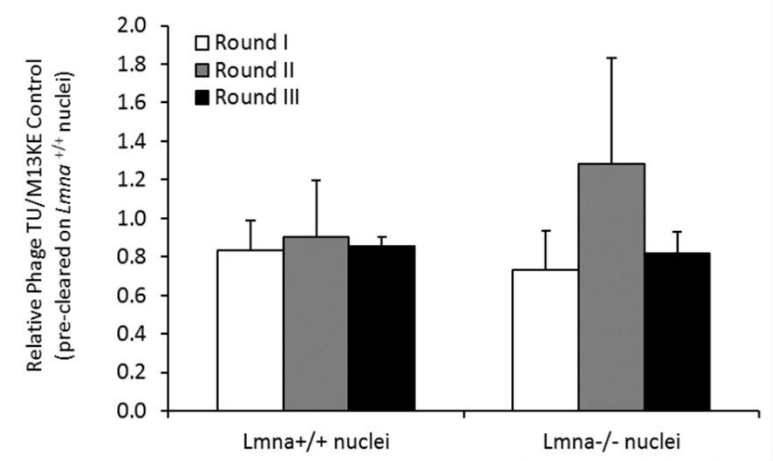
Round I
Round II
Round III
Relative Phage TU/M13KE Control
(pre-cleared on Lmna +/+ nuclei)
2.0
1.8
1.6
1.4
1.2
1.0
0.8
0.6
0.4
0.2
0.0
Lmna+/+ nuclei
Lmna-/- nuclei

b)

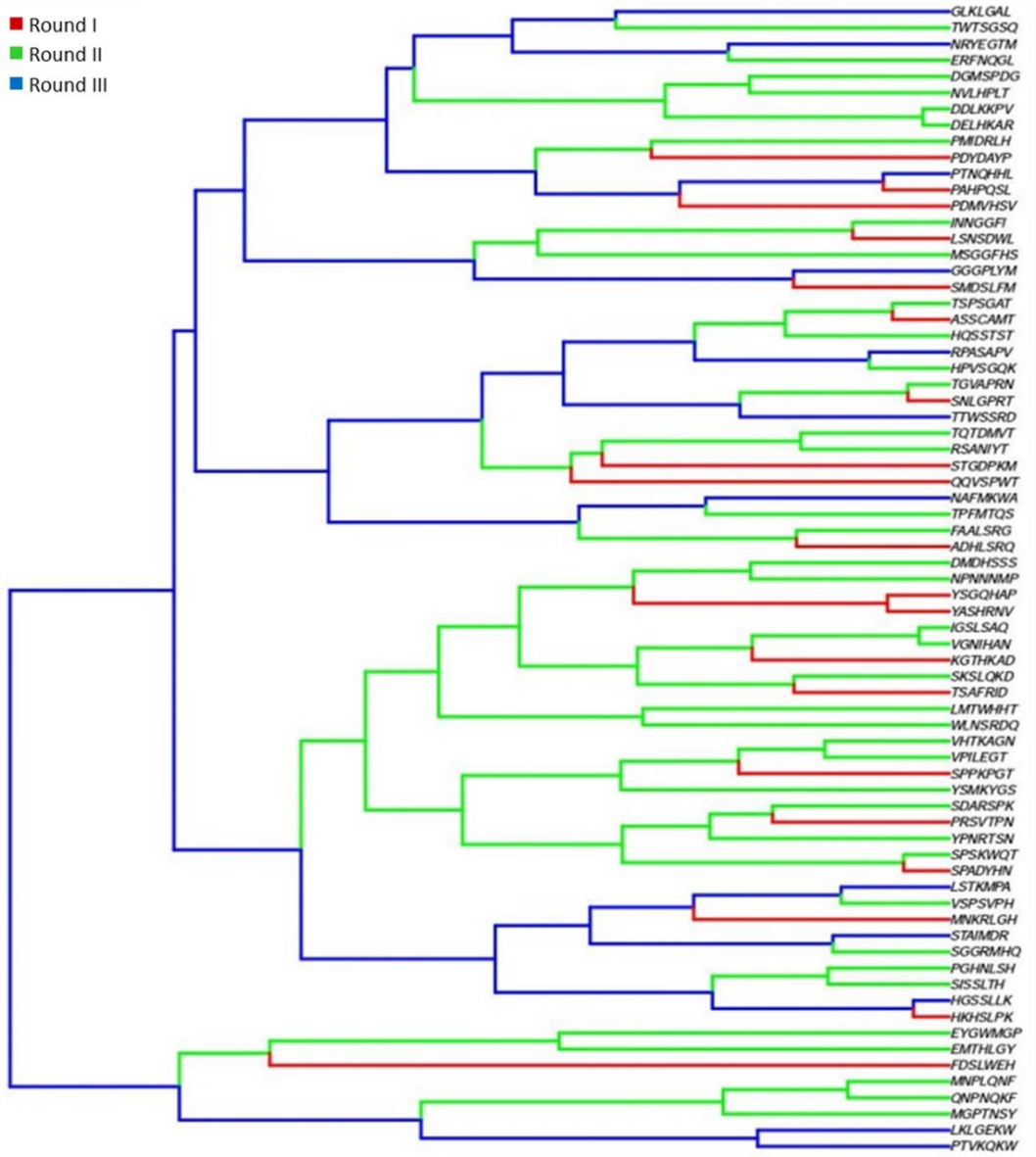
Round I
Round II
Round III
GLKLGAL
TWTSGSQ
NRYEGTM
ERFNQGL
DGMSPDG
NVLHPLT
DDLKKPV
DELHKAR
PMIDRLH
PDYDAYP
PTNQHHL
PAHPQSL
PDMVHSV
INNGGFI
LSNSDWL
MSGGFHS
GGGPLYM
SMDSLFM
TSPSGAT
ASSCAMT
HQSSTST
RPASAPV
HPVSGQK
TGVAPRN
SNLGPRT
TTWSSRD
TQTDMVT
RSANIYT
STGDPKM
QQVSPWT
NAFMKWA
TPFMTQS
FAALSRG
ADHLSRQ
DMDHSSS
NPNNNMP
YSGQHAP
YASHRNV
IGSLSAQ
VGNIHAN
KGTHKAD
SKSLQKD
TSAFRID
LMTWHHT
WLNSRDQ
VHTKAGN
VPILEGT
SPPKPGT
YSMKYGS
SDARSPK
PRSVTPN
YPNRTSN
SPSKWQT
SPADYHN
LSTKMPA
VSPSVPH
MNKRLGH
STAIMDR
SGGRMHQ
PGHNLSH
SISSLTH
HGSSLLK
HKHSLPK
EYGWMGP
EMTHLGY
FDSLWEH
MNPLQNF
QNPNQKF
MGPTNSY
LKLGEKW
PTVKQKW

Figure 14. Differential Phage Display Bio-panning on MEF Nuclei Using the BRASIL Method Post Pre-clearing the Ph.D.–C7C Library on *Lmna*$^{+/+}$ MEF Nuclei (Screen 3). (*a*) Phage binding was performed on nuclei from either MEF cells expressing WT *Lmna* or deficient in A-type lamins. No significant enrichment in phage binding to either *Lmna*$^{+/+}$ or *Lmna*$^{-/-}$ nuclei was obtained following 3 successive rounds of bio-panning. Results represent the mean ratio of phage TU counts ± STDEV of 2 independent repeats; each done in duplicates. (*b*) Clustering analysis of identified peptides with preferential binding to *Lmna*$^{-/-}$ nuclei was performed using the statistical programming language R and the scoring matrix PAM30. A panel of 20 peptides from Round I and 50 peptides from each of Rounds II and III were analyzed.

9. Sequence Determination of the Phage Inserts & Clustering Analysis for Clones Selected from Screen 3

To identify peptides displayed by phages that were recovered from *Lmna*$^{-/-}$ MEF nuclei in Screen 3, the phage inserts for a panel of 20 phage clones from Round I and 50 clones from each of Rounds II and III selected from the output for the *Lmna*$^{-/-}$ MEF nuclei were PCR amplified, sequenced, and analyzed. Clustering analysis of the recovered peptides shows that the diversity of peptides substantially decreases in Round II and even more so in Round III in that we recovered 38 different peptides in Round II and only 12 different peptides in Round III (Figure 14b). Of the 50 sequenced clones from Round II, 5 peptides appeared more than once. Moreover, the 50 sequenced clones from Round III are represented by only 12 different peptide sequences, 6 of which were repeated more than once. The percent frequency of occurrence of these peptides is shown in Table 2. In contrast, all 20 peptides from Round I were different (data not shown). Notably, peptide sequences from Round II show a greater level of clustering than peptides from Rounds I and III, consistent with a higher number of sequenced clones than Round I and a higher

a)

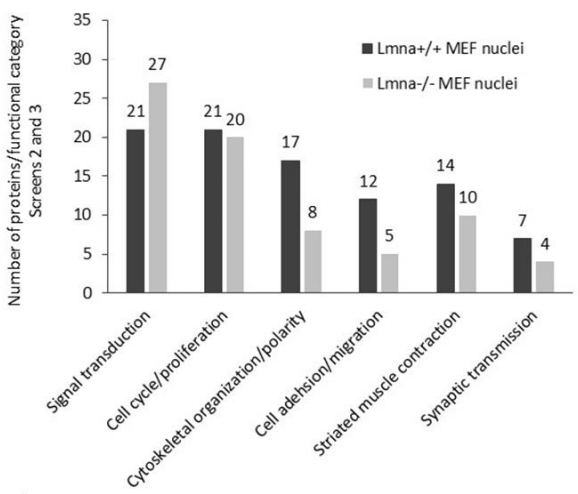

b)

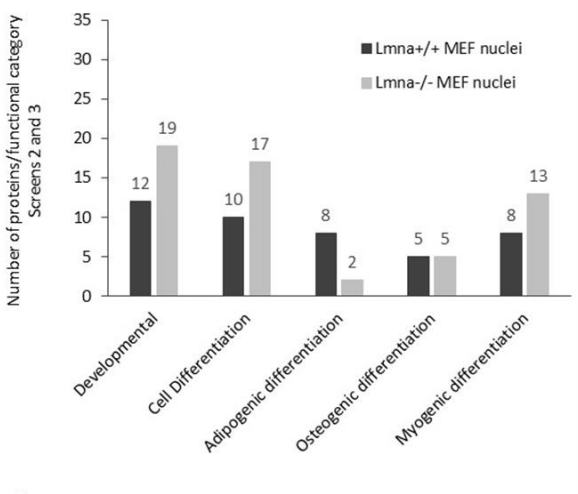

c)

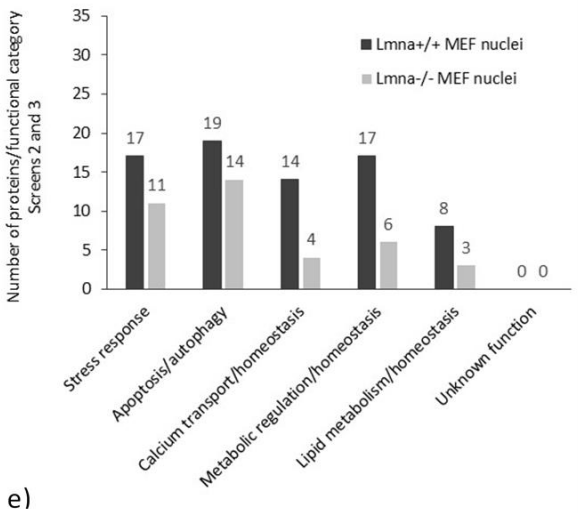

d)

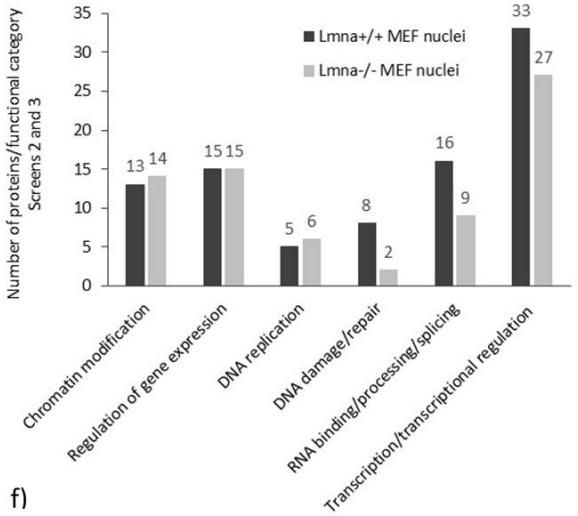

e)

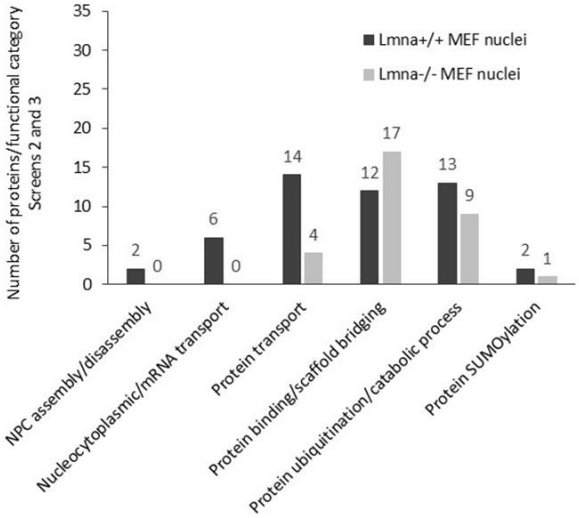

f)

Screens 2-3	Round	No. of peptides	No. of protein mimics
Lmna$^{+/+}$ MEF nuclei	II	10	45
Lmna$^{+/+}$ MEF nuclei	III	7	33
Lmna$^{-/-}$ MEF nuclei	II	5	29
Lmna$^{-/-}$ MEF nuclei	III	6	30

Figure 15. Functional Stratification of the Proteins Mimicked by the Peptides Uncovered by Differential Phage Display Bio-panning on *Lmna*$^{+/+}$ (Screen 2) and *Lmna*$^{-/-}$ (Screen 3) MEF Nuclei.
(*a*-*e*) Bar graph labels indicate the number of proteins per functional category. (*f*) The chart shows the total number of selected peptides and their protein mimics derived from BLAST analysis for each type of nuclei per bio-panning round.

number of different peptide sequences than Round III. Moreover, overlap between peptide sequences from the three rounds was also noted (Figure 14b).

10. High Frequency Peptides Recovered from Screen 3 & The Proteins They Mimic

Peptides recovered from Screen 3 with a frequency of occurrence ≥ 2% are listed in Table 2. Matching motifs in putative proteins mimicked by these peptides, which were obtained by protein-protein BLAST analysis are listed in Table 2 and Supplementary Table 2. Profiling the proteome of *Lmna*$^{-/-}$ MEF nuclei using differential phage display biopanning with BRASIL followed by protein-protein BLAST analysis, we identified a panel of proteins that preferentially interact with the NE lacking A-type lamins (Table 2 and Supplementary Table 2). A number of these proteins are A-type lamin interactors as validated by previous studies, and/or reported as dysregulated in the context of A-type lamin loss or mutation (see Discussion). In contrast to the somewhat limited functional proteomic profile that we obtained from direct phage display biopanning on *Lmna*$^{-/-}$ MEF nuclei (Screen 1), the uncovered proteins from Screen 3 are much more diverse in terms of molecular functions and biological processes (Figure 15b).

11. HuR Protein Localization is Altered in Lmna$^{-/-}$ in Comparison to Lmna$^{+/+}$ MEF Cells

Immunofluorescence staining of HuR protein in *Lmna*$^{-/-}$ and *Lmna*$^{+/+}$ MEF cell lines showed that HuR protein is mainly localized to the nucleus in *Lmna*$^{-/-}$ cell line as opposed to *Lmna*$^{+/+}$ cell line where it is mainly cytoplasmic (Figure 16a). Western Blot analysis of HuR protein expression in total, cytoplasmic and nuclear protein fractions from *Lmna*$^{+/+}$ and *Lmna*$^{-/-}$ MEF cell lines showed a 19-fold increase in nuclear HuR protein expression in *Lmna*$^{-/-}$ (19 ± 14.6) in comparison to *Lmna*$^{+/+}$ MEF cell line (Figure 16b). The results represent the mean ratio of nuclear HuR densitometry signal, normalized to that of Lamin B1, from three independent repeats. However; this increase was not statistically significant as determined by one-way analysis of variance (ANOVA) ($p = 0.286$) (Figure 16c). Conversely, a 2.6-fold decrease in cytoplasmic HuR protein expression was noted in *Lmna*$^{-/-}$ (0.38 ± 0.08) in comparison to *Lmna*$^{+/+}$ MEF cell line (Figure 16c, d). The results represent the mean ratio of cytoplasmic HuR densitometry signal, normalized to that of GAPDH, from three independent repeats. This decrease was statistically significant ($p = 0.001$). No significant change in total HuR protein expression was noted in *Lmna*$^{-/-}$ (1.09 ± 0.08) in comparison to *Lmna*$^{+/+}$ MEF cell line ($p = 0.333$) (Figure 16c, d). Total HuR was normalized to GAPDH and the mean ratio was calculated from three independent repeats. Interestingly, a cleavage product of 24kDa appeared in the nuclear fraction of *Lmna*$^{+/+}$ but not *Lmna*$^{-/-}$ MEF cell line (Figure 16b). As controls for the purity of cytoplasmic and nuclear fractions, GAPDH protein only appeared in the cytoplasmic protein fraction while Lamin B1 protein only appeared in the nuclear protein fraction (Figure 16b).

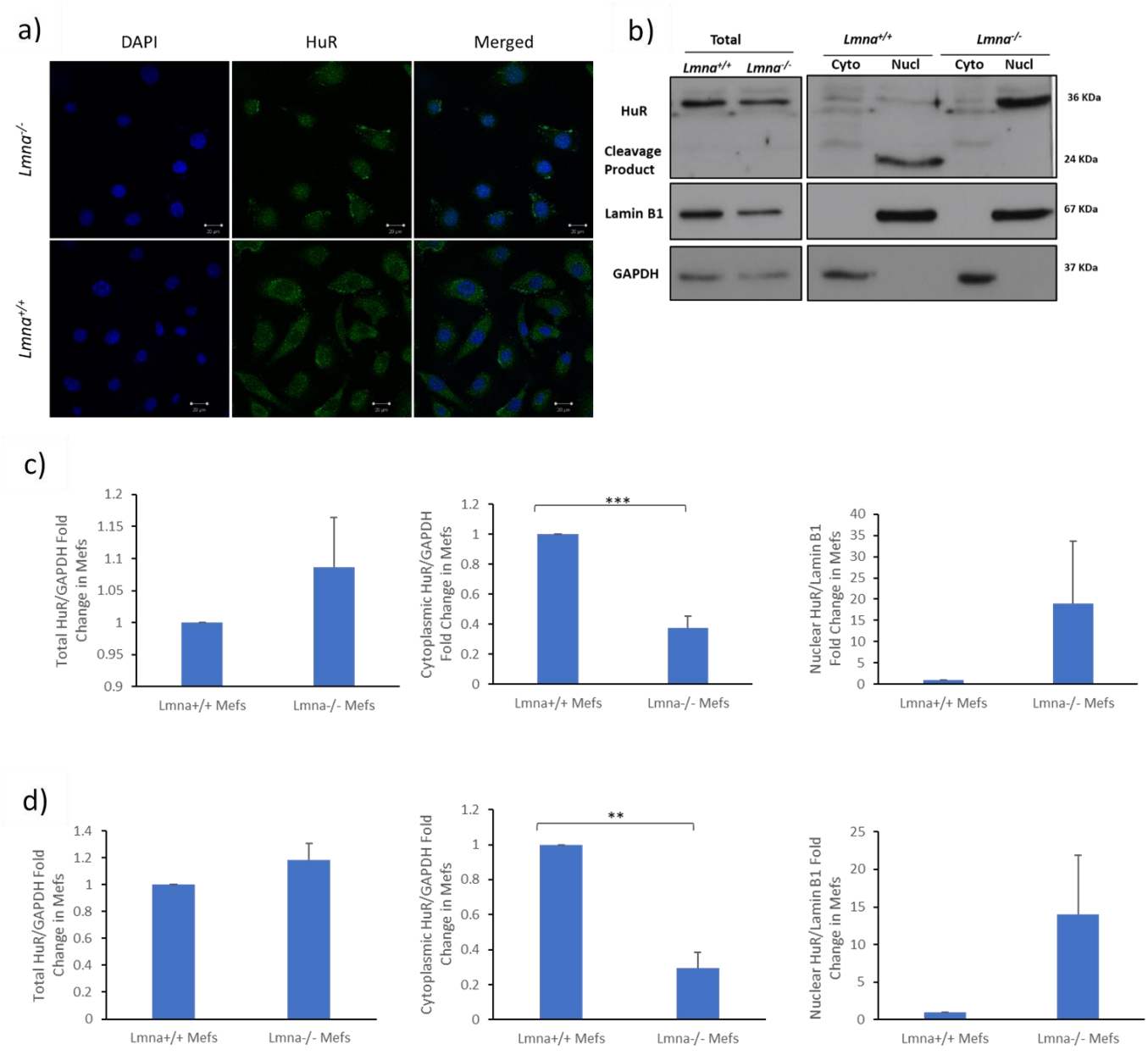

Figure 16. HuR Protein Expression and Sub-cellular Localization in MEF Cell Lines. *(a)* Representative confocal microscope images showing immunofluorescence staining of HuR protein in *Lmna*$^{-/-}$ in comparison to *Lmna*$^{+/+}$ MEF cell line. HuR protein preferentially localizes to the nucleus in *Lmna*$^{-/-}$ cell line while it mainly localizes in the cytoplasm in *Lmna*$^{+/+}$ cell line. Nuclei were visualized by counterstaining with 4′,6-diamidino-2-phenylindole (DAPI). *(b)* Western Blot analysis of HuR protein expression in total, cytoplasmic and nuclear protein fractions from *Lmna*$^{+/+}$ and *Lmna*$^{-/-}$ MEF cell lines. An increase in nuclear HuR protein expression was noted in *Lmna*$^{-/-}$ in comparison to *Lmna*$^{+/+}$ MEF cell line. A cleavage product of 24kDa appeared in the nuclear fraction of *Lmna*$^{+/,}$ but not *Lmna*$^{-/-}$ MEF cell line. GAPDH and Lamin B1 proteins were used as loading controls

and for assessment of the purity of cytoplasmic and nuclear protein fractions. *(c, d)* Quantification of HuR densitometry signal, normalized to that of the GAPDH loading control for total and cytoplasmic protein fractions and to that of the Lamin B1 loading control for nuclear fractions. A statistically significant decrease in cytoplasmic HuR protein expression was noted in *Lmna*$^{-/-}$ in comparison *Lmna*$^{+/+}$ MEF cell line. Although an increase in nuclear HuR protein expression was noted in *Lmna*$^{-/-}$ in comparison *Lmna*$^{+/+}$ MEF cell line, this increase was not statistically significant. Results represent average ± SEM of 3 independent experiments. Significance was assessed by one-way analysis of variance (ANOVA) followed by Dunnett's post hoc test. A probability level of $p \leq 0.05$ was considered significant. (***$p \leq 0.001$, **$p \leq 0.01$).

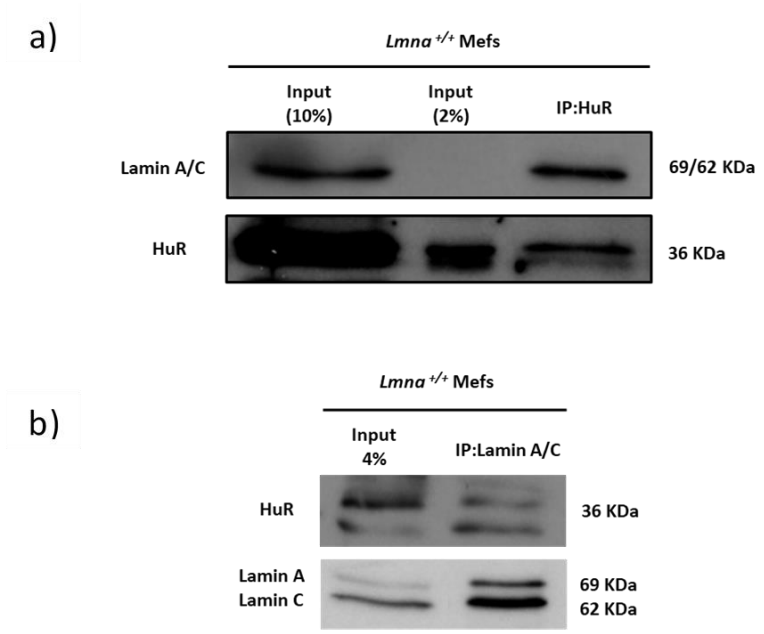

Figure 17. Co-immunoprecipitation (Co-IP) Analysis to Examine Interaction Between Lamin A/C and HuR Proteins in *Lmna*$^{+/+}$ MEF Cell Line.
(a) Co-IP was performed using HuR antibody-coupled Dynabeads. Immunoblotting using Lamin A/C and HuR antibodies showed that both proteins co-immunoprecipitate together in *Lmna*$^{+/+}$ MEF cell line. *(b)* Co-IP was performed using Lamin A/C antibody-coupled Dynabeads. Immunoblotting using Lamin A/C and HuR antibodies showed that both proteins co-immunoprecipitate together in *Lmna*$^{+/+}$ MEF cell line. Results represent three independent experiments in case of Lamin A/C antibody-coupled Dynabeads and one repeat in case of HuR antibody-coupled Dynabeads.

12. HuR Protein Interacts with Lamin A/C

In an attempt to validate one of the targets obtained in our differential phage display screens in this study, we tested whether HuR protein binds Lamin A/C, co-immunoprecipitation assays were performed using both anti-HuR and anti-Lamin A/C-coupled beads. Lamin A/C protein was immunoprecipitated using beads coupled to an antibody against HuR. Probing for HuR was done as a control (Figure 17a). On the other hand, HuR was pulled down using beads coupled to an antibody against Lamin A/C. Probing for Lamin A/C was done as a control (Figure 17b).

E. Discussion

Proteomic profiling of nuclei from *Lmna*$^{+/+}$ or *Lmna*$^{-/-}$ MEF cells by direct phage display using BRASIL resulted in significant enrichment in phage binding to both types of nuclei following three successive rounds of biopanning (Screen 1). The data suggest preferential phage binding to *Lmna*$^{+/+}$ nuclei relative to nuclei derived from *Lmna*$^{-/-}$ cells, which was particularly evident in Round II (Figure 11a). Consistent with the pattern obtained in Screen 1, differential phage display biopanning (Screen 2) resulted in significant enrichment in phage binding to *Lmna*$^{+/+}$ nuclei that was noted as early as Round II (Figure 13a). The lack of further enrichment, in terms of phage TU counts, in Round III is probably due to the effect the selected phages may have on bacterial host replication such as causing a slower bacterial replication cycle. Notably, despite pre-clearing the Ph.D.–C7C library on *Lmna*$^{-/-}$ MEF nuclei, we still noted significant subsequent enrichment in phage binding to *Lmna*$^{-/-}$ nuclei in Round II, which persisted in Round III

(Figure 13a). These findings indicate that pre-clearing the phage library on lamin A/C null nuclei may not have fully quenched the library from peptides that have binding affinities to *Lmna*$^{-/-}$ nuclei. This could be explained in part by either weak and transient interactions between these peptides and their binding partners in *Lmna*$^{-/-}$ NE, and/or a low copy number of the binding partners in *Lmna*$^{-/-}$ NE that is inadequate to quench the homing phage displayed peptides during the pre-clearing steps. In contrast, pre-clearing the phage library on *Lmna*$^{+/+}$ MEF nuclei (Screen 3) resulted in no subsequent enrichment in phage binding to either type of nuclei by Round II or Round III (Figure 14a), which is indicative that pre-clearing the phage library on *Lmna*$^{+/+}$ nuclei efficiently quenched the library from peptides that have binding affinities to either type of nuclei. This data could be explained, in part, by strong interactions between these peptides and their binding partners in *Lmna*$^{+/+}$ NE, and/or a copy number of the binding partners in *Lmna*$^{+/+}$ nuclei that is adequately high to quench the homing phage displayed peptides during the pre-clearing steps.

Clustering analysis of the peptides derived from Screen 1 shows a decrease in the diversity of peptide sequences in Rounds II and III in comparison to Round I (Figure 11b and Figure 11c). This is an expected outcome for screens with successful enrichment of phage particles displaying peptides that have more selectivity in binding to the target(s) of interest, hence yielding less diversity across successive rounds of biopanning. Similarly, a decrease in the diversity of peptides recovered from successive rounds of biopanning was also noted in the two differential phage display screens (Figure 13b and Figure 14b). Interestingly, bioinformatic analysis of peptides derived from Screens 2 and 3 revealed that distinct peptides from two or three different rounds cluster together, which is indicative that

although these peptides are different, they are similar in terms of characteristics of amino acid sequences and likely have similar binding properties (Figure 13b and Figure 14b). Moreover, the heptapeptide HPVSGQK was recovered at a frequency of 7% in Screen 2, Round III biopanning on *Lmna*$^{+/+}$ nuclei and at a frequency of 4% in Screen 3, Round II biopanning on *Lmna*$^{-/-}$ nuclei, thus suggesting that the proteins mimicked by this peptide namely pleckstrin homology domain-containing family A members 5, 6, and 7 (PKHA5, PKHA6, PKHA7) and the chromodomain-helicase-DNA-binding protein 6 (CHD6) have their interacting partners retained in both types of nuclei, regardless of the status of A-type lamin expression. It is worthwhile mentioning that all the enriched peptides obtained in all three screens differ from the target-unrelated peptides that were previously reported for M13 phage display libraries [289,290], thus ruling out the likelihood that any of the three screens yielded high frequency peptides which interact nonspecifically with various items and reagents in the experimental procedures.

In validation of the experimental modality that we used for the proteomic profiling of nuclei, several proteins uncovered in Screen 1—with matching motifs to the high frequency peptides that were derived from direct phage display biopanning on *Lmna*$^{+/+}$ nuclei (Table 1)—were previously reported as A-type lamin interactors and some of them are altered in laminopathies. These include the epidermal growth factor (EGF) [103], protein ELYS also known as AT-hook-containing transcription factor 1 or MEL28 nucleoporin [102,291,292], emerin [102,291,293-298], desmoplakin (DESP) [299], nuclear RNA export factor 1 (NXF1) [300], the E3 SUMO-protein ligase RanBP2 [102], and pre-lamin A/C [103,301]. Similarly, some of the proteins uncovered in Screen 2— with matching motifs to the high frequency

peptides that were derived from differential phage display bio-panning on *Lmna*$^{+/+}$ nuclei (Table 2 and Supplementary Table 1)—were previously reported as lamin A interactors. These include vascular endothelial growth factor receptor 2 (VEGFR2) [302], ubiquitin carboxyl-terminal hydrolase 7 (Usp7) [303], nuclear envelope pore membrane protein POM121 [102,291], nuclear pore complex protein NU133 [102,291], fibronectin [304], and proline-rich protein 14 (PRR14) [305].

A result that further validates our experimental approach is that one of the proteins uncovered in Screen 1, with a matching motif to the high frequency peptide MVRDHSV that was derived from direct phage display biopanning on *Lmna*$^{-/-}$ nuclei (Table 1), is nesprin-1 (SYNE1), a lamin A/C interactor that was shown to be disorganized in *Lmna*$^{-/-}$ cardiomyocytes and implicated in the nuclear and the cytoskeletal defects noted in lamin A/C-deficient cardiomyopathy [279,306,307]. Similarly, several of the proteins uncovered in Screen 3—with matching motifs to the high frequency peptides that were derived from differential phage display biopanning on *Lmna*$^{-/-}$ nuclei (Table 2 and Supplementary Table 2)—were previously reported as lamin A/C interactors that are dysregulated in the context of laminopathies. For instance, matrin-3 (MATR3) with a matching motif to the high frequency heptapeptide SGGRMHQ, is an RNA-binding nucleoplasmic protein that co-immunoprecipitates with lamin A and their interaction is disrupted by myopathic *LMNA* mutations [90]. Additionally, the transcription factor myogenin (MYOG) with a matching motif to the high frequency peptide QNPNQKF is transcriptionally and functionally altered in C2C12 myoblasts expressing myodystrophic *Lmna* mutations that impair myogenic differentiation [308]. Likewise, the closely related myogenic factor 5 (MYF5) with a matching

motif to the same heptapeptide is upregulated in replicative myoblasts lacking A-type lamins that exhibit impaired myogenesis [262]. Moreover, the related myoblast determination protein 1 (MYOD1), also with a matching motif to the peptide QNPNQKF, is upregulated in compensation for a molecular block to differentiation in *Emd* null muscle characterized by regeneration defects and delayed myogenic differentiation [276]. Notably, runt-related transcription factor 2 (RUNX2), with a matching motif to the peptide SISSLTH, physically interacts with lamin A during the process of calcification in that its nuclear translocation is abrogated with the knockdown of lamin A [309]. In support of this, another study demonstrated that the osteogenic transcription factor capacity of RUNX2 is influenced by its co-localization with MAN-1, a NE protein that is increased in expression in the absence of lamin A/C [310].

Though some of the identified proteins in these screens were previously reported as A-type lamin interactors that are altered in laminopathies, many have not been reported in this context. By virtue of their nuclear expression and localization as well as their functional relevance, they warrant further investigation as putative functional partners that may be dysregulated in the absence of lamin A/C. Herein, we will discuss select examples from each screen. For instance, nuclear receptor coactivator 2 (NCOA2), with a matching motif to the high frequency peptide HNASRNT that was derived from direct phage display biopanning on *Lmna*$^{+/+}$ nuclei in Screen 1, was also uncovered by differential biopanning on *Lmna*$^{+/+}$ nuclei in Screen 2 as it matched to the peptide TPESRHE. Highly expressed in the nucleus, NCOA2 has histone acetyltransferase activity and is implicated in the transcriptional regulation of lipid metabolism and white adipocyte differentiation by

interacting with the peroxisome proliferator-activated receptor gamma (PPARγ) [311,312]. Moreover, the oxidoreductase 7-dehydrocholesterol reductase (DHCR7) that mimics the peptide ASKSTHD which was enriched in Screen 1 is also implicated in lipid biosynthesis and in the regulation of cell proliferation and cell differentiation by virtue of its interplay with the sterol regulatory element binding protein 1 (SREBP-1), a lamin A interacting partner [313,314]. Likewise, the mediator of RNA polymerase II transcription subunit 12 (MED12), a ubiquitin protein ligase, which is mimicked by the peptide LKHGMNK that was enriched in Screen 2 is involved in the transcriptional regulation of white adipocyte differentiation, and canonical Wnt signaling pathway with proposed implications in cardiovascular diseases [315,316]. Among the proteins uncovered in Screen 2, both the THO complex subunit 1 (THOC1) and the serine/threonine-protein kinase mTOR have motifs with strong homology to the peptide LKLGEKW that exhibited preferential binding to *Lmna*$^{+/+}$ nuclei. Implicated in transcriptional regulation and mRNA splicing, THOC1 also functions in mRNA export to the cytoplasm and its absence has been linked to genomic instability associated with DNA breaks [317,318]. A central regulator of cellular metabolism, growth, and survival in response to growth factors and stress signals, mTOR has roles in cardiac muscle development and contraction in addition to a plethora of other functions [319]. A recent study reported on its implication in *LMNA* associated cardiomyopathy by impairing autophagy [320], whereas an earlier study had demonstrated that mTOR interacts with the nuclear lamina-associated NE transmembrane protein NET39 (Ppapdc3), and in part mediates its regulation of myoblast differentiation [321].

Notably, the tubulin polyglutamylase TTLL4, mimicked by the peptide PLNKPYL that was enriched with preferential binding to *Lmna*$^{+/+}$ nuclei in Screen 2, mediates the initiation of polyglutamylation of nucleosome assembly proteins NAP1L1 and NAP1L4 [322]. Intriguingly, cytosolic carboxypeptidase-like protein 5 (CBPC5: CCP5), a metallocarboxypeptidase that mediates deglutamylation in proteins such as tubulins [323,324], hence performing the inverse function to TTLL4, was recovered by profiling *Lmna*$^{-/-}$ nuclei in Screen 3. Similarly, the ubiquitin carboxyl-terminal hydrolase 7 (Usp7) protein, a lamin A interactor that we uncovered in Screen 2 counteracts the opposing ubiquitin ligase activity of the zinc finger protein TRIM27 [325], a protein which is implicated in the regulation of actin nucleation and mimicked by the peptide MVRDHSV that was recovered at high frequency from direct profiling of *Lmna*$^{-/-}$ nuclei in Screen 1. Furthermore, among the protein mimics uncovered in Screen 3 with preferential binding to *Lmna*$^{-/-}$ nuclei is the nuclear receptor subfamily 1 group D member 2 (NR1D2), a transcription factor that regulates lipid and energy homeostasis in skeletal muscle by repression of genes involved in lipid metabolism and myogenesis whereas it acts as a transcriptional activator of SREBP1 [326,327]. Likewise, uncovered in Screen 3 with preferential binding to *Lmna*$^{-/-}$ nuclei is the protein catenin alpha-like protein 1 (CTNL1), also known as alpha-catulin which promotes cellular proliferation by modulating the Rho signaling pathway and downregulating E-cadherin [328,329].

Functional stratification of the proteins obtained in Screen 1 suggests that the proteomic repertoire that interacts with the *Lmna*$^{+/+}$ nuclei is larger and more functionally diverse than the one that interacts with nuclei in the absence of lamin A/C (Figure 12),

which goes in line with the more prominent enrichment in phage binding to *Lmna*$^{+/+}$ nuclei in comparison to *Lmna*$^{-/-}$ nuclei (Figure 11a). However, functional stratification of the proteins uncovered using differential phage display biopanning (Screens 2 and 3 respectively) uncovered a broader and more functionally diverse proteome that interacts with either type of nuclei with overlapping and distinct functional distribution patterns (Figure 15). Accounting for the discrepancy in yields between the direct and differential screens, it is plausible that performing pre-clearing steps in the differential screens enhanced phage binding to target(s) of interest by reducing steric hindrances and competition among phage particles, hence resulting in enrichment and recovery of a larger pool of interactors. Nonetheless, using differential phage display biopanning, we still noted more functional diversity in the panel of 78 proteins that were uncovered from *Lmna*$^{+/+}$ nuclear profiling in comparison to the 59 proteins that were obtained from *Lmna*$^{-/-}$ nuclear profiling. This could be influenced by the difference in the number of protein mimics uncovered per screen which could be attributed in part to the higher number of peptides that were enriched in Screen 2, which yielded 17 distinct peptides with a frequency ≥ 2%, in comparison to Screen 3 which yielded 11 distinct peptides with a frequency ≥ 2%. However, the larger pool of peptides derived from Screen 2 does not explain in full the wider spectrum of molecular functions and biological processes associated with the proteins they mimic in comparison to the narrower bio-functional spectrum of the proteins obtained in Screen 3. Remarkably, in comparison to *Lmna*$^{-/-}$ MEF nuclei, differential profiling of *Lmna*$^{+/+}$ nuclei unveiled a larger number of proteins that are implicated in cytoskeletal organization and cell polarity, cell adhesion and migration, regulation of

adipogenic differentiation, regulation of striated muscle contraction and/or synaptic transmission, calcium ion transport and homeostasis, metabolic regulation including lipid homeostasis, stress response, apoptosis and/or autophagy, DNA damage and repair, RNA processing and splicing, nucleocytoplasmic transport, NPC assembly, protein transport, and protein ubiquitination and catabolic process (Figure 15). By contrast, differential profiling of *Lmna*$^{-/-}$ nuclei unveiled a larger number of proteins that are implicated in signal transduction, developmental regulation, cell differentiation, striated muscle differentiation, and protein scaffolding and bridging (Figure 15). Notably, differential profiling of both types of nuclei gave similar yields of proteins implicated in cell proliferation and cell cycle, osteoblast differentiation, regulation of gene expression, chromatin modification, DNA replication and transcription. Accordingly, the apparent gaps in proteomic functional distribution suggest that proteins implicated in these processes may be dysregulated in terms of expression, localization, and/or function in the absence of lamin A and in the context of laminopathies. A number of these processes including RNA splicing and protein ubiquitination have only recently started to gain attention in the laminopathy field [283,330], yet our findings provide support for more research efforts in these areas. In this study, we validate that A-type lamins interact with and influence the subcellular localization of HuR, an mRNA-binding protein that stabilizes mRNA by binding to AU-rich elements (ARE) in the 3'-untranslated region of mRNA transcripts. Through its mRNA stabilizing function, HuR regulates the expression of several myogenic factors, such as myogenin. The promyogenic function of HuR depends on its cytoplasmic localization, which is mediated by the cleavage of a fraction of cytoplasmic HuR. Caspases cleave HuR and generate two

cleavage products, one of which is HuR-CP1 (24kDa) that competes with uncleaved HuR for Transportin2 (TRN2) binding, thus preventing its nuclear import. HuR then accumulates in the cytoplasm and stabilizes mRNA of myogenic factors.

Moreover, the proteins unveiled in our proteomic screens that have not been studied in the context of lamin A loss or laminopathies, stand out as new players that are worthy of further investigation. Studying the effects of *Lmna* loss and mutations on the expression, localization, and function of some of these NE homing proteins will offer new clues into the molecular mechanisms responsible for the phenotypic complexity and the tissue-specific impaired function in laminopathies including a better understanding of the causes for debilitating diseases such as dilated cardiomyopathy and Emery-Dreifuss muscular dystrophy. Additionally, our results establish phage display biopanning using BRASIL as a promising tool to investigate changes in NE composition and accessibility in response to deletion of specific NE proteins such that this technical modality could be used in a wide range of applications.

F. Supplementary Figures and Tables

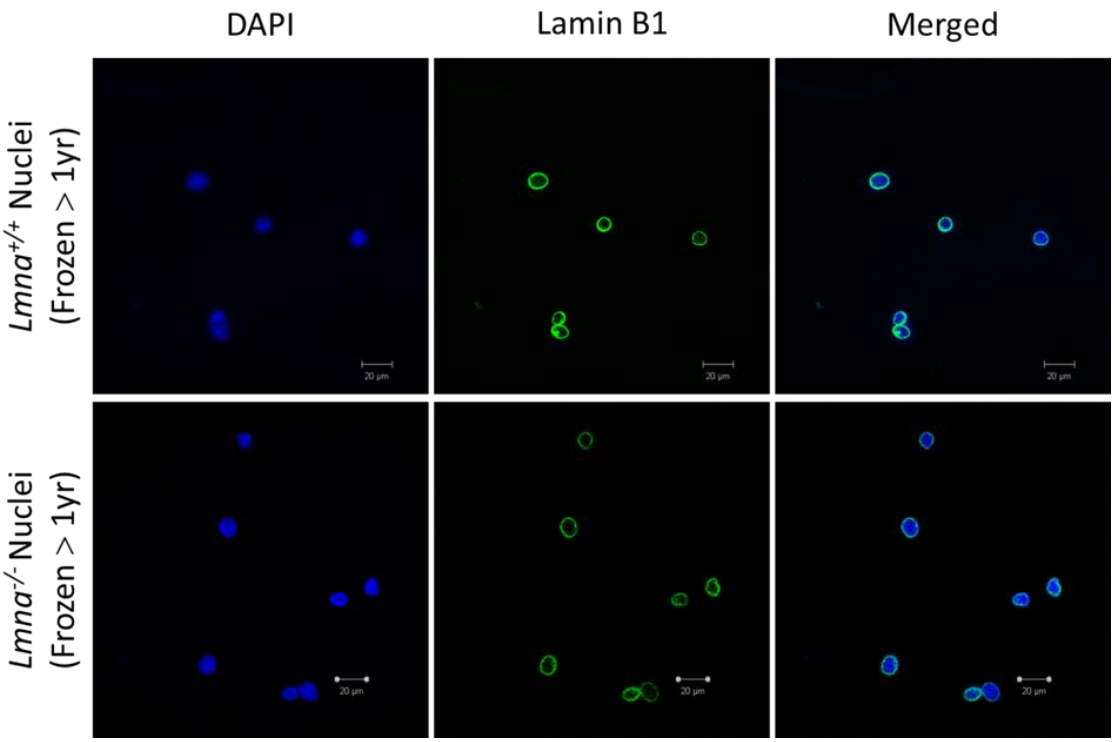

Supplementary Figure 1. Immunofluorescence Staining of Lamin B1 in Nuclei Isolated from MEF Cell Lines.
Representative confocal microscope images showing immunofluorescence staining of Lamin B1 protein in nuclei isolated from *Lmna*$^{+/+}$ and *Lmna*$^{-/-}$ MEF cell lines post long-term storage at -80°C prior to Lamin B1 staining. Nuclear integrity was preserved in *Lmna*$^{+/+}$ nuclei, following nuclear isolation and storage, as shown by continuous Lamin B1 staining at the nuclear rim. The first row shows *Lmna*$^{+/+}$ nuclei that were stored at -80°C for ~1 year before performing Lamin B1 staining. The second panel shows *Lmna*$^{-/-}$ nuclei that were stored at -80°C for ~ 1 year more before performing Lamin B1 staining. Nuclei were also counterstained with 4′,6-diamidino-2-phenylindole (DAPI).

Supplementary Table 1. A list of peptides derived from differential phage display bio-panning on *Lmna*$^{+/+}$ MEF nuclei using pre-cleared Ph.D.–C7C library and the BRASIL method (Screen 2).

Matching motifs in candidate proteins mimicked by the phage inserts were obtained by protein-protein BLAST analysis based on the Max score, E-value, and Identity.

Round	Peptide (% Frequency)	Matching Motif	Protein Mimic (Gene)	UniProtKB Accession
R II	FHATKAR	97-**HATKA**-101	Cleavage and polyadenylation specificity factor subunit 3: CPSF3 (*Cpsf3*)	Q9QXK7
	(11)	152-**ATKAR**-156	Signal recognition particle 54 kDa protein: SRP54 (*Srp54*)	P14576
		409-**ATKAR**-413	U4/U6 small nuclear ribonucleoprotein Prp31: PRP31 (*Prpf31*)	Q8CCF0
		1630-**H**Q**TKAR**-1635	Zinc finger homeobox protein 3: ZFHX3 (*Zfhx3*)	Q61329
	ETYTSKA	323-**ETYTS**-327	cAMP-responsive element-binding protein 3-like protein 1: CR3L1 (*Creb3l1*)	Q9Z125
	(11)	525-**ETYTS**-529	Kinesin-like protein KIF3B (*Kif3b*)	Q61771
		20-**TYTSK**-24	Fibroblast growth factor 1: FGF1 (*Fgf1*)	P61148
		159-**TYTSK**-163	Zinc finger protein 60: ZFP60 (*Zfp60*)	P16374
		212-**ET**F**TSK**-217	TFIIH basal transcription factor complex helicase XPB subunit: ERCC3 (*Ercc3*)	P49135
	TPYHTLK	73-**TPYHT**-77	Atp2a3 protein: Sarcoplasmic/ER calcium ATPase 3: Atp2a3 (*Atp2a3*)	Q91YM6
	(9)	155-**PYHTL**-159	Zinc finger protein SNAI3 (*Snai3*)	Q9QY31
		96-**YHTLK**-100	Gamma-enolase: Enolase 2: ENOG (*Eno2*)	P17183
		635-**TPYH**I**L**-640	Protein-arginine deiminase type-3: PADI3 (*Padi3*)	Q9Z184
	LPIMQGH	80-**LPIMQ**-84	Peroxisomal biogenesis factor 19: PEX19 (*Pex19*)	Q8VCI5
	(8)	227-**PIMQG**-231	Cyclin-dependent kinase 9: CDK9 (*Cdk9*)	Q99J95
		736-**LP**VV**QGH**-742	E3 ubiquitin-protein ligase UBR2 (*Ubr2*)	Q6WKZ8
		43-**LP**L**M**P**GH**-49	Protein phosphatase 2, regulatory subunit B'', alpha (*Ppp2r3a*)	Q4VA48
		1658-M**PIMQ**-1662	Protein PRR14L (*Prr14l*)	E9Q7C4
	EHYTAAI	249-Q**HYTAA**-254	CUGBP Elav-like family member 3: CELF3 (*Celf3*)	Q8CIN6
	(8)	376-**HY**S**AAI**-381	Protein SMG5 (*Smg5*)	Q6ZPY2
		382-**HYT**E**AI**-387	Stress-induced-phosphoprotein 1: STIP1 (*Stip1*)	Q60864
		38-**E**NF**TAAI**-44	Protein Slc22a29: Solute carrier family 22. member 29 (*Slc22a29*)	Q8BWG6
		170-**YTAAI**-174	Cyclin-dependent kinase 11B: CD11B: p58 CDK11 (*Cdk11b, Cdc2l1*)	P24788
		170-**YTAAI**-174	DnaJ homolog subfamily C member 3: DNJC3 (*Dnajc3*)	Q91YW3
	LKHGMNK	862-**KHGMN**-866	Mediator of RNA polymerase II transcription subunit 12: MED12 (*Med12*)	A2AGH6
	(8)	377-**LKH**A**MN**-382	Mediator of RNA polymerase II transcription subunit 23: MED23 (*Med23*)	Q80YQ2
		97-**LK**NN**MNK**-103	Prospero homeobox protein 1: PROX1 (*Prox1*)	P48437
		628-**KHGM**D-632	Calcium-dependent secretion activator 2: CAPS2 (*Cadps2*)	Q8BYR5
	GMMPTKV	1282-**GMMPS**K-1287	Vascular endothelial growth factor receptor 2: VEGFR2: KDR (*Kdr*)	P35918
	(6)	969-**MPTKV**-973	Eukaryotic translation initiation factor 4E transporter: 4ET (*Eif4enif1*)	Q9EST3
		1-**MMPT**P**V**-6	T-complex protein 1 subunit eta: TCPH (*Cct7*)	P80313
		32-**MMPT**-35	Ubiquitin carboxyl-terminal hydrolase 7: USP7 (*Usp7*)	E9PXY8
		771-**MMPT**-774	FH1/FH2 domain-containing protein 1: FHOD1 (*Fhod1*)	Q6P9Q4
	TPESRHE	89-**TP**D**SR**Q**E**-95	Thioredoxin reductase 1: TRXR1 (*Txnrd1*)	Q9JMH6
	(6)	373-**ESRHE**-377	Double-stranded RNA-specific adenosine deaminase: DSRAD (*Adar*)	Q99MU3
		57-**ESRHE**-61	Estrogen receptor beta: ESR2 (*Esr2*)	O08537
		288-**ESRHE**-292	Nuclear receptor coactivator 2: NCOA2 (*Ncoa2*)	Q61026
	NQEIASR	24-**NQEIA**-28	Nucleoplasmin-3: Nucleophosmin-3: NPM3 (*Npm3*)	Q9CPP0
	(4)	303-**NQEIA**-307	TGF-beta-activated kinase 1 and MAP3K7-binding protein 1: TAB1 (*Tab1*)	Q8CF89
		44-**NE**E**IAS**-49	Calmodulin-binding transcription activator 2: CAMTA2 (*Camta2*)	B0QZH4
		2054-**EIASR**-2058	Alstrom syndrome protein 1 homolog: ALMS1 (*Alms1*)	Q8K4E0
	PLNKPYL	177-**LNKPYL**-182	Mitogen-activated protein kinase kinase kinase 4: M3K4 (*Map3k4*)	O08648
	(4)	169-**PLNK**M**YL**-175	E3 UFM1-protein ligase 1: UFL1 (*Ufl1*)	Q8CCJ3
		116-**LNKP**F**L**-121	Calnexin: CALX (*Canx*)	P35564
		747-L**HKPYL**-752	Tubulin polyglutamylase TTLL4 (*Ttll4*)	Q80UG8
R III	MSTGLSS	411-**STGLSS**-416	Kelch-like protein 2: KLHL2 (*Klhl2*)	Q8JZP3
	(14)	1-**MSTGL**-5	Septin-5: SEPT5 (*Sept5*)	Q9Z2Q6
		477-**MSTGL**-481	Hydroperoxide isomerase ALOXE3: lipoxygenase-3: LOXE3 (*Aloxe3*)	Q9WV07
		1271-**M**N**TGL**P**S**-1277	Myomegalin: MYOME (*Pde4dip*)	Q80YT7

	1434-**MST**A**LS**-1439	Myoferlin: MYOF (*Myof*)	Q69ZN7
NSSFVRS (11)	40-**NST**F**VRS**-46	E3 ubiquitin-protein ligase UBR4 (*Ubr4*)	A2AN08
	426-**NSSFV**P**S**-432	Pericentriolar material 1 protein: PCM1 (*Pcm1*)	Q9R0L6
	82-**SSFVR**-86	Nuclear envelope pore membrane protein POM 121: PO121 (*Pom121*)	Q8K3Z9
	463-**NSSFV**-467	PR domain zinc finger protein 2: Prdm2 (*Prdm2*)	A2A7B5
RGATPMS (11)	267-**RGATP**K**S**-273	Protocadherin 1: Cadherin-Like Protein 1: PCDH1 (*Pcdh1*)	Q8CFX3
	132-**ATPMS**-136	AT-rich interactive domain-containing protein 3B: ARI3B (*Arid3b*)	Q9Z1N7
	480-**GATPM**-484	Acetyl-coenzyme A synthetase: ACSA (*Acss2*)	Q9QXG4
	146-**ATPMS**-150	Voltage-gated calcium channel, alpha-1-G subunit: Cacna1g (*Cacna1g*)	Q9WUT2
	629-**RG**-**TPMS**-634	Nuclear pore complex protein Nup133: NU133 (*Nup133*)	Q8R0G9
HPVSGQK (7)	23-**HPV**T**GQ**-28	Pleckstrin homology domain-containing family A member 5: PKHA5 (*Plekha5*)	E9Q6H8
	21-**HPV**T**GQ**-26	Pleckstrin homology domain-containing family A member 6: PKHA6 (*Plekha6*)	Q7TQG1
	37-**HPV**T**GQ**-42	Pleckstrin homology domain-containing family A member 7: PKHA7 (*Plekha7*)	Q3UIL6
	2249-**HPV**T**GQ**-2254	Chromodomain-helicase-DNA-binding protein 6: CHD6 (*Chd6*)	A3KFM7
LKLGEKW (7)	276-**LGEKW**-280	Syntaxin-4: STX4 (*Stx4*)	P70452
	509-**KLGE**R**W**-514	Protein Utrn (*Utrn*)	E9Q6R7
	88-**K**I**GEKW**-93	Fibronectin: FN1 (*Fn1*)	Q4KL80
	128-**KLGE**M**W**-133	High mobility group protein B1: HMGB1 (*Hmgb1*); also HMGB2, HMGB3	P63158
	580-**KLGE**Q**W**-585	THO complex subunit 1: THOC1 (*Thoc1*)	Q8R3N6
	1752-**LKLGE**-**W**-1757	Serine/threonine-protein kinase mTOR: mTOR (*Mtor*)	Q9JLN9
SWNQMRG (5)	94-**WNQM**-97	Truncated Wilms' tumor protein: WT1 (*Wt1*)	Q199A7
	324-**WNQM**-327	Sodium/hydrogen exchanger 1: SL9A1 (*Slc9a1*)	Q61165
	342-**SW**R**QMR**-347	Calpain-13: CAN13 (*Capn13*)	Q3UW68
	266-**WNQ**T**GMR**-272	Histone deacetylase 6: HDAC6 (*Hdac6*)	Q9Z2V5
SDARSPK (5)	187-**DAR**N**PK**-192	Global transcription activator SNF2L2: Smarca2 protein: SMCA2 (*Smarca2*)	Q6DIC0
	26-E**ARSPK**-31	Proline-rich protein 14: PRR14 (*Prr14*)	Q7TPN9
	633-**DARSP**-637	Protein kinase C gamma type: KPCG (*Prkcg*)	P63318
	1140-**SD**S**RSP**-1145	RPA-interacting protein: RIP (*Rpain*)	Q9CWY9
	2128-**SD**S**RSP**-2133	Nuclear receptor corepressor 1 isoform 2: NCOR1 (*Ncor1*)	E9Q9Y2

Supplementary Table 2. A list of peptides recovered from differential phage display bio-panning on *Lmna*$^{-/-}$ MEF nuclei using pre-cleared Ph.D.-C7C library and the BRASIL method (Screen 3).

Matching motifs in candidate proteins mimicked by the phage inserts were obtained by protein-protein BLAST analysis based on the Max score, E-value, and Identity.

Round	Peptide % Frequency	Matching Motif	Protein Mimic (Gene)	UniProtKB Accession
R II	SGGRMHQ (14)	374-**GGRMH**-378	Nuclear receptor subfamily 1 group D member 2: NR1D2 (*Nr1d2*)	Q60674
		32-**SG**A**RM**P**HQ**-39	SWI/SNF-related matrix-associated actin-dependent regulator of chromatin subfamily D member 3: SMRD3 (*Smarcd3*)	Q6P9Z1
		252-**GRMH**-255	Aurora kinase B: AURKB (*Aurkb*)	O70126
		294-**GRMH**-297	Aurora kinase A: AURKA (*Aurka*)	P97477
		43-**GRM**N**Q**-47	Matrin-3: MATR3 (*Matr3*)	Q8K310
		302-**GGR**E**HQ**-307	Transcription factor GATA-6 (*Gata6*)	Q61169
	QNPNQKF (12)	17-**PNQK**Y-21	Homocysteine-responsive endoplasmic reticulum-resident ubiquitin-like domain member 2 protein: HERP2 (*Herpud2*)	Q6NYI0
		125-**NQKF**-128	Cold shock domain-containing protein C2: CSDC2 (*Csdc2*)	Q91YQ3
		111-**NPNQ**- 114	Myogenin: MYOG (*Myog*)	P12979
		123-**NPNQ**-126	Myogenic factor 6: MYF6 (*Myf6*)	P15375
		113-**NPNQ**- 116	Myogenic factor 5: MYF5 (*Myf5*)	P24699
		139-**NPNQ**-142	Myoblast determination protein 1: MYOD1 (*Myod1*)	P10085
		186-**NPNQ**-189	ELAV-like protein 1: ELAV1: ELAV1: Hu-antigen R: HuR (*Elavl1*)	P70372
		232-**QNPN**- 235	RNA-binding motif, single-stranded-interacting protein 1: RBMS1 (*Rbms1*)	Q91W59
		145-**QNPN**-148	Nucleobindin-2: NUCB2 (*Nucb2*)	P81117
		526-**NPNQ**-529	Nuclear cap-binding protein subunit 1: NCBP1 (*Ncbp1*)	Q3UYV9
	HPVSGQK (4)	23-**HPV**T**GQ**-28	Pleckstrin homology domain-containing family A member 5: PKHA5 (*Plekha5*)	E9Q6H8
		21-**HPV**T**GQ**-26	Pleckstrin homology domain-containing family A member 6: PKHA6 (*Plekha6*)	Q7TQG1
		37-**HPV**T**GQ**-42	Pleckstrin homology domain-containing family A member 7: PKHA7 (*Plekha7*)	Q3UIL6
		2249-**HPV**T**GQ**-2254	Chromodomain-helicase-DNA-binding protein 6: CHD6 (*Chd6*)	A3KFM7
	SISSLTH (4)	489-**SISSLT**-494	Runt-related transcription factor 2: RUNX2 (*Runx2*)	Q08775
		185-**SISSLT**-190	E3 ubiquitin-protein ligase RBBP6 (*Rbbp6*)	P97868
		147- **ISSLSH**-152	Adenylate cyclase type 4: ADCY4 (*Adcy4*)	Q91WF3
		1640-IG**SLTH**-1645	Protein Shroom3: SHRM3 (*Shroom3*)	Q9QXN0
	HQSSTST (4)	425-**HQSSTS**-430	Vam6/Vps39-like protein: VPS39 (*Vps39*)	Q8R5L3
		43-**QSSTST**-48	Serine/threonine-protein phosphatase 2A 56 kDa regulatory subunit gamma isoform: 2A5G (*Ppp2r5c*)	Q60996
		61-**HQS**N**TS**-66	Alpha-1-antiproteinase: A1AT: Serpin A1 (*Serpina1*)	Q63969
		1014-H**SSSTST**-1020	Sorbin & SH3 domain-containing protein 2: SRBS2 (*Sorbs2*)	Q3UTJ2
		3805-**HQSST**-3809	Histone-lysine N-methyltransferase EHMT2 (*Ehmt2*)	Q9Z148
R III	PTNQHHL (44)	155-PGS**QHHL**-161	Protein Wnt-7b: WNT7B (*Wnt7b*)	P28047
		513-**PTYQHHL**-519	NACHT, LRR and PYD domains-containing protein 1b allele 2: NL1B2 (*Nlrp1b*)	A1Z198
		255-**PTNQ**QPTL**HL**-264	Cytosolic carboxypeptidase-like protein 5: CBPC5: CCP5 (*Agbl5*)	Q09M02
		93-**PTRQHH**-98	BTB/POZ domain-containing protein 10: BTBDA (*Btbd10*)	Q80X66
	NAFMKWA (16)	104-**NAFM**V**WA** -110	Transcription factor SOX-8 (*Sox8*)	Q04886
		73-**NAFM**V**WA**-79	Transcription factor SOX-17 (*Sox17*)	Q61473
		107-**NAFM**V**WA**-113	Transcription factor SOX-6 (*Sox6*)	P40645
		84-**NAFM**V**WA**-90	Transcription factor SOX-18 (*Sox18*)	P43680
		50-**NAFM**V**WA**-56	Transcription factor SOX-7 (*Sox7*)	P40646
		190-**NAFM**V**WA**-196	Transcription factor SOX-5 (*Sox5*)	P35710
		109-**NAFM**V**WA**-115	Transcription factor SOX-10 (*Sox10*)	Q04888
		110-**NAFM**V**WA**-116	Transcription factor SOX-9 (*Sox9*)	Q04887
		223-**FMKW**-226	Inositol 1,4,5-trisphosphate receptor type 1: ITPR1 (*Itpr1*)	P11881
	PTVKQKW (10)	56-PE**VKQKW**-62	Nuclear factor 1 A-type: NFIA (*Nfia*)	Q02780
		58-**VKQKW**-62	Nuclear factor 1 C-type: NFIC (*Nfic*)	P70255
		56-PEI**KQKW**-62	Nuclear factor 1 X-type: NFIX (*Nfix*)	P70257
		85-**TV**Q**QKW**-90	Synaptotagmin-7: SYT7 (*Syt7*)	Q9R0N7

GLKLGAL (8)	67-**LKLGAL**-72	Rho GTPase-activating protein p115: ARHGAP4 (*Arhgap4*)	Q8VHL8
	334-**LKLGAL**-339	Pseudouridylate synthase 7: Protein Pus7 (*Pus7*)	Q91VU7
	516-**G**Q**KLGAL**-522	PR domain zinc finger protein 8: PRDM8 (*Prdm8*)	Q8BZ97
	568-**GLKLG**LL-574	Catenin alpha-like protein 1: Alpha-catulin: CTNL1 (*Ctnnal1*)	O88327
	326-**LKLGS**L-331	PHD finger protein 20: PHF20 (*Phf20*)	Q8BLG0
HGSSLLK (6)	34-**HGSSL**M**K**-40	Lysine-specific demethylase 7A: KDM7A (*Kdm7a*)	Q3UWM4
	489-**HGSSLL**-494	Probable ATP-dependent RNA helicase DDX31 (*Ddx31*)	Q6NZQ2
	447-**GSSLLK**-452	Oxidation resistance protein 1: OXR1 (*Oxr1*)	Q4KMM3
	222-**HGS**A**LL**-227	Hairy/enhancer-of-split related to YRPW motif protein 2: HEY2 (*Hey2*)	Q9QUS4
GGGPLYM (4)	362-**GGG**E**LYM**-368	Obscurin: OBSCN (*Obscn*)	A2AAJ9
	169-**GGPLY**-173	Abl interactor 1: ABI1 (*Abi1*)	Q8CBW3
	179-**GGPLY**-183	Mitochondrial dynamics protein MID49 (*Mief2*)	Q5NCS9
	491-**GGPLY**-495	SRC kinase signaling inhibitor 1: SRCN1 (*Srcin1*)	Q9QWI6

CHAPTER III

PHAGE DISPLAY BIOPANNING ON THE C-TERMINAL FRAGMENT OF RBM20 PROTEIN

A. Abstract

Cardiomyopathies are cardiac muscle disorders with relatively high incidence rate and elevated risk of sudden death. Mutations in the *RBM20* gene, which codes for the splicing factor RNA binding motif protein 20 (RBM20), have been identified as a cause for Dilated Cardiomyopathy (DCM). The mechanisms by which DCM arises from *RBM20* mutations are not fully understood and the protein interactome of Rbm20 is not well-established. We employed a phage display-based approach to identify binding partners of the C-terminal fragment of recombinant human RBM20 protein (C-RBM20). Two screens of phage display biopanning were performed using the heptapeptide PhD CX_7C phage library. Screen 1 was performed without acid elution to identify partners that bind C-RBM20 weakly and Screen 2 was performed with acid elution to identify strong binders to C-RBM20. Four successive rounds of biopanning resulted in significant enrichment in phage binding to C-RBM20 in both screens. Sequencing the inserts in nearly 200 phage plaques recovered from the four rounds of each screen, we identified multiple high and low frequency binding peptides to C-RBM20. Bioinformatic analysis showed clustering of peptides within the same screen and within the same round of each screen. Blast analysis revealed potential protein mimics which were both distinct and overlapping between screens. In addition to finding few proteins that are closely related to previously reported Rbm20 interactors, our assays identified novel RBM20 binding proteins. Interestingly,

nesprin-1 appeared in multiple rounds of both screens and lamin B1 appeared in round III of Screen 2. Co-immunoprecipitation assays on protein lysates from differentiated mouse C2C12 myoblasts and mouse left ventricular cardiac tissue showed that RBM20 interacts with nesprin-1, lamin A/C and lamin B1. This was also validated using proximity ligation assays in human Rhabdomyosarcoma cells. This work reveals novel interacting partners of C-RBM20 and provides better insights into the molecular mechanisms implicated in its role in cardiomyopathies.

B. Introduction

Cardiomyopathies are a diverse group of heart muscle disorders that affect the normal mechanical and electrical activities of the heart[331]. DCM is a common type of cardiomyopathy characterized by dilation of the left or both ventricles and impaired systolic function in the absence of abnormal loading conditions or coronary artery disease[332,333]. DCM affects 1 in 250-500 individuals with a high mortality rate, mainly due to heart failure and sudden cardiac death[334,335]. More than 400 mutations affecting 60 genes have been linked to DCM[132]. The DCM-associated genes have various functions that can be broadly grouped into muscle contraction, ion-handling and nuclear functions. Most DCM-causing mutations (25%) occur in the *TTN* gene which encodes the striated muscle protein titin[134,176]. The 364 exons of human *Ttn* encode the largest known protein and undergo extensive alternative splicing, giving rise to developmentally regulated and tissue-specific isoforms. The cardiac specific titin isoforms differ from the skeletal muscle isoforms by the presence of a unique N2B element[336]. In addition to its role in sarcomere assembly and muscle contraction, cardiac titin plays a major role in generating passive tension during

diastole and elasticity during systole[337,338]. Recently, genetic mutations in titin splicing regulator RBM20 were shown to be causative of DCM in about 2-3% of all DCM cases[180,195,196].

RBM20 is an RNA binding protein exclusive to vertebrates[339]. The expression of RBM20 follows a tissue-specific pattern characterized by predominant expression in striated muscle particularly in cardiac muscle[208]. RBM20 proteins from various vertebrate species share six conserved domains: A leucine (L) rich region at the N-terminus, a zinc finger domain (Znf1), an RNA-binding RNA recognition motif (RRM), an arginine/serine (RS) rich region, a glutamate (E) rich region, and a second zinc finger domain (Znf2) at the C-terminus[208,340] (Figure 18a). Following its identification in 2009 as a DCM-causing gene, studies from Rbm20-deficient rats and human DCM patients revealed a role of RBM20 as a heart-specific alternative splicing regulator[180]. Gou et al. identified, by high throughput RNA-sequencing of cardiac transcriptome, 31 genes that are differentially spliced depending on RBM20. Conserved between rats and humans, the identified genes were enriched for functions related to the sarcomere, sarcoplasmic reticulum, heart failure and cardiomyopathy by both gene ontology and medical subject heading terms (MeSH)[208]. Among the identified genes, titin was the most differentially spliced target of RBM20; whereby RBM20 deficiency led to a switch in titin isoform expression favoring longer titin isoforms (N2BA) and fetal-like isoforms (N2BA-G) over the shorter isoform (N2B) that is mainly expressed in adults. These observations were made in both a DCM patient with an inactivating heterozygote missense mutation (S635A) in the RS domain of RBM20 and a rat strain with a spontaneous loss-of-function mutation that deletes 13 of the 14 exons of the *Rbm20* gene[208]. In the normal heart, Rbm20 expression was first detected between

embryonic days E7.5 and E8.5 of *in vivo* mouse cardiogenesis, in a timely manner with the expression of cardiac progenitor markers[207]. In addition, RBM20 expression in differentiating C2C12 myoblasts was shown to correlate with sarcomere assembly which supports its role in regulating myofibril formation and function[208]. This is in line with the observation of disorganized sarcomeres in cardiomyocytes derived from human induced pluripotent stem cells of DCM patients with different RBM20 mutations[341,342]. However; despite the early expression of Rbm20 in the heart, splicing regulation of titin does not occur until the perinatal period whereby a switch in cardiac titin isoform expression leads to the rapid replacement of the longer and more compliant fetal N2BA isoforms by the shorter and stiffer adult N2B isoform which becomes predominantly expressed in rats by the first week after birth[218,220]. Although the mechanisms regulating titin alternative splicing are not fully understood, RBM20 is known to play an important role in this process, thus contributing to the regulation of passive stiffness and diastolic function of the heart[218,219,337]. Splicing regulation by Rbm20 has been addressed by a few studies; however, the detailed molecular mechanisms still need to be elucidated. High throughput sequencing of pre-mRNA from crosslinking and immunoprecipitation of endogenous Rbm20 in rat cardiomyocytes revealed 18 direct targets of Rbm20, including titin (*Ttn*), Calcium/calmodulin-dependent protein kinase II delta (*Camk2d*), Myomesin 1 (*Myom1*), Ryanodine receptor 2 (*Ryr2*) and Myosin heavy chain 7 (*Myh7*)[212]. Rbm20-regulated exons were enriched for mutually exclusive exons that often regulate expression of tissue-specific splice variants[212,213]. Binding of Rbm20 to a UCUU-containing RNA recognition element in intronic regions flanking the target exon was shown to predominantly repress exon splicing[208,212,343]. However, full-length RBM20 or the RRM domain does not necessarily

bind to any RNA molecule containing the UCUU motif which suggests that RNA recognition is probably regulated by additional elements and/or RNA-binding proteins[212,245].

Most DCM-causing mutations in RBM20 map to a 5 amino acid stretch in the RS domain, comprised of the amino acids serine-arginine-serine-arginine-proline (RSRSP) at positions 634-638[340]. Recent findings have shown that both serine residues in this mutational hotspot are constitutively phosphorylated and that this posttranslational modification of the RSRSP stretch is crucial for RBM20 nuclear localization and splicing function[344]. The RS region of RBM20 and other SR proteins has long been suggested to play a role in mediating protein-protein interactions[345]. Therefore, dynamic phosphorylation and dephosphorylation of the RS region, during development and in disease conditions, might regulate Rbm20 splicing function through altering protein-protein interactions that might be affected by Rbm20 subcellular localization[346]. However, the RS region does not seem to be the only region responsible for the pathogenesis of DCM. This view is supported by a proteomic study showing that the DCM-causing mutation S635A in the RS region of Rbm20 only affects its binding to alternative splicing factors while retaining interactions with core splicing factors[212]. The same study also showed that most Rbm20 interacting proteins belonged to complex A and not to later-stage complexes of the catalytic spliceosome, which might be suggestive that Rbm20 recruitment represses splicing by preventing the assembly of spliceosomal complexes beyond complex A[212]. It might be possible that interactions between RBM20 and alternative splicing factors are essential for RBM20 function. Alternatively, other important protein interactions might have been masked by the numerous spliceosomal protein interactors recovered by this study.

Moreover, the identified interacting partners were not mapped to a specific region or domain in the full-length RBM20 protein. Another study showed that both the RRM domain and the C-terminus of RBM20 are "necessary and sufficient" for RBM20 splicing activity, thus highlighting the importance of the Znf2 domain for RBM20 function[245]. Moreover, the importance of the C-terminus in RBM20 function and disease pathogenesis is supported by the identification of several DCM-causing mutations in the C-terminus of RBM20[195,258,340]. Since the RRM domain is implicated in RNA recognition, RRM deficient mice exhibit splicing defects; however, they do not recapitulate the DCM phenotype in terms of dilated left ventricle and impaired systolic function[347]. In addition, DCM-causing mutations in the RRM domain are very rare and none of the reported mutations are familial in nature[346]. Accordingly, we set out to identify proteins that interact with the C-terminal domain of human RBM20 protein by employing a phage display-based approach. We performed two screens using the heptapeptide PhD CX_7C phage library. Screen 1 was performed without acid elution to identify partners that bind C-RBM20 weakly and Screen 2 was performed with acid elution to identify strong binders to C-RBM20. Following successive rounds of biopanning, we obtained significant enrichment in phage binding to C-RBM20 in both screens and we identified multiple binding peptides to C-RBM20. Bioinformatic analysis showed clustering of peptides within the same screen and within the same round of each screen. Blast analysis revealed potential protein mimics, which were both distinct and overlapping between screens. In addition to finding few previously reported Rbm20 interactors, our assays mainly identified novel RBM20 binding proteins. Co-immunoprecipitation and proximity ligation assays were employed to validate interactions between RBM20 and each of nesprin-1, lamin A/C and lamin B1. This work

reveals novel interacting partners of C-RBM20 and provides better insights into the molecular mechanisms implicated in its role in cardiomyopathies.

C. Materials and Methods

1. Cell Culture

C2C12 cells were obtained from Dr. Nemer Laboratory (American University of Beirut, Lebanon). Cells were maintained in Dulbecco's Modified Eagle's Medium DMEM-AQ media (D0819, Sigma-Aldrich), supplemented with 1% penicillin streptomycin (DE17-602E, Lonza), 20% fetal bovine Serum (F9665, Sigma-Aldrich) and 1% sodium pyruvate (S8636, Sigma-Aldrich). Cells were differentiated by decreasing the fetal bovine serum concentration to 0.5% in the differentiation media. Human rhabdomyosarcoma (RD) cells were obtained from European Collection of Authenticated Cell Cultures (ECACC). Cells were maintained in Dulbecco's Modified Eagle's Medium DMEM-AQ media (D0819, Sigma-Aldrich), supplemented with 1% penicillin streptomycin (DE17-602E, Lonza), 10% fetal bovine Serum (F9665, Sigma-Aldrich) and 1% sodium pyruvate (S8636, Sigma-Aldrich). 1x phosphate buffered saline (PBS) without calcium and magnesium (17-517Q, Lonza) and 1x trypsin-EDTA (T4049, Sigma) were used for washing and detaching cells. Cells were visualized using a standard phase contrast microscope (Olympus microscope, Axiovert 200, Zeiss).

2. Animals & Tissue Lysate Preparation

Wild type C57-BL/6 mice from the lab of Dr. Jan Lammerding were used. Approved IACUC protocols were followed in maintaining, breeding and euthanizing mice.

Tissues isolated from a single mouse were considered a single replicate. The heart was harvested, washed in PBS to remove the blood, and cut into right and left ventricles before snap freezing in liquid nitrogen. 10 µg tissue sections from the left ventricle were then cut on dry ice and homogenized in 500 µl RIPA lysis buffer supplemented with phosphatase (PhosSTOP, Roche) and protease inhibitors (complete EDTA-free, Roche). The TissueLyser II from Qiagen and metallic beads from McMaster-Carr were used for tissue homogenization.

3. Host Bacterial Strain Maintenance

The F+ recA+ *E. coli* host strain ER2738 was used for M13KE insert-less phage (N0316S, NEB) propagation. Supplied as a non-competent 50% glycerol culture as part of the Ph.D.–C7C Phage Display Peptide Library Kit (E8120S, NEB), ER2738 colonies or lawns were grown on 100mm LB-Agar (M1151, HiMedia) plates supplemented with Tet (T3383, Sigma Aldrich). Plates were incubated at 37°C overnight and stored wrapped with parafilm at 4°C in the dark. ER2738 was propagated weekly and new cultures were streaked from glycerol stock once per month. ER2738 cultures were grown in LB Broth (J106, AMRESO) and bulk amplified in LB Broth + Tet.

4. Phage Display Bio-panning on C-RBM20

The Ph.D.–C7C Phage Display Peptide Library Kit (E8120S, NEB) was used. The library has filamentous phage particles displaying random peptides with the cyclic arrangement CX7C (C, Cysteine; X, any amino acid residue) at a diversity of 10^9 transducing units (TU). This library was used along with the control M13KE insert-less

phage to pan on C-RBM20 (Cloud-Clone Corp., RPN021Hu01). Separate wells of a 96-well plate were coated with 50 µl of either 5µg C-RBM20 in PBS or PBS only in an overnight incubation at 4°C. Wells were then blocked with 200µl of 3% BSA in PBS for 1hr at 37°C. M13KE phage or the library phage was diluted in PBS supplemented with protease inhibitors (22020009-1, Bioworld) to a concentration of $1x10^9$TU/µl. Pre-clearing was performed by adding each of M13KE phage or the library phage into PBS-coated wells and incubating for 30min at room temperature. Phage binding was performed by transferring precleared phage into C-RBM20 coated wells and incubating for 30min at room temperature. After the binding step, the phage was rescued by adding 200µl of host bacterial strain, ER2738 grown to mid-log phase ($OD_{600} \sim 0.5$), for 1hr at room temperature with gentle pipetting every 15 min. To identify strong binding partners of C-RBM20 bound phage was eluted with Glycine-HCl and neutralized with Tris-HCl before rescuing by infection of competent *E. coli* cells. After 1hr, the phage-infected bacterial culture was serially diluted in LB Broth + Tet and different dilutions were mixed with top agarose and overlaid on top of LB agar/IPTG/X-Gal plates. The plates were left to dry in the dark and incubated at 37°C for 14hr. Plaques from the different dilutions were counted. Well-separated plaques were picked and stored in 30% glycerol (E520, AMRESCO) in 96-well plates at -20°C. The eluted phage was bulk amplified, isolated, and titer tested (see below) prior to its use in the following round of bio-panning. Four successive rounds of bio-panning were performed whereby the amplified eluted phage pool from one round was used as input in the successive round with a pre-clearing step on PBS-coated wells before each successive round of bio-panning. The eluted phage was used at a concentration of $1x10^9$TU/µl. Dilution was done based on the calculated phage titer.

5. Bulk Amplification and Isolation of Eluted Phage

Phage-infected bacterial culture (mid-log phase) was diluted 1:10 in LB Broth + Tet, bulk amplified at 37°C, 180rpm shaker for 5h, then transferred into a clean round bottom tube and bacterial sedimentation was performed by centrifugation at 6000rpm, 4°C for 15min. The phage-containing supernatant was transferred into a fresh tube, re-spun and phage particles precipitation was performed by transferring the supernatant into a clean tube and adding PEG:NaCl (1:5) (PEG 8000 Powder, V3011, Promega; NaCl, 0241, AMRESCO). The tube was mixed gently by tilting upside down and incubated on ice in the cold room overnight. Subsequently, the round bottom tube was centrifuged at 14000rpm, 4°C for 15min. The supernatant was discarded; the phage pellet was suspended in 1ml cold PBS (without calcium and magnesium), transferred into a clean microfuge tube and re-spun for 5min. The supernatant was mixed with 200µl of PEG-NaCl in a clean tube and incubated on ice for at least 1h. After centrifugation at 14000rpm, 4°C for 10min, the supernatant was discarded and the phage pellet was re-suspended in 250µl cold PBS, re-spun for 1min and transferred into a clean microfuge tube. The bulk amplified phage suspension was stored at 4°C for 2 weeks or at -20°C for long term storage.

6. Phage Titer Determination

ER2738 was inoculated from a fresh plate into 20ml LB broth and incubated at 37°C, 180rpm shaker until it reached mid-log growth (OD_{600} ~ 0.5). Phage serial dilutions were prepared in PBS and 1µl of each dilution was used to infect 100µl of ER2738 culture at room temperature for 30min (performed in triplicates per dilution). 50mm LB-Agar

plates supplemented with IPTG/X-Gal (R0391/R0401, Fermentas) were pre-warmed at room temperature. Top agar consisting of LB Broth and agarose (A9593, Sigma) was molten in microwave and kept at 48°C in water bath. Then, 1.5ml top agar was mixed with 100µl of each infection and overlaid on LB agar/IPTG/X-Gal plates. Allowed to solidify at room temperature for 5-10min, the plates were incubated at 37°C for 14h. Subsequently, the dilution that gave non-overlapping plaques (less than 100 plaques) was chosen for determining the titer. The average count was determined by counting plaques on triplicate plates corresponding to that dilution. Then, phage titer in transducing units (TU) was obtained by multiplying the average count by the dilution factor for those plates.

7. PCR Amplification of Phage Inserts and Agarose Gel Electrophoresis

A 326bp stretch of the phage genome, surrounding the random peptide inserts, was amplified by performing PCR directly on the phage plaques using the Phusion Flash High-Fidelity PCR Master Mix (F-548L, Thermo Scientific) and the PTC-200 DNA Engine Peltier Thermal Cycler (ALS 1296, Bio-Rad). The forward primer: 5′-TGTCGGCGCAACTATCGGTATCAA-3′, and reverse primer: 5′-TAGCATTCCACAGACAGCCCTCTA-3′ (Sigma) were used. Each PCR reaction consisted of 7µl DNase/RNase free water (W4502, Sigma), 10µl Phusion Flash High-Fidelity PCR Master Mix, 1µl of each primer (8µM), and 1µl of each phage clone pre-stored in glycerol stock. PCR was performed in 0.2ml thin-walled PCR tubes with flat caps (AB-0620, Thermo Scientific) and the protocol consisted of: 94°C step for 3min to break bacterial cell walls followed by 50 cycles of denaturation at 94°C for 10s, annealing at 60°C for 30s, and extension at 72°C for 30s. PCR products were stored at –20°C. To check

for the presence of insert, PCR amplicons were run on 2% agarose gels in 1xTBE buffer (0658, AMRESCO) in an electric field alongside Direct Load DNA Step Ladder (D3812, Sigma). Samples were prepared for loading by mixing 2µl of PCR-amplified clones with 1µl of 6x DNA Loading Dye (R0611, Thermo Scientific) and 3µl of DNase/RNase free water. Samples were run at 100V and the bands were visualized using the Molecular Imager Chemidoc XRS System (170-8070, Bio-Rad) using the Quantity One 1-D Analysis Software (170-9600).

8. Purification of PCR Amplicons and Sequencing

Purification of PCR amplicons was performed using the GenElute PCR Clean-Up Kit (NA1020, Sigma-Aldrich). GenElute plasmid mini spin columns were prepared for DNA binding by adding 0.5ml of the column preparation solution to each column and spinning at 12,000xg for 1min. After discarding the eluate, the PCR reaction was mixed with binding solution (1:5 v/v), transferred into the mini spin column and centrifuged at 16000x g for 1min. The eluate was discarded, and the column was washed by 0.5ml of diluted wash solution. This was followed by centrifugation and discarding the eluate. Another centrifugation step was done to remove excess ethanol. The column was then transferred into a fresh collection tube and incubated with 30µl DNase/RNase free water at room temperature for 5min. Purified DNA was eluted by centrifugation at 16000xg for 2min. The purified PCR amplification products were stored at -20°C. Sequencing was performed at Macrogen Inc. (South Korea) such that 30µl of each PCR reaction, corresponding to a single phage clone, along with 5µM of the sequencing primer M13F: 5′-TGTCGGCGCAACTATCGGTATCAA-3′ (Sigma) were placed in Hard-Shell PCR plates

with 96-wells (HSP9601, Bio-Rad) and sealed with Optical Flat Cap Strips (TCS0803, Bio-Rad), then sent for sequencing.

9. Processing of Sequencing Reads and Clustering Analysis of Derived Peptides

The statistical programming language R was used to write a script that processes the sequencing reads. This script reads fasta files generated by sequencing of phage clones, identifies nucleotide sequences surrounding the heptapeptide insert in the phage amplicon, cuts out the nucleotide sequence corresponding to the insert, and translates it into an amino acid sequence. The program also identifies and excludes amplicons with no insert or with inserts longer than 7 amino acids. The final list of different peptide sequences was clustered (R function *hclust*) based on the amino acid scoring matrix PAM30.

10. Bioinformatic Analysis of Peptide Sequences

To identify proteins that are mimicked by the uncovered peptides, protein-protein BLAST analysis of the peptide sequences was performed. The search was set to non-redundant protein sequence in the mouse taxid (http://blast.ncbi.nlm.nih.gov). Multiple protein mimics were determined for each sequence and were selected from the full BLAST list of hits based on the Max score, E-value and Identity. Furthermore, mimics were selected based on their nuclear expression score, tissue expression profile, and biofunctional relevance particularly to, muscle tissue, heart function, myopathies, and cardiomyopathies as determined by the Gene Cards (http://www.genecards.org/) and UniProt (http://www.uniprot.org) databases, and PubMed (http://www.ncbi.nlm.nih.gov/pubmed) search of the biomedical literature.

11. Co-Immunoprecipitation

The Dynabeads Co-Immunoprecipitation Kit (14321D, Novex) was used according to the manufacturer's instructions. Briefly, 1.5 mg of Dynabeads M-270 Epoxy were coupled to 10 µg of either nesprin-1 (abcam, ab192234), lamin A/C (sc-6215, SANTA CRUZ BIOTECHNOLOGY), normal rabbit IgG or normal goat IgG by an overnight incubation on a roller at 37°C. The beads were then washed and blocked with 0.1 % BSA in PBS before incubation with 0.07 g protein extracts on a roller at 4°C for 1 hour. Supplied as 5x IP buffer with the Dynabeads Co-Immunoprecipitation Kit, the protein extraction buffer was used at 1x dilution after supplementing with protease inhibitors (22020009-1, Bioworld). Finally, the beads were washed, and the purified protein complex was eluted and used directly for SDS-PAGE. Immunoblotting was performed using nesprin-1 (ab192234, abcam), lamin A/C (sc-6215, SANTA CRUZ BIOTECHNOLOGY) and RBM20 (sc-243941, SANTA CRUZ BIOTECHNOLOGY) antibodies. HRP-conjugated secondary antibodies (ab97023, ab97110, abcam; 111-035-144, Jackson Immunoresearch) were used at a dilution of 1:5000. Bands were detected using ECL western blotting substrate kit (ab65628, abcam) and the bands were visualized using the Molecular Imager Chemidoc XRS System (170-8070, Bio-Rad) and the Quantity One 1-D Analysis Software (170-9600).

For animal tissues, protein A resin beads were used. Protein A slurry was prepared by hydrating the resin with water, resuspending with lysis buffer and incubating with primary antibodies against nesprin-1 (Mannes1A (7A12), Hybridoma Bank), lamin A/C (sc-518013, sc-376248, SANTA CRUZ BIOTECHNOLOGY), lamin B1 (Protein Tech

(12987-1-AP); abcam (ab16048); Santa Cruz (sc-374015)) while rotating at 4 °C overnight. Tissue lysates were prepared and incubated with protein A slurry at 4 °C for 2 hrs-overnight. Extra lysates were removed by spinning the suspension and pelleting the resin. The pellet was then extensively washed with lysis buffer and once with Tris-HCl on ice and resuspended with SDS loading buffer. The final sample was boiled and loaded into 4-12% Bis-Tris polyacrylamide gel and separated by SDS-PAGE following a standard protocol. Immunoblotting was performed using nesprin-1 (Mannes1A (7A12), Hybridoma Bank), lamin A/C (sc-376248, SANTA CRUZ BIOTECHNOLOGY), lamin B1 (sc-374015, SANTA CRUZ BIOTECHNOLOGY) and RBM20 (NBP2-27509, Novus Biologicals) antibodies. IRDye 680 LT and IRDye 8000 CW (LI-COR) secondary antibodies were used and bands were detected using Odyssey® CLx imaging system (LI-COR).

12. Proximity Ligation Assay

Cells were seeded on coverslips, fixed in PFA for 20 min and washed 4 times with PBS. Fixed cells were then permeabilized with 0.2% Triton-X, followed by another set of washes with PBS. The Duolink Proximity Ligation Assay from Sigma was used according to the manufacturer's recommendations. All staining steps were performed in a humidity chamber and all washing steps were performed at room temperature. Blocking using the Duolink Blocking Solution was performed for 1hr at 37°C. Primary antibodies against Nesprin-1 (), Lamin A/C (), Lamin B1(), and Rbm20 () were diluted 1:50 in Duolink Antibody Diluent and incubated overnight at 4°C. The cells were washed twice with Wash Buffer A before incubation with plus and minus PLA probes for 1hr at 37°C. Ligation was then performed after washing with Wash Buffer A and incubation with the ligase solution

for 30 min at 37°C. This was followed by washing with Wash Buffer A and amplification with the polymerase solution for 100 min at 37°C. Finally, cells were washed with Wash Buffer B and coverslips were mounted on slides using the Duolink In Situ Mounting Medium with DAPI. Images were acquired with the ZEN 2009 Light Edition confocal microscope, using the 60x oil objective. Images were analyzed by the ZEN 2009 Light Edition software.

13. Immunofluorescence Staining

Rhabdomyosarcoma (RD) cells were seeded on coverslips in 6-well plates. Cells were washed with PBS and then fixed with 4% formaldehyde for 20 min at room temperature. Cells were then washed with PBS and permeabilized with 0.5% TritonX-100 for 10 min at room temperature. After washing, cells were blocked with 3% BSA for 1hr at room temperature and incubated with primary antibodies against RBM20 (PAN021Hu01), nesprin-1 (abcam, ab192234) and lamin A/C (sc-6215, SANTA CRUZ BIOTECHNOLOGY) in an overnight incubation at 4°C. After washing with PBS, cells were incubated with Alexa Fluor-conjugated secondary antibodies (ab150113, ab150115, abcam) for 1hr at room temperature. Coverslips were mounted on slides using the ultraCruz Hard-set mounting medium (sc-359850, SANTA CRUZ BIOTECHNOLOGY). Images were acquired with an upright fluorescent microscope using the 40x objective.

D. Results and Discussion

1. Phage Display Biopanning on C-RBM20 Without Acid Elution (Screen 1)

To identify weak binding partners of RBM20, phage display biopanning on C-RBM20 was performed without acid elution. The Ph.D.-C7C phage display peptide library kit was used. Alongside the library phage, the M13KE insert-less phage was used as a control. Phage particles displaying random heptapeptides were allowed to bind RBM20-coated or PBS-coated wells of a 96-well plate (Figure 18b). Unbound phage was washed, and bound phage was eluted by infection of competent *E. coli* cells. Serial dilutions were plated on agarose top on IPTG-X-Gal plates supplemented with tetracycline (Tet) and bacteriophage plaques were counted post overnight incubation to determine the phage transducing unit (TU) counts. Four successive rounds of biopanning were performed such that the output from each round was amplified, titered, and used as input in the subsequent round. The ratio of TUs of phage binding to C-RBM20 relative to TUs of the insert-less control phage M13KE were calculated. Significant enrichment in phage binding to C-RBM20 was first obtained in Round III of biopanning whereby the mean ratio of phage TU counts (2.38 ± 0.10) was significantly higher than that obtained in Round I (1.14 ± 0.15) or Round II (1.09 ± 0.09); $p=0.002$ and $p=0.001$ respectively in unpaired two-tailed t-test, hence indicating a 2.1-fold increase in relative phage binding to C-RBM20 in Round III in comparison to Round I (Figure 19a). The mean ratio of phage TU counts stayed in Round IV (3.33 ± 0.35) significantly higher than in Round I and Round II; $p=0.005$ and $p=0.004$ for the difference between Round I and IV and between Round II and IV, respectively in unpaired two-tailed t-test, hence indicating a 2.9-fold and 3.1-fold increase in relative phage binding to C-RBM20 in Round IV in comparison to Round I and Round II respectively. The results represent the mean ratio of phage TU counts (phage library/M13KE per sample) ± SEM of 3 independent repeats. The increase in the mean

ratio of phage TU counts from Round III to Round IV was not significant, which suggests that enrichment is reached in round three and continues in Round IV with no further increase in enrichment. No significant enrichment in phage binding to the control PBS coated wells was obtained (Figure 19a).

2. Sequence Determination of the Phage Inserts & Clustering Analysis for Clones Selected from Screen 1

To identify peptides displayed by phages that were recovered from binding to C-RBM20 without acid elution (Screen 1), the phage inserts for a panel of 47 phage clones from Round I, 54 clones from Round II, 52 clones from Round III and 56 clones from Round IV were PCR amplified, sequenced, and analyzed. To process and analyze the sequencing reads, we developed a program using the statistical programming language R to identify the heptapeptide insert in the sequenced phage amplicon, and to perform clustering analysis of the recovered peptides using the scoring matrix Point Accepted Mutation 30 (PAM30). Amino acid substitution matrices describe the rate at which one amino acid in a sequence changes to another amino acid over time. The substitution rates given by such matrices can therefore be used to score sequence alignments in proteins based on the similarity between amino acid sequences[288]. Clustering analysis of the recovered peptides showed a total of 9 different peptide sequences obtained from the different rounds of Screen 1 (Figure 19b). The diversity of peptides increased from Round I (2 peptides) to Round II (3 peptides) to Round III (6 peptides) then decreased to a single peptide in Round IV. Peptide clustering was noted for each round; however, peptide sequences from Round II showed a lower level of clustering than peptides from Rounds I and III. The two peptides

recovered from Round I differed by one amino acid. Although low level of clustering was noted between the different peptide sequences of the different rounds, identical peptide sequences were recovered from different rounds of Screen 1 (MVRDHSV and FPTHNMH). The percent frequency of occurrence of these peptides, determined by the number of times that each peptide sequence appeared in the total number of sequenced phage clones, is shown in Table 3 and in Supplementary Table 3. Notably, the heptapeptide sequence, MVRDHSV, first appeared at a very high frequency (94 %) in Round II of Screen 1 and persisted in Rounds III and IV at 88% and 100 % respectively (Table 3). The appearance of this peptide in the last three rounds of Screen 1 and its sole appearance in Round IV strongly suggest that proteins mimicked by this peptide interact with C-Rbm20. The absence of MVRDHSV from Round I could be explained by the preferential binding of strong interacting partners to C-RBM20 in the presence of competition and steric hindrance from the large phage library. Upon bulk amplification of the output of Round I, weak binding peptides are enriched and recovered better than strong binding partners, without acid elution, thus resulting in their enhanced appearance in Round II. Bulk amplification of the output of Round II, further enriches weak binding partners over strong binding partners in Round III. This explains the increase in peptide diversity from Round I to Round II and from Round II to Round III despite the significant enrichment in Round III relative to Rounds I and II. Finally, weak binding partners with the best binding properties are enriched in Round IV. This explains the significant enrichment obtained in Round IV and is supported by the decrease in diversity of peptides to one peptide in Round IV.

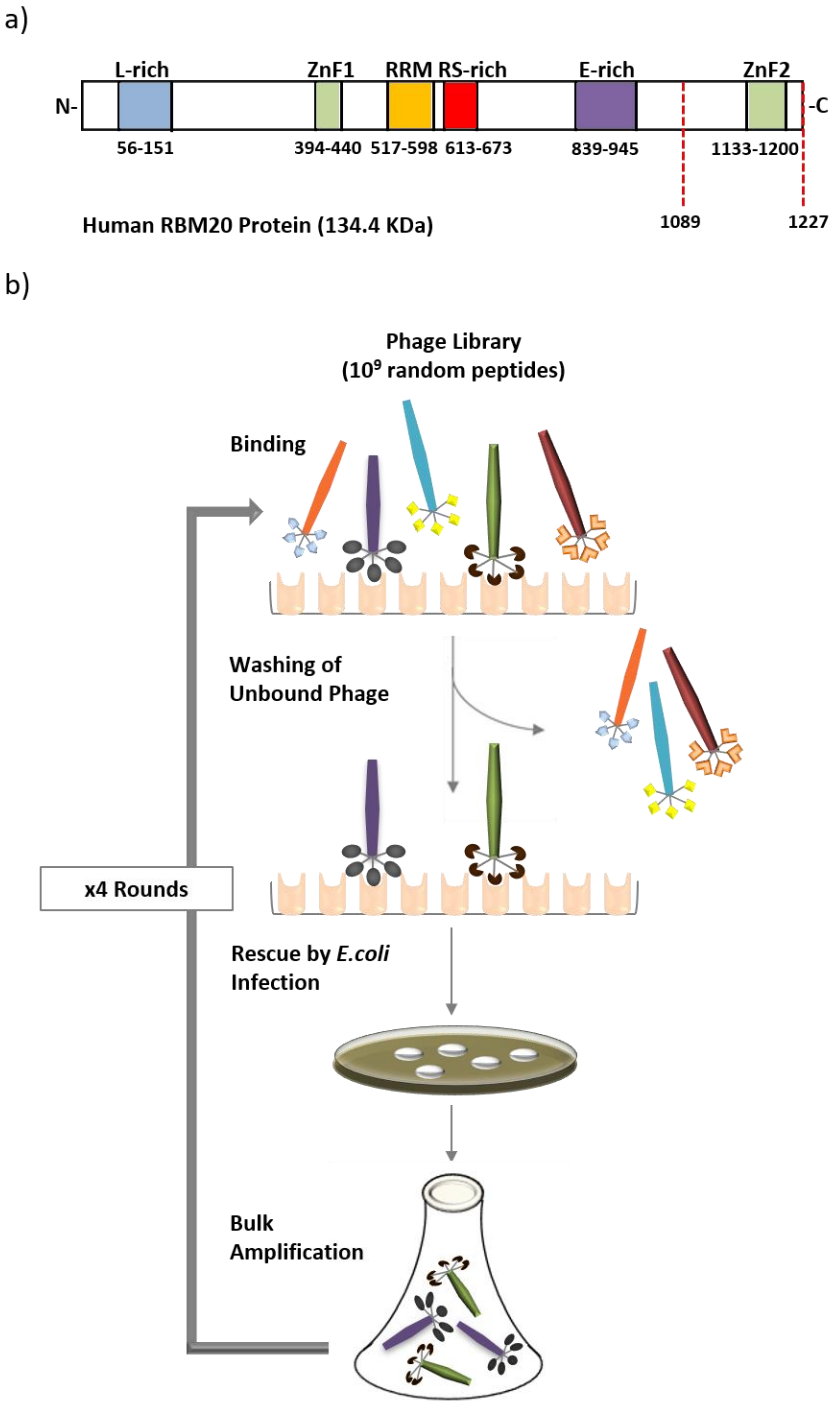

Figure 18. Phage Display Biopanning Strategy on the C-terminal Fragment of Recombinant Human RBM20 Protein (C-RBM20).

a) A schematic diagram of human RBM20 protein showing the different domains relative to the N-terminal and C-terminal ends and the amino acids corresponding to each domain. The dashed lines mark the C-terminal fragment used in our phage display screens and the

amino acids that it spans. b) A schematic diagram showing the experimental strategy for phage display bio-panning on C-RBM20. The Ph.D.−C7C library with a diversity of $1x10^9$ heptapeptides per µl was used. The library was allowed to bind to C-RBM20 coated wells and unbound phage was washed. Bound phage was rescued by *E. coli* infection (Screen 1). In Screen 2, an acid elution and neutralization step preceded *E. coli* infection to select for peptides with strong binding affinities to C-RBM20. Serial dilutions were then streaked on tetracycline supplemented IPTG-X-Gal plates with agarose top to count the phage transducing units (TU) post overnight incubation. Colonies were picked and the phage output post amplification and titration in bacteria was used as input for the subsequent biopanning round to enrich for phage particles that bind C-RBM20 with high frequency. In total, four rounds of biopanning were performed. In parallel, the same biopanning procedure was performed with insertless M13KE phage as a control. The library was precleared on PBS-coated wells before binding and before each subsequent round to remove non-specific binding peptides.

3. High Frequency Peptides Recovered from Screen 1 & The Proteins They Mimic

To determine the protein mimics of recovered peptide sequences from Screen 1, protein-protein BLAST analysis was performed. The search was set to non-redundant protein sequences in the homo-sapiens taxid. Multiple protein mimics were determined for each sequence. These mimics were selected from the full list of BLAST hits based on the Max score, E-value and Identity. Furthermore, mimics were selected based on their relevance to cardiomyopathies, DCM-causing genes, heart muscle and spliceosome as determined by gene card, protein card and Pubmed searches. Multiple protein mimics with putative binding abilities to C-RBM20 were recovered. Select protein mimics of high frequency peptides from the different rounds of Screen 1 and their matching motifs are listed in Table 3 from the full list in Supplementary Table 3. Interestingly, the predominant heptapeptide sequence MVRDHSV, that was highly enriched in Rounds II (94%), III (88%) and IV (100%) of Screen 1, appeared to mimic nesprin-1 (nuclear envelope spectrin repeat protein 1) by BLAST analysis (Table 3). Nesprin-1 is a scaffolding protein that is highly expressed in skeletal and cardiac muscle[11]. It was first described as a nuclear membrane

protein that interacts with SUN (Sad1p/UNC84) and emerin proteins of the inner nuclear membrane in association with the nuclear lamina proteins lamin A/C to form the LINC complex (Linker of Nucleoskeleton and Cytoskeleton), thus coupling the cytoskeleton to the nucleoskeleton[348]. Nesprin-1 is now known to have multiple isoforms that vary in size and subcellular localization[349]. While Uniprot database recognizes 12 isoforms of nesprin-1, at least 20 validated and hypothetical isoforms have been built by identifying alternative start and termination sites in the nesprin-1 gene[349,350]. Mutations in nesprin-1 have been shown to cause DCM as well as Emery-Dreifuss Muscular Dystrophy (EDMD)[351-354]. These diseases result from malfunction in one or more of its roles within the LINC complex, particularly mechanotransduction signaling, nuclear morphology, nuclear positioning and chromatin organization[10]. For example, a DCM-associated splice-site variant of nesprin-1 has been shown to have an inconsistent nuclear envelope distribution with abnormal nuclear morphology and undermined actin organization[355]. Furthermore, DCM-causing mutations in nesprin-1 have been shown to disrupt its interactions with Lamin A/C and SUN proteins at the nuclear envelope and cause defects in myogenesis[354]. Full length human nesprin-1 consists of three domains: C-terminal KASH domain that integrates into the nuclear envelope, N-terminal domain that interacts with the cytoskeleton, and a central spectrin-repeat containing rod domain that mediates protein-protein interactions[349]. The five-amino acid matching motif of MVRDHSV spans the amino acids 6884-6888 of nesprin-1 thus localizing to spectrin repeat 59 in the central rod domain. This spectrin repeat is present in isoforms 1, 2, 4 and 8 of nesprin-1 according to UniProt database (http://www.uniprot.org) suggesting that these isoforms of nesprin-1 interact with C-RBM20.

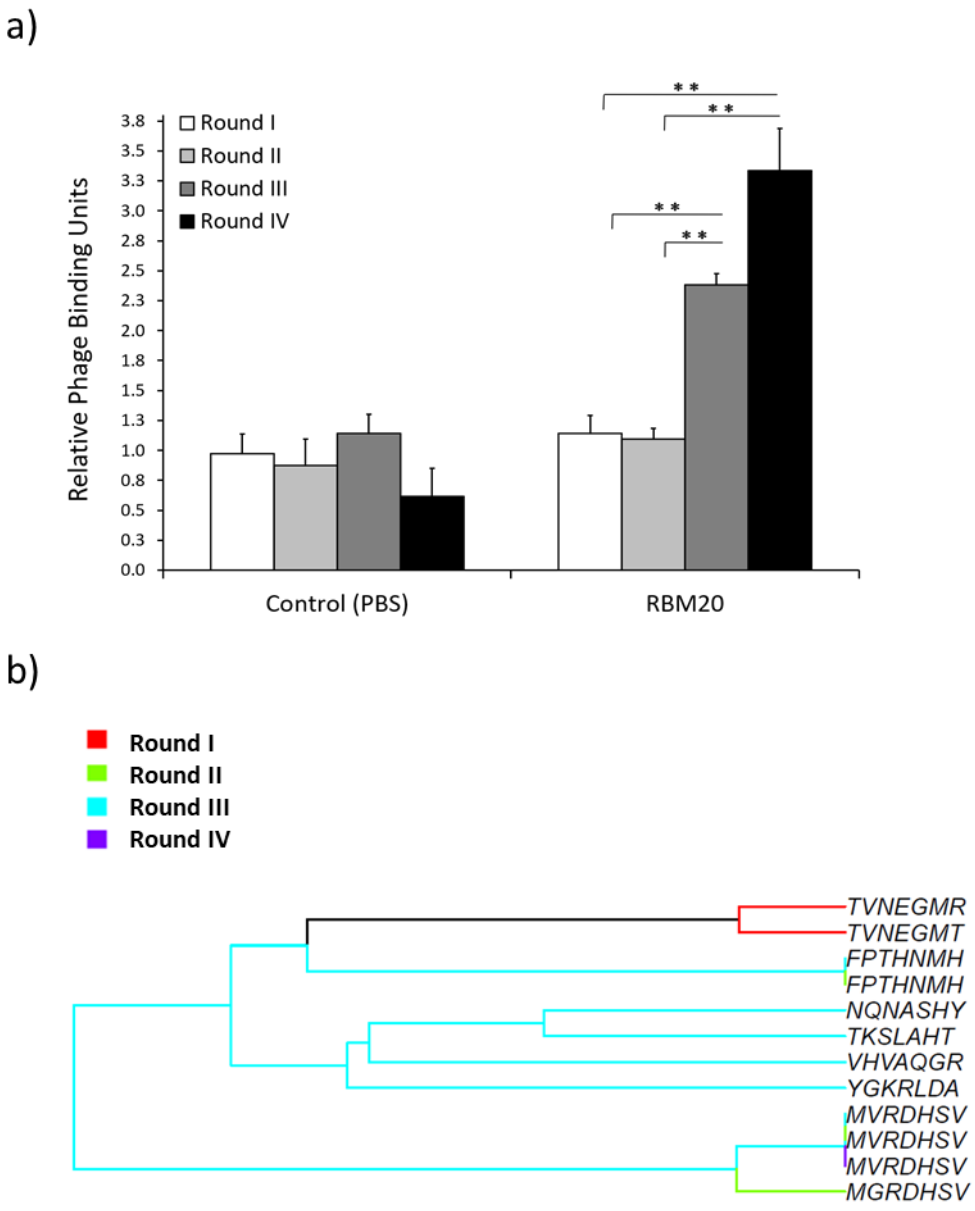

Figure 19. Phage display Bio-panning on C-RBM20 Without Acid Elution (Screen 1). a) Phage display biopanning was performed on C-RBM 20 using the Ph.D.-C7C library. Phage binding was allowed, and bound phage was eluted by *E.coli* infection to identify partners that bind C-RBM20 weakly. Following successive rounds of bio-panning, significant enrichment in phage binding was obtained in Rounds III & IV in comparison to Round I as determined by a 2.1- and 2.9-fold change in relative phage binding units

respectively. No significant enrichment in phage binding to the control PBS-coated wells was obtained. Results represent the mean ratio of phage TU counts (phage library/M13KE control insertless phage) ± SEM of 3 independent repeats; (**, $p<0.01$; unpaired two-tailed t-test). b) Clustering analysis of peptides derived from four successive rounds of bio-panning on C-RBM20 without acid elution (Screen 1). Approximately, 50 peptides were analyzed from each round.

4. Phage Display Biopanning on C-RBM20 With Acid Elution (Screen 2)

To identify strong binding partners of RBM20, phage display biopannig on C-RBM20 was performed according to the same method described above. However; following phage library incubation and washing of unbound phage, bound phage was eluted with Glycine-HCl and neutralized with Tris-HCl before rescue by infection of competent *E. coli* cells. Following four successive rounds of bio-panning, significant enrichment in phage binding to C-RBM20 was not obtained until Round IV of biopanning whereby the mean ratio of phage TU counts (1.39 ± 0.11) was significantly higher than that obtained in Round I (0.70 ± 0.06) or Round II (0.83 ± 0.08); $p=0.01$ and $p=0.01$ respectively in unpaired two-tailed t-test (Figure 20a), hence indicating a 2-fold and a 1.7-fold increase in relative phage binding to C-RBM20 in Round IV in comparison to Round I and Round II respectively. The results represent the mean ratio of phage TU counts (phage library/M13KE per sample) ± SEM of 3 independent repeats. No significant enrichment in phage binding to the control PBS-coated wells was obtained (Figure 20a).

Table 3. High frequency peptides from phage display bio-panning on the C-terminal fragment of recombinant RBM20 protein without acid elution and their corresponding protein mimics, matching motifs and accession numbers.

Round	Peptide (% Frequency)	Matching motif	Protein Mimic (Gene)	UniprotKB Accession Number
Round I	TVNEGMT (98%)	651-**INEGMT**-656	Piwi-like protein 1 (PIWIL 1)	Q96J94
		36-**VNEGM**-40	Neurogenic locus notch homolog protein 2 (NOTCH2)	Q04721
		228-**VNEGM**-232	Probable cation-transporting ATPase 13A5 (ATP13A5)	Q4VNC0
		490-**TVTDGMT**-496	Protein sidekick-1 (SDK1)	Q7Z5N4
		647-**VTEGMT**-652	Cullin-9 (CUL9)	Q8IWT3
		1190-**VNAGMT**-1195	Dedicator of cytokinesis protein 9 (DOCK9)	Q9BZ29
	TVNEGMR (2%)	36-**VNEGM**-40	Neurogenic locus notch homolog protein 2 (NOTCH2)	Q04721
		228-**VNEGM**-232	Probable cation-transporting ATPase 13A5 (ATP13A5)	Q4VNC0
		104-**TVSEGAMR**-111	MHC class II regulatory factor RFX1 (RFX1)	P22670
		136-**VNEGKKMR**-143	Interleukin-6 receptor subunit beta (IL6ST)	P40189
		478-**TVHEGLR**-484	Scm-like with four MBT domains protein 1 (SFMBT1)	Q9UHJ3
		56-**TVNEAASMR**-64	Insulin-like growth factor 1 receptor (IGF1R)	P08069
		27-**VNEGVR**-32	Intersectin-1 (ITSN1)	Q15811
Round II	MVRDHSV (94%)	6834-**MVRDH**-6838	Nesprin-1 (SYNE1)	Q8NF91
		346-**MIRDHEV**-352	Rho GTPase-activating protein 25 (ARHGAP25)	P42331
		1650-**MVVDHSV**-1656	Protein furry homolog (FRY)	Q5TBA9
		173-**VREHSV**-178	Kinesin-like protein KIF13B (KIF13B)	Q9NQT8
		472-**MVRQHS**-477	Zinc finger protein ZXDC (ZXDC)	Q2QGD7
		622-**VREHSV**-627	Protein FAM83G (FAM83G)	A6ND36
	FPTHNMH (4%)	219-**FPTHN**-223	Coiled-coil domain-containing protein 153 (CCDC153)	Q494R4
		440-**FPPVCTHNM**-448	Glycogen [starch] synthase, muscle (GYS1)	P13807
		697-**PTHDM**-701	Cysteine--tRNA ligase (CARS)	P49589
		503-**HNMH**-506	Wilms tumor protein (WT1)	P19544
		26-**HNMH**-29	RQCD1 protein (RQCD1)	D5MQE1
		95-**HNMH**-98	Interleukin-33 (IL33)	O95760
Round III	MVRDHSV (88%)	6834-**MVRDH**-6838	Nesprin-1 (SYNE1)	Q8NF91
		346-**MIRDHEV**-352	Rho GTPase-activating protein 25 (ARHGAP25)	P42331
		1650-**MVVDHSV**-1656	Protein furry homolog (FRY)	Q5TBA9
		173-**VREHSV**-178	Kinesin-like protein KIF13B (KIF13B)	Q9NQT8
		472-**MVRQHS**-477	Zinc finger protein ZXDC (ZXDC)	Q2QGD7
		622-**VREHSV**-627	Protein FAM83G (FAM83G)	A6ND36
	YGKRLDA (4%)	947-**GKRLDA**-952	Bromodomain-containing protein 1 (BRD1)	O95696
		1337-**YGKRLE**-1342	Telomerase protein component 1 (TEP1)	Q99973
		429-**YGKRLKA**-435	ATP-dependent DNA helicase DDX11 (DDX11)	Q96FC9
		936-**YQKRLDA**-942	Rho guanine nucleotide exchange factor 11	O15085
		1783-**YGKRL**-1787	(ARHGEF11)	Q7Z408
		658-**YRKRLDA**-664	CUB and sushi domain-containing protein 2 (CSMD2)	Q49AG3
			Zinc finger BED domain-containing protein 5 (ZBED5)	
Round IV	MVRDHSV (100%)	6834-**MVRDH**-6838	Nesprin-1 (SYNE1)	Q8NF91
		346-**MIRDHEV**-352	Rho GTPase-activating protein 25 (ARHGAP25)	P42331
		1650-**MVVDHSV**-1656	Protein furry homolog (FRY)	Q5TBA9
		173-**VREHSV**-178	Kinesin-like protein KIF13B (KIF13B)	Q9NQT8
		472-**MVRQHS**-477	Zinc finger protein ZXDC (ZXDC)	Q2QGD7
		622-**VREHSV**-627	Protein FAM83G (FAM83G)	A6ND36

a)

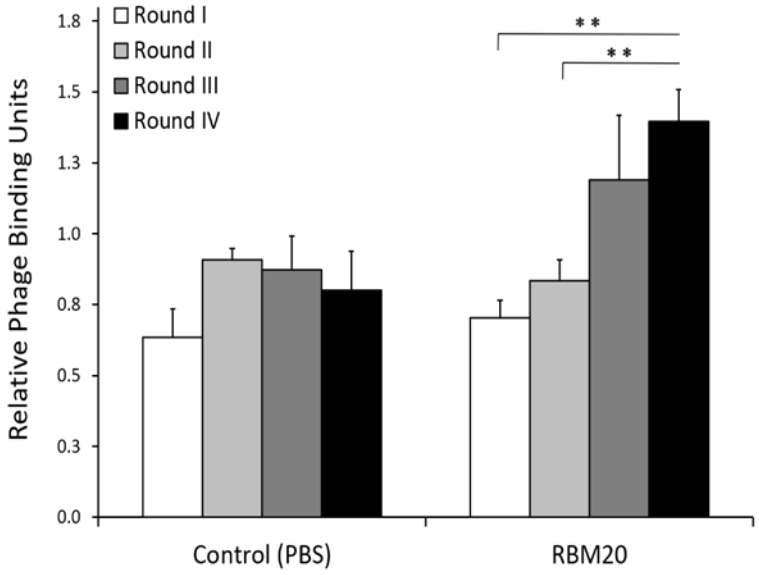
Round I
Round II
Round III
Round IV
Relative Phage Binding Units
1.8
1.5
1.3
1.0
0.8
0.5
0.3
0.0
**
**
Control (PBS)
RBM20

b)

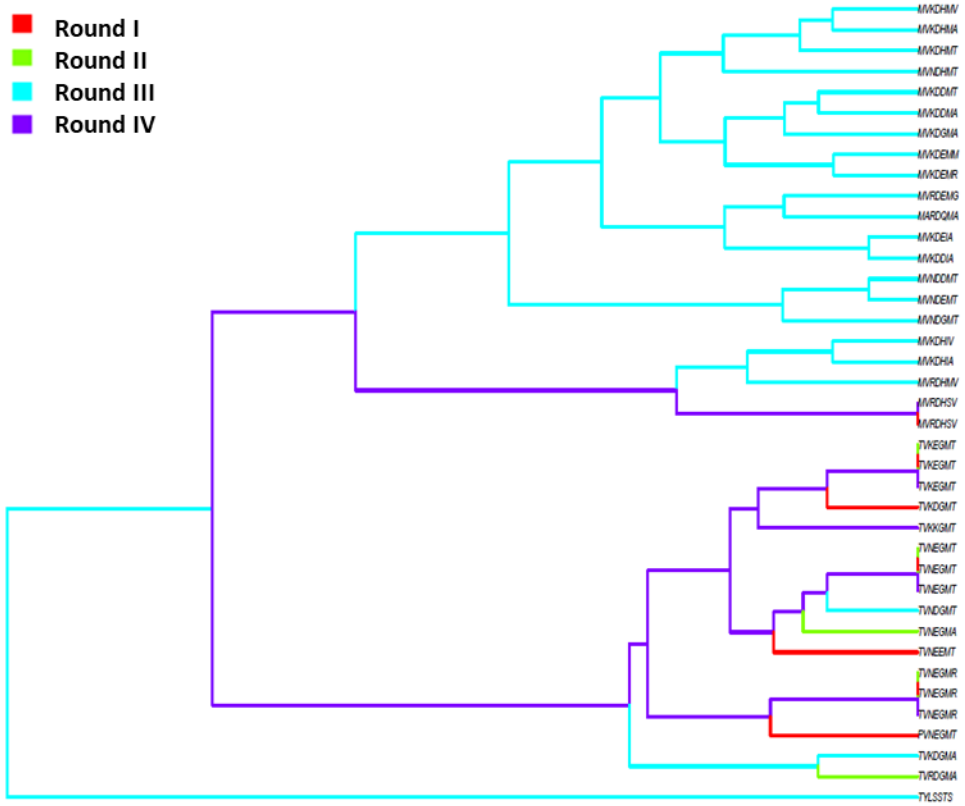
Round I
Round II
Round III
Round IV

Figure 20. Phage display bio-panning on C-RBM20 with acid elution (Screen 2).
a) Phage display biopanning was performed on C-RBM20 using the Ph.D.-C7C library. Phage binding was allowed, and bound phage was rescued by acid elution and *E. coli* infection to identify strong binding partners of C-RBM20. Following successive rounds of bio-panning, significant enrichment in phage binding was obtained in Round IV in comparison to Round I and II as determined by a 2-fold and 1.7-fold increase in relative phage binding units in Round IV in comparison to Round I and Round II respectively. No significant enrichment in phage binding to the control PBS-coated wells was obtained. Results represent the mean ratio of phage TU counts (phage library/M13KE control insertless phage) ± SEM of 3 independent repeats; (**, $p<0.01$; unpaired two-tailed t-test). b) Clustering analysis of peptides derived from four successive rounds of bio-panning on C-RBM20 with acid elution (Screen 2). Approximately, 50 peptides were analyzed from each round.

5. Sequence Determination of the Phage Inserts & Clustering Analysis for Clones Selected from Screen 2

To identify peptides displayed by phages that were recovered from binding to C-RBM20 with acid elution (Screen 2), the phage inserts for a panel of 50 phage clones from Round I, 53 clones from Round II, 51 clones from Round III and 52 clones from Round IV were PCR amplified, sequenced, and analyzed. Clustering analysis of the recovered peptides shows a total of 32 different peptide sequences obtained from the different rounds of Screen 2 (Figure 20b). The diversity of the peptides increased from Round I (7 peptides) and Round II (5 peptides) to Round III (22 peptides) then decreased in Round IV (5 peptides). Peptide clustering was noted for each round; however, the peptides mainly localized to wide clusters with the widest cluster belonging to Round III which is in line with the highest diversity of peptides obtained from this round. Like Screen 1, same peptide sequences were recovered from different rounds of Screen 2, three of which were different in one or two amino acids (MVRDHSV, TVKEGMT, TVNEGMT and TVNEGMR).

Table 4. High frequency peptides from phage display bio-panning on the C-terminal fragment of recombinant RBM20 protein, with acid elution, and their corresponding protein mimics, matching motifs and accession numbers.

Round	Peptide (% Frequency)	Matching motif	Protein Mimic	UniprotKB Accession Number
Round I	TVNEGMT (86%)	651-**INEGMT**-656	Piwi-like protein 1 (PIWIL 1)	Q96J94
		36-**VNEGM**-40	Neurogenic locus notch homolog protein 2 (NOTCH2)	Q04721
		228-**VNEGM**-232	Probable cation-transporting ATPase 13A5 (ATP13A5)	Q4VNC0
		490-**TVTDGMT**-496	Protein sidekick-1 (SDK1)	Q7Z5N4
		647-**VTEGMT**-652	Cullin-9 (CUL9)	Q8IWT3
		1190-**VNAGMT**-1195	Dedicator of cytokinesis protein 9 (DOCK9)	Q9BZ29
	TVKEGMT (4%)	490-**TVTDGMT**-496	Protein sidekick-1 (SDK1)	Q7Z5N4
		647-**VTEGMT**-652	Cullin-9 (CUL9)	Q8IWT3
	TVNEGMR (2%)	36-**VNEGM**-40	Neurogenic locus notch homolog protein 2 (NOTCH2)	Q04721
		228-**VNEGM**-232	Probable cation-transporting ATPase 13A5 (ATP13A5)	Q4VNC0
		104-**TVSEGAMR**-111	MHC class II regulatory factor RFX1 (RFX1)	P22670
		136-**VNEGKKMR**-143	Interleukin-6 receptor subunit beta (IL6ST)	P40189
		478-**TVHEGLR**-484	Scm-like with four MBT domains protein 1 (SFMBT1)	Q9UHJ3
		56-**TVNEAASMR**-64	Insulin-like growth factor 1 receptor (IGF1R)	P08069
		27-**VNEGVR**-32	Intersectin-1 (ITSN1)	Q15811
	PVNEGMT (2%)	1189-**PVNAGMT**-1195	Dedicator of cytokinesis protein 9 (DOCK9)	Q9BZ29
		651-**INEGMT**-656	Piwi-like protein 1 (PIWIL 1)	Q96J94
		36-**VNEGM**-40	Neurogenic locus notch homolog protein 2 (NOTCH2)	Q04721
		228-**VNEGM**-232	Probable cation-transporting ATPase 13A5 (ATP13A5)	Q4VNC0
		67-**PVSEGM**-72; 79-**EGM**-81	Protein TANC2 (TANC2)	Q9HCD6
		462-**PVLEGMT**-468	Double-stranded RNA-specific adenosine deaminase (ADAR)	P55265
	MVRDHSV (2%)	6834-**MVRDH**-6838	Nesprin-1 (SYNE1)	Q8NF91
		346-**MIRDHEV**-352	Rho GTPase-activating protein 25 (ARHGAP25)	P42331
		1650-**MVVDHSV**-1656	Protein furry homolog (FRY)	Q5TBA9
		173-**VREHSV**-178	Kinesin-like protein KIF13B (KIF13B)	Q9NQT8
		472-**MVRQHS**-477	Zinc finger protein ZXDC (ZXDC)	Q2QGD7
		622-**VREHSV**-627	Protein FAM83G (FAM83G)	A6ND36
Round II	TVNEGMT (72%)	651-**INEGMT**-656	Piwi-like protein 1 (PIWIL 1)	Q96J94
		36-**VNEGM**-40	Neurogenic locus notch homolog protein 2 (NOTCH2)	Q04721
		228-**VNEGM**-232	Probable cation-transporting ATPase 13A5 (ATP13A5)	Q4VNC0
		490-**TVTDGMT**-496	Protein sidekick-1 (SDK1)	Q7Z5N4
		647-**VTEGMT**-652	Cullin-9 (CUL9)	Q8IWT3
		1190-**VNAGMT**-1195	Dedicator of cytokinesis protein 9 (DOCK9)	Q9BZ29
	TVKEGMT (21%)	490-**TVTDGMT**-496	Protein sidekick-1 (SDK1)	Q7Z5N4
		647-**VTEGMT**-652	Cullin-9 (CUL9)	Q8IWT3
	TVNEGMA (4%)	36-**VNEGM**-40	Neurogenic locus notch homolog protein 2 (NOTCH2)	Q04721
		986-**VDEGMA**-991	IARS protein (IARS)	Q6P0M4
		228-**VNEGM**-232	Probable cation-transporting ATPase 13A5 (ATP13A5)	Q4VNC0
		1906-**NEGMA**-1910	Kalirin (KALRN)	O60229
		209-**NEGMA**-213	DNA repair protein RAD51 homolog 4 (RAD51D)	O75771
		151-**NEGMA**-155	Transcription elongation factor A protein-like 4 (TCEAL4)	Q96EI5
		170-**VSEGMA**-175	Protein-tyrosine kinase 2-beta (PTK2B)	Q14289
	TVNEGMR (2%)	36-**VNEGM**-40	Neurogenic locus notch homolog protein 2 (NOTCH2)	Q04721
		228-**VNEGM**-232	Probable cation-transporting ATPase 13A5 (ATP13A5)	Q4VNC0

		104-**TVSEGAMR**-111	MHC class II regulatory factor RFX1 (RFX1)	P22670
		136-**VNEGKKMR**-143	Interleukin-6 receptor subunit beta (IL6ST)	P40189
		478-**TVHEGLR**-484	Scm-like with four MBT domains protein 1 (SFMBT1)	Q9UHJ3
		56-**TVNEAASMR**-64	Insulin-like growth factor 1 receptor (IGF1R)	P08069
		27-**VNEGVR**-32	Intersectin-1 (ITSN1)	Q15811
	TVRDGMA (2%)	34-**TVRDGM**-39	Serine/threonine-protein kinase A-Raf (ARAF)	P10398
		4649-**VREGMA**-4654	E3 ubiquitin-protein ligase HERC2 (HERC2)	O95714
		152-**VREGMA**-157	Cyclin-A1 (CCNA1)	P78396
		203-**RDGMA**-207	Beta-spectrin (HSpTB1)	Q71VG1
		493-**TVRNSMA**	Unconventional myosin-IXa (MYO9A)	B2RTY4
	MVKDHMA (27%)	47-**LVKNHMA**-53	Spermatogenesis-associated protein 7 (SPATA7)	Q9P0W8
		263-**MVIEHMA**-269	Thioredoxin reductase 1, cytoplasmic (TXNRD1)	Q16881
		167-**MVIEHMA**-173	Selenoprotein K (SELK)	A8K0M9
		459-**MVKDEM**-464	Protein argonaute-2 (AGO2)	Q9UKV8
		329-**MLEDHMA**-335	TBCC domain-containing protein 1(TBCCD1)	Q9NVR7
		1-**MVKNQM**-6	RNA-binding protein 28 (Rbm28)	Q9NW13
		6846-**MVRDHL**-6851	Nesprin-1 (SYNE1)	Q8NF91
	MVKDDMA (20%)	459-**MVKDEM**-464	Protein argonaute-2 (AGO2)	Q9UKV8
		922-**MVKDD**-926	Phosphatidylinositol 4,5-bisphosphate 3-kinase catalytic subunit alpha isoform (PIK3CA)	P42336
		399-**VKDDM**-403	Protein argonaute-2 (AGO1)	Q9UL18
		324-**MVKDD**-328	Tubulin polyglutamylase TTLL11 (TTLL11)	Q8NHH1
		334-**MVKDD**-338	Intracellular hyaluronan-binding protein 4 (HABP4)	Q5JVS0
		627-**MVVNGKDDM**-635	Gamma-adducin (ADD3)	Q9UEY8
Round III	MVKDHIA (12%)	376-**MIKEHI**-381	Importin-5 (IPO5)	O00410
		167-**VKDHI**-171	Cytokine receptor-like factor 3 (CRLF3)	Q8IUI8
		796-**MTKDQIA**-802	Protein FAM13A (FAM13A)	O94988
		1028-**MIKDQI**-1033	Cytoplasmic dynein 2 heavy chain 1 (DYNC2H1)	Q8NCM8
		414-**MVKEH**-418	Rap guanine nucleotide exchange factor 2 (RAPGEF2)	Q9Y4G8
	MVKDDMT (6%)	459-**MVKDEMT**-465	Protein argonaute-2 (AGO2)	Q9UKV8
		922-**MVKDD**-926	Phosphatidylinositol 4,5-bisphosphate 3-kinase (PI3K)	P42336
		324-**MVKDD**-328	Tubulin polyglutamylase TTLL11 (TTLL11)	Q8NHH1
		334-**MVKDD**-338	Intracellular hyaluronan-binding protein 4 (HABP4)	Q5JVS0
	TVNDGMT (2%)	490-**TVTDGMT**-496	Protein sidekick-1 (SDK1)	Q7Z5N4
		42-**NDGMT**-46	1-phosphatidylinositol 4,5-bisphosphate phosphodiesterase delta-4 (PLCD4)	Q9BRC7
		20-**VSDGMT**-25	Helicase SRCAP (SRCAP)	Q6ZRS2
		1190-**VNAGMT**-1195	Dedicator of cytokinesis protein 9 (DOCK9)	Q9BZ29
		329-**TVNDG**-333	Advillin (AVIL)	O75366
	TVNEGMT (88%)	651-**INEGMT**-656	Piwi-like protein 1 (PIWIL 1)	Q96J94
		36-**VNEGM**-40	Neurogenic locus notch homolog protein 2 (NOTCH2)	Q04721
		228-**VNEGM**-232	Probable cation-transporting ATPase 13A5 (ATP13A5)	Q4VNC0
		490-**TVTDGMT**-496	Protein sidekick-1 (SDK1)	Q7Z5N4
		647-**VTEGMT**-652	Cullin-9 (CUL9)	Q8IWT3
		1190-**VNAGMT**-1195	Dedicator of cytokinesis protein 9 (DOCK9)	Q9BZ29
Round IV	TVNEGMR (6%)	36-**VNEGM**-40	Neurogenic locus notch homolog protein 2 (NOTCH2)	Q04721
		228-**VNEGM**-232	Probable cation-transporting ATPase 13A5 (ATP13A5)	Q4VNC0
		104-**TVSEGAMR**-111	MHC class II regulatory factor RFX1 (RFX1)	P22670
		136-**VNEGKKMR**-143	Interleukin-6 receptor subunit beta (IL6ST)	P40189
		478-**TVHEGLR**-484	Scm-like with four MBT domains protein 1 (SFMBT1)	Q9UHJ3
		56-**TVNEAASMR**-64	Insulin-like growth factor 1 receptor (IGF1R)	P08069
		27-**VNEGVR**-32	Intersectin-1 (ITSN1)	Q15811
	MVRDHSV (2%)	6834-**MVRDH**-6838	Nesprin-1 (SYNE1)	Q8NF91
		346-**MIRDHEV**-352	Rho GTPase-activating protein 25 (ARHGAP25)	P42331
		1650-**MVVDHSV**-1656	Protein furry homolog (FRY)	Q5TBA9

	173-**VREHSV**-178	Kinesin-like protein KIF13B (KIF13B)	Q9NQT8
	472-**MVRQHS**-477	Zinc finger protein ZXDC (ZXDC)	Q2QGD7
	622-**VREHSV**-627	Protein FAM83G (FAM83G)	A6ND36
TVKEGMT (2%)	2715-**VKEGM**-2719	Fibrocystin (PKHD1)	P08F94
	39-**VKEGM**-43	Synaptotagmin-16 (SYT 16)	Q17RD7
	273-**KEGMT**-277	Enoyl-CoA hydratase, mitochondrial (ECHS1)	P30084
	132-**VKEGM**-136	Peptidyl-prolyl cis-trans isomerase A (PPIA)	P62937
	647-**VTEGMT**-652	Cullin-9 (CUL9)	Q8IWT3
TVKKGMT (2%)	239-**KKGMT**-243	Kinetochore-associated protein 1 (KNTC1)	P50748
	2-**VKKGM**-6	Exportin-6 (XPO6)	Q96QU8
	230-**VKKGM**-234	Inositol-trisphosphate 3-kinase B (ITPKB)	P27987
	332-**KKGMT**-336	Transient receptor potential cation channel subfamily V member 1 (TRPV1)	Q8NER1
	92-**VKKAMT**-97	Hepatocyte nuclear factor 4-alpha (HNF4)	P41235
	470-**TVKKEPHESLGMT**-482	Ligand of Numb protein X 2 (LNX2)	Q8N448
	1016-**VKKDMT**-1021	Rap guanine nucleotide exchange factor 6 (RAPGEF6)	Q8TEU7
	226-**TVKKEM**-231	Chromodomain-helicase-DNA-binding protein 9 (CHD9)	Q3L8U1
	657-**TVKTGM**-662	Synaptojanin-1 (SYNJ1)	O43426

In addition, overlap between peptides from the four rounds was clearly seen by the clustering of the different colors in the dendrogram, thus indicating that these peptide sequences have similar characteristics which likely underlie their binding to C-RBM20 and ensure their appearance in different biopanning rounds. The increase in peptide diversity in Round III could be explained by lack of representation of all strong binding peptides in Rounds I and II in the sequenced phage clones due to steric hindrance by the large phage library which may have selected for peptides that bind at high frequency. Bulk amplification of outputs from Rounds I and II may have resulted in better representation of both high and low frequency binders in the sequenced phage clones that were enriched from Rounds II to III. Select peptides exhibiting preferential binding to C-RBM20 were then enriched in Round IV, thus resulting in the decreased diversity.

The percent frequency of occurrence of some of these peptides, determined by the number of times that each peptide sequence appeared in the total number of sequenced phage clones, is shown in Table 4 and Supplementary Table 4. Notably, the heptapeptide sequence, MVRDHSV, which appeared at very high frequencies (88%-100%) in several rounds of Screen 1 (Table 3) also appeared in multiple rounds of Screen 2, yet at a very low frequency (2%) (Table 4), which further supports its weak interaction with C-RBM20. And while the peptide sequence TVNEGMT only appeared in the first round of Screen I (98%), it persisted throughout different rounds of Screen 2 (86% in Round I, 72% in Round II and 88% in Round IV) which supports its strong interaction with C-RBM20. Similarly, a peptide differing by one amino acid, TVNEGMR, only appeared in Round I of Screen 1 (2%) whereas it appeared in different rounds of Screen 2 (2% in Round I, 2% in Round II, and 6% in Round III) yet at much lower frequencies than TVNEGMT. This is suggestive that although TVNEGMT was enriched as a strong binding peptide, it binds C-Rbm20 with lower affinity than TVNEGMR as a result of one amino acid change. Another possible explanation is that phage particles carrying this peptide might have slow replicative cycle in *E. coli* due to a potentially negative effect that they have on bacterial growth or survival, thus resulting in their recovery at low frequency.

Clustering analysis of all peptides recovered from both screens shows a higher diversity of peptides recovered from Screen 2 in comparison to Screen 1 (Figure 21). Peptides recovered from the two screens are localized in two separate clusters except for TVNEGMT and TVNEGMR which were recovered by both screens and TYLSSTS which was recovered by Screen 2 but clusters with peptides from Screen 1.

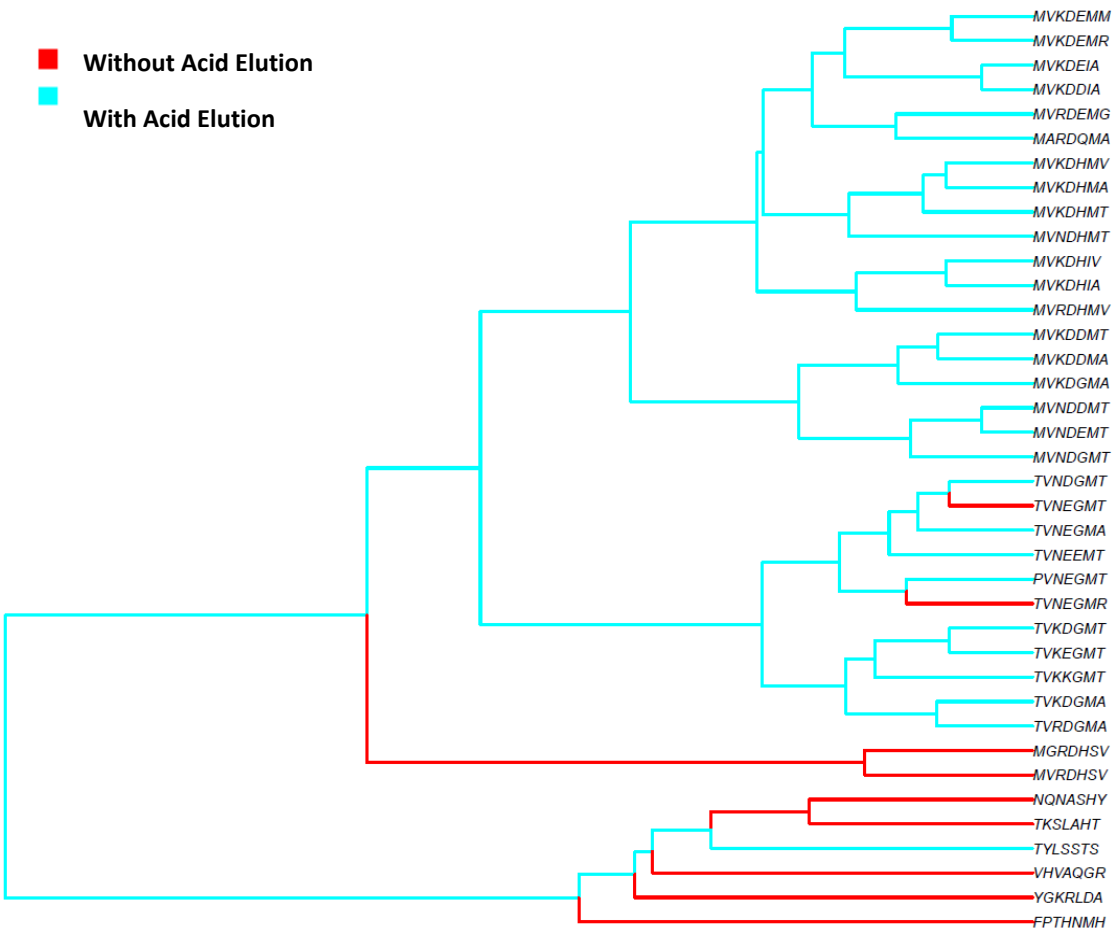

Figure 21. Clustering Analysis of Peptides from Screens 1 and 2 of Phage Display Bio-panning on C-RBM20.
Screen 1 was performed without acid elution to recover weak binding partners, while Screen 2 was performed with acid elution to recover strong binding partners. Four successive rounds of bio-panning were performed per screen. Approximately, 200 peptides were analyzed from each screen with 50 peptides from each round. The dendrogram reveals clustering of peptides within each Screen of phage display bio-panning on C-RBM20.

6. High Frequency Peptides Recovered from Screen 2 & The Proteins They Mimic

To determine the protein mimics of recovered peptide sequences from Screen 2, protein-protein BLAST analysis was performed according to the above criteria. Multiple protein mimics with putative binding abilities to C-RBM20 were recovered. Select protein

mimics of high frequency peptides and their matching motifs from the different rounds of Screen 2 are listed in Table 4 and the full list is listed in Supplementary Table 4. Notably, nesprin-1 reappeared in Screen II not only as a protein mimicked by the sequence MVRDHSV which was recovered by both screens, but also as a protein mimicked by other peptide sequences specific to Screen II (MVKDHMA, MVRDHMV and MVKDHMT). The matching motives in the peptide sequences recovered from Screen II localized to spectrin repeats 20, 30, 32, 35, 59, 62 and 63 in nesprin-1. Accordingly, the matching motifs of the peptide mimics from Screen II are present in isoforms 1, 2, 4, 7, 8 and 10 of nesprin-1 according to UniProt database (http://www.uniprot.org) and in a total of 16 isoforms when taking into account curated isoforms of nesprin-1[349,350]. Interestingly, isoform 10 of nesprin-1 which lacks the C-terminal KASH domain (also known as Drop1) has been shown to be implicated in human carcinomas and may play a role in chromatin organization[350,356]. In addition, A-kinase anchor protein 9 (AKAP-9), a centrosomal protein component of the microtubule organizing center that binds nesprin-1α[18], was also recovered by Screen II. Nesprin-1α is a short skeletal and cardiac-specific isoform that localizes to both the outer and inner nuclear membranes[10,357]. The matching motifs of the peptide mimics of nesprin-1 do not localize to this isoform; however, given the high homology between different spectrin repeats, the possibility of interaction between nesprin-1α and the C-terminal or other domains of RBM20 cannot be ruled out. Furthermore, since AKAP-9 is a cytoplasmic protein that interacts with nesprin-1α at the outer nuclear membrane, the predominant nuclear localization of RBM20 suggests that interaction with nesprin-1α might occur at the inner nuclear membrane at AKAP-9 binding site of nesprin-1α. This is consistent with the localization of nesprin-1α to both the outer and inner nuclear

membranes and might provide a possible explanation for the appearance of AKAP-9 in our screen. A KASH-less 50 KDa isoform of nesprin-1 has been detected in mRNA processing bodies (PBs), where it associates with microtubules and RNA-induced silencing complex (RISC) proteins such as Ago2 (Protein Argonaute-2)[358]. PBs are dynamic nonmembrane-bound ribonucleoprotein foci involved in posttranscriptional gene regulation, including miRNA-mediated gene silencing[359,360]. Interestingly, Ago2 was mimicked by multiple peptides recovered by Screen II. Thus, the appearance of both nesprin-1 and Ago2 in our screen is suggestive that specific isoforms of RBM20 might localize to cytoplasmic PBs where they interact with both nesprin-1 and Ago2. This is supported by findings showing that the nuclear matrix RNA binding protein, matrin-3, also localizes to PBs where it plays a role in miRNA-dependent gene silencing and interacts with both nesprin-1 and Ago2[361]. Matrin-3 is a paralogue to RBM20 that also acts as an RNA binding protein and repressor of alternative splicing[362].RBM20 and matrin-3 have been shown to interact with each other and with common proteins, such as the splicing co-regulator PTBP1[212,362,363]. As such it would be interesting to investigate whether RBM20 also localizes to PBs and plays a similar role to matrin-3 in miRNA-dependent gene silencing. In addition to its role in the RISC complex, human Ago2 has been shown to localize to the nucleus where it plays a role in regulating alternative splicing both by modulating RNA polymerase II elongation rate and histone modifications[364]. As such, Ago2 might as well interact with RBM20 in the nucleus. Supporting its putative interaction with RBM20 is the interaction of Ago 2 with several RNA binding motif proteins (RBM8, RBM14, RBM16 and RBM39)[364]. The appearance of nesprin-1 in both phage display screens, particularly as a top hit in Screen I, its implication in DCM and the appearance of multiple nesprin-1 interacting proteins in our

screens, strongly proposes it as a putative interacting partner with RBM20. As such, we selected nesprin-1 for validation by Co-IP and proximity ligation assays (see below). In addition to nesprin-1, other DCM-related proteins were also mimicked by peptides recovered by our screens. Importantly, *TTN*, the most commonly mutated gene in DCM and the genuine mRNA splicing target of RBM20[134,176], was mimicked by the peptides MVKDHMT, MVKDEIA, TVKDGMA and TVKDGMT recovered in Screen II. In addition to its role in the sarcomere, titin is present in the nucleus where it has been shown to interact with A and B type lamins[365]. Although the significance of this interaction is yet to be revealed, it might be related to the role of nuclear titin in chromatin organization. In fact, not only nuclear titin protein but also titin pre-mRNA has recently been shown to play a role in genome organization by bringing together foci of RBM20 target genes during cardiogenesis, thus facilitating RBM20-mediated alternative splicing[366]. In addition to titin, lamin B1 also appeared as a putative C-RBM20 binding protein. Due to the similar structural organization of lamin B1 and lamin A/C and their close association and interaction with each other and with other common binding partners[367], we opted to test the putative interaction between RBM20 and each of lamin B1 and lamin A/C. Although lamin A/C did not appear as a hit in our screens, the fact that *LMNA* is the second most commonly mutated gene in DCM and the similarity in the disease manifestation of *LMNA* and *RBM20* mutations[178,340], encouraged us to test whether lamin A/C also interacts with RBM20. Furthermore, a study by Maatz *et al.* revealed several RBM20-interacting proteins (RBM10, SF3B3, PRPF12, PRPF19, PRPF31, U2AF2) that have also been reported to interact with lamin A/C[212,340].

7. Rbm20 protein interacts with nesprin-1, lamin A/C and lamin B1

Co-IP assays were performed using antibody-coupled beads with antibodies against nesprin-1, lamin A/C and lamin B1 alongside normal rabbit, goat or mouse IgG-coupled beads, which served as controls. Co-IP was first performed in differentiated C2C12 myoblasts using nesprin-1 antibody and normal rabbit IgG-coupled beads. Probing for Rbm20 and nesprin-1 by western blotting showed that the 75 KDa isoform of Rbm20 is pulled down by the 112 KDa isoform of nesprin-1 and to a lesser extent by the 131 KDa isoform of nesprin-1 (Figure 22a). Interestingly, the obtained nesprin-1 bands correspond to muscle specific isoforms: isoform 3 or nesprin-1α (112.4 KDa), isoform 9 or nesprin-1α_2 (111.6 KDa) and isoform 11 or myne-1 (131 KDa). Since these isoforms were not recovered by our phage display screens, their shared homology with the recovered isoforms might explain their interaction with Rbm20 in Co-IP. The appearance of these specific isoforms in Co-IP might be governed by their muscle-specific expression and thus their abundance in differentiated C2C12 myoblasts. Another explanation is that the interaction between these isoforms and RBM20 might require other domains in addition to the C-terminal domain, which might explain their appearance in Co-IP but not in phage display biopanning against C-RBM20. Moreover, peptides mimicking these isoforms could have been recovered by our screens but might not have been picked when randomly selecting clones for sequencing. Pull down assays were also performed using anti-lamin A/C antibody-coupled beads and normal goat IgG-coupled beads. Western blot analysis showed that the same isoform of Rbm20 that interacts with nesprin-1 co-immunoprecipitates with lamin A/C in protein lysates from differentiated C2C12 myoblasts (Figure 22b).

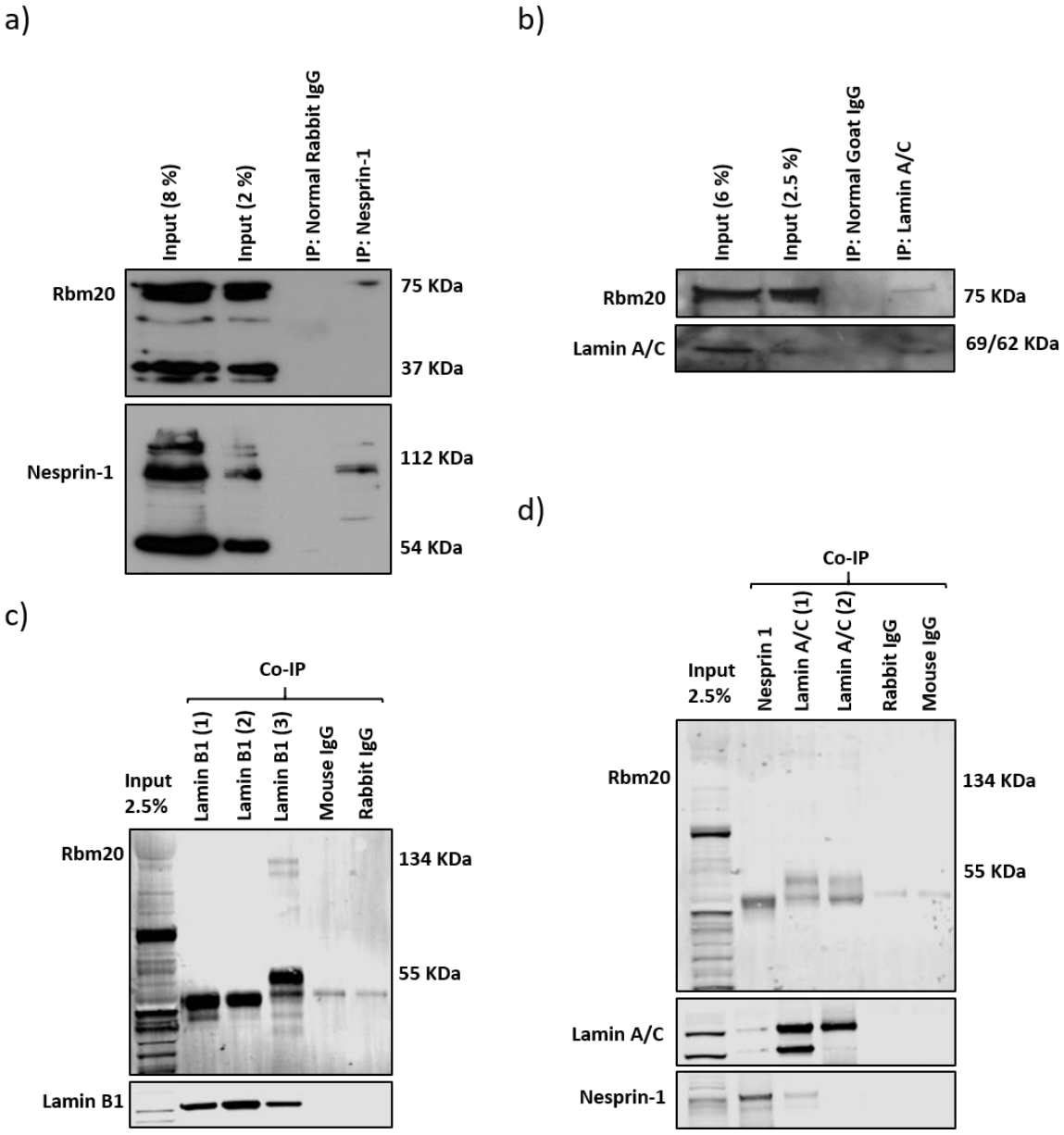

Figure 22. Rbm20 Co-immunoprecipitates with Nesprin-1, Lamin A/C and Lamin B1 in Differentiated C2C12 Myoblasts and in Mouse Heart Muscle Tissue.
Co-IP assays were performed with protein extracts from C2C12 myoblasts 2 days post differentiation a) and b) or with heart muscle tissue from wild type C57 mice c) and d). a) Co-IP assays were performed using anti-nesprin-1 antibody and normal rabbit IgG-coupled beads. Probing for Rbm20 and nesprin-1 showed that Rbm20 is pulled down by nesprin-1 in differentiated C2C12 cells. b) Pull down assays were performed using anti-lamin A/C and normal goat IgG-coupled beads. Western blotting showed that Rbm20 is pulled down by lamin A/C in differentiated C2C12 cells. c) Pull down assays were performed by coupling one nesprin-1 antibody and 2 lamin A/C antibodies to protein A agarose beads

alongside normal rabbit and mouse IgG-coupled beads. Both lamin A/C antibodies pulled down RBM20 and antibody 1 pulled down both RBM20 and nesprin-1 in heart muscle tissue from mice. d) Pull down assays were performed by coupling 3 lamin B1 antibodies to protein A agarose beads alongside normal rabbit and mouse IgG-coupled beads. Lamin B1 (antibody 3) pulled down RBM20 in heart muscle tissue from mice.

These results were confirmed in heart muscle tissue harvested from wild type mice (Figure 22c). One nesprin-1 antibody and two different lamin A/C antibodies were coupled to protein A agarose beads and used alongside normal rabbit and mouse IgG-coupled beads. Both lamin A/C antibodies pulled down RBM20, while it was not pulled down by the nesprin-1 antibody used. In addition, lamin A/C (antibody 1) pulls down both RBM20 and nesprin-1α (112 KDa). The bands corresponding to RBM20 appeared at 55 KDa and to a lesser extent at 130 KDa. The 55 KDa band likely corresponds to a 507 amino acid polypeptide of RBM20 that has been reported by the Mouse Genome Informatics (MGI) website (http://www.informatics.jax.org/sequence/marker/MGI:1920963?provider=UniProt). By calculating the molecular weight from the amino acid number, using the molecular weight Promega calculator, this polypeptide corresponds to 55.77 KDa. On the other hand, the 130 KDa band corresponds to the canonical RBM20 isoform in mice. The appearance of RBM20, nesprin-1 and lamin A/C bands in the same blot indicates that these three proteins interact in the same complex, most probably at the inner nuclear membrane. Next, we tested the interaction between lamin B1 and RBM20 in heart muscle tissue lysates using three different lamin B1 antibodies coupled to protein A agarose beads and normal mouse and rabbit IgG-coupled beads (Figure 22d). Both isoforms of RBM20 (55 and 130 KDa) were pulled down by lamin B1 (antibody 3).

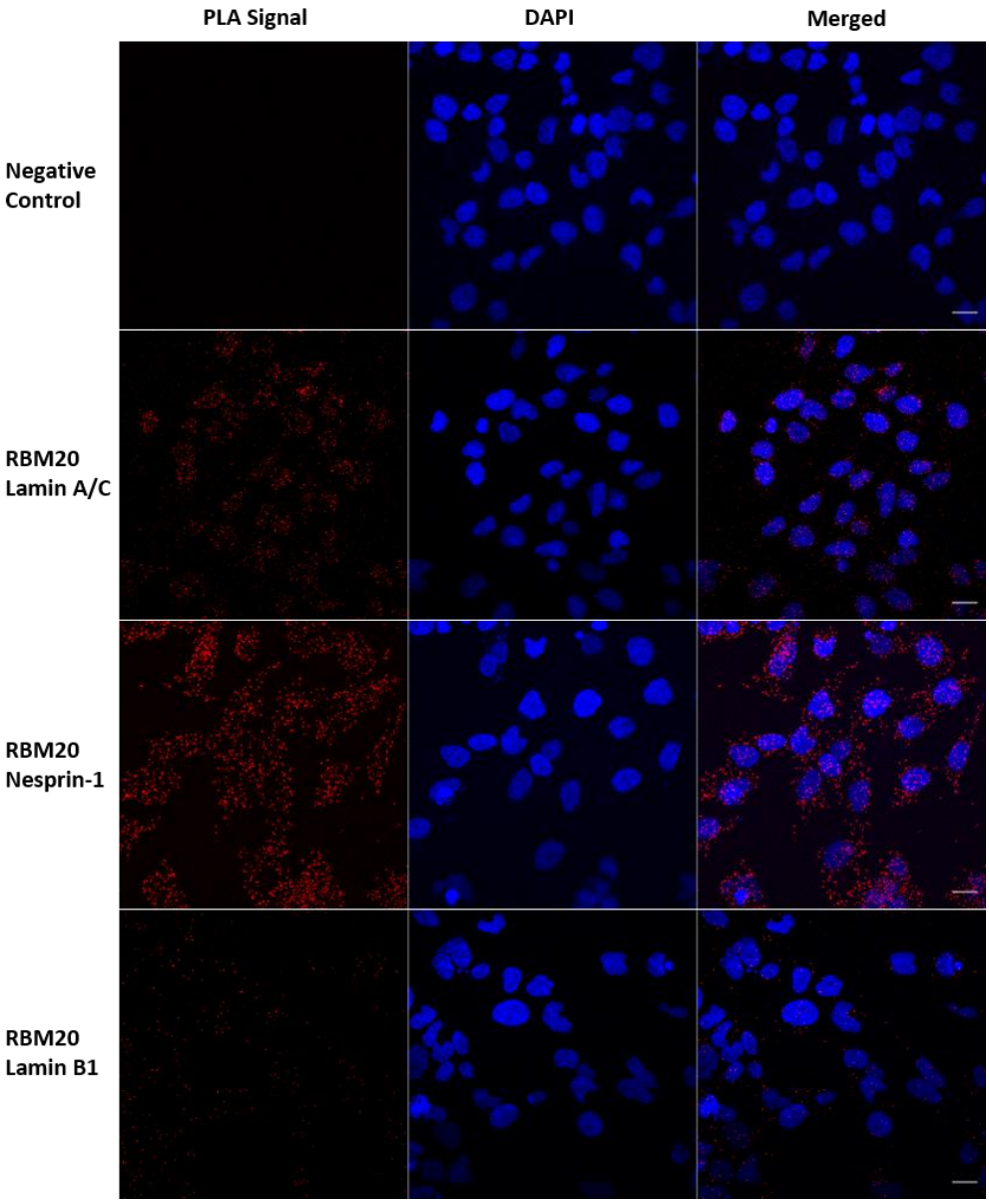

Figure 23. Detection of Interaction Between RBM20 and each of Lamin A/C, Lamin B1 and Nesprin-1 in Human Rhabdomyosarcoma (RD) Cells by Proximity Ligation Assay.

Representative maximum intensity projection images of confocal z stacks, showing proximity ligation assay (PLA) signals in red and nuclei in blue. PLA for the interaction between Rbm20 and each of lamin A/C, nesprin-1 and lamin B1 is shown versus the negative control. Scale bar = 20 µm.

Interaction between Rbm20 and each of lamin A/C, lamin B1 and nesprin-1 was confirmed by Proximity Ligation Assay (PLA) in human Rhabdomyosarcoma (RD) cells (Figure 23). Furthermore, double immunofluorescence staining of RBM20 and lamin A/C and RBM20 and nesprin-1 was performed in RD cells in which RBM20 was shown to co-localizes with each of lamin A/C and nesprin-1 (Figure 24).

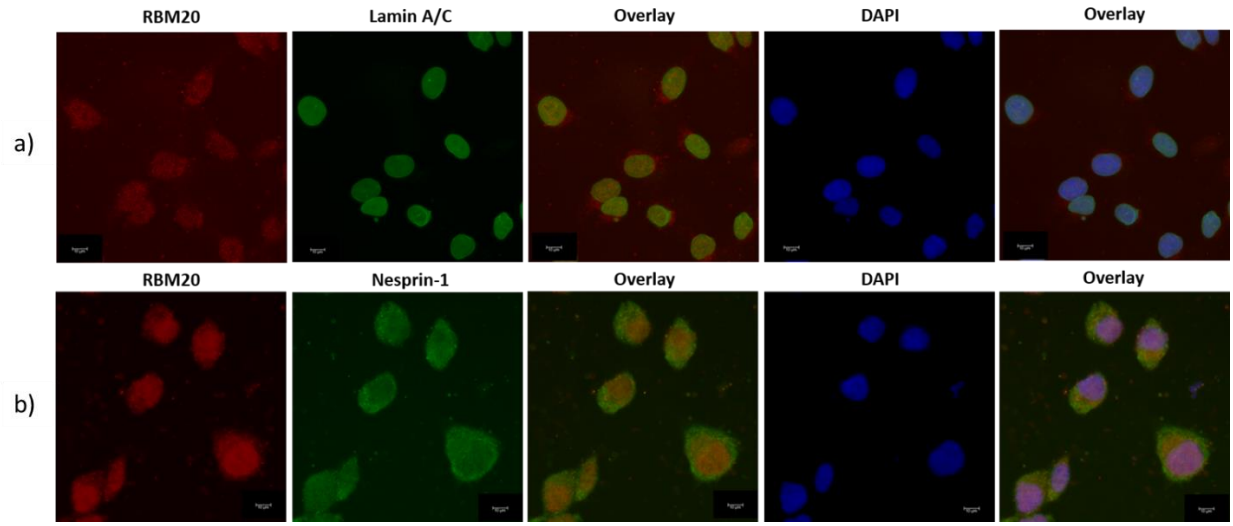

Figure 24. RBM20 protein co-localizes with lamin A/C and nesprin-1 in human Rhabdomyosarcoma (RD) cell line.
Double immunofluorescence staining of RBM20 and lamin A/C and RBM20 and nesprin-1 were performed in RD cells. Representative upright fluorescent microscope images (400x) show that RBM20 co-localizes with each of lamin A/C *(A)* and nesprin-1 *(B)* in RD cells.

Thus, our results show that RBM20 interacts with nesprin-1α, lamin A/C and lamin B1 both *in vitro* and *in vivo*. This interaction most likely occurs at the inner nuclear membrane where all these proteins share a common localization. In addition to nesprin-1α,

lamin A/C and lamin B1, this work revealed proteins that are closely related to Rbm20 interacting partners reported by previous studies. While our phage display method revealed NUDT18, CCDC153, CCDC39, RBMY1A1, RBM28, DDX11, ZNF324, ZNF511, ZNF609, ZNF66 and ZNFX1 as putative proteins that interact with C-RBM20, Maatz *et al.* identified by mass spectrometry NUDT21, CCDC47, RBM4, RBM14, RBM15, RRBMX, DDX5, DDX41 and ZNF207 as RBM20 interacting partners. In addition, our screens identified novel RBM20 interacting proteins, thus providing a better insight into the molecular mechanisms implicated in its role in cardiomyopathies.

E. Supplementary Tables

Supplementary Table 3. High frequency peptides from phage display bio-panning on the C-terminal fragment of recombinant RBM20 protein without acid elution and their corresponding protein mimics, matching motifs and UniprotKB accession numbers.

Round	Peptide (% Frequency)	Matching motif	Protein Mimic (Gene)	UniprotKB Accession Number
Round I	TVNEGMT (98%)	651-**INEGMT**-656	Piwi-like protein 1 (PIWIL 1)	Q96J94
		36-**VNEGM**-40	Neurogenic locus notch homolog protein 2 (NOTCH2)	Q04721
		228-**VNEGM**-232	Probable cation-transporting ATPase 13A5 (ATP13A5)	Q4VNC0
		490-**TVTDGMT**-496	Protein sidekick-1 (SDK1)	Q7Z5N4
		647-**VTEGMT**-652	Cullin-9 (CUL9)	Q8IWT3
		1190-**VNAGMT**-1195	Dedicator of cytokinesis protein 9 (DOCK9)	Q9BZ29
	TVNEGMR (2%)	36-**VNEGM**-40	Neurogenic locus notch homolog protein 2 (NOTCH2)	Q04721
		228-**VNEGM**-232	Probable cation-transporting ATPase 13A5 (ATP13A5)	Q4VNC0
		104-**TVSEGAMR**-111	MHC class II regulatory factor RFX1 (RFX1)	P22670
		136-**VNEGKKMR**-143	Interleukin-6 receptor subunit beta (IL6ST)	P40189
		478-**TVHEGLR**-484	Scm-like with four MBT domains protein 1 (SFMBT1)	Q9UHJ3
		56-**TVNEAASMR**-64	Insulin-like growth factor 1 receptor (IGF1R)	P08069
		27-**VNEGVR**-32	Intersectin-1 (ITSN1)	Q15811
Round II	MVRDHSV (94%)	6834-**MVRDH**-6838	Nesprin-1 (SYNE1)	Q8NF91
		346-**MIRDHEV**-352	Rho GTPase-activating protein 25 (ARHGAP25)	P42331
		1650-**MVVDHSV**-1656	Protein furry homolog (FRY)	Q5TBA9
		173-**VREHSV**-178	Kinesin-like protein KIF13B (KIF13B)	Q9NQT8
		472-**MVRQHS**-477	Zinc finger protein ZXDC (ZXDC)	Q2QGD7
		622-**VREHSV**-627	Protein FAM83G (FAM83G)	A6ND36
	FPTHNMH (4%)	219-**FPTHN**-223	Coiled-coil domain-containing protein 153 (CCDC153)	Q494R4
		440-**FPPVCTHNM**-448	Glycogen [starch] synthase, muscle (GYS1)	P13807
		697-**PTHDM**-701	Cysteine--tRNA ligase (CARS)	P49589
		503-**HNMH**-506	Wilms tumor protein (WT1)	P19544
		26-**HNMH**-29	RQCD1 protein (RQCD1)	D5MQE1
		95-**HNMH**-98	Interleukin-33 (IL33)	O95760
	MGRDHSV (2%)	926-**MGRDH**-930	Dedicator of cytokinesis protein 2 (DOCK2)	Q92608
		994-**RDHSV**-998	Bromodomain adjacent to zinc finger domain 1A (BAZ1A)	Q9NRL2
		797-**LGRDHS**-802	Sortilin-related VPS10 domain containing receptor 3 (SORCS3)	Q9UPU3
		811-**GRNHSV**-816	Bone morphogenetic protein receptor type-2 precursor (BMPR-II)	Q13873
		116-**GREHSV**-121	Probable bifunctional dTTP/UTP pyrophosphatase/methyltransferase protein isoform 1 (ASMTL)	O95671
		479-**RDHSV**-483	Male-specific lethal 1 homolog isoform X1(MSL1)	Q68DK7
		476-**LGRDHS**-481	8-oxo-dGDP phosphatase (NUDT18)	Q6ZVK8
		377-**LGRDHS**-382	RNA binding motif protein, Y-linked, family 1, member A1 (RBMY1A1)	P0DJD3
Round III	MVRDHSV (88%)	6834-**MVRDH**-6838	Nesprin-1 (SYNE1)	Q8NF91
		346-**MIRDHEV**-352	Rho GTPase-activating protein 25 (ARHGAP25)	P42331
		1650-**MVVDHSV**-1656	Protein furry homolog (FRY)	Q5TBA9
		173-**VREHSV**-178	Kinesin-like protein KIF13B (KIF13B)	Q9NQT8
		472-**MVRQHS**-477	Zinc finger protein ZXDC (ZXDC)	Q2QGD7
		622-**VREHSV**-627	Protein FAM83G (FAM83G)	A6ND36
	YGKRLDA (4%)	947-**GKRLDA**-952	Bromodomain-containing protein 1 (BRD1)	O95696

		1337-**YGKRLE**-1342	Telomerase protein component 1 (TEP1)	Q99973
		429-**YGKRLKA**-435	ATP-dependent DNA helicase DDX11 (DDX11)	Q96FC9
		936-**YQKRLDA**-942	Rho guanine nucleotide exchange factor 11	O15085
		1783-**YGKRL**-1787	(ARHGEF11)	Q7Z408
		658-**YRKRLDA**-664	CUB and sushi domain-containing protein 2 (CSMD2)	Q49AG3
			Zinc finger BED domain-containing protein 5 (ZBED5)	
	TKSLAHT (2%)	327-**TKSLVAHT**-334	protein Mdm4 (MDM4)	O15151
		1020-**TSSLAHT**-1026	Connector enhancer of kinase suppressor of ras 2 isoform 1 (CNKSR2)	Q8WXI2
		2901-**TKALTHT**-2907	WD repeat-containing protein 87 (WDR87)	Q6ZQQ6
		531-**KNLAHT**-536	RAN binding protein 10 (RANBP10)	Q6VN20
		196-**TKALAH**-201	tRNA modification GTPase GTPBP3, mitochondrial (GTPBP3)	Q969Y2
		2483-**SLAHT**-2487; 4106-**SLLHT**-4110	Histone-lysine N-methyltransferase 2D (KMT2D)	O14686
		3784-**KSLAH**-3788; 954-**TKSL**-957	Microtubule-actin crosslinking factor 1 (MACF1)	Q9UPN3
		544-**SLAHT**-548; 1960-**KSLAH**-1964	Neuroblastoma-amplified sequence (NBAS)	A2RRP1
		152-**KSLAH**-156	Mitogen-activated protein kinase kinase kinase 14 (MAP3K14)	Q99558
		385-**SLAHT**-389	TBC1 domain family, member 2 (TBC1D2)	Q9BYX2
		163-**SLAHT**-167	DNA-binding protein RFX2 (RFX2)	P48378
		145-**KSLAH**-149; 348-**TKSL**-351	Serine/threonine-protein kinase PLK3 (PLK3)	Q9H4B4
	FPTHNMH (4%)	219-**FPTHN**-223	Coiled-coil domain-containing protein 153 (CCDC153)	Q494R4
		440-**FPPVCTHNM**-448	Glycogen [starch] synthase, muscle (GYS1)	P13807
		697-**PTHDM**-701	Cysteine--tRNA ligase (CARS)	P49589
		503-**HNMH**-506	Wilms tumor protein (WT1)	P19544
		26-**HNMH**-29	RQCD1 protein (RQCD1)	D5MQE1
		95-**HNMH**-98	Interleukin-33 (IL33)	O95760
	VHVAQGR (2%)	446-**VHVEQGR**-452	AMP deaminase 2 (AMPD2)	Q01433
		613-**IHVAQG**-618	Pericentriolar material 1 protein (PCM1)	Q15154
		273-**VHVAQ**-277	MHC class II regulatory factor RFX1 (RFX1)	P22670
		1264-**HVAQG**-1268	Biorientation of chromosomes in cell division protein 1-like 1 (BOD1L1)	Q8NFC6
		1107-**VHVAEG**-1112	Myosin light chain kinase (MYLK)	Q15746
	NQNASHY (2%)	102-**NQNASLY**-108	Protein FAM209B (FAM209B)	Q5JX69
		1304-**QHASHY**-1309	Zinc finger protein 609 (ZNF609)	O15014
		357-**NQDASH**-362	Testis-specific Y-encoded-like protein 2 (TSPYL2)	Q9H2G4
		737-**QNASH**-741	Manganese-transporting ATPase 13A1 (ATP13A1)	Q9HD20
		344-**QNASH**-348	Ras guanyl-releasing protein 3 (RASGRP3)	Q8IV61
		297-**QNASPHY**-303	Tyrosine-protein phosphatase non-receptor type 18 (PTPN18)	Q99952
		603-**NQNAS**-607	MAX gene-associated protein isoform 1 (MGA)	Q8IWI9
Round IV	MVRDHSV (100%)	6834-**MVRDH**-6838	Nesprin-1 (SYNE1)	Q8NF91
		346-**MIRDHEV**-352	Rho GTPase-activating protein 25 (ARHGAP25)	P42331
		1650-**MVVDHSV**-1656	Protein furry homolog (FRY)	Q5TBA9
		173-**VREHSV**-178	Kinesin-like protein KIF13B (KIF13B)	Q9NQT8
		472-**MVRQHS**-477	Zinc finger protein ZXDC (ZXDC)	Q2QGD7
		622-**VREHSV**-627	Protein FAM83G (FAM83G)	A6ND36

Supplementary Table 4. High frequency peptides from phage display bio-panning on the C-terminal fragment of recombinant RBM20 protein with acid elution and their corresponding protein mimics, matching motifs and UniprotKB accession numbers.

Round	Peptide (% Frequency)	Matching motif	Protein Mimic	UniprotKB Accession Number
Round I	TVNEGMT (86%)	651-**INEGMT**-656	Piwi-like protein 1 (PIWIL 1)	Q96J94
		36-**VNEGM**-40	Neurogenic locus notch homolog protein 2 (NOTCH2)	Q04721
		228-**VNEGM**-232	Probable cation-transporting ATPase 13A5 (ATP13A5)	Q4VNC0
		490-**TVTDGMT**-496	Protein sidekick-1 (SDK1)	Q7Z5N4
		647-**VTEGMT**-652	Cullin-9 (CUL9)	Q8IWT3
		1190-**VNAGMT**-1195	Dedicator of cytokinesis protein 9 (DOCK9)	Q9BZ29
	TVKEGMT (4%)	490-**TVTDGMT**-496	Protein sidekick-1 (SDK1)	Q7Z5N4
		647-**VTEGMT**-652	Cullin-9 (CUL9)	Q8IWT3
	TVNEGMR (2%)	36-**VNEGM**-40	Neurogenic locus notch homolog protein 2 (NOTCH2)	Q04721
		228-**VNEGM**-232	Probable cation-transporting ATPase 13A5 (ATP13A5)	Q4VNC0
		104-**TVSEGAMR**-111	MHC class II regulatory factor RFX1 (RFX1)	P22670
		136-**VNEGKKMR**-143	Interleukin-6 receptor subunit beta (IL6ST)	P40189
		478-**TVHEGLR**-484	Scm-like with four MBT domains protein 1 (SFMBT1)	Q9UHJ3
		56-**TVNEAASMR**-64	Insulin-like growth factor 1 receptor (IGF1R)	P08069
		27-**VNEGVR**-32	Intersectin-1 (ITSN1)	Q15811
	PVNEGMT (2%)	1189-**PVNAGMT**-1195	Dedicator of cytokinesis protein 9 (DOCK9)	Q9BZ29
		651-**INEGMT**-656	Piwi-like protein 1 (PIWIL 1)	Q96J94
		36-**VNEGM**-40	Neurogenic locus notch homolog protein 2 (NOTCH2)	Q04721
		228-**VNEGM**-232	Probable cation-transporting ATPase 13A5 (ATP13A5)	Q4VNC0
		67-**PVSEGM**-72; 79-**EGM**-81	Protein TANC2 (TANC2)	Q9HCD6
		462-**PVLEGMT**-468	Double-stranded RNA-specific adenosine deaminase (ADAR)	P55265
	MVRDHSV (2%)	6834-**MVRDH**-6838	Nesprin-1 (SYNE1)	Q8NF91
		346-**MIRDHEV**-352	Rho GTPase-activating protein 25 (ARHGAP25)	P42331
		1650-**MVVDHSV**-1656	Protein furry homolog (FRY)	Q5TBA9
		173-**VREHSV**-178	Kinesin-like protein KIF13B (KIF13B)	Q9NQT8
		472-**MVRQHS**-477	Zinc finger protein ZXDC (ZXDC)	Q2QGD7
		622-**VREHSV**-627	Protein FAM83G (FAM83G)	A6ND36
	TVNEEMT (2%)	2449-**TANEEMT**-2455; 710-**VNSKSEEMT**-718; 482-**TVNED**-486; 1060-**TVGEE**-1064	A-kinase anchor protein 9 (AKAP9)	Q99996
		2013-**VNQEMT**-2018	Small subunit processome component 20 homolog (UTP20)	O75691
		1248-**VNEEM**-1252	Calcium-dependent secretion activator 1 (CADPS)	Q9ULU8
	TVKDGMT (2%)	490-**TVTDGMT**-496	Protein sidekick-1 (SDK1)	Q7Z5N4
		200-**TVKDGKT**-206	60 kDa heat shock protein, mitochondrial (HSPD1)	P10809
		3192-**VKDGM**-3196	E3 SUMO-protein ligase (RanBP2)	P49792
		746-**KDGMT**-750	Ankyrin repeat domain-containing protein 50 (ANKRD50)	Q9ULJ7
		34-**TVRDGM**-39	Serine/threonine-protein kinase A-Raf (ARAF)	P10398
		318-**TVRDGM**-323	Aprataxin isoform e (APTX)	Q7Z2E3
		31274-**TVKDSM**-31279; 2209-**KDGM**-2212; 32514-**DGMT**-32517; 23840-**KDSMT**-23844; 26400-**KDSMT**-26404; 16559-**TVKDVGKT**-16566; 2324-**TVKD**-2327; 16404-**TVKD**-	Titin isoform IC (TTN)	Q8WZ42

		16407; 16704-**TVKD**-16707; 17107-**TVKD**-17110; 18678-**TVKD**-18681; 28416-**TVKD**-28419; 6397-**TEKDPMT**-6403; 26914-**VKDG**-26917; 30339-**DGM**-30341; 22069-**KDHMT**-22073; 35082-**VKSQMT**-35087		
Round II	TVNEGMT (72%)	651-**INEGMT**-656	Piwi-like protein 1 (PIWIL 1)	Q96J94
		36-**VNEGM**-40	Neurogenic locus notch homolog protein 2 (NOTCH2)	Q04721
		228-**VNEGM**-232	Probable cation-transporting ATPase 13A5 (ATP13A5)	Q4VNC0
		490-**TVTDGMT**-496	Protein sidekick-1 (SDK1)	Q7Z5N4
		647-**VTEGMT**-652	Cullin-9 (CUL9)	Q8IWT3
		1190-**VNAGMT**-1195	Dedicator of cytokinesis protein 9 (DOCK9)	Q9BZ29
	TVKEGMT (21%)	490-**TVTDGMT**-496	Protein sidekick-1 (SDK1)	Q7Z5N4
		647-**VTEGMT**-652	Cullin-9 (CUL9)	Q8IWT3
	TVNEGMA (4%)	36-**VNEGM**-40	Neurogenic locus notch homolog protein 2 (NOTCH2)	Q04721
		986-**VDEGMA**-991	IARS protein (IARS)	Q6P0M4
		228-**VNEGM**-232	Probable cation-transporting ATPase 13A5 (ATP13A5)	Q4VNC0
		1906-**NEGMA**-1910	Kalirin (KALRN)	O60229
		209-**NEGMA**-213	DNA repair protein RAD51 homolog 4 (RAD51D)	O75771
		151-**NEGMA**-155	Transcription elongation factor A protein-like 4 (TCEAL4)	Q96EI5
		170-**VSEGMA**-175	Protein-tyrosine kinase 2-beta (PTK2B)	Q14289
	TVNEGMR (2%)	36-**VNEGM**-40	Neurogenic locus notch homolog protein 2 (NOTCH2)	Q04721
		228-**VNEGM**-232	Probable cation-transporting ATPase 13A5 (ATP13A5)	Q4VNC0
		104-**TVSEGAMR**-111	MHC class II regulatory factor RFX1 (RFX1)	P22670
		136-**VNEGKKMR**-143	Interleukin-6 receptor subunit beta (IL6ST)	P40189
		478-**TVHEGLR**-484	Scm-like with four MBT domains protein 1 (SFMBT1)	Q9UHJ3
		56-**TVNEAASMR**-64	Insulin-like growth factor 1 receptor (IGF1R)	P08069
		27-**VNEGVR**-32	Intersectin-1 (ITSN1)	Q15811
	TVRDGMA (2%)	34-**TVRDGM**-39	Serine/threonine-protein kinase A-Raf (ARAF)	P10398
		4649-**VREGMA**-4654	E3 ubiquitin-protein ligase HERC2 (HERC2)	O95714
		152-**VREGMA**-157	Cyclin-A1 (CCNA1)	P78396
		203-**RDGMA**-207	Beta-spectrin (HSpTB1)	Q71VG1
		493-**TVRNSMA**	Unconventional myosin-IXa (MYO9A)	B2RTY4
Round III	MVKDHMA (27%)	47-**LVKNHMA**-53	Spermatogenesis-associated protein 7 (SPATA7)	Q9P0W8
		263-**MVIEHMA**-269	Thioredoxin reductase 1, cytoplasmic (TXNRD1)	Q16881
		167-**MVIEHMA**-173	Selenoprotein K (SELK)	A8K0M9
		459-**MVKDEM**-464	Protein argonaute-2 (AGO2)	Q9UKV8
		329-**MLEDHMA**-335	TBCC domain-containing protein 1(TBCCD1)	Q9NVR7
		1-**MVKNQM**-6	RNA-binding protein 28 (Rbm28)	Q9NW13
		6846-**MVRDHL**-6851	Nesprin-1 (SYNE1)	Q8NF91
	MVKDDMA (20%)	459-**MVKDEM**-464	Protein argonaute-2 (AGO2)	Q9UKV8
		922-**MVKDD**-926	Phosphatidylinositol 4,5-bisphosphate 3-kinase catalytic subunit alpha isoform (PIK3CA)	P42336
		399-**VKDDM**-403	Protein argonaute-2 (AGO1)	Q9UL18
		324-**MVKDD**-328	Tubulin polyglutamylase TTLL11 (TTLL11)	Q8NHH1
		334-**MVKDD**-338	Intracellular hyaluronan-binding protein 4 (HABP4)	Q5JVS0
		627-**MVVNGKDDM**-635	Gamma-adducin (ADD3)	Q9UEY8
	MVKDHIA (12%)	376-**MIKEHI**-381	Importin-5 (IPO5)	O00410
		167-**VKDHI**-171	Cytokine receptor-like factor 3 (CRLF3)	Q8IUI8
		796-**MTKDQIA**-802	Protein FAM13A (FAM13A)	O94988
		1028-**MIKDQI**-1033	Cytoplasmic dynein 2 heavy chain 1 (DYNC2H1)	Q8NCM8
		414-**MVKEH**-418	Rap guanine nucleotide exchange factor 2 (RAPGEF2)	Q9Y4G8
	MVKDDMT (6%)	459-**MVKDEMT**-465	Protein argonaute-2 (AGO2)	Q9UKV8

	922-**MVKDD**-926	Phosphatidylinositol 4,5-bisphosphate 3-kinase (PI3K)	P42336
	324-**MVKDD**-328	Tubulin polyglutamylase TTLL11 (TTLL11)	Q8NHH1
	334-**MVKDD**-338	Intracellular hyaluronan-binding protein 4 (HABP4)	Q5JVS0
TVNDGMT (2%)	490-**TVTDGMT**-496	Protein sidekick-1 (SDK1)	Q7Z5N4
	42-**NDGMT**-46	1-phosphatidylinositol 4,5-bisphosphate phosphodiesterase delta-4 (PLCD4)	Q9BRC7
	20-**VSDGMT**-25	Helicase SRCAP (SRCAP)	Q6ZRS2
	1190-**VNAGMT**-1195	Dedicator of cytokinesis protein 9 (DOCK9)	Q9BZ29
	329-**TVNDG**-333	Advillin (AVIL)	O75366
MARDQMA (2%)	1-**MSQDQMA**-7	Zinc finger protein 324A isoform X1 (ZNF324)	O75467
	432-**MARDQ**-436	Apolipoprotein B-100 precursor, partial (APOB)	P04114
	236-**RDQMA**-240	Sarcoplasmic/endoplasmic reticulum calcium ATPase 1 (ATP2A1)	O14983
	264-**MACPRDQM**-271	Transcription regulator protein BACH2	Q9BYV9
	204-**RDQMA**-208; 670-**ARAIMA**-675	Catenin alpha-1 (CTNNA1)	P35221
	287-**AREQMA**-292	Zinc finger protein 64 (ZFP64)	Q9NTW7
	346-**MAEIRDQM**-353	Lamin-B1 (LMNB1)	P20700
	1256-**MSMDQMA**-1262	Protein PRRC2C (PRRC2C)	Q9Y520
MVNDHMT (2%)	13-**VNGHMT**-18	Retinoic acid receptor beta (RARB)	P10826
	754-**MVEEHM**-759	Structural maintenance of chromosomes protein 6 (SMC6)	Q96SB8
	459-**MVKDEMT**-465	Protein argonaute-2 (AGO2)	Q9UKV8
	252-**VNSHMT**-257	CDKN2A-interacting protein (CDKN2AIP)	Q9NXV6
MVKDHMV (2%)	844-**KDHMV**-848	Unhealthy ribosome biogenesis protein 2 homolog (URB2)	Q14146
	257-**KDHMV**-261	H/ACA ribonucleoprotein complex subunit DKC1	O60832
	177-**KDHMV**-181	(DKC1)	Q8NB15
	459-**MVKDEM**-464; 135-**EHMV**-138	Zinc finger protein 511 (ZNF511) Protein argonaute-2 (AGO2)	Q9UKV8
	1-**MVKNQM**-6		O15318
	473-**IKEHMV**-478	DNA-directed RNA polymerase III subunit RPC7 (POLR3G) Chromatin assembly factor 1 subunit A (CHAF1A)	Q13111
MVRDHMV (2%)	6846-**MVRDHL**-6851; 7127-**DHMV**-7130	Nesprin-1 (SYNE1)	Q8NF91
	6 -**MTRDHM**-11	Dual specificity tyrosine-phosphorylation-regulated kinase 2 (DYRK2)	Q92630
	515-**VRDHM**-519	zinc finger MYM-type protein 2 (ZMYM2)	Q9UBW7
	1-**MPRDHM**-6	Methyltransferase-like protein 8 (METTL8)	Q9H825
	128-**VRDNMV**-133	Apoptosis-inducing factor 1, mitochondrial (AIFM1)	O95831
	60-**VRDHLV**-65	Glycogen phosphorylase, liver form (PYGL)	P06737
	459-**MVKDEMT**-465	Protein argonaute-2 (AGO2)	Q9UKV8
	72-**MVEDEM**-77	RING finger protein 10 (RNF10)	Q8N5U6
	28-**MVNQEM**-33	HAUS augmin-like complex subunit 2 (HAUS2)	Q9NVX0
	507-**NDEMT**-511	NACHT, LRR and PYD domains-containing protein 10 (NLRP10)	Q86W26
	56-**MVADEM**-61	DNA annealing helicase and endonuclease ZRANB3 (ZRANB3)	Q5FWF4
	181-**MVSDDM**-186	Mediator of RNA polymerase II transcription subunit 18 (MED18)	Q9BUE0
	1638-**MVNPEM**-1643	TPR and ankyrin repeat-containing protein 1 (TRANK1)	O15050
	344-**INDEM**-348	Protein mono-ADP-ribosyltransferase PARP14 (PARP14)	Q460N5
	19-**MVSDGMT**-25	Helicase SRCAP (SRCAP)	Q6ZRS2
	2013-**VNQEMT**-2018; 1813-**VNDE**-1816	Small subunit processome component 20 homolog (UTP20)	O75691
	326-**MIDEDMT**-332	Integrin-linked protein kinase (ILK)	Q13418

MVNDEMT (2%)	459-**MVKDEMT**-465	Protein argonaute-2 (AGO2)	Q9UKV8
	72-**MVEDEM**-77	RING finger protein 10 (RNF10)	Q8N5U6
	28-**MVNQEM**-33	HAUS augmin-like complex subunit 2 (HAUS2)	Q9NVX0
	507-**NDEMT**-511	NACHT, LRR and PYD domains-containing protein 10 (NLRP10)	Q86W26
	56-**MVADEM**-61	DNA annealing helicase and endonuclease ZRANB3 (ZRANB3)	Q5FWF4
	181-**MVSDDM**-186	Mediator of RNA polymerase II transcription subunit 18 (MED18)	Q9BUE0
	1638-**MVNPEM**-1643	TPR and ankyrin repeat-containing protein 1 (TRANK1)	O15050
	344-**INDEM**-348	Protein mono-ADP-ribosyltransferase PARP14 (PARP14)	Q460N5
	19-**MVSDGMT**-25	Helicase SRCAP (SRCAP)	Q6ZRS2
	2013-**VNQEMT**-2018; 1813-**VNDE**-1816	Small subunit processome component 20 homolog (UTP20)	O75691
	326-**MIDEDMT**-332	Integrin-linked protein kinase (ILK)	Q13418
MVNDGMT (2%)	19-**MVSDGMT**-25	Helicase SRCAP (SRCAP)	Q6ZRS2
	42-**NDGMT**-46	1-phosphatidylinositol 4,5-bisphosphate phosphodiesterase delta-1 (PLCD1)	P51178
	92-**MVNDG**-96	Glutathione S-transferase P (GSTP1)	P09211
	985-**MVDEGM**-990	Isoleucine--tRNA ligase, cytoplasmic (IARS)	P41252
	459-**MVKDEMT**-465	Protein argonaute-2 (AGO2)	Q9UKV8
	244-**MVNSGM**-249	Serine/threonine-protein kinase RIO3 (RIOK3)	O14730
	91-**MVNHGM**-96	DNA-directed RNA polymerase III subunit RPC1 (POLR3A)	O14802
	491-**VTDGMT**-496	Protein sidekick-1 (SDK1)	Q7Z5N4
MVKDEMR (2%)	459-**MVKDEM**-464	Protein argonaute-2 (AGO2)	Q9UKV8
	1-**MVKNQMR**-7	DNA-directed RNA polymerase III subunit RPC7 (POLR3G)	O15318
	2036-**LVKNEMR**-2042; 2398-**MVRDE**-2402	Pericentrin (PCNT)	O95613
	72-**MVEDEM**-77	RING finger protein 10 (RNF10)	Q8N5U6
	157-**MVKDE**-161	Mothers against decapentaplegic homolog 4 (SMAD4)	Q13485
	124-**VKDEM**-128	Zinc finger protein 662 (ZNF662)	Q6ZS27
	391-**MVKDALR**-397	N-alpha-acetyltransferase 35, NatC auxiliary subunit (NAA35)	Q5VZE5
	901-**VKDELR**-906	NFX1-type zinc finger-containing protein 1 (ZNFX1)	Q9P2E3
	67-**MEKDEM**-72	TBC1 domain family member 16 (TBC1D16)	Q8TBP0
MVKDHIV (2%)	18-**IKDHIV**-23	Peroxisome proliferator-activated receptor gamma coactivator 1-alpha (PPARGC1A)	Q9UBK2
	376-**MIKEHI**-381	Importin-5 (IPO5)	O00410
MVRDEMG (2%)	327-**LVRDEMG**-333	Dynein heavy chain 1, axonemal (DNAH1)	Q9P2D7
	354-**MVRAVGDEMG**-363	Serine/threonine-protein kinase 4 (STK4)	Q13043
	459-**MVKDEM**-464	Protein argonaute-2 (AGO2)	Q9UKV8
	56-**MVADEMG**-62	DNA annealing helicase and endonuclease ZRANB3 (ZRANB3)	Q5FWF4
	2398-**MVRDE**-2402	Pericentrin (PCNT)	O95613
	2119-**MVRDE**-2123	Ubiquitin carboxyl-terminal hydrolase 24 (USP24)	Q9UPU5
	579-**VREEMG**-584	Protein flightless-1 homolog (FLII)	Q13045
	402-**VRDEM**-406	Protein argonaute-3 (AGO3)	Q9H9G7
	153-**MVRDERR**-159	Calumenin (CALU)	O43852
MVKDHMT (2%)	459-**MVKDEMT**-465	Protein argonaute-2 (AGO2)	Q9UKV8
	22069-**KDHMT**-22073; 6399-**KDPMT**-6403; 20187-**EHMT**-20190; 35082-**VKSQMT**-35087; 23840-**KDSMT**-23844; 26400-**KDSMT**-26404; 27086-**KDQM**-27089; 29583-**MVSEHL**-29588	Titin (TTN)	Q8WZ42

	1-**MVKNQM**-6	DNA-directed RNA polymerase III subunit RPC7 (POLR3G)	O15318
MVNDDMT (2%)	459-**MVKDEMT**-465	Protein argonaute-2 (AGO2)	Q9UKV8
	181-**MVSDDM**-186	Mediator of RNA polymerase II transcription subunit 18 (MED18)	Q9BUE0
	326-**MIDEDMT**-332	Integrin-linked protein kinase (ILK)	Q13418
	158-**NDDMT**-162	Anillin (ANLN)	Q9NQW6
	19-**MVSDGMT**-25	Helicase SRCAP (SRCAP)	Q6ZRS2
	1-**MVNKDM**-6	Serine/threonine-protein kinase Sgk1 (SGK1)	O00141
	59-**MINIDMT**-65	E3 SUMO-protein ligase EGR2 (EGR2)	P11161
MVKDDIA (2%)	922-**MVKDD**-926; 130-**MVKD**-133; 1017-**DDIA**-1020	Phosphatidylinositol 4,5-bisphosphate 3-kinase catalytic subunit alpha isoform (PIK3CA)	P42336
	324-**MVKDD**-328	Tubulin polyglutamylase TTLL11 (TTLL11)	Q8NHH1
	334-**MVKDD**-338	Intracellular hyaluronan-binding protein 4 (HABP4)	Q5JVS0
	70-**MVNKDDI**-76	sacsin isoform 1 (SACS)	Q9NZJ4
	642-**IKDDIA**-647	E3 ubiquitin-protein ligase Praja-2 (PJA2)	O43164
TYLSSTS (2%)	555-**TYLSST**-560; 860-**LSST**-863; 511-**SSTS**-514; 583-**SSTS**-586	Protein HEG homolog 1 (HEG1)	Q9ULI3
	1080-**TYLSSKS**-1086; 1760-**SSTS**-1763; 1073-**LSPTS**-1077	CDK5 regulatory subunit-associated protein 2 (CDK5RAP2)	Q96SN8
	565-**TYLAST**-570	Dipeptidyl peptidase 4 (DPP4)	P27487
	415-**TYLNST**-420	PHD finger protein 21A (PHF21A)	Q96BD5
MVKDEMM	162-**MVKDEM**-167	Protein argonaute-2 (AGO2)	Q9UKV8
	471-**KDEM**-475	Ras guanyl-releasing protein 3 (RASGRP3)	Q8IV61
	157-**MVKDE**-161	Mothers against decapentaplegic homolog 4 (SMAD4)	Q13485
	72-**MVEDEM**-77	RING finger protein 10 (RNF10)	Q8N5U6
	124-**VKDEM**-128	Zinc finger protein 662 (ZNF662)	Q6ZS27
	274-**IRDEMM**-279	Probable global transcription activator SNF2L1 (SMARCA1)	P28370
	67-**MEKDEML**-73		
	2472-**KDDMM**-2476; 218-**VKSQM**-222	TBC1 domain family member 16 (TBC1D16)	Q8TBP0
	810-**KDDMM**-814; 247-**KDDM**-250	Vacuolar protein sorting-associated protein 13A (VPS13A)	Q96RL7
	241-**VKTEMM**-246	LIM and calponin homology domains-containing protein 1 (LIMCH1)	Q9UPQ0
	1-**MVKNQM**-6; 19-**VKKVMM**-24	Zinc finger and BTB domain-containing protein 16 (ZBTB16)	Q05516
MVKDGMA (2%)	459-**MVKDEM**-464	Protein argonaute-2 (AGO2)	Q9UKV8
	39-**MVKDG**-43	E3 ubiquitin-protein ligase HERC2 (HERC2)	O95714
	3192-**VKDGM**-3196	E3 SUMO-protein ligase RanBP2 (RANBP2)	P49792
	19-**MVSDGM**-24	Helicase SRCAP (SRCAP)	Q6ZRS2
	986-**VDEGMA**-991	Isoleucine-tRNA ligase, cytoplasmic (IARS)	P41252
	163-**KDGMA**-167	Obscurin-like protein 1 (OBSL1)	O75147
MVKDEIA (2%)	459-**MVKDE**-463	Protein argonaute-2 (AGO2)	Q9UKV8
	157-**MVKDE**-161	Mothers against decapentaplegic homolog 4 (SMAD4)	Q13485
	39-**MVKDGEI-**45	E3 ubiquitin-protein ligase HERC2 (HERC2)	O95714
	106-**LVKDDIA**-112	Butyrophilin-like protein 9 (BTNL9)	Q6UXG8
	339-**IKDEIA**-344	Inhibitor of nuclear factor kappa-B kinase-interacting protein (IKBIP)	Q70UQ0
	33-**MTKDEI**-38	Heat-stable enterotoxin receptor (GUCY2C)	P25092
	472-**VKDEI**-476; 147-**MVADE**-151	Huntingtin (HTT)	P42858
	796-**MTKDQIA**-802	Protein FAM13A (FAM13A)	O94988
	97-**VKDEI**-101	Coiled-coil domain-containing protein 39 (CCDC39)	Q9UFE4
	390-**VKDEI**-394	Serine/threonine-protein phosphatase 2A regulatory subunit B'' subunit gamma (PPP2R3C)	Q969Q6

		359-**VKDEI**-363	Titin (TTN)	Q8WZ42
	TVKDGMA (2%)	3192-**VKDGM**-3196	E3 SUMO-protein ligase RanBP2 (RANBP2)	P49792
		34-**TVRDGM**-39	V-raf murine sarcoma 3611 viral oncogene-like protein isoform 2 (ARAF)	A0A0S2Z3F2
		318-**TVRDGM**-323	Aprataxin (APTX)	Q7Z2E3
		31274-**TVKDSM**-31279; 2209-**KDGM**-2212; 2324-**TVKD**-2327; 16404-**TVKD**-16407; 16559-**TVKD**-16562; 16704-**TVKD**-16707; 17107-**TVKD**-17110; 18678-**TVKD**-18681; 28416-**TVKD**-28419; 26914-**VKDG**-26917; 2188-**KDTMA**-2192; 30339-**DGM**-30341	Titin (TTN)	Q8WZ42
		163-**KDGMA**-167		
		163-**KDGMA**-167	Obscurin-like protein 1 (OBSL1)	O75147
		145-**KDGMA**-149	ETS-related transcription factor Elf-3 (ELF3)	P78545
	TVNEGMR (6%)	36-**VNEGM**-40	Neurogenic locus notch homolog protein 2 (NOTCH2)	Q04721
		228-**VNEGM**-232	Probable cation-transporting ATPase 13A5 (ATP13A5)	Q4VNC0
		104-**TVSEGAMR**-111	MHC class II regulatory factor RFX1 (RFX1)	P22670
		136-**VNEGKKMR**-143	Interleukin-6 receptor subunit beta (IL6ST)	P40189
		478-**TVHEGLR**-484	Scm-like with four MBT domains protein 1 (SFMBT1)	Q9UHJ3
		56-**TVNEAASMR**-64	Insulin-like growth factor 1 receptor (IGF1R)	P08069
		27-**VNEGVR**-32	Intersectin-1 (ITSN1)	Q15811
	MVRDHSV (2%)	6834-**MVRDH**-6838	Nesprin-1 (SYNE1)	Q8NF91
		346-**MIRDHEV**-352	Rho GTPase-activating protein 25 (ARHGAP25)	P42331
		1650-**MVVDHSV**-1656	Protein furry homolog (FRY)	Q5TBA9
		173-**VREHSV**-178	Kinesin-like protein KIF13B (KIF13B)	Q9NQT8
		472-**MVRQHS**-477	Zinc finger protein ZXDC (ZXDC)	Q2QGD7
		622-**VREHSV**-627	Protein FAM83G (FAM83G)	A6ND36
Round IV	TVKEGMT (2%)	2715-**VKEGM**-2719	Fibrocystin (PKHD1)	P08F94
		39-**VKEGM**-43	Synaptotagmin-16 (SYT 16)	Q17RD7
		273-**KEGMT**-277	Enoyl-CoA hydratase, mitochondrial (ECHS1)	P30084
		132-**VKEGM**-136	Peptidyl-prolyl cis-trans isomerase A (PPIA)	P62937
		647-**VTEGMT**-652	Cullin-9 (CUL9)	Q8IWT3
	TVKKGMT (2%)	239-**KKGMT**-243	Kinetochore-associated protein 1 (KNTC1)	P50748
		2-**VKKGM**-6	Exportin-6 (XPO6)	Q96QU8
		230-**VKKGM**-234	Inositol-trisphosphate 3-kinase B (ITPKB)	P27987
		332-**KKGMT**-336	Transient receptor potential cation channel subfamily V member 1 (TRPV1)	Q8NER1
		92-**VKKAMT**-97	Hepatocyte nuclear factor 4-alpha (HNF4)	P41235
		470-**TVKKEPHESLGMT**-482	Ligand of Numb protein X 2 (LNX2)	Q8N448
		1016-**VKKDMT**-1021	Rap guanine nucleotide exchange factor 6 (RAPGEF6)	Q8TEU7
		226-**TVKKEM**-231	Chromodomain-helicase-DNA-binding protein 9 (CHD9)	Q3L8U1
		657-**TVKTGM**-662	Synaptojanin-1 (SYNJ1)	O43426

CHAPTER IV

THE ROLE OF RBM20 IN LAMIN A/C-RELATED CARDIOMYOPATHIES

A. Abstract

Cardiomyopathies are among the leading causes of premature sudden death with more than 60 genes linked to them, including *LMNA* which codes for the nuclear lamina proteins lamin A/C, and *EMD* which codes for the inner nuclear membrane protein emerin. Recently, mutations in *RBM20* which codes for the muscle-specific splicing factor, RNA binding motif protein 20 (RBM20), have also been associated with familial cardiomyopathies. Studies have shown that lamin A/C regulates the expression and nuclear localization of several splicing factors, including matrin-3, a paralog to RBM20. Matrin-3 was also shown to interact with lamin A/C and this interaction was disrupted by myopathic lamin A/C mutation. We have previously shown that lamin A/C interacts with Rbm20 both *in vitro* and *in vivo*. However, the functional relationship between lamin A/C and Rbm20 has not been explored. Due to its muscle-specific function and implication in cardiomyopathy, we hypothesized that Rbm20 might contribute to the striated muscle phenotypes caused by most *LMNA* mutations. Accordingly, we aimed at investigating potential deregulations in RBM20 in the context of *LMNA* and *EMD* loss and/or mutation. We used mouse embryo fibroblast (MEF) lines derived from mice lacking the expression of lamin A/C ($Lmna^{-/-}$) or emerin ($Emd^{-/y}$) which have an Emery-Dreifuss Muscular Dystrophy (EDMD) phenotype, or mice expressing the *Lmna* N195K homozygote mutation ($Lmna^{N195K/N195K}$) which have the Dilated Cardiomyopathy (DCM) phenotype in addition to

muscular dystrophy[368]. Real-Time PCR quantification, Western Blot analysis and immunofluorescence staining were performed on these cell lines versus WT controls. Rbm20 showed a significant reduction in transcript and protein levels in all three mutant MEFs, while there was no change in its subcellular localization (Dana Sedki, unpublished data). We also tested *Lmna* null MEFs that were transduced by retroviral infection to re-express the *Lmna* WT or different mutant forms that result in EDMD (E358K, L530P). The reduction in *Rbm20* was reversed, both at the transcript and protein levels, upon re-expression of *Lmna* confirming the direct effect of lamina disruption on the expression of Rbm20. We validated these findings, *in vivo*, whereby a decrease in the protein expression levels of Rbm20 was noted in both the left ventricles and Tibialis Anterior (TA) muscles of $Lmna^{-/-}$ and $Lmna^{N195K/N195K}$ mice of both genders. In the $Lmna^{H222P/H222P}$ mouse model, which closely resembles human disease in terms of late onset EDMD and DCM, a significant decrease in Rbm20 transcript levels was noted in the left ventricles but not TA muscles of both genders. The reduction in Rbm20 was associated with a decrease in the N2B isoform of titin, a splicing target of Rbm20, in female mice only. Despite the decrease in Rbm20 expression at the transcript level, no significant change was noted at the protein level. Finally, we tested whether Rbm20 expression in $Lmna^{-/-}$ and $Lmna^{N195K/N195K}$ MEFs can be restored by insulin, an upstream regulator of Rbm20 through the PI3K-AKT-mTOR signaling pathway. While insulin treatment significantly increased AKT phosphorylation, it failed to upregulate Rbm20 transcript and protein levels in $Lmna^{-/-}$ and $Lmna^{N195K/N195K}$ MEFs, suggesting a defect in the PI3K-AKT-mTOR pathway downstream AKT phosphorylation. Our findings highlight the implication of Rbm20 in lamin A/C

cardiomyopathies and put it forward as an appealing target for pharmacological intervention.

B. Introduction

Lamins are nuclear intermediate filaments mainly localized to the nuclear envelope, and to a lesser extent in the nucleoplasm[28,66]. A-type lamins together with B-type lamins are the major components of the nuclear lamina, a protein meshwork underlying the inner nuclear membrane. The most common A-type lamins, lamins A and C are encoded by the *LMNA* gene, while the major B-type lamins, lamin B1 and B2 are encoded by the *LMNB1* and *LMNB2* genes, respectively[29]. Assembly of lamins into higher order filaments at the nuclear envelope, allows them to impart structural and mechanical support to the nucleus[42,369]. Moreover, the interaction of lamins with several nuclear envelope proteins, transcription factors, DNA-binding proteins as well as chromatin, allows them to have a plethora of functions that range from structural organization, transcriptional regulation as well as DNA replication and repair[41]. As such, it is not surprising that mutations in the *LMNA* gene are responsible for a wide range of human diseases collectively called Laminopathies, that are usually manifested as tissue-specific disorders, yet in some cases as multisystem diseases[107,108]. Tissues affected by *LMNA* mutations include muscular, nervous and adipose tissues[112]. However, most of the over 450 *LMNA* mutations (http://www.umd.be/LMNA/) result in striated muscle disorders such as Emery Dreifuss Muscular Dystrophy (EDMD) and Dilated Cardiomyopthay (DCM)[104,106,370]. EDMD is a slowly progressive muscle weakening and wasting disorder that primarily affects skeletal muscles and is often associated with joint deformities, rigid spine and cardiomyopathy[371].

DCM is a cardiac muscle disease characterized by ventricular dilation and conduction system defects in the absence of skeletal muscle involvement[106]. It remains unclear how mutations in the ubiquitously expressed *LMNA* gene result in tissue-specific phenotypes, particularly affecting striated muscle tissues. Evidence from previous studies has pointed out to the importance of lamin A/C interactions with nuclear envelope proteins, such as emerin, and their implications in the pathogenesis of muscle-specific effects in the presence of *LMNA* mutations. For instance, a recent study has shown that lamin A/C mutations cause mislocalization of emerin from the inner nuclear membrane[171]. Through a mechanism involving disturbed actin polymerization, emerin displacement resulted in decreased nuclear localization of Megakaryocytic Acute Leukemia (MKL1) and impaired MKL1/SRF signaling. The importance of this finding is illustrated by the role that Serum Response Factor (SRF) and its cofactor MKL1 play in regulating several muscle-specific genes, thus providing mechanistic insight into the muscle-specific effects of *LMNA* mutations[372]. Furthermore, lamin A/C mutations have been shown to disrupt lamin A/C-nesprin interactions thereby causing alterations in the Linker of Nuceloskeleton and Cytoskeleton (LINC) complex, nucleo-cytoskeletal coupling and mechanotransduction[72,150,373]. Similarly, mutations in nesprin and other LINC complex components such as SUN (Sad-1/UNC-84) proteins and emerin also disrupt nucleo-cytoskeletal coupling and mechanotransduction[374]. The implications of undermined nucleo-cytoskeletal coupling in the emergence of muscle-specific disease could be attributed to altered nuclear morphology/increased nuclear fragility which might result in nuclear and cellular damage and/or altered mechanosensitive gene expression[25,150]. The effects of such defects are likely most pronounced in mechanically stressed tissues such as the heart and skeletal muscles. Supporting these

mechanistic insights are findings linking mutations in nesprin1/2, SUN1/2 and emerin to EDMD and/or DCM[16,351,375]. Despite the important mechanistic insights provided by these and other studies, a comprehensive understanding of the pathogenesis of laminopathies remains lacking, which justifies the lack of an effective treatment. Accordingly, studying other Lamin A/C interacting partners that are similarly affected by lamin A/C mutations would not only provide a deeper mechanistic insight into the disease pathogenesis but might also reveal potential drug targets. As such we screened for protein candidates whose mutations cause striated muscle disease. We refined our search to DCM-causing proteins characterized by nuclear localization and muscle-specific expression. A culprit that met these criteria was the alternative splicing factor RNA Binding Motif Protein 20 (RBM20). RBM20 is a nuclear RNA binding protein that is mainly expressed in striated muscle with the highest amounts in cardiac muscle[208]. Titin is the most prominent splicing target of RBM20[208,212]. Alternative splicing of titin results in many protein isoforms, the most common are N2B and N2BA isoforms[217]. N2B isoform is short and rigid while N2BA isoforms are longer and more compliant[218]. The relative ratio of short to long titin isoforms is developmentally regulated and is a determining factor of myocardial passive stiffness[218,219]. Cardiac N2BA is predominantly expressed during fetal life; however, N2B isoform becomes mainly expressed within few weeks after birth to adapt to the increasing filling pressure[218,220,221]. Mutations in RBM20 have been associated with DCM at a rate of 3% of all DCM cases, thus making it one of the most commonly affected genes in DCM[181]. Furthermore, DCM-associated *RBM20* mutations ranked first for the youngest mean age of heart transplantation and correlated with advanced disease[195,376]. Remarkably, DCM-associated RBM20 loss or mutation caused a switch in the expression of titin isoforms, in

favor of the longer and more compliant isoforms[208]. Both *LMNA* and *RBM20* mutations often caused phenotypically similar progressive DCM with conduction system defects, arrhythmias and poor outcome[376]. Moreover, lamin A/C has been shown to interact with various splicing factors including matrin-3, a paralog to Rbm20. LaminA/C-matrin-3 interaction was disrupted by myopathic *LMNA* mutations[377]. In addition, lamin A/C knock down resulted in reduced expression levels and disrupted nuclear organization of matrin-3 as well as other splicing activators and small nuclear ribonucleoproteins (snRNPs)[378].

We have previously shown that lamin A/C interacts with Rbm20 both *in vitro* and *in vivo* (Unpublished Data), but the implications of this interaction are not known. We sought to gain a better understanding of the mechanisms by which *LMNA* mutations result in the striated muscle phenotypes of EDMD and DCM by investigating potential deregulations in RBM20 in the context of *LMNA* cardiomyopathies. Rbm20 showed a significant reduction in transcript and protein levels in $Lmna^{-/-}$, $Emd^{-/y}$ and $Lmna^{N195K/N195K}$ MEFs, while there was no change in its subcellular localization (Dana Sedki, unpublished data). The reduction in *Rbm20* was reversed, both at the transcript and protein levels, upon re-expression of *Lmna* confirming the direct effect of lamina disruption on the expression of RBM20. A decrease in the protein expression levels of Rbm20 was also noted in the left ventricles and TA muscle tissue from $Lmna^{-/-}$ and $Lmna^{N195K/N195K}$ mice of both genders. On the other hand, $Lmna^{H222P/H222P}$ mice of both genders showed a significant decrease in Rbm20 transcript levels in the left ventricles but not the TA muscle. This decrease was associated with a reduction in the N2B isoform of titin in female mice only. Surprisingly, no significant change was noted in Rbm20 protein levels in $Lmna^{H222P/H222P}$ mice of both genders. Finally, insulin treatment failed to upregulate Rbm20 transcript and protein levels

despite AKT activation in *Lmna*$^{-/-}$ and *Lmna*$^{N195K/N195K}$ MEFs, suggesting a defect in the PI3K-Akt-mTOR signaling pathway downstream AKT phosphorylation. Our findings provide a better insight into the mechanisms by which *LMNA* mutations result in EDMD and DCM and demonstrate, for the first time, the implication of Rbm20 in lamin A/C cardiomyopathies.

C. Materials and Methods

1. Cell Lines

Immortalized mouse embryonic fibroblasts (MEFs) were a kind gift from Dr. Jan Lammerding (Cornell, NY). MEFs were isolated from *Lmna* knockout (*Lmna*$^{-/-}$), *Lmna*$^{N195K/N195K}$ (*Lmna* N195K) and emerin deficient (*EMD*$^{-/y}$) mice as well as from wild-type (WT) control mice[276,286]. While *Lmna*$^{-/-}$ and *EMD*$^{-/y}$ are previously described mouse models of EDMD[276,286], *Lmna* N195K is an established mouse model of DCM[164]. Additionally, a panel of lamin A/C-deficient MEF cell lines retrovirally transfected to express the *LMNA* WT or mutant forms that result in EDMD (E358K, L530P) were kindly provided by Dr. Jan Lammerding (Cornell, NY). Briefly, WT or mutant lamin A variants, E358K and L530P were cloned into a bicistronic retroviral vector (pRetroX-IRES-ZsGreen1, Clontech). The expression vectors were then transfected into 293GPG retroviral packaging cell line (kind gift from Richard C. Mulligan, Harvard Medical School, Massachusetts) based on the manufacturer specifications. ZsGreen1 retroviral vector without lamin A insert was used to generate the mock control cells. Afterwards, viral supernatants were filtered and retrovirally infected into lamin A/C-deficient MEFs. The efficiency of gene transfer was assayed 5 days after retroviral infection by flow cytometric

probing of ZsGreen1 levels. Following cell sorting, genetically modified cells that expressed the *LMNA* WT were labelled *Lmna-/-* DJ1-WT-S and those that expressed the mutant forms of lamin A were termed *Lmna-/-* DJ1-E358K-S and *Lmna-/-* DJ1-L530P-S in comparison to their mock control *Lmna-/-* DJ1-mock-S.

2. Cell Culture

All cells were cultured in 37°C and 5% CO2 humidified incubators. Adherent MEFs were maintained in Dulbecco's Modified Eagle's Medium DMEM-AQ media (D0819, Sigma-Aldrich), supplemented with 1% penicillin-streptomycin (DE17-602E, Lonza), 10% Fetal bovine serum (FBS) (F9665, Sigma-Aldrich) and 1% sodium pyruvate (S8636, Sigma-Aldrich). Monolayer cells were propagated at 80% confluence. 1X Phosphate Buffered Saline without Ca and Mg (PBS) (17-517Q, Lonza) and 1X Trypsin (Cat Number, Lonza) were used for rinsing and detaching cells, respectively. Cells were visualized using a standard phase contrast microscope (Olympus microscope, Axiovert 200, Zeiss).

3. Animals, Tissue Harvest & Tissue Lysate Preparation

All animal work was conducted in the lab of Dr. Jan Lammerding (Cornell, NY) in accordance to the Cornell University Institutional Animal Care and Use Committee (IACUC). Mice were anesthesized with isofluorane and euthanized by cervical dislocation. All mice were harvested post disease onset. *Lmna* null mice and litter mate controls were harvested between 4 and 5 weeks of age. *Lmna* N195K mice and litter mate controls were harvested between 10 and 15 weeks of age. *Lmna* H222P mice and litter mate controls were

harvested at 28 weeks of age. Hearts were harvested, washed in PBS until blood was cleared, cut into right and left ventricles and snap frozen in liquid nitrogen. Tibialis anterior (TA) muscles were harvested and snap frozen in liquid nitrogen. Heart and TA tissues were stored at –80°C until needed. Tissue lysates were prepared by homogenizing 10 µg of tissues in 500 µl RIPA lysis buffer supplemented with phosphatase (PhosSTOP, Roche) and protease inhibitors (complete EDTA-free, Roche). The TissueLyser II from Qiagen and metallic beads from McMaster-Carr were used for tissue homogenization. Tissues isolated from a single mouse were considered a single replicate.

4. RNA Extraction and Reverse Transcription

RNA was extracted from MEF cell lines using the RNA isolation RNeasy kit (74104, Qiagen) according to the manufacturer's instructions. RNA samples were quantified and assessed for purity and integrity using the Nanodrop Spectrophotometer (Thermonanodrop 2000C, Central Research Science Lab (CRSL) facility, AUB). 1µg of total RNA was reverse transcribed into cDNA using the iScript cDNA Synthesis Kit (170-8891, Bio-Rad) following the manufacturer's protocol. Briefly, each RNA sample was mixed with 4µl of the 5X iScript Reaction Mix, 1µl of iScript reverse transcriptase and adjusted to a total volume of 20µl with nuclease free sterile water (Amresco). Reverse transcription was carried out in the DNA engine machine (Peltier thermal cycler, Bio-Rad) following a protocol that consists of 5min annealing step at 25°C, 30min extension step at 42°C and a final 5min step at 85°C to heat inactivate the iScript reverse transcriptase. cDNA samples were stored at -20°C.

For animal tissues, tissue lysates for RNA extraction were prepared by homogenizing 10 µg of tissues in 500 µl RIPA lysis buffer supplemented with phosphatase (PhosSTOP, Roche) and protease inhibitors (complete EDTA-free, Roche). The TissueLyser II from Qiagen and metallic beads from McMaster-Carr were used for tissue homogenization. Tissues isolated from a single mouse were considered a single replicate.

5. Quantitative Real Time PCR

Real-Time PCR quantification of gene expression was performed using the iQ SYBR Green Supermix (S4438, Sigma-Aldrich) with specific primer pairs for each gene (Table 5). Unless otherwise indicated, primer sequences were obtained from the MGH/Harvard Medical School Primer Bank Database (www.pga.mgh.harvard.edu/primerbank) which is a database of previously validated primers. cDNA samples and primers were diluted in nuclease free water into 1:20 and 1:10 working dilutions, respectively. Subsequently, 4µl of cDNA were added to 1µl of each of the forward and reverse primers, 6.5µl of nuclease free water and 12.5µl of the iQ SYBR Green Supermix to a final volume of 25µl. The Real Time PCR reaction was performed using the c-1000 Touch thermal cycler (Bio-Rad, CRSL facility, AUB). The protocol consisted of an initial heating step to 50°C for 2min followed by a DNA denaturation or melting step at 95°C, an annealing step at 60°C for 1min and an extension step at 72°C for 30sec. This process was repeated for 40 cycles before the final extension step at 72°C for 10min. Experimental results were recorded and analyzed using the Bio-Rad CFX Manager Software.

Table 5. Primer pairs used for Real Time PCR quantification of Rbm20 and titin isoforms.

	Forward Primer (5'-3')	Reverse Primer (5'-3')	Source
Rbm20 (mouse)	GGCCAAAACAAGCCCGATATT	CCCTGTCTGAGGTAGGCTCT	Sigma
Titin N2BA (mouse)	CTCCAGCCAAAGACGGTGG	GCAGTGAGAAGTTTATCGGGTTC	Pair 1 MGH
Titin N2BA (mouse)	GGCATCTCCAGGACGTTACTC	TTCACTCTGCCTTGAGGTTTAAG	Pair 2 MGH
Titin N2BA (mouse) Muscle specific	GCCGGCACCTAAAGAAGTTG	GTGGGGCTTCTGGCTTTTTG	Pair 3 Self-designed
Titin N2B (mouse) Heart Specific	GGAGTACACCTGCAAAGCCT	TGCGGCTTAGGTTCAGGAAG	Self-designed

6. Western Blot Analysis

MEF cell lines were lysed in RIPA lysis buffer (R-0278, Sigma-Aldrich) supplemented with Protease Inhibitor Cocktail (P-8340, Sigma-Aldrich) and phosphatase inhibitors (22020009-1, Bioworld). Protein quantification was performed using the Optiblot Bradford Reagent (ab119216, Abcam) and the SpectraMax ascent software (Multiskan EX, Thermo lab Systems). 15-30 µg of proteins were separated using 10% or 12% Tris-glycine polyacrylamide gels in Tris-glycine running buffer. The gels and buffers were prepared according to standard recipes and SDS-page was performed according to standard protocols. Proteins were transferred to a polyvinylidene fluoride (PVDF) membrane (162-0177, Bio-Rad). membrane at 4˚C for 2.5hrs at a voltage of 100 V. Membranes were blocked using 5% milk in phosphate-buffered saline containing 0.1% Tween-20. Primary antibodies (Table 6) were diluted in 1% milk in phosphate-buffered saline containing 0.1%

Tween-20 and incubated overnight at 4˚C. HRP-conjugated secondary antibodies (ab97023, ab97110, abcam; 111-035-144, Jackson Immunoresearch) were used at a dilution of 1:5000. Protein bands were detected using ECL western blotting substrate kit (ab65628, abcam) and visualized using the Molecular Imager Chemidoc XRS System (170-8070, Bio-Rad) and the Quantity One 1-D Analysis Software (170-9600). Band intensities were quantified using the Image J software. Western blot analysis of animal tissue lysates was performed in the lab of Dr. Jan Lammerding (Cornell, NY). Protein quantification was performed using Bio-Rad Protein Assay Dye and 20-30 μg of protein lysates were separated using a 4-12% Bis-Tris polyacrylamide gel and MOPS running buffer following a standard SDS-Page protocol. Proteins were transferred to a polyvinylidene fluoride (PVDF) membrane at 4˚C for 2.5hrs at 100 V. Membranes were blocked using 3% BSA in tris-buffered saline containing 0.1% Tween-20. Primary antibodies (Table) were diluted in the same blocking solution and incubated for either 1hr at room temperature or overnight at 4˚C. Protein bands were detected using either IRDye 680LT or IRDye 800CW (LI-COR) secondary antibodies, imaged on an Odyssey® CLx imaging system (LI-COR) and analyzed in Image Studio Lite (LI-COR).

Table 6. List of used antibodies, vendors and catalog numbers.

Antibody	Vendor	Catalog Number
Rbm20	Novus Biologicals	NBP2-27509
H3	abcam	ab195277
Tubulin Alpha	Hybridoma Bank	4A1
Tubulin Betta	Hybridoma Bank	E7
GAPDH (14C10)	Cell Signaling	2118
p-AKT (S473) (D9W9U)	Cell Signaling	12694S
AKT (2H10)	Cell Signaling	2967S

7. Statistical Analysis

All data is expressed as mean ± standard error of the mean (SEM) from at least 3 independent experiments per group. Statistical analysis was performed using IBM SPSS Statistics 20. Comparisons between two groups were carried out using two-tailed student t-test, while comparisons of several groups to a control were performed using one-way ANOVA followed by 2-sided Dunnett post hoc test. * denotes $p \leq 0.05$, ** denotes $p \leq 0.01$, and *** denotes $p \leq 0.001$.

D. Results

1. Rbm20 Transcript Levels in Lamin A/C Knockout and Retrovirally Transduced MEF Cell Panel

Previous results from our lab showed that Rbm20 is significantly downregulated both at the transcript and protein levels in MEFs derived from mice lacking the expression of lamin A/C (*Lmna*$^{-/-}$) or emerin (*Emd*$^{-/y}$) which have the EDMD phenotype, or mice expressing the *Lmna* N195K homozygote mutation (*Lmna*$^{N195K/N195K}$) which have the DCM phenotype[379]. To assess if this reduction is a direct effect of lamina disruption by *Lmna* loss or mutation, Rbm20 transcript levels were assessed by qPCR in *Lmna*$^{-/-}$ MEFs versus WT MEFs and upon retroviral transfection of *Lmna*$^{-/-}$ MEFs by WT lamin A (*Lmna*$^{-/-}$ DJ1-WT-S) or different mutant lamin forms that cause EDMD (*Lmna*$^{-/-}$ DJ1-E358K-S and *Lmna*$^{-/-}$ DJ1-L530P-S) in comparison to *Lmna*$^{-/-}$ MEFs transduced with an empty vector (*Lmna*$^{-/-}$ DJ1-mock-S). Significant decrease in Rbm20 expression was observed in both *Lmna*$^{-/-}$ and *Lmna*$^{-/-}$ DJ1-mock-S MEFs in comparison to WT MEFs, whereby the mean fold change in

Rbm20 expression in *Lmna*$^{-/-}$ MEFs (0.16 ± 0.05) and *Lmna*$^{-/-}$ DJ1-mock-S MEFs (0.12 ± 0.04) was significantly lower than that in WT MEFs; *p=0.000* and *p=0.000* respectively in one-way ANOVA followed by 2-sided Dunnett t-test (Figure 25a), hence indicating a 6.3-fold and 8.3-fold decrease in Rbm20 expression respectively. On the other hand, significant increase in Rbm20 transcript levels was observed upon restoration of WT lamin A or lamin E358K mutant form, but not lamin L530P mutant form, whereby the mean fold change in Rbm20 expression in *Lmna*$^{-/-}$ DJ1-WT-S (1.97 ± 0.31) and *Lmna*$^{-/-}$ DJ1-E358K-S (1.96 ± 0.23) was significantly higher than that in *Lmna*$^{-/-}$ DJ1-mock-S; *p=0.043* and *p=0.045* respectively, hence indicating an approximate 2-fold increase in Rbm20 expression in both cell lines (Figure 25b). The results represent the mean fold change in Rbm20 expression relative to 18S ± SEM from six independent repeats; done in duplicates.

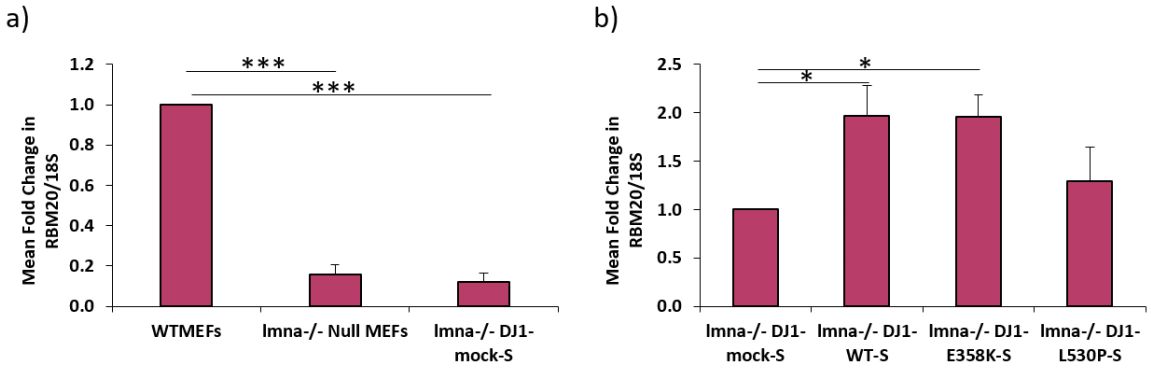

Figure 25. Rbm20 Transcript Levels in Lamin A/C Knockout MEFs and Retrovirally Transduced MEF Cell Panel.
Real-Time PCR quantification was performed in WT MEFs, lamin A/C knockout MEFs (*Lmna*$^{-/-}$ MEFs) and in MEF cell lines modified by retroviral transfection to re-express the *Lmna* WT or mutant forms that result in EDMD (E358K, L530P) & their mock control (*Lmna*$^{-/-}$ DJ1-mock-S). *(a)* Rbm20 transcript levels were significantly reduced in *Lmna*$^{-/-}$ MEFs relative to WT MEFs. Retroviral transfection by an empty vector did not have any

effect on the expression levels of Rbm20. *(b)* Re-expression of *Lmna* WT or the E358K mutant but not the L530P form significantly reversed the reduction in Rbm20 expression. Results represent mean fold change in relative Rbm20 expression normalized to 18S ± SEM of 6 independent experiments; done in duplicates (*p<0.05; ***p<0.001 by one-way Anova).

2. Rbm20 Protein Expression Levels in Lamin A/C Knockout and Retrovirally Transduced MEF Cell Panel

At the protein level, western blot analysis revealed a decrease in Rbm20 expression in both *Lmna*$^{-/-}$ null and *Lmna*$^{-/-}$ DJ1-mock-S MEFs in comparison to WT MEFs, as obtained by Image J densitometry quantification of Rbm20 protein bands corresponding to the high (122 KDa) and low molecular weight (75 KDa) isoforms (Figure 26). Significant decrease in the high molecular weight isoform was noted in both *Lmna*$^{-/-}$ null and *Lmna*$^{-/-}$ DJ1-mock-S MEFs in comparison to WT MEFs, whereby the mean fold change in *Lmna*$^{-/-}$ MEFs (0.5 ± 0.1) and *Lmna*$^{-/-}$ DJ1-mock-S MEFs (0.6 ± 0.1) was significantly lower than that in WT MEFs; $p=0.000$ and $p=0.001$ respectively in one-way ANOVA followed by 2-sided Dunnett t-test, hence indicating a 2-fold and 1.7-fold decrease in expression of the high molecular weight isoform respectively. A significant 1.7-fold decrease in the mean fold change was also noted in the low molecular weight isoform in *Lmna*$^{-/-}$ DJ1-mock-S MEFs in comparison to WT MEFs (0.6 ± 0.1; $p=0.035$). Although a 1.25-fold decrease was obtained in the low molecular weight isoform in *Lmna*$^{-/-}$ MEFs (0.8 ± 0.1) in comparison to WT MEFs, this decrease was not significant ($p=0.431$) (Figure 26b). Significant increase in the protein expression levels of the high molecular weight isoform of Rbm20 was observed upon restoration of WT lamin A (1.4 ± 0.2; $p=0.035$) but

not lamin E358K (1 ± 0.1; *p=0.999*) or lamin L530P (1 ± 0.1; *p=0.992*) mutant forms (Figure 26c). Thus, the high molecular weight isoform of Rbm20 increased by 1.4 folds in *Lmna*$^{-/-}$ DJ1-WT-S. A slight nonsignificant increase in the low molecular weight isoform of Rbm20 was observed upon restoration of WT lamin A (1.3 ± 0.1) and lamin E358K mutant (1.3 ± 0.2) but not lamin L530P mutant (1.1 ± 0.2) form (Figure 26c). The results represent the mean fold change in Rbm20 expression relative to GAPDH ± SEM from seven independent repeats.

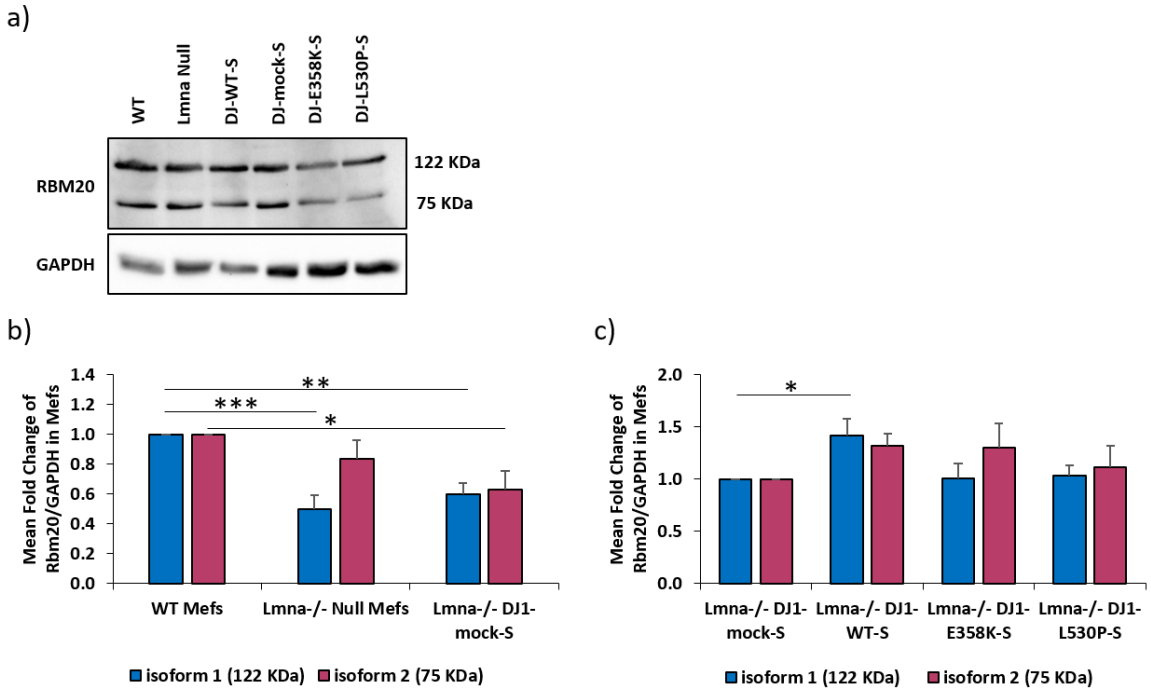

Figure 26. Western Blot Analysis of Rbm20 Protein Expression Levels in Lamin A/C Knockout MEFs and Retrovirally Transduced MEF Cell Panel.
(a) Western blot analysis was performed in WT MEFs, Lamin A/C knockout MEFs (*Lmna*$^{-/-}$ MEFs) and in MEF cell lines modified by retroviral transfection to re-express the *Lmna* WT or mutant forms that result in EDMD (E358K, L530P) & their mock control (*Lmna*$^{-/-}$ DJ1-mock-S). *(b)* Protein expression levels of the 122KDa and the 75KDa isoforms of Rbm20 were reduced in *Lmna*$^{-/-}$ MEFs and *Lmna*$^{-/-}$ DJ1-mock-S relative to WT MEFs.

Significant reduction in the 122KDa isoform was observed in *Lmna*$^{-/-}$ Null MEFs and in both isoforms upon retroviral transfection by an empty vector. *(b)* Re-expression of *Lmna* WT but not the E358K or the L530P mutant forms significantly reversed the reduction in Rbm20 expression. Results represent mean fold change in relative Rbm20 densitometry signal normalized to GAPDH ± SEM of 7 independent experiments (* $p<0.05$; ** $p<0.01$; *** $p<0.001$ by one-way Anova).

3. Rbm20 Protein Expression Levels in Striated Muscle Tissue from Lamin A/C Knockout (Lmna$^{-/-}$) Mice

To validate our results *in vivo*, we assessed the protein expression levels of Rbm20 in striated muscle tissue from *Lmna*$^{-/-}$ mice. The homozygous deletion of *Lmna* in mice results in EDMD and DCM with conduction defects[286]. *Lmna*$^{-/-}$ mice appear similar to their WT littermates at birth; however, they soon suffer from skeletal muscle dystrophy, retarded growth and die by four to six weeks of age[286]. Hence, we performed western blot analysis on protein lysates from the left ventricle and Tibialis Anterior (TA) muscle of *Lmna*$^{-/-}$ mice (Mut) between 4-5 weeks of age in comparison to age and gender-matched *Lmna*$^{+/-}$ (Het) and WT mice. The main Rbm20 isoforms appeared at 75 and 37 KDa in both tissues (Figure 27). Interestingly, we noted a tissue-specific expression of Rbm20 whereby the 75 KDa isoform was mainly expressed in the heart while the 37 KDa isoform was the main isoform in the TA muscle. A decrease in the protein expression levels of both isoforms was noted in the left ventricle of *Lmna*$^{-/-}$ mice of both genders (Figure 27a). Quantification of western blot densitometry signals revealed a 1.4-fold decrease in the 75 KDa isoform in the left ventricles of *Lmna*$^{-/-}$ mice of both genders. While the mean fold change in expression was significantly lower in female mice (0.7 ± 0.0; $p=0.023$), the decrease was not significant in male mice (0.7 ± 0.1; $p=0.218$), as determined by one-way ANOVA followed

by 2-sided Dunnett t-test (Figure 27b). Similarly, a significant decrease in expression of the 37 KDa isoform of Rbm20 was observed in female *Lmna*$^{-/-}$ mice, whereby the mean fold change of expression of this isoform in *Lmna*$^{-/-}$ mice (0.6 ± 0.0) was significantly lower than that in WT mice; *p=0.005;* hence indicating a 1.7-fold decrease in expression. Although a 1.7-fold decrease in the 37 KDa isoform was also obtained in male *Lmna*$^{-/-}$ mice relative to WT mice, this decrease was not significant (0.6 ± 0.1; *p=0.255*).

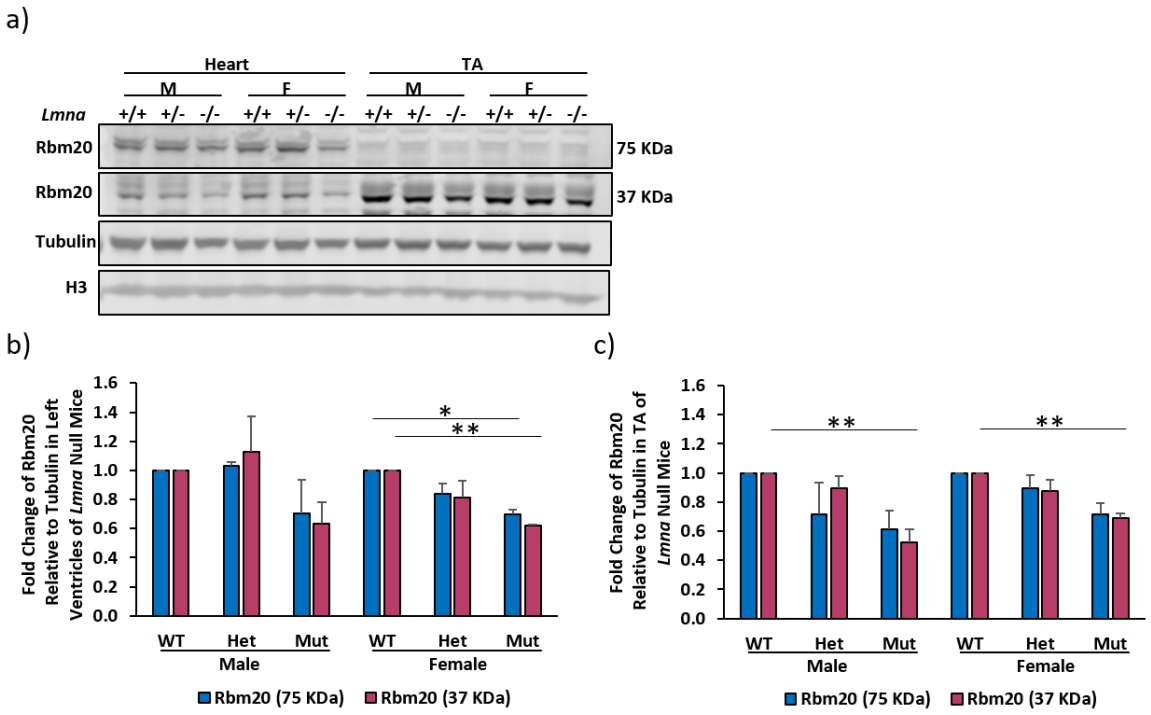

Figure 27. Western Blot Analysis of Rbm20 Protein Expression in the Left Ventricle and TA Muscle of Lamin A/C Knockout (*Lmna*$^{-/-}$) Mice.
(a) Representative western blot. *(b)* A decrease in the expression of both isoforms of Rbm20 (75KDa and 37KDa) was noted in the left ventricle of *Lmna*$^{-/-}$ mice (Mut) relative to WT mice. This decrease was significant in female but not male mice. *(c)* A decrease in the expression of both isoforms of Rbm20 was also noted in the TA of *Lmna*$^{-/-}$ mice (Mut) relative to WT mice. This decrease was significant for the 37KDa but not the 75KDa isoform in both genders. Data represents mean fold change in relative Rbm20 densitometry signal normalized to tubulin alpha ± SEM from three independent repeats. (*p<0.05; **p<0.01 by one-way Anova).

In the TA, a significant decrease in the expression of the 37 KDa isoform of Rbm20 was observed in *Lmna*$^{-/-}$ mice of both genders in comparison to WT mice, whereby the mean fold change in expression in male (0.5 ± 0.1) and female (0.7 ± 0.0) *Lmna*$^{-/-}$ mice was significantly lower than that in WT mice; *p=0.003* and *p=0.009* respectively in one-way ANOVA followed by 2-sided Dunnett t-test (Figure 27c), hence indicating a 2-fold and 1.4-fold decrease in the expression of the 37 KDa isoform respectively. Although a similar decrease in expression of the 75 KDa isoform was noted in *Lmna*$^{-/-}$ mice relative to WT mice of both genders, this decrease was not significant. The results represent the mean fold change in Rbm20 expression relative to tubulin alpha ± SEM from three independent repeats. Similar results were obtained by normalizing Rbm20 expression levels to H3 house-keeping gene.

4. Rbm20 Protein Expression Levels in Striated Muscle Tissue from Lmna N195K mice

Next, we assessed the protein expression levels of RBM20 in *knock-in* mice carrying the *Lmna* N195K mutation *Lmna*$^{N195K/N195K}$ in a C57BL/6 background (*Lmna* N195K). *Lmna* N195K mice are an established model of DCM[164]. In the specific background used, these mice suffer from skeletal muscle dystrophy in addition to DCM and, on average, die by 10 weeks of age[368]. Rbm20 protein expression levels were tested in left ventricle and TA muscle tissues from *Lmna* N195K (Mut) mice between 10-15 weeks of age in comparison to age and gender matched *Lmna*$^{N195k/+}$ (Het) and WT mice (Figure 28a, Figure 29a). Interestingly, Rbm20 expression was downregulated in the left ventricles

of female *Lmna* N195K mice, whereby the mean fold change of expression of each of the 75 KDa (0.53 ± 0.05; *p=0.000*) and the 37 KDa (0.51 ± 0.02; *p=0.000*) isoforms was significantly lower relative to WT mice, thus representing an approximate 2-fold decrease in each isoform. In addition, a significant 1.2-fold decrease in the 37 KDa (0.85 ± 0.03; *p=0.004*) but not the 75KDa isoform was noted in heterozygote female mice (Figure 28b).

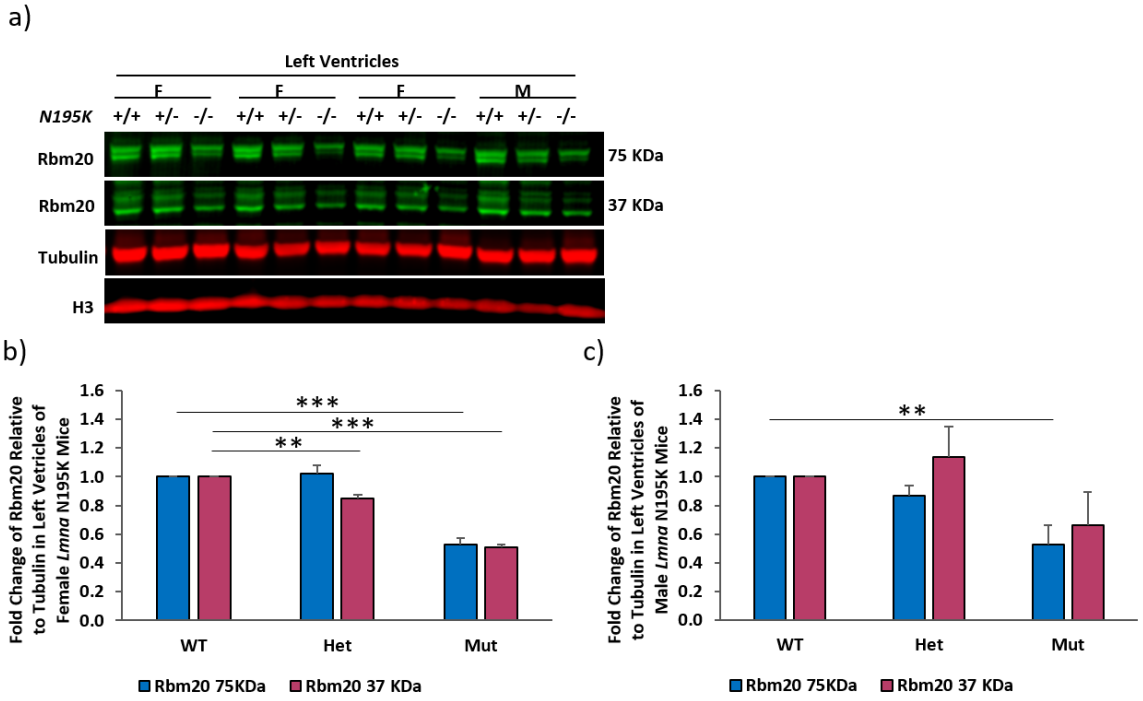

Figure 28. Western Blot Analysis of Rbm20 Protein Expression in the Left Ventricle of *Knock-in* Mice Carrying the *Lmna* N195K Mutation *Lmna*$^{N195K/N195K}$ (*Lmna* N195K). *(a)* Representative western blot. *(b)* A significant decrease in the expression of both isoforms of Rbm20 (75KDa and 37KDa) was noted in the left ventricle of female *Lmna N195K* (Mut) mice relative to WT mice. A significant decrease in the expression of the 37KDa isoform was also noted in heterozygote (Het) mice relative to WT mice. *(c)* A decrease in the expression of both isoforms of Rbm20 was also noted in male *Lmna N195K* mutant mice relative to WT mice. This decrease was significant for the 75KDa but not the 37KDa isoform. Data represents mean fold change in relative Rbm20 densitometry signal normalized to tubulin alpha ± SEM from three independent repeats for female mice and five independent repeats for male mice. (**p<0.01; ***p<0.001 by one-way Anova).

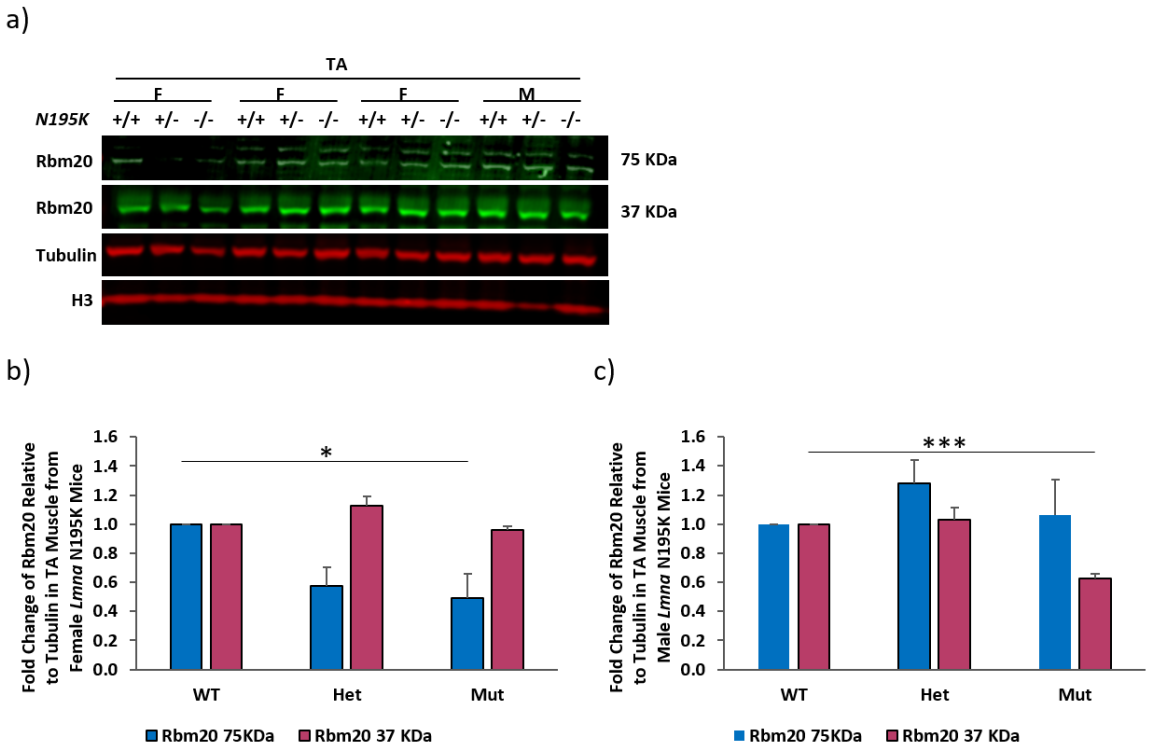

Figure 29. Western Blot Analysis of Rbm20 Protein Expression in the TA Muscle of *Knock-in* Mice Carrying the *Lmna* N195K Mutation $Lmna^{N195K/N195K}$ (*Lmna* N195K). *(a)* Representative western blot. *(b)* A significant decrease in the expression of the 75 KDa isoform of Rbm20 was noted in the TA muscle of female *Lmna N195K* (Mut) mice relative to WT mice. *(c)* A significant decrease in the expression of the 37 KDa isoform of Rbm20 was noted in male *Lmna N195K* mice relative to WT mice. Data represents mean fold change in relative Rbm20 densitometry signal normalized to tubulin alpha ± SEM from three independent repeats. (*p<0.05; ***p<0.001 by one-way Anova).

In the left ventricles of male mice, a significant decrease was observed in the 75KDa isoform of Rbm20 (0.52 ± 0.14; *p=0.006*). This decrease was approximately 2-fold less than expression in WT mice and, therefore, very similar to the decrease observed in

female mice. A decrease in expression of the 37 KDa isoform was also noted in male left ventricles; however, this decrease was not significant (Figure 28c).

In the TA muscle of female *Lmna* N195K mice, a significant 2-fold decrease in expression of the 75 KDa (0.49 ± 0.17; *p=0.044*) but not the 37 KDa isoform of Rbm20 was noted relative to WT mice (Figure 29b). On the other hand, a significant decrease was noted in the 37KDa (0.62 ± 0.03; *p=0.001*) but not the 75KDa isoform of Rbm20 in the TA muscle from male *Lmna* N195K mice, thus representing a 1.6-fold decrease in expression relative to WT mice (Figure 29c). The results represent the mean fold change in Rbm20 expression relative to tubulin alpha ± SEM from three independent repeats in case of female mice and 5 independent repeats in case of male mice. Similar results were obtained by normalizing Rbm20 expression levels to H3 house-keeping gene. Statistical significance was determined by one-way ANOVA followed by 2-sided Dunnett t-test.

5. Transcript Levels of Rbm20 and Titin Isoforms in Left Ventricle and TA Muscle Tissues from H222P Mice

Both $Lmna^{-/-}$ and $Lmna^{N195K/N195K}$ mice models have early disease onset and mortality, both of which are far from the kinetics observed in human disease. As such, we sought to determine if Rbm20 is similarly deregulated in a more relevant context with respect to disease pathogenesis. To that end, we utilized the knock-in mice model with the $Lmna^{H222P/H222P}$ mutation (*Lmna* H222P). These mice have delayed disease onset, diminished disease severity and a relatively long life expectancy with a 50% mortality rate of about 22-weeks[368]. Hence, Rbm20 expression levels in heart and TA muscle tissues from *Lmna* H222P (Mut) mice at 28 weeks of age were compared to age and gender matched

Lmna$^{H222P/+}$ (Het) and WT mice. First, we assessed the expression of Rbm20 at the transcript level by real time PCR analysis of cDNA from left ventricle and TA muscle tissues. In the left ventricle, significant decrease in Rbm20 expression was observed in both male and female *Lmna* H222P mice in comparison to WT mice, whereby the mean fold change in Rbm20 expression in male (0.5 ± 0.1) and female (0.4 ± 0.1) mutant mice was significantly lower than in WT mice; *p=0.033* and *p=0.01* respectively in one-way ANOVA followed by 2-sided Dunnett t-test, hence indicating a 2-fold and 2.5-fold decrease in Rbm20 expression respectively (Figure 30a). To test the effects of the decrease in RBM20 expression on its function as an alternative splicing factor, we assessed the expression levels of different isoforms of titin, a prominent target of Rbm20 splicing. In line with the decrease in Rbm20 expression in the heart, a significant decrease in the N2B isoform of titin was observed in the left ventricles of both heterozygous (0.8 ± 0.0; *p=0.042*) and mutant (0.5 ± 0.1; *p=0.001*) female mice but not male mice in comparison to WT controls, thus indicating a 1.25-fold and 2-fold decrease in expression respectively (Figure 30b). Surprisingly, a significant decrease in the N2BA isoform of titin was observed in the left ventricles of both heterozygous (0.7 ± 0.1; *p=0.018*) and mutant (0.3 ± 0.1; *p=0.001*) female mice but not male mice in comparison to WT controls, thus indicating a 1.4-fold and 3.3-fold decrease in expression respectively (Figure 30c). Using a different primer pair to assess the expression of the N2BA isoform of titin, we did not obtain a significant change in expression in the left ventricles of *Lmna* H222P mutant or heterozygous mice relative to WT mice of both genders (Figure 30d). This result is reflective of the complex splicing of N2BA isoforms in the heart and is suggestive that different N2BA isoforms are affected differently by Rbm20 downregulation.

In the TA, no significant change in Rbm20 transcript levels was observed in both male and female *Lmna* H222P mice in comparison to WT mice (Figure 30e). Consistent with the absence of significant change in Rbm20 expression in the TA muscle of *Lmna* H222P mice, no significant change was obtained in the expression of the skeletal-muscle specific N2BA isoform in the TA muscle of *Lmna* H222P mice in comparison to WT mice of both genders (Figure 30f). The results represent the mean fold change in expression relative to GAPDH, 18S & Rn7sk ± SEM from three independent repeats.

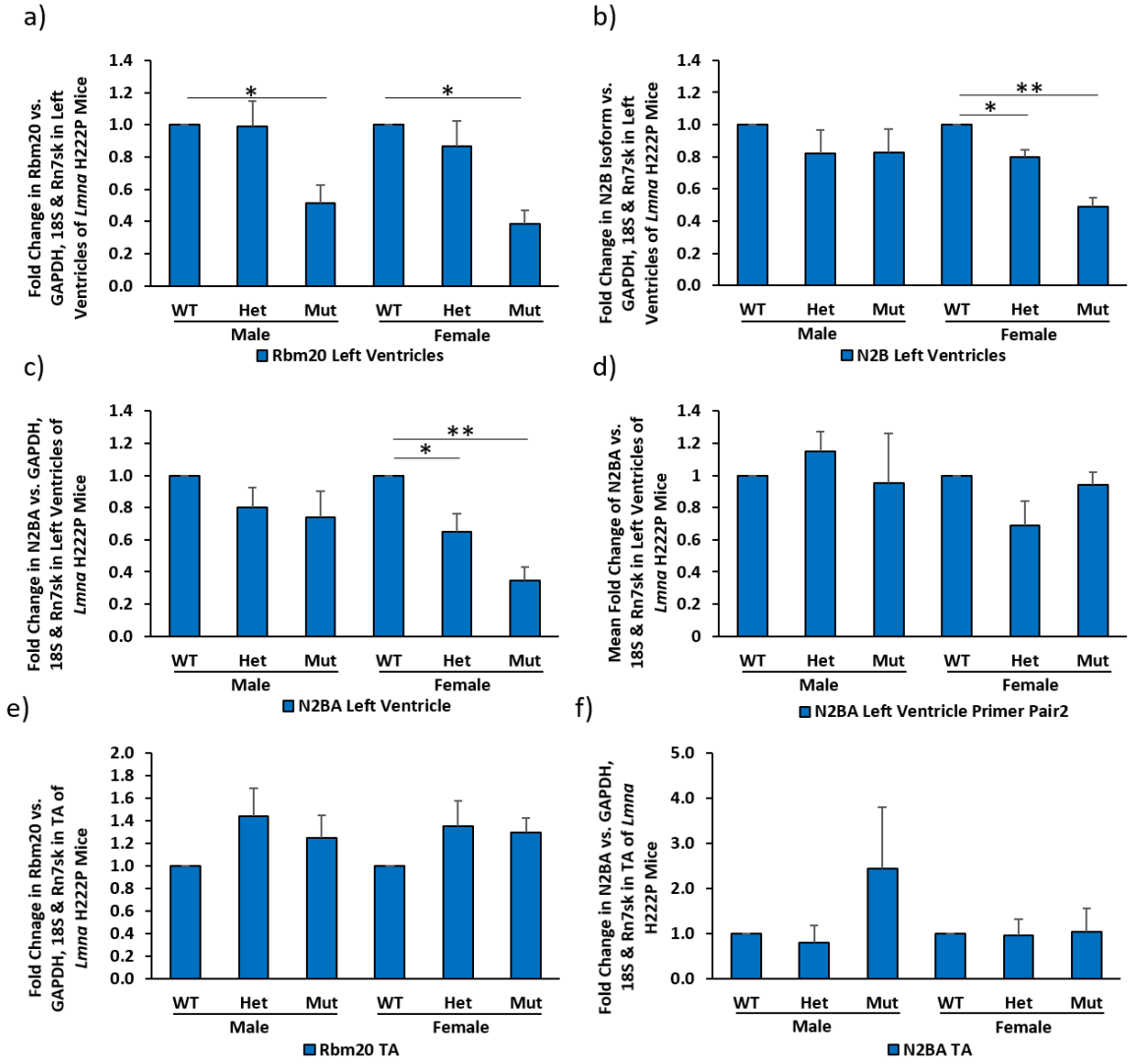

Figure 30. Real-Time PCR Quantification of Rbm20 and Titin Isoforms in the Heart and TA Muscle of *Knock-in* Mice Carrying the *Lmna* H222P Mutation $Lmna^{H222P/H222P}$ (*Lmna* H222P).

(a) Rbm20 transcript levels were significantly reduced in the left ventricle of *Lmna H222P* mice (Mut) relative to WT mice of both genders. *(b)* N2B transcript levels were significantly reduced in the left ventricle of female *Lmna H222P* mice but not male mice relative to WT mice. *(c)* N2BA transcript levels were significantly reduced in the left ventricle of female *Lmna H222P* mice but not male mice (using N2BA primer pair 1). *(d)* N2BA transcript levels assessed with a different N2BA primer (N2BA primer pair 2) were unchanged in the left ventricles of *Lmna H222P* mice of both genders. *(e)* In the TA, no significant change in Rbm20 transcript levels was noted in *Lmna H222P* mice relative to WT mice of both genders. *(f)* No significant change in N2BA transcript levels was noted in the TA muscle of *Lmna H222P* mice relative to WT mice of both genders (using the skeletal muscle specific N2BA primer pair 3). Results represent mean fold change in

relative expression normalized to GAPDH, 18S & Rn7sk ± SEM of 3 independent experiments; done in duplicates (*p<0.05; **p<0.01 by one-way Anova).

6. Rbm20 Protein Expression Levels in Left Ventricle and TA Muscle Tissues from H222P Mice

Second, we assessed the protein expression levels of Rbm20 in heart and TA muscle tissues from *Lmna* H222P mutant mice at 28 weeks of age in comparison to age and gender matched heterozygous and WT mice. Despite the downregulation in Rbm20 transcript levels in the left ventricles of *Lmna* H222P mice relative to WT mice of both genders, no change was observed at the protein level in neither the 75KDa nor the 37KDa isoform (Figure 31a). In the TA muscle of *Lmna* H222P mice, no change in the protein expression levels of both isoforms of Rbm20 was also noted (Figure 31b); nonetheless, this was consistent with the absence of deregulation in Rbm20 transcript levels in the TA muscle of *Lmna* H222P mice of both genders. The results represent the mean fold change in Rbm20 expression relative to H3 ± SEM from three independent repeats. Statistical significance was determined by one-way ANOVA followed by 2-sided Dunnett t-test.

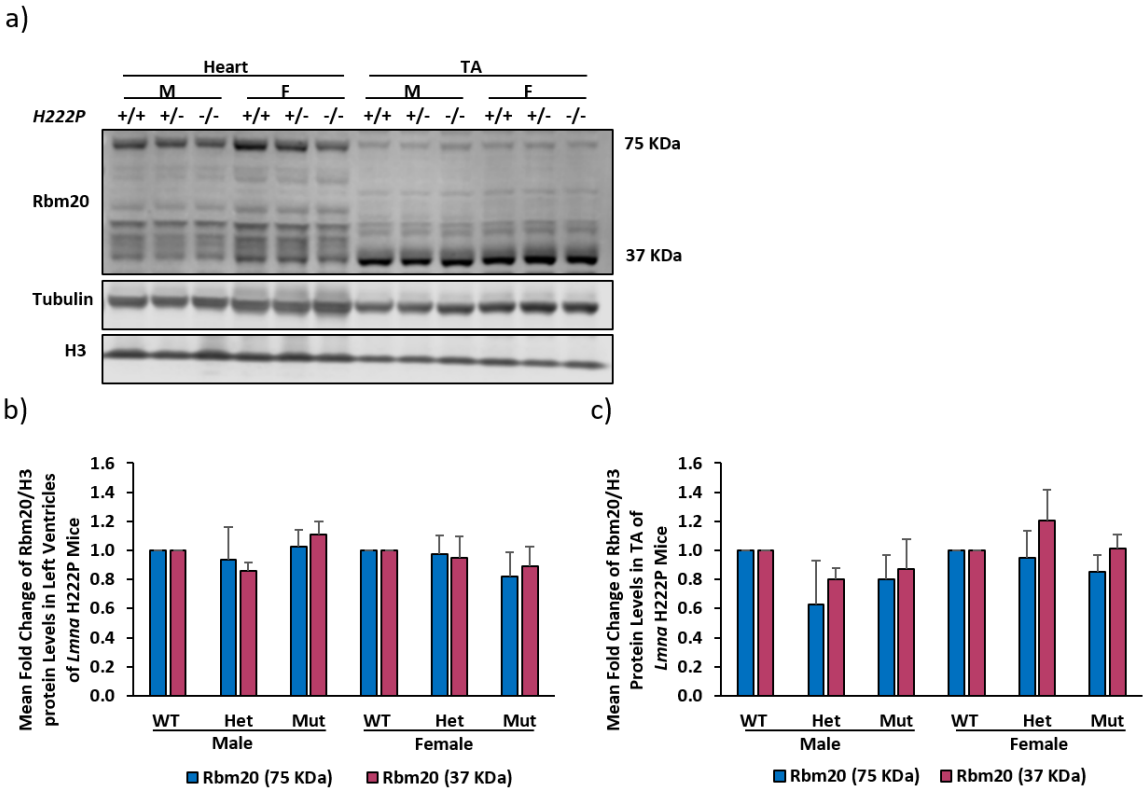

Figure 31. Western Blot Analysis of Rbm20 Protein Expression in the Heart and TA Muscle of *Knock-in* Mice Carrying the *Lmna* H222P Mutation $Lmna^{H222P/H222P}$ (*Lmna H222P*).
(a) Representative blot. No significant change in expression of the 75 KDa and the 37 KDa isoforms of Rbm20 was noted in the left ventricle *(b)* or the TA muscle *(c)* of *Lmna* H222P (Mut) or heterozygous (Het) mice relative to WT mice of both genders. Data represents mean fold change in relative Rbm20 densitometry signal normalized to H3 ± SEM from three independent repeats. Statistical significance was determined by one-way Anova.

7. The Ratio of p-AKT/AKT Protein Expression Levels in Lmna Knockout, N195K Mutant and WT MEFs in Response to Insulin

Although upstream regulation of RBM20 has been poorly understood, recent work revealed that insulin increases the expression of both Rbm20 and the N2B titin isoform in neonatal rat cardiomyocytes through the PI3K-AKT-mTOR kinase axis[238]. As such, we set out to test whether insulin treatment can restore Rbm20 protein levels in $Lmna^{-/-}$ and

Lmna$^{N195K/N195K}$ MEFs. Accordingly, we serum starved *Lmna*$^{-/-}$, *Lmna*$^{N195K/N195K}$ and WT MEFs for 14-16hrs and treated them with 180nM insulin for different timepoints (15 min, 2hrs, 24hrs and 48hrs). To assess the activation levels of AKT, a key effector kinase in the insulin signaling pathway[380], we performed western blot analysis of protein of protein expression levels of p-AKT relative to AKT. The ratio of p-AKT/AKT was quantified by image J densitometry analysis in cells at baseline conditions, in serum starved cells and in insulin treated cells. In WT MEFs, serum starvation resulted in a decrease in baseline AKT phosphorylation levels (2.9 ± 0.5). Treatment of serum starved cells with 180nM of insulin caused an increase in AKT activation levels, reaching a peak at 15 min whereby the mean fold change in p-AKT expression (10.6 ± 3.9; *p=0.05*) was significantly higher than in serum starved cells, hence indicating a 10.6-fold increase in p-AKT expression. AKT phosphorylation levels deteriorated beyond 15 min but stayed higher than levels in serum starved cells; however, the increase in p-AKT/AKT levels at 2hrs (10.1 ± 4.1), 24hrs (4.4 ± 0.8) and 48hrs (7 ± 0.9) relative to serum starved cells was not significant (Figure 32a). In *Lmna* Null MEFs, serum starvation also resulted in a decrease in baseline AKT phosphorylation levels (5.6 ± 2.8); however, the response to insulin treatment was amplified in comparison to WT MEFs, whereby the mean fold change in p-AKT/AKT expression at 15 min (17.1 ± 2.5), 2hrs (26.4 ± 4.8) and 24hrs (18.8 ± 4.3) was significantly higher than that in serum starved controls; *p=0.017*, *p=0.001* and *p=0.009* respectively. Accordingly, the peak of AKT activation occurred at 2hrs, followed by a decrease at 24hrs until reaching low levels (8.3 ± 2.8) at 48 hrs (Figure 32b).

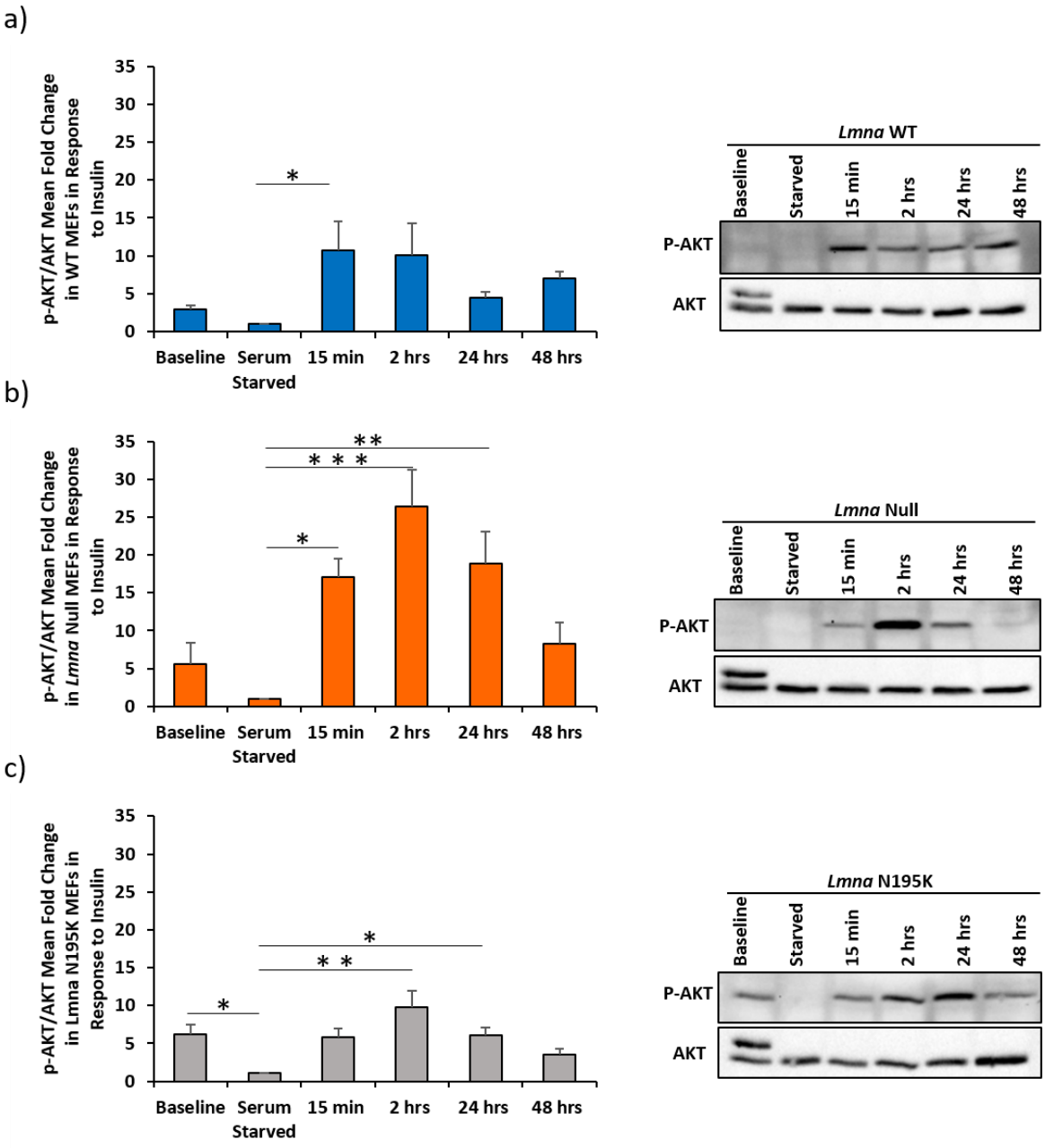

Figure 32. Western Blot Analysis of p-AKT/AKT Protein Expression Levels in WT MEFs, Lamin A/C Knockout MEFs and *Lmna*$^{N195K/N195K}$ MEFs in Response to Treatment with 180 nM Insulin.

(a) In WT MEFs, baseline p-AKT/AKT levels dropped upon serum starvation, then increased significantly at 15min of insulin treatment. p-AKT/AKT activation levels remained high at 2hrs and then dropped at 24 and 48hrs. *(b)* In lamin A/C knockout MEFs, a decrease in baseline p-AKT/AKT levels was also noted upon serum starvation, followed by a significant increase at 15min, 2hrs and 24hrs of insulin treatment. p-AKT/AKT levels

started to drop at 24hrs, but only returned to low levels at 48hrs. *(c)* In *Lmna*$^{N195K/N195K}$ MEFs, baseline p-AKT/AKT levels were significantly higher than in serum starved cells. Insulin treatment induced a significant increase in p-AKT/AKT levels at 2 and 24hrs of insulin treatment, after which cessation in AKT activation was noted at 48hrs. Results represent mean fold change in p-AKT densitometry signal normalized to AKT densitometry signal ± SEM from three independent experiments. (* $p<0.05$; ** $p<0.01$; *** $p<0.001$ by one-way Anova).

In *Lmna* N195K MEFs, p-AKT/AKT levels at baseline were significantly higher than in serum starved *Lmna* N195K MEFs, whereby the mean fold change in p-AKT/AKT expression at baseline was (6.2 ± 1.3; *p=0.045*). Accordingly, baseline levels of p-AKT/AKT were the highest in *Lmna* N195K MEFs followed by *Lmna* Null MEFs followed by WT MEFs with a significant change in *Lmna* N195K MEFs only. In addition, the peak of AKT activation was also delayed but the intensity of response to insulin treatment was comparable to WT MEFs, whereby the mean fold change in p-AKT/AKT expression at 2hrs (9.8 ± 2.2) and 24hrs (6.1 ± 1.0) was significantly higher than that in serum starved controls; *p=0.001* and *p=0.05* respectively. Although an increase was noted in p-AKT/AKT expression levels at 15 min (5.8 ± 1.2), it was not significant; and the levels of AKT activation dropped beyond baseline levels at 48hrs (5.8 ± 3.5) (Figure 32c). Results represent the mean fold change in p-AKT expression relative to AKT ± SEM from three independent repeats. Statistical significance was determined by one-way Anova followed by Dunnett t-test.

8. Rbm20 Transcript Levels in WT, Lmna Knockout and N195K Mutant MEFs in Response to 180nM Insulin

To determine if insulin treatment can induce Rbm20 transcription in WT, *Lmna*$^{-/-}$ and *Lmna*$^{N195K/N195K}$ MEFs, Rbm20 transcript levels were assessed by real time PCR following serum starvation and treatment with 180 nM of insulin for 15min, 2hrs, 24hrs and 48hrs. Rbm20 transcript levels were also assessed at baseline conditions and after 14-16hrs of serum starvation. In all three cell lines, there was no change in Rbm20 expression levels between baseline and serum starved cells (Figure 33). Insulin treatment triggered an increase in the expression levels of Rbm20 in WT MEFs but not in *Lmna*$^{-/-}$ and *Lmna*$^{N195K/N195K}$ MEFs. The increase in Rbm20 expression occurred as early as 15min and stayed at high levels up to 2hrs after insulin stimulation. Although not significant, the mean fold change in Rbm20 expression at 15 min (3.4 ± 1.8) and 2hrs (3.5 ± 2.3) was notably higher than that in serum starved cells, hence indicating a 3.4-fold and 3.5-fold increase in expression, respectively. At 24hrs, the expression levels of Rbm20 declined (1.6 ± 0.5) but were still higher than levels in serum starved cells. By 48hrs, the insulin-induced boost in Rbm20 transcription died out and Rbm20 transcript levels became comparable to serum starved levels (0.8 ± 0.3). No significant change in Rbm20 transcript levels was noted in response to insulin treatment in *Lmna*$^{-/-}$ MEFs (Figure 33b) or *Lmna*$^{N195K/}$N195K MEFs (Figure 33c) relative to their corresponding serum starved cells. Results represent the mean fold change in Rbm20 expression relative to 18S ± SEM from three independent repeats. Statistical significance was determined by one-way Anova followed by Dunnett t-test.

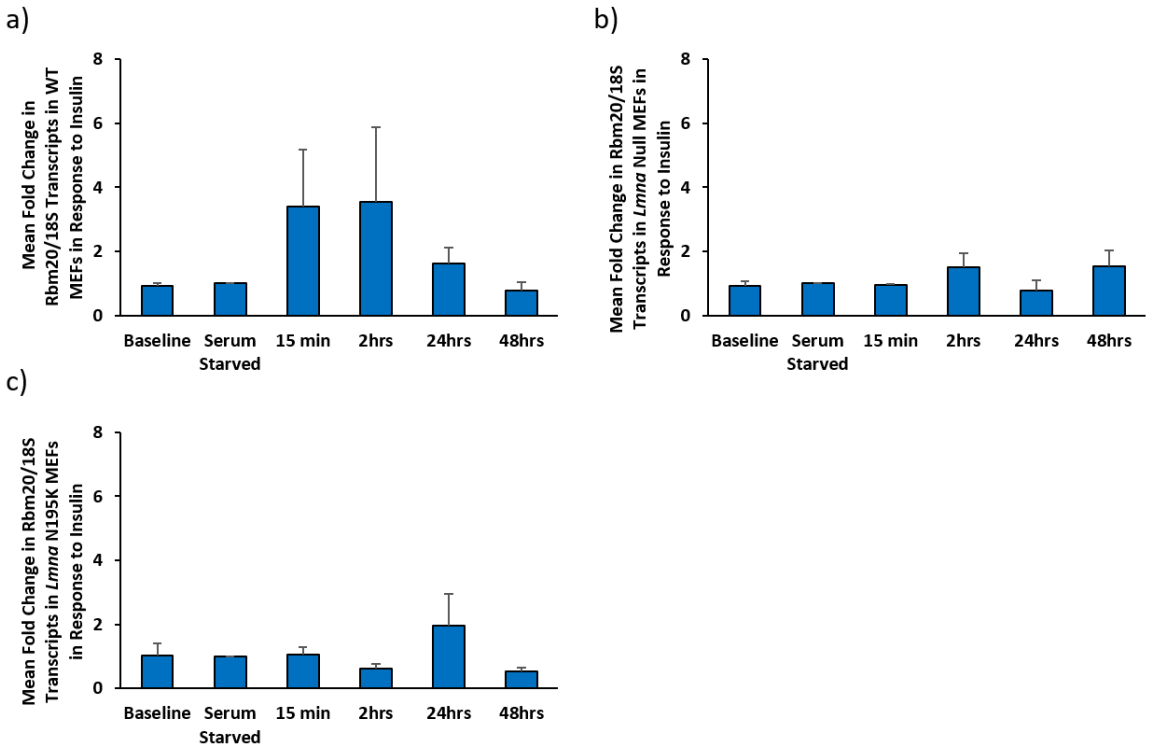

Figure 33. Rbm20 Transcript Levels in WT, *Lmna* Knockout and *Lmna* N195K Mutant MEFs in Response to 180nM Insulin.

Real-Time PCR quantification was performed in WT, *Lmna*$^{-/-}$ and *Lmna*$^{N195K/\mathrm{N195K}}$ MEFs at baseline conditions, after 14-16hrs of serum starvation and upon insulin treatment for 15min, 2hrs, 24hrs and 48hrs. *(a)* Rbm20 transcript levels were induced in WT MEFs at 15min and 2hrs of insulin treatment. No significant change in Rbm20 transcript levels was noted in response to insulin treatment in *Lmna*$^{-/-}$ MEFs *(b)* or *Lmna*$^{N195K/\mathrm{N195K}}$ MEFs *(c)* relative to serum starved cells. Results represent the mean fold change in Rbm20 expression relative to 18S ± SEM from three independent repeats. Statistical significance was determined by one-way Anova followed by Dunnett t-test.

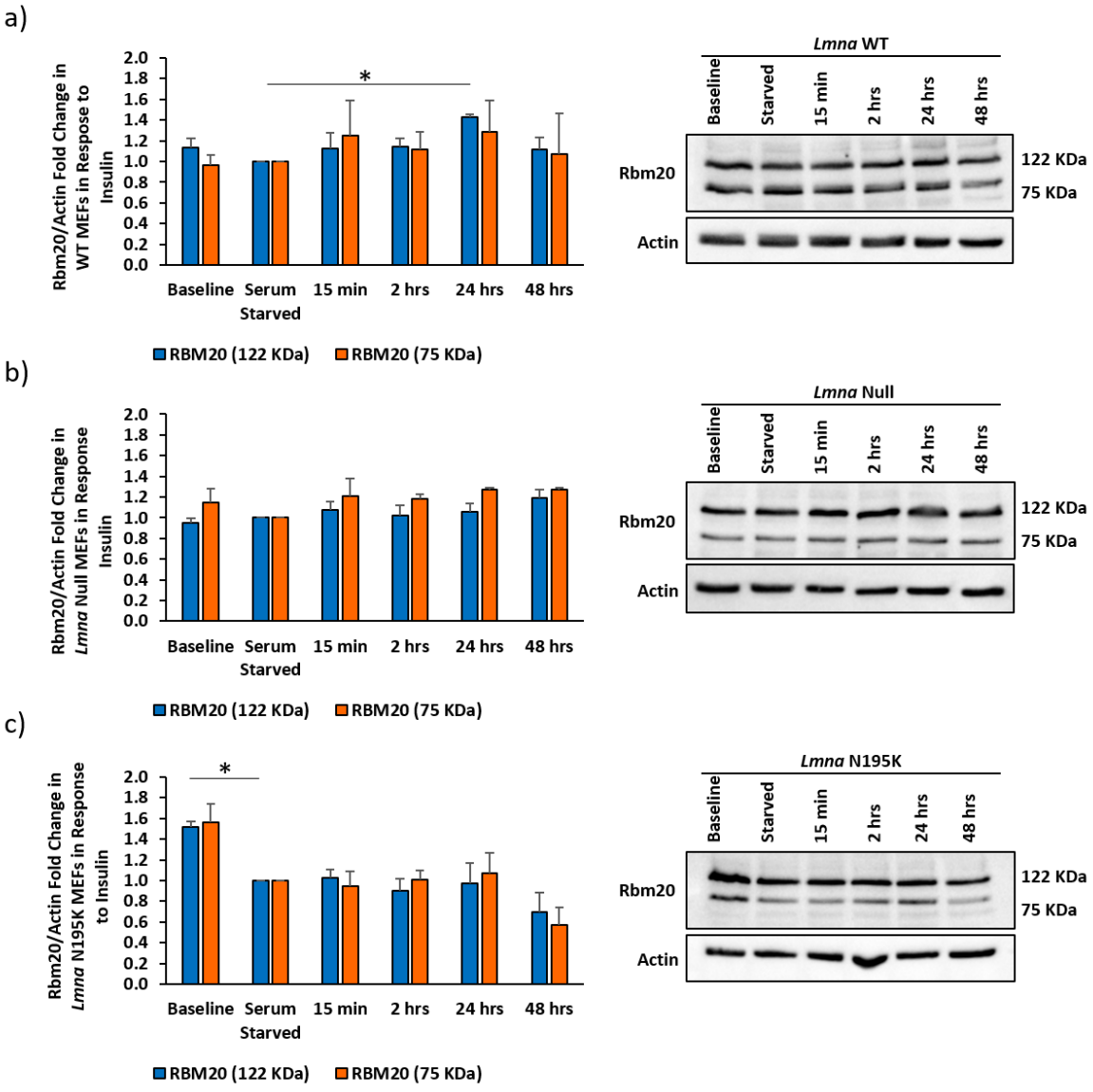

Figure 34. Rbm20 Protein Expression Levels in WT, *Lmna* Knockout and *Lmna* N195K Mutant MEFs in Response to 180nM Insulin.

Western blot analysis was performed in WT, *Lmna*$^{-/-}$ and *Lmna*$^{N195K/N195K}$ MEFs at baseline conditions, after 14-16hrs of serum starvation and upon insulin treatment for 15min, 2hrs, 24hrs and 48hrs. *(A)* Protein expression levels of the 112KDa isoform of Rbm20 were significantly increased in WT MEFs 24hrs post insulin treatment. *(B)* No significant change in Rbm20 protein expression levels was noted in response to insulin treatment in *Lmna*$^{-/-}$ MEFs. *(C)* In *Lmna*$^{N195K/N195K}$ MEFs a significant decrease in expression of the 112 KDa isoform of Rbm20 was observed between baseline and serum starved cells, but no significant change in Rbm20 protein expression levels was noted in response to insulin treatment. Results represent the mean fold change in Rbm20 expression relative to Actin ±

SEM from three independent repeats. Statistical significance was determined by one-way Anova followed by Dunnett t-test.

9. Rbm20 Protein Expression Levels in WT, Lmna Knockout and Lmna N195K Mutant MEFs in Response to 180nM Insulin

To assess if insulin treatment can upregulate Rbm20 protein expression levels, MEFs were serum starved for 14-16 hrs and treated with 180 nM of insulin for different timepoints (15 min, 2hrs, 24hrs and 48hrs). Rbm20 protein expression levels were assessed by western blot analysis at baseline, after serum starvation and following insulin treatment. In WT MEFs, a significant increase in the expression of the 112KDa isoform of Rbm20 was noted at 24hrs post insulin treatment, whereby the mean fold change in expression (1.43 ± 0.03; *p=0.014*) was significantly higher than in serum starved cells, hence indicating a 1.43-fold increase in expression (Figure 34a). In $Lmna^{-/-}$ and $Lmna^{N195K/N195K}$ MEFs, no significant change in expression of either isoform of Rbm20 was observed at all timepoints of insulin treatment (Figure 34b, c). However; a notable decrease in expression of both isoforms of Rbm20 was observed between baseline and serum starved $Lmna^{N195K/N195K}$ MEFs, whereby the mean fold change in expression of the 112KDa isoform (1.51 ± 0.1) and the 75KDa isoform (1.57 ± 0.2) was higher than in serum starved MEFs. This decrease was statistically significant for the 112KDa isoform but not the 75KDa isoform; *p=0.033* and *p=0.077* respectively. Results represent the mean fold change in Rbm20 expression relative to Actin ± SEM from three independent repeats. Statistical significance was determined by one-way Anova followed by Dunnett t-test.

E. Discussion

The question of how mutations in the ubiquitously expressed *LMNA* gene cause an array of tissue-specific diseases has always been a dilemma that provoked scientific research. The involvement of lamins in many cellular functions led to the emergence of two main hypothesis. The first postulates that mutations in lamins disrupt their interactions with tissue-specific transcription factors, hence leading to deregulation in gene expression. The second associates the striated muscle phenotypes from most *LMNA* mutations with increased nuclear fragility and damage in mechanically stressed tissues such as the heart and skeletal muscles[29]. While evidence supporting the "gene regulation" hypothesis mainly focused on deregulation in transcription factors, less attention was paid on splicing which represents an important aspect of gene regulation. Although lamin A/C has been associated with splicing factors and splicing factor compartments, the role of lamin A/C in splicing remains controversial[381]. Here we show that Rbm20, a muscle-specific splicing factor implicated in cardiomyopathy, is deregulated in the context of *Lmna* loss or mutation both *in vitro* and *in vivo*. Previous results from our lab have also shown deregulation in Rbm20 both at the transcript and protein levels in an *Emd* null MEFs background. We also showed that lamin A/C interacts with Rbm20. Emerin is already known to interact with lamin A/C at the NE and this interaction is required for the correct localization of emerin at the inner nuclear membrane[171,382]. Taken together, this suggests the existence of a biofunctional interplay between lamin A/C, Rbm20 and emerin. The reduction in Rbm20 transcript levels in the context of emerin loss and lamin A/C loss or mutation may be linked to the roles that both lamin A/C and emerin play in genome organization and gene regulation. Spatial genome organization and chromosome positioning have been shown to be disrupted in cells

from patients with EDMD as well as other NE diseases[383]. A very recent study also showed that loss of either lamin A/C or emerin affects the nuclear localization of nuclear myosin 1 (NM1), an emerin interacting protein; and their combined depletion alters chromatin organization and mobility through NM1 and actin polymerization, with effects on gene regulation[384].

The significant decrease in Rbm20 transcript levels in *Lmna*$^{-/-}$ MEFs in comparison to WT MEFs was rescued upon restoration of WT lamin A. This confirms the direct effect of lamina disruption on *RBM20* gene regulation. The increased expression of RBM20 transcript levels upon restoring lamin E358K mutant form, but not lamin L530P mutant form, suggests that the E358K mutation is more tolerated in terms of *Rbm20* gene regulation. While the E358K mutation localizes to the rod domain, the L530P mutation occurs in the tail of lamin A/C[385]. As such, it is not surprising that different mutations affecting different regions of the molecule have different consequences. In fact, five different rod domain mutations in lamin A/C, including the E358K mutation, were shown to influence lamina assembly but not interaction with emerin in nucleoplasmic foci. This is consistent with findings demonstrating an effect of the E358K mutation on lamin A/C dimerization[386]. On the other hand, three mutations in the tail region of lamin A/C, including the EDMD R527P mutation located three amino acids away from the L530P mutation, disrupted binding to emerin while preserving lamin A/C localization at the nuclear rim[385]. A following study showed that the L530P mutation lowers the ability of lamin A but not lamin C from binding to emerin[387]. Furthermore, the L530P mutation was shown to reduce binding to F-actin as well as cross-linking actin filaments *in vitro*[388]. Given the role of nuclear actin polymerization in gene transcription[389,390] and its

susceptibility to disrupted lamin A/C-emerin interaction[171], the effect of the L530P mutation on both emerin and F-actin binding might explain the inability of the L530P lamin mutant to restore Rbm20 transcription. At the protein level, while restoration of WT lamin A to *Lmna*$^{-/-}$ MEFs resulted in significant increase in the protein expression levels of Rbm20 relative to mock-treated cells, both E358K and L530P mutations failed to induce Rbm20 protein expression. The increase in Rbm20 transcript but not protein levels upon restoration of the E358K mutant form might be suggestive that while lamin A/C NE localization is not essential for Rbm20 transcription, it might be important for mRNA processing, stability or export from the nucleus to the cytoplasm. These processes might be mediated by Rbm20 itself. Several RBP proteins including RBM10 have been reported to autoregulate their own mRNA splicing[391-393]. Furthermore, in addition to their canonical RNA splicing role, they are known to have roles in mRNA export and stability and translation[394]. As we have shown by different assays that Rbm20 interacts with lamin A/C as well as with other NE proteins, such as lamin B1 and nesprin1, it is tempting to speculate that in addition to being localized to the nucleoplasm, Rbm20 associates with these proteins at the nuclear envelope to mediate RNA export and/or stabilizes RNA in the cytoplasm. As such, the E358K mutation could possibly disrupt the interaction between lamin A/C and Rbm20 with consequent effects on other Rbm20 functions.

Western blot analysis of protein lysates from mouse straited muscle tissues revealed a tissue-specific expression of Rbm20 isoforms whereby the 75 KDa isoform was mainly expressed in the left ventricles and the 37KDa isoform was mainly expressed in the TA muscle. A decrease in the protein expression levels of both isoforms was noted in left ventricles and TA muscle tissues from both *Lmna*$^{-/-}$ mice and *Lmna* N195K mice of both

genders. While the decrease in each isoform was statistically significant in the left ventricles of female *Lmna*$^{-/-}$ mice, it wasn't significant in male mice due to increased variability in expression of Rbm20 isoforms. Such variability could be attributed to genetic differences between individual male mice and could be reduced by increasing the number of repeats to more than three mice per group. Furthermore, while a significant decrease in the expression of the 75 KDa isoform was noted in the TA of female *Lmna* N195K mice relative to WT mice, a significant decrease was noted in the 37KDa but not the 75KDa isoform in male *Lmna* N195K mice. This gender-dependent isoform expression was not observed in the left ventricles of *Lmna* N195K mice, whereby a reduction in both isoforms was observed in both genders. The initial study that introduced the *Lmna* N195K mice model reported an earlier death in homozygous male mice in comparison to female mice[164]. Although mice of both genders die from arrythmia, the significant reduction in the TA-specific isoform of Rbm20 in the TA of male *Lmna* N195K mice but not female mice, might contribute to a more severe skeletal muscular dystrophy in male mice. Nonetheless, a better understanding of the role of each isoform of Rbm20 and whether they have overlapping roles, is needed to explain our results in the context of the reported gender-based differences in the *Lmna* N195K mice model.

Although a significant reduction was noted at the transcript level in the left ventricles of *Lmna* H222P mice of both genders, no decrease in expression of either Rbm20 isoform was observed at the protein level. A possible explanation for this outcome is that increased stability of Rbm20 mRNA or protein might compensate for the reduction in Rbm20 transcript levels. Since a significant reduction in Rbm20 protein expression levels was noted in the left ventricles of both *Lmna* N195K and *Lmna*$^{-/-}$ mice of both genders,

increased stability of Rbm20 mRNA or protein is most likely to occur in the context of the H222P mutation only. This might be due to upregulation of signaling pathways in *Lmna* H222P mice that influence Rbm20 protein and/or mRNA turnover. Indeed, *Lmna* H222P mice are characterized by hyperactivation of mitogen activated signaling pathways including ERK1/2, JNK and p38α as well as PI3K/AKT pathway[140,148,320,395]. All of these pathways have been shown to be implicated in mRNA turnover by increasing mRNA stability[396]. For instance, the p38 pathway regulates the stability of mRNAs containing AU-rich elements (ARE) in their 3' untranslated region (UTR) by phosphorylating ARE-binding proteins (ARE-BP) such as HuR, AUF, KSRP and TTP[396]. Phosphorylation of Tristetraprolin (TTP) and K-homology splicing regulator protein (KSRP) at serine and threonine residues, respectively, has been shown to decrease their binding affinity to ARE, thereby inhibiting their mRNA decay activities and promoting mRNA stability[397,398]. In addition to promoting mRNA stability, the p38 pathway has been shown to induce eIF-4E-dependent mRNA translation[399]. Similarly, ERK dependent phosphorylation of AU-rich binding factor 1 (AUF1) induces its dissociation from its mRNA upon a conformational change catalyzed by the prolyl isomerase Pin1. As such, AUF1 dissociation prevents exosome recruitment and mRNA degradation and allows binding of stabilizing factors such as hnRNP C which reinforces mRNA stability[400]. Also, PI3K/AKT-dependent phosphorylation of KSRP and BRF1 prevents their mRNA decay activities[401,402]. While TTP, KSRP and AUF promote mRNA degradation, HuR activation increases mRNA stability and has been shown to be induced by AMPK and p38α pathways[403] and recently by the mTORC2/AKT/HSF1 axis[404]. As such, hyperactivation of these pathways in *Lmna* H222P mice might contribute to increased stability and/or enhanced translation of Rbm20

mRNA, thus overcoming the reduction in Rbm20 transcript levels. Moreover, *Lmna* H222P mice have longer life span and slower disease progression than *Lmna* N195K and *Lmna*$^{-/-}$ mice[141]. Accordingly, putative deregulation in Rbm20 protein levels might be seen in the left ventricles at the onset of the cardiac phenotype, that is, around 20 weeks of age. Other compensatory mechanisms might be activated towards the end stage of the disease thus resulting in enhanced mRNA stability. It is note mentioning that no change in Rbm20 protein expression was observed in the left ventricles of male *Lmna* H222P mice aged 10-15 weeks, that is, before the onset of the cardiac phenotype (Data not shown).

One of the most studied functions of Rbm20 is regulating titin mRNA splicing by favoring the expression of the short N2B isoform over the longer N2BA isoforms. Despite the absence of deregulation in Rbm20 at the protein level, the reduction in Rbm20 at the transcript level was associated with a significant reduction in the transcripts of the N2B titin isoform in the left ventricles of *Lmna* H222P mice, particularly in female mice. The reduction in the expression of the N2B isoform might be due to decreased phosphorylation and nuclear import of Rbm20 despite its constant protein expression. Although previously we did not observe any change in Rbm20 subcellular localization in *Lmna*$^{-/-}$ and *Lmna*$^{N195K/N195K}$ MEFs, different mechanisms might arise from different *Lmna* mutations and in different cellular contexts. As such, it would be interesting to assess the levels of phosphorylated Rbm20 in left ventricles of *Lmna* H222P mice as well as its subcellular localization. Moreover, cytoplasmic localization of Rbm20 would increase the stability of its own mRNA at the expense of its nuclear splicing function. Despite the reduction in N2B titin isoform expression, we did not obtain a significant change in expression of the N2BA isoform in left ventricles of *Lmna* H222P mice relative to WT mice of both genders.

Testing N2BA transcript expression levels with a different primer pair showed a reduction in expression with a similar expression pattern to the N2B isoform. Due to the wide range of sizes and complex alternative splicing of the N2BA isoforms, these results do not rule out increased expression in other longer N2BA isoforms that are not captured by the primer pairs used. In fact, Rbm20 deficiency in a rat strain with a spontaneous loss-of-function mutation in the *Rbm20* gene shows persistent expression of the giant titin isoform N2BA-G that becomes the most predominantly expressed isoform[208]. However, it cannot be determined from our results whether the reduction in the transcript levels of the N2B isoform is due to reduced transcription or altered alternative splicing especially with recent evidence pointing to a role of Rbm20 in transcription[405]. Anyhow, the role of reduced expression or altered alternative splicing of the N2B titin isoform in the disease pathogenesis of *Lmna* H222P mice can only be determined after assessing its expression at the protein level.

In the TA, no significant change in the transcript/protein levels of Rbm20 or the transcripts of the TA-specific N2BA titin isoform was observed in *Lmna* H222P mice at 28 weeks of age. In *Lmna* H222P mice, the initial disease phenotype, characterized by deterioration in muscle function, first appears at around 10 weeks of age. However, these mice continue to live up to 24-28 weeks, until they eventually die of cardiac failure. Since the skeletal muscle phenotype precedes the cardiac phenotype in these mice, the deregulation in Rbm20 expression might occur earlier in the TA, coinciding with or shortly after the initial appearance of the skeletal muscle phenotype.

Insulin treatment has been shown to induce upregulation of RBM20 both at the transcript and protein levels in cultured neonatal rat cardiomyocytes[238]. This increase in RBM20 gene expression could result from the activation of mTOR via the PI3K/AKT pathway[242].To assess whether insulin treatment can restore Rbm20 protein levels in *Lmna* Null and *Lmna* N195K MEFs, we first determined whether these cells are responsive to insulin by measuring AKT activation levels upon insulin stimulation. While p-AKT/AKT protein levels were similar between *Lmna* N195K MEFs and WT MEFs, we noted hyperactivation of AKT in *Lmna* Null MEFs. This result is in accordance with the reported hyperactivation of ERK1/2 and AKT/mTORC1 signaling pathways in the hearts of laminopathy patients as well as in hearts of *Lmna* H222P mice[140,148]. *In vitro* studies showed enhanced binding of total ERK1/2 to lamin A/C variant bearing the H222P amino acid substitution. In addition, sequestration of p-ERK1/2 was noted in the nuclear lamina of *Lmna* H222P mutant C2C12 myoblasts. This enhanced lamin A/C-ERK1/2 interaction was suggested to contribute to ERK1/2 activation in striated muscle tissue of *Lmna* H222P mice; and resulted in increased expression of the dual specific protein phosphatase 4 (DUSP4) which linked ERK1/2 to hyperactivation of the AKT/mTORC1 signaling pathway[320]. DUSP4 upregulation correlated with an elevated expression of cardiomyopathy markers[320] and its deletion attenuated the cardiac phenotype and improved survival[406]. Although this proposed disease mechanism falls short in explaining ERK1/2 hyperactivation in *Lmna* null MEFs, the properties of the entire lamina could hypothetically be disrupted in the absence of lamin A/C which may also result in ERK1/2 nuclear sequestration and AKT hyperactivation. In addition, ERK1/2 hyperactivation in laminopathies have been shown to be a consequence of other factors, such as elevated

levels of transforming growth factor beta 2 (TGF β2) that has been detected in serum, myoblast and fibroblast cultures from EDMD patients as well as *Lmna* H222P mice[407]. The elevated TGF β2 levels were associated with the expression of fibrogenic markers and impairment of myogenic differentiation. Although TGF β2 is an important mediator of fibrosis[161], which occurs at a later stage of the cardiac disease, hyperactivation of MAPK signaling has been noted before the appearance of significant cardiac phenotype, which suggests that induction of MAPK signaling by TGF β2 is a causative factor rather than a secondary effect of disease progression[148]. Moreover, AKT kinase activity regulates lamin A levels throughout the cell cycle. AKT enhances lamin A transcription in interphase to support lamin turnover and targets pre-lamin A for lysosomal degradation in dividing cells when the lamina dissociates[408]. Therefore, it is tempting to speculate that activation of AKT occurs as part of a physiological feedback mechanism in response to low levels of lamin A under normal conditions as well as in disease, thus explaining the elevated levels of AKT in *Lmna* deficient MEFs.

Baseline levels of AKT activation were higher in both $Lmna^{-/-}$ and $Lmna^{N195K/N195K}$ MEFs in comparison to WT MEFs. In $Lmna^{N195K/N195K}$ MEFs, although p-AKT activation levels were comparable to WT levels, baseline p-AKT levels were significantly higher than in serum starved cells, which is suggestive that the AKT/mTORC1 signaling pathway is also activated in these cells. The absence of hyperactivation in p-AKT following serum starvation could be attributed to the sensitivity of these cells to serum starvation which was noted by increased cell death in serum starved cells relative to untreated cells at baseline conditions. On the other hand, serum starvation did not induce cell death in neither $Lmna^{-/-}$ MEFs nor WT MEFs.

In WT MEFs, p-AKT induction commenced at 15min then started to decline by 24hrs. This was comparable to *Lmna*$^{N195K/N195K}$ MEFs. On the other hand, in *Lmna*$^{-/-}$ MEFs, although AKT activation also started to decline at 24hrs it remained at very high levels at 24 and 48hrs in comparison to WT MEFs. The PI3K/AKT/mTORC1 signaling pathway is controlled by well-established negative feedback loops that act at different levels of the pathway. Among these negative feedback loops is S6K1-dependent phosphorylation of IRS1 that targets it for proteasomal degradation and inhibits signaling downstream receptor tyrosine kinase receptor[155]. As such, defects in negative feedback mechanisms that control the PI3K/AKT/mTORC1 pathway might contribute to the prolonged activation of p-AKT in *Lmna*$^{-/-}$ MEFs. Moreover, termination of this pathway in a timely manner is essential for proper cellular function. For instance, it has been reported that prolonged AKT activation is involved in the development of cardiomyopathy as opposed to the beneficial effects of transient AKT activation in cardiac function[409,410]. In *Lmna*$^{N195K/N195K}$ MEFs, despite the significant p-AKT activation at baseline levels, the response to insulin treatment was not elevated as in *Lmna*$^{-/-}$ MEFs. As mentioned earlier, sensitivity of these cells to serum starvation might contribute to this outcome. On the other hand, the decreased response to insulin might be due to overactivation of p-AKT at baseline levels. A similar response has been reported in *LMNA* mutant myoblasts featuring hyperactivated YAP/TAZ pathway that gets paradoxically reduced in response to mechanical stimulation[172].

In WT MEFs, p-AKT induction at 15min and 2hrs of insulin treatment resulted in a concomitant increase in Rbm20 transcription. Consequently, a significant increase in Rbm20 protein levels was noted at 24 hrs. Despite the significant increase in p-AKT levels

in both *Lmna*$^{-/-}$ and *Lmna*$^{N195K/N195K}$ MEFs, insulin stimulation failed to induce Rbm20 expression at both the transcript and protein levels in both cell lines. Due to the complexity of the PI3K/AKT/mTORC1 signaling pathway and its communication with other pathways, decoupling between different players of this pathway has been reported previously. For instance, while knockdown of *Dusp4* in *Lmna* H222P mice counteracted AKT hyperactivation, it did not reduce mTORC1 levels[320]. Moreover, prolonged activation of p-AKT signaling through overexpression of IRS1 in myoblasts prohibited myogenic differentiation through AKT-dependent phosphorylation and nuclear exclusion of FoxO1[411]. The same study showed that initial AKT activation, but long-term termination (at around 18hrs) is required for myogenic differentiation. Given the importance of Rbm20 in myogenic differentiation and its induction, along with other muscle-specific genes, in a timely manner with sarcomere assembly[207,208], it is tempting to speculate that a similar mechanism downstream prolonged p-AKT activation prevents induction of Rbm20 in *Lmna*$^{-/-}$ MEFs. Moreover, reduction in Rbm20 expression levels in these cells and in animal tissues might be a direct effect of lamin A/C loss or mutation rather than prolonged p-AKT activation. This is supported by the finding that lamin A/C associates with Caveolin-2 at the inner nuclear membrane and that this association is required for oligomerization and activity of Caveolin-2 in epigenetic regulation of insulin responsive genes[412]. It is note mentioning that the increase in Rbm20 protein expression levels in response to insulin treatment of WT MEFs was modest, which could result from the low expression levels of Rbm20 in MEFs in comparison to skeletal muscle cells or cardiomyocytes that normally have high expression levels of Rbm20. As such, we cannot rule out an improved Rbm20 response to insulin in a more relevant cell model such as primary skeletal muscle cells or

cardiomyocytes from *Lmna* Null or *Lmna* N195K mice. Improved Rbm20 expression in response to insulin in striated muscle cells with *LMNA* mutations would set forth a promising treatment for these disorders through restoring Rbm20 expression levels.

Our findings provide insight into the pathogenic mechanisms of EDMD and DCM caused by *LMNA* mutations. This work shows that an intact nuclear lamina is required for proper regulation of Rbm20 expression and most likely function, thus highlighting the role of RBP and splicing regulation in the tissue-specific phenotypes of lamin A/C mutations. Whether deregulation in Rbm20 expression is a direct effect of lamin mutations or altered signaling pathways in laminopathies needs to be further investigated. Furthermore, assessment of Rbm20 phosphorylation levels as well as protein expression levels of titin isoforms is essential to validate the deregulation in Rbm20 function in the context of lamin mutations.

CHAPTER V

CONCLUSION

Mutations in lamins cause a wide array of tissue-specific diseases collectively called laminopathies[413]. Based on structural and functional roles of lamins, two main hypotheses were proposed to explain the cellular pathophysiological observations associated with *LMNA* mutations. The "structural hypothesis" postulates that lamin mutations confer nuclear fragility and mechanical instability in mechanically stressed tissues such as striated muscle tissues. The "gene regulation" hypothesis states that *LMNA* mutations cause disrupted gene regulation, either by direct interaction with chromatin and DNA-binding proteins or through interactions with tissue-specific transcription factors[29]. The pathogenesis in lamin A/C related cardiomyopathies is likely multifold, as various nuclear functions are affected including gene expression and nuclear morphology as well as many other cellular processes. In this work, we investigated the interplay between both structural and gene regulation hypotheses by studying the effect of lamina loss on both structural and regulatory proteins that home to the nuclear envelope. In addition, we investigated the role of the RNA splicing factor Rbm20 that regulates gene expression, both through its alternative splicing function and its newly discovered role in gene transcription[405]. Not only does Rbm20 affect gene regulation, but also sarcomere structure and function through splicing of several sarcomeric proteins such as titin[208]. As such, in addition to its gene regulatory role, it has an indirect effect on structural and mechanical stability of striated muscle cells.

Our results show that *Lmna* loss affects proteins that home to the nuclear envelope, including HuR, which shows decreased cytoplasmic localization and increased nuclear sequestration in the absence of lamin A/C. HuR is an RNA binding protein (RBP) that stabilizes several myogenic mRNA transcripts in the cytoplasm and prevents their degradation, hence playing a role in post transcriptional gene regulation[414]. A few studies have also reported a role of HuR in mRNA splicing, export and translation[415]. We also show that lamin A/C loss or mutation results in deregulated expression of Rbm20, another RBP, both *in vitro* and *in vivo*. Rbm20 gene deregulation was associated with potential alterations in its RNA splicing function. Using phage display screening and several validation assays for protein-protein interactions, we showed that Rbm20 interacts with lamin A/C, lamin B1 and nesprin-1. Thus, our findings highlight RBPs as a new class of proteins that interact with lamin A/C and that are affected by lamin A/C mutations.

Lamin A/C mutations are associated with deregulation in many signaling pathways such as MAPK and PI3K/AKT/mTOR among other signaling pathways[140]. As such, it is intriguing to know whether disrupted expression or subcellular localization of these and other RBPs is a direct effect of lamin mutations or a consequence of disrupted signaling pathways in laminopathies. The PI3K/AKT/mTOR signaling pathway has been shown to regulate the expression and splicing function of Rbm20 through an unknown mechanism[238]. Our results show that stimulation of this pathway by insulin does not restore Rbm20 expression levels in *Lmna* Null and N195K mutant MEFs despite p-AKT activation. While this result could be attributed to the role of lamin A/C in oligomerization and activation of epigenetic regulators of insulin responsive genes at the nuclear envelope (NE)[412], an increase in Rbm20 expression might be needed to activate negative feedback mechanisms

that normally counteract activation of the PI3K/AKT/mTOR signaling pathway. As such, downregulation in Rbm20 expression might contribute to the deregulated PI3K/AKT/mTOR signaling pathway. In fact, this might not be far from true as homozygous knockout of Rbm20 in rats has recently been shown to significantly upregulate TGF β2[405]. TGF β2 has previously been reported to be hyperactivated in the context of lamin mutations, and was suggested to contribute to ERK1/2 activation in striated muscle tissue of *Lmna* H222P mice[407]. In addition, ERK1/2 has been linked to hyperactivation of PI3K/AKT/mTORC1 signaling pathway through increased expression of the dual specific protein phosphatase 4 (DUSP4)[320]. Thus, lamin A/C loss or mutation might lead to downregulation in Rbm20 through compromised epigenetic regulation in response to the PI3K/AKT/mTOR signaling pathway, and Rbm20 downregulation, in turn, might lead to the observed hyperactivation of this pathway in the context of *Lmna* loss or mutation. Interestingly, mTOR has been shown to directly phosphorylate HuR at a specific serine residue (S202)[416]. Phosphorylation of the same serine residue by Cyclin dependent kinase 1 (Cdk1) has been shown to promote HuR nuclear localization[417]. Therefore, it is tempting to speculate that while Rbm20 regulation by PI3K/AKT/mTOR is dependent on lamin A/C, phosphorylation of HuR by hyperactivated mTOR does not require lamin A/C, thus resulting in HuR nuclear sequestration. Accordingly, reduced cytoplasmic availability of HuR might result in compromised stability of myogenic mRNA.

This work reveals novel lamin A/C and Rbm20 interacting partners and provides insight into novel disease mechanisms in laminopathies. Our work suggests that an interplay between lamin A/C, RBPs and deregulated signaling pathways might result in reduced expression, altered splicing and/or reduced mRNA stability of myogenic genes,

hence explaining the frequent muscle-specific effects of *Lmna* mutations and providing new promising targets for therapeutic intervention.

BIBLIOGRAPHY

1 McCulloch, R. & Navarro, M. The protozoan nucleus. *Molecular and biochemical parasitology* **209**, 76-87, doi:10.1016/j.molbiopara.2016.05.002 (2016).

2 Cremer, T. *et al.* Chromosome territories, interchromatin domain compartment, and nuclear matrix: an integrated view of the functional nuclear architecture. *Critical reviews in eukaryotic gene expression* **10**, 179-212 (2000).

3 Zhong, Z., Wilson, K. L. & Dahl, K. N. Beyond lamins other structural components of the nucleoskeleton. *Methods in cell biology* **98**, 97-119, doi:10.1016/s0091-679x(10)98005-9 (2010).

4 Stewart, C. L., Roux, K. J. & Burke, B. Blurring the boundary: the nuclear envelope extends its reach. *Science (New York, N.Y.)* **318**, 1408-1412, doi:10.1126/science.1142034 (2007).

5 Maurer, M. & Lammerding, J. The Driving Force: Nuclear Mechanotransduction in Cellular Function, Fate, and Disease. *Annual review of biomedical engineering* **21**, 443-468, doi:10.1146/annurev-bioeng-060418-052139 (2019).

6 Tapley, E. C. & Starr, D. A. Connecting the nucleus to the cytoskeleton by SUN-KASH bridges across the nuclear envelope. *Current opinion in cell biology* **25**, 57-62, doi:10.1016/j.ceb.2012.10.014 (2013).

7 Horn, H. F. *et al.* A mammalian KASH domain protein coupling meiotic chromosomes to the cytoskeleton. *J Cell Biol* **202**, 1023-1039, doi:10.1083/jcb.201304004 (2013).

8 Shindo, Y. *et al.* Lrmp/Jaw1 is expressed in sweet, bitter, and umami receptor-expressing cells. *Chemical senses* **35**, 171-177, doi:10.1093/chemse/bjp097 (2010).

9 Morimoto, A. *et al.* A conserved KASH domain protein associates with telomeres, SUN1, and dynactin during mammalian meiosis. *J Cell Biol* **198**, 165-172, doi:10.1083/jcb.201204085 (2012).

10 Zhou, C., Rao, L., Shanahan, C. M. & Zhang, Q. Nesprin-1/2: roles in nuclear envelope organisation, myogenesis and muscle disease. *Biochemical Society transactions* **46**, 311-320, doi:10.1042/bst20170149 (2018).

11 Zhang, Q. *et al.* Nesprins: a novel family of spectrin-repeat-containing proteins that localize to the nuclear membrane in multiple tissues. *Journal of cell science* **114**, 4485-4498 (2001).

12 Horn, H. F. *et al.* The LINC complex is essential for hearing. *The Journal of clinical investigation* **123**, 740-750, doi:10.1172/jci66911 (2013).

13 Simpson, J. G. & Roberts, R. G. Patterns of evolutionary conservation in the nesprin genes highlight probable functionally important protein domains and isoforms. *Biochemical Society transactions* **36**, 1359-1367, doi:10.1042/bst0361359 (2008).

14 Zhang, Q., Ragnauth, C., Greener, M. J., Shanahan, C. M. & Roberts, R. G. The nesprins are giant actin-binding proteins, orthologous to Drosophila melanogaster muscle protein MSP-300. *Genomics* **80**, 473-481 (2002).

15 Zhang, Q. *et al.* Nesprin-2 is a multi-isomeric protein that binds lamin and emerin at the nuclear envelope and forms a subcellular network in skeletal muscle. *Journal of cell science* **118**, 673-687 (2005).

16 Zhou, C. *et al.* Novel nesprin-1 mutations associated with dilated cardiomyopathy cause nuclear envelope disruption and defects in myogenesis. *Human molecular genetics* **26**, 2258-2276, doi:10.1093/hmg/ddx116 (2017).

17 Wilson, M. H. & Holzbaur, E. L. Nesprins anchor kinesin-1 motors to the nucleus to drive nuclear distribution in muscle cells. *Development (Cambridge, England)* **142**, 218-228, doi:10.1242/dev.114769 (2015).
18 Gimpel, P. *et al.* Nesprin-1alpha-Dependent Microtubule Nucleation from the Nuclear Envelope via Akap450 Is Necessary for Nuclear Positioning in Muscle Cells. *Current biology : CB* **27**, 2999-3009.e2999, doi:10.1016/j.cub.2017.08.031 (2017).
19 Roux, K. J. *et al.* Nesprin 4 is an outer nuclear membrane protein that can induce kinesin-mediated cell polarization. *Proceedings of the National Academy of Sciences of the United States of America* **106**, 2194-2199, doi:10.1073/pnas.0808602106 (2009).
20 Wilhelmsen, K. *et al.* Nesprin-3, a novel outer nuclear membrane protein, associates with the cytoskeletal linker protein plectin. *J Cell Biol* **171**, 799-810, doi:10.1083/jcb.200506083 (2005).
21 Ketema, M., Kreft, M., Secades, P., Janssen, H. & Sonnenberg, A. Nesprin-3 connects plectin and vimentin to the nuclear envelope of Sertoli cells but is not required for Sertoli cell function in spermatogenesis. *Mol Biol Cell* **24**, 2454-2466, doi:10.1091/mbc.E13-02-0100 (2013).
22 Fridkin, A., Penkner, A., Jantsch, V. & Gruenbaum, Y. SUN-domain and KASH-domain proteins during development, meiosis and disease. *Cellular and molecular life sciences : CMLS* **66**, 1518-1533, doi:10.1007/s00018-008-8713-y (2009).
23 Sosa, B. A., Kutay, U. & Schwartz, T. U. Structural insights into LINC complexes. *Current opinion in structural biology* **23**, 285-291, doi:10.1016/j.sbi.2013.03.005 (2013).
24 Lombardi, M. L. *et al.* The interaction between nesprins and sun proteins at the nuclear envelope is critical for force transmission between the nucleus and cytoskeleton. *The Journal of biological chemistry* **286**, 26743-26753, doi:10.1074/jbc.M111.233700 (2011).
25 Lu, W. *et al.* Nesprin interchain associations control nuclear size. *Cellular and molecular life sciences : CMLS* **69**, 3493-3509, doi:10.1007/s00018-012-1034-1 (2012).
26 Zhang, J. *et al.* Nesprin 1 is critical for nuclear positioning and anchorage. *Human molecular genetics* **19**, 329-341, doi:10.1093/hmg/ddp499 (2010).
27 Banerjee, I. *et al.* Targeted ablation of nesprin 1 and nesprin 2 from murine myocardium results in cardiomyopathy, altered nuclear morphology and inhibition of the biomechanical gene response. *PLoS genetics* **10**, e1004114, doi:10.1371/journal.pgen.1004114 (2014).
28 Fisher, D. Z., Chaudhary, N. & Blobel, G. cDNA sequencing of nuclear lamins A and C reveals primary and secondary structural homology to intermediate filament proteins. *Proceedings of the National Academy of Sciences of the United States of America* **83**, 6450-6454 (1986).
29 Ho, C. Y. & Lammerding, J. Lamins at a glance. *Journal of cell science* **125**, 2087-2093, doi:10.1242/jcs.087288 (2012).
30 Rober, R. A., Weber, K. & Osborn, M. Differential timing of nuclear lamin A/C expression in the various organs of the mouse embryo and the young animal: a developmental study. *Development (Cambridge, England)* **105**, 365-378 (1989).
31 Yang, S. H., Jung, H. J., Coffinier, C., Fong, L. G. & Young, S. G. Are B-type lamins essential in all mammalian cells? *Nucleus (Austin, Tex.)* **2**, 562-569, doi:10.4161/nucl.2.6.18085 (2011).
32 Eckersley-Maslin, M. A., Bergmann, J. H., Lazar, Z. & Spector, D. L. Lamin A/C is expressed in pluripotent mouse embryonic stem cells. *Nucleus (Austin, Tex.)* **4**, 53-60, doi:10.4161/nucl.23384 (2013).

33 Constantinescu, D., Gray, H. L., Sammak, P. J., Schatten, G. P. & Csoka, A. B. Lamin A/C expression is a marker of mouse and human embryonic stem cell differentiation. *Stem cells (Dayton, Ohio)* **24**, 177-185, doi:10.1634/stemcells.2004-0159 (2006).
34 Yang, S. H. *et al.* An absence of both lamin B1 and lamin B2 in keratinocytes has no effect on cell proliferation or the development of skin and hair. *Human molecular genetics* **20**, 3537-3544, doi:10.1093/hmg/ddr266 (2011).
35 Kim, Y., Zheng, X. & Zheng, Y. Proliferation and differentiation of mouse embryonic stem cells lacking all lamins. *Cell research* **23**, 1420-1423, doi:10.1038/cr.2013.118 (2013).
36 Lin, F. & Worman, H. J. Structural organization of the human gene encoding nuclear lamin A and nuclear lamin C. *The Journal of biological chemistry* **268**, 16321-16326 (1993).
37 Machiels, B. M. *et al.* An alternative splicing product of the lamin A/C gene lacks exon 10. *The Journal of biological chemistry* **271**, 9249-9253 (1996).
38 Davies, B. S. *et al.* Investigating the purpose of prelamin A processing. *Nucleus (Austin, Tex.)* **2**, 4-9, doi:10.1093/hmg/ddq158

10.4161/nucl.2.1.13723 (2011).
39 Gerace, L. & Blobel, G. The nuclear envelope lamina is reversibly depolymerized during mitosis. *Cell* **19**, 277-287, doi:10.1016/0092-8674(80)90409-2 (1980).
40 Dechat, T., Gesson, K. & Foisner, R. Lamina-independent lamins in the nuclear interior serve important functions. *Cold Spring Harbor symposia on quantitative biology* **75**, 533-543, doi:10.1101/sqb.2010.75.018 (2010).
41 Burke, B. & Stewart, C. L. The nuclear lamins: flexibility in function. *Nature reviews. Molecular cell biology* **14**, 13-24, doi:10.1038/nrm3488 (2013).
42 Stuurman, N., Heins, S. & Aebi, U. Nuclear lamins: their structure, assembly, and interactions. *Journal of structural biology* **122**, 42-66, doi:10.1006/jsbi.1998.3987 (1998).
43 Heitlinger, E. *et al.* The role of the head and tail domain in lamin structure and assembly: analysis of bacterially expressed chicken lamin A and truncated B2 lamins. *Journal of structural biology* **108**, 74-89 (1992).
44 Sasse, B., Aebi, U. & Stuurman, N. A tailless Drosophila lamin Dm0 fragment reveals lateral associations of dimers. *Journal of structural biology* **123**, 56-66, doi:10.1006/jsbi.1998.4006 (1998).
45 Shimi, T. *et al.* Structural organization of nuclear lamins A, C, B1, and B2 revealed by superresolution microscopy. *Mol Biol Cell* **26**, 4075-4086, doi:10.1091/mbc.E15-07-0461 (2015).
46 Kolb, T., Maass, K., Hergt, M., Aebi, U. & Herrmann, H. Lamin A and lamin C form homodimers and coexist in higher complex forms both in the nucleoplasmic fraction and in the lamina of cultured human cells. *Nucleus (Austin, Tex.)* **2**, 425-433, doi:10.4161/nucl.2.5.17765 (2011).
47 Kapinos, L. E. *et al.* Characterization of the head-to-tail overlap complexes formed by human lamin A, B1 and B2 "half-minilamin" dimers. *Journal of molecular biology* **396**, 719-731, doi:10.1016/j.jmb.2009.12.001 (2010).
48 Barton, L. J., Soshnev, A. A. & Geyer, P. K. Networking in the nucleus: a spotlight on LEM-domain proteins. *Curr Opin Cell Biol* **34**, 1-8, doi:10.1016/j.ceb.2015.03.005 (2015).
49 Lin, F. *et al.* MAN1, an inner nuclear membrane protein that shares the LEM domain with lamina-associated polypeptide 2 and emerin. *The Journal of biological chemistry* **275**, 4840-4847, doi:10.1074/jbc.275.7.4840 (2000).

50 Wilson, K. L. & Foisner, R. Lamin-binding Proteins. *Cold Spring Harbor perspectives in biology* **2**, a000554, doi:10.1101/cshperspect.a000554 (2010).
51 Guelen, L. *et al.* Domain organization of human chromosomes revealed by mapping of nuclear lamina interactions. *Nature* **453**, 948-951, doi:10.1038/nature06947 (2008).
52 Jamin, A. & Wiebe, M. S. Barrier to Autointegration Factor (BANF1): interwoven roles in nuclear structure, genome integrity, innate immunity, stress responses and progeria. *Curr Opin Cell Biol* **34**, 61-68, doi:10.1016/j.ceb.2015.05.006 (2015).
53 Haraguchi, T. *et al.* BAF is required for emerin assembly into the reforming nuclear envelope. *Journal of cell science* **114**, 4575-4585 (2001).
54 Solovei, I. *et al.* LBR and lamin A/C sequentially tether peripheral heterochromatin and inversely regulate differentiation. *Cell* **152**, 584-598, doi:10.1016/j.cell.2013.01.009 (2013).
55 Gonzalez, J. M., Navarro-Puche, A., Casar, B., Crespo, P. & Andres, V. Fast regulation of AP-1 activity through interaction of lamin A/C, ERK1/2, and c-Fos at the nuclear envelope. *J Cell Biol* **183**, 653-666, doi:10.1083/jcb.200805049 (2008).
56 de Las Heras, J. I. *et al.* Tissue-specific NETs alter genome organization and regulation even in a heterologous system. *Nucleus (Austin, Tex.)* **8**, 81-97, doi:10.1080/19491034.2016.1261230 (2017).
57 Spector, D. L. Nuclear domains. *Journal of cell science* **114**, 2891-2893 (2001).
58 Misteli, T. Protein dynamics: implications for nuclear architecture and gene expression. *Science (New York, N.Y.)* **291**, 843-847, doi:10.1126/science.291.5505.843 (2001).
59 Stanek, D. & Fox, A. H. Nuclear bodies: news insights into structure and function. *Curr Opin Cell Biol* **46**, 94-101, doi:10.1016/j.ceb.2017.05.001 (2017).
60 Huang, S. & Spector, D. L. U1 and U2 small nuclear RNAs are present in nuclear speckles. *Proceedings of the National Academy of Sciences of the United States of America* **89**, 305-308, doi:10.1073/pnas.89.1.305 (1992).
61 Maul, G. G., Negorev, D., Bell, P. & Ishov, A. M. Review: properties and assembly mechanisms of ND10, PML bodies, or PODs. *Journal of structural biology* **129**, 278-287, doi:10.1006/jsbi.2000.4239 (2000).
62 Pirrotta, V. & Li, H. B. A view of nuclear Polycomb bodies. *Current opinion in genetics & development* **22**, 101-109, doi:10.1016/j.gde.2011.11.004 (2012).
63 Shimi, T. *et al.* The A- and B-type nuclear lamin networks: microdomains involved in chromatin organization and transcription. *Genes & development* **22**, 3409-3421, doi:10.1101/gad.1735208 (2008).
64 Moir, R. D., Montag-Lowy, M. & Goldman, R. D. Dynamic properties of nuclear lamins: lamin B is associated with sites of DNA replication. *J Cell Biol* **125**, 1201-1212, doi:10.1083/jcb.125.6.1201 (1994).
65 Bronshtein, I. *et al.* Loss of lamin A function increases chromatin dynamics in the nuclear interior. *Nature communications* **6**, 8044, doi:10.1038/ncomms9044 (2015).
66 Naetar, N., Ferraioli, S. & Foisner, R. Lamins in the nuclear interior - life outside the lamina. *Journal of cell science* **130**, 2087-2096, doi:10.1242/jcs.203430 (2017).
67 Kind, J. & van Steensel, B. Stochastic genome-nuclear lamina interactions: modulating roles of Lamin A and BAF. *Nucleus (Austin, Tex.)* **5**, 124-130, doi:10.4161/nucl.28825 (2014).
68 Gesson, K., Vidak, S. & Foisner, R. Lamina-associated polypeptide (LAP)2alpha and nucleoplasmic lamins in adult stem cell regulation and disease. *Seminars in cell & developmental biology* **29**, 116-124, doi:10.1016/j.semcdb.2013.12.009 (2014).

69 Cesarini, E. *et al.* Lamin A/C sustains PcG protein architecture, maintaining transcriptional repression at target genes. *J Cell Biol* **211**, 533-551, doi:10.1083/jcb.201504035 (2015).
70 Lund, E. *et al.* Lamin A/C-promoter interactions specify chromatin state-dependent transcription outcomes. *Genome research* **23**, 1580-1589, doi:10.1101/gr.159400.113 (2013).
71 Buxboim, A. *et al.* Matrix elasticity regulates lamin-A,C phosphorylation and turnover with feedback to actomyosin. *Current biology : CB* **24**, 1909-1917, doi:10.1016/j.cub.2014.07.001 (2014).
72 Zwerger, M. *et al.* Myopathic lamin mutations impair nuclear stability in cells and tissue and disrupt nucleo-cytoskeletal coupling. *Human molecular genetics* **22**, 2335-2349, doi:10.1093/hmg/ddt079 (2013).
73 Misteli, T., Caceres, J. F. & Spector, D. L. The dynamics of a pre-mRNA splicing factor in living cells. *Nature* **387**, 523-527, doi:10.1038/387523a0 (1997).
74 Carmo-Fonseca, M., Pepperkok, R., Carvalho, M. T. & Lamond, A. I. Transcription-dependent colocalization of the U1, U2, U4/U6, and U5 snRNPs in coiled bodies. *The Journal of cell biology* **117**, 1-14 (1992).
75 Spector, D. L. Nuclear organization of pre-mRNA processing. *Current opinion in cell biology* **5**, 442-447 (1993).
76 O'Keefe, R. T., Mayeda, A., Sadowski, C. L., Krainer, A. R. & Spector, D. L. Disruption of pre-mRNA splicing in vivo results in reorganization of splicing factors. *The Journal of cell biology* **124**, 249-260 (1994).
77 Beyer, A. L. & Osheim, Y. N. Splice site selection, rate of splicing, and alternative splicing on nascent transcripts. *Genes & development* **2**, 754-765 (1988).
78 Jackson, D. A., Hassan, A. B., Errington, R. J. & Cook, P. R. Visualization of focal sites of transcription within human nuclei. *The EMBO journal* **12**, 1059-1065 (1993).
79 Wansink, D. G. *et al.* Fluorescent labeling of nascent RNA reveals transcription by RNA polymerase II in domains scattered throughout the nucleus. *The Journal of cell biology* **122**, 283-293 (1993).
80 Cmarko, D. *et al.* Ultrastructural analysis of transcription and splicing in the cell nucleus after bromo-UTP microinjection. *Molecular biology of the cell* **10**, 211-223 (1999).
81 Jagatheesan, G. *et al.* Colocalization of intranuclear lamin foci with RNA splicing factors. *Journal of cell science* **112 (Pt 24)**, 4651-4661 (1999).
82 Kumaran, R. I., Muralikrishna, B. & Parnaik, V. K. Lamin A/C speckles mediate spatial organization of splicing factor compartments and RNA polymerase II transcription. *The Journal of cell biology* **159**, 783-793, doi:10.1083/jcb.200204149 (2002).
83 Spann, T. P., Goldman, A. E., Wang, C., Huang, S. & Goldman, R. D. Alteration of nuclear lamin organization inhibits RNA polymerase II-dependent transcription. *The Journal of cell biology* **156**, 603-608, doi:10.1083/jcb.200112047 (2002).
84 Vecerova, J. *et al.* Formation of nuclear splicing factor compartments is independent of lamins A/C. *Molecular biology of the cell* **15**, 4904-4910, doi:10.1091/mbc.E04-07-0645 (2004).
85 Jahn, D. *et al.* A truncated lamin A in the Lmna -/- mouse line: implications for the understanding of laminopathies. *Nucleus (Austin, Tex.)* **3**, 463-474, doi:10.4161/nucl.21676 (2012).

86 Lin, S., Coutinho-Mansfield, G., Wang, D., Pandit, S. & Fu, X. D. The splicing factor SC35 has an active role in transcriptional elongation. *Nat Struct Mol Biol* **15**, 819-826, doi:10.1038/nsmb.1461 (2008).
87 Yuryev, A. *et al.* The C-terminal domain of the largest subunit of RNA polymerase II interacts with a novel set of serine/arginine-rich proteins. *Proceedings of the National Academy of Sciences of the United States of America* **93**, 6975-6980 (1996).
88 Ding, J. H. *et al.* Dilated cardiomyopathy caused by tissue-specific ablation of SC35 in the heart. *The EMBO journal* **23**, 885-896, doi:10.1038/sj.emboj.7600054 (2004).
89 Gruenbaum, Y., Margalit, A., Goldman, R. D., Shumaker, D. K. & Wilson, K. L. The nuclear lamina comes of age. *Nature reviews. Molecular cell biology* **6**, 21-31, doi:10.1038/nrm1550 (2005).
90 Depreux, F. F. *et al.* Disruption of the lamin A and matrin-3 interaction by myopathic LMNA mutations. *Human molecular genetics* **24**, 4284-4295, doi:10.1093/hmg/ddv160 (2015).
91 Gallego, M. E., Gattoni, R., Stevenin, J., Marie, J. & Expert-Bezancon, A. The SR splicing factors ASF/SF2 and SC35 have antagonistic effects on intronic enhancer-dependent splicing of the beta-tropomyosin alternative exon 6A. *The EMBO journal* **16**, 1772-1784, doi:10.1093/emboj/16.7.1772 (1997).
92 Xu, X. *et al.* ASF/SF2-regulated CaMKIIdelta alternative splicing temporally reprograms excitation-contraction coupling in cardiac muscle. *Cell* **120**, 59-72, doi:10.1016/j.cell.2004.11.036 (2005).
93 Zhang, T. *et al.* The cardiac-specific nuclear delta(B) isoform of Ca2+/calmodulin-dependent protein kinase II induces hypertrophy and dilated cardiomyopathy associated with increased protein phosphatase 2A activity. *The Journal of biological chemistry* **277**, 1261-1267, doi:10.1074/jbc.M108525200 (2002).
94 Zhang, T. *et al.* The deltaC isoform of CaMKII is activated in cardiac hypertrophy and induces dilated cardiomyopathy and heart failure. *Circulation research* **92**, 912-919, doi:10.1161/01.RES.0000069686.31472.C5 (2003).
95 Feng, Y. *et al.* SRp38 regulates alternative splicing and is required for Ca(2+) handling in the embryonic heart. *Developmental cell* **16**, 528-538, doi:10.1016/j.devcel.2009.02.009 (2009).
96 Havugimana, P. C. *et al.* A census of human soluble protein complexes. *Cell* **150**, 1068-1081, doi:10.1016/j.cell.2012.08.011 (2012).
97 Kim, J. H., Hahm, B., Kim, Y. K., Choi, M. & Jang, S. K. Protein-protein interaction among hnRNPs shuttling between nucleus and cytoplasm. *Journal of molecular biology* **298**, 395-405, doi:10.1006/jmbi.2000.3687 (2000).
98 Martinez-Contreras, R. *et al.* hnRNP proteins and splicing control. *Advances in experimental medicine and biology* **623**, 123-147 (2007).
99 Lleres, D., Denegri, M., Biggiogera, M., Ajuh, P. & Lamond, A. I. Direct interaction between hnRNP-M and CDC5L/PLRG1 proteins affects alternative splice site choice. *EMBO reports* **11**, 445-451, doi:10.1038/embor.2010.64 (2010).
100 Ajuh, P. *et al.* Functional analysis of the human CDC5L complex and identification of its components by mass spectrometry. *The EMBO journal* **19**, 6569-6581, doi:10.1093/emboj/19.23.6569 (2000).
101 Makarova, O. V. *et al.* A subset of human 35S U5 proteins, including Prp19, function prior to catalytic step 1 of splicing. *The EMBO journal* **23**, 2381-2391, doi:10.1038/sj.emboj.7600241 (2004).

102 Roux, K. J., Kim, D. I., Raida, M. & Burke, B. A promiscuous biotin ligase fusion protein identifies proximal and interacting proteins in mammalian cells. *J Cell Biol* **196**, 801-810, doi:10.1083/jcb.201112098 (2012).
103 Zhong, N., Radu, G., Ju, W. & Brown, W. T. Novel progerin-interactive partner proteins hnRNP E1, EGF, Mel 18, and UBC9 interact with lamin A/C. *Biochem Biophys Res Commun* **338**, 855-861, doi:10.1016/j.bbrc.2005.10.020 (2005).
104 Bonne, G. *et al.* Mutations in the gene encoding lamin A/C cause autosomal dominant Emery-Dreifuss muscular dystrophy. *Nature genetics* **21**, 285-288, doi:10.1038/6799 (1999).
105 Bonne, G., Leturcq, F. & Ben Yaou, R. in *GeneReviews(R)* (eds R. A. Pagon *et al.*) (University of Washington, Seattle

University of Washington, Seattle. GeneReviews is a registered trademark of the University of Washington, Seattle. All rights reserved., 1993).
106 Fatkin, D. *et al.* Missense mutations in the rod domain of the lamin A/C gene as causes of dilated cardiomyopathy and conduction-system disease. *The New England journal of medicine* **341**, 1715-1724, doi:10.1056/nejm199912023412302 (1999).
107 Worman, H. J. & Bonne, G. "Laminopathies": a wide spectrum of human diseases. *Exp Cell Res* **313**, 2121-2133, doi:10.1016/j.yexcr.2007.03.028 (2007).
108 Szeverenyi, I. *et al.* The Human Intermediate Filament Database: comprehensive information on a gene family involved in many human diseases. *Human mutation* **29**, 351-360, doi:10.1002/humu.20652 (2008).
109 Cao, H. & Hegele, R. A. Nuclear lamin A/C R482Q mutation in canadian kindreds with Dunnigan-type familial partial lipodystrophy. *Human molecular genetics* **9**, 109-112 (2000).
110 Broers, J. L., Ramaekers, F. C., Bonne, G., Yaou, R. B. & Hutchison, C. J. Nuclear lamins: laminopathies and their role in premature ageing. *Physiological reviews* **86**, 967-1008, doi:10.1152/physrev.00047.2005 (2006).
111 Brown, C. A. *et al.* Novel and recurrent mutations in lamin A/C in patients with Emery-Dreifuss muscular dystrophy. *American journal of medical genetics* **102**, 359-367 (2001).
112 Bertrand, A. T., Chikhaoui, K., Yaou, R. B. & Bonne, G. Clinical and genetic heterogeneity in laminopathies. *Biochemical Society transactions* **39**, 1687-1692, doi:10.1042/bst20110670 (2011).
113 Hoorntje, E. T. *et al.* Lamin A/C-Related Cardiac DiseaseCLINICAL PERSPECTIVE: Late Onset With a Variable and Mild Phenotype in a Large Cohort of Patients With the Lamin A/C p.(Arg331Gln) Founder Mutation. *Circulation: Genomic and Precision Medicine* **10**, e001631 (2017).
114 van Berlo, J. H. *et al.* Meta-analysis of clinical characteristics of 299 carriers of LMNA gene mutations: do lamin A/C mutations portend a high risk of sudden death? *Journal of molecular medicine (Berlin, Germany)* **83**, 79-83, doi:10.1007/s00109-004-0589-1 (2005).
115 Becane, H. M. *et al.* High incidence of sudden death with conduction system and myocardial disease due to lamins A and C gene mutation. *Pacing and clinical electrophysiology : PACE* **23**, 1661-1666 (2000).
116 Perez-Serra, A. *et al.* A novel mutation in lamin a/c causing familial dilated cardiomyopathy associated with sudden cardiac death. *Journal of cardiac failure* **21**, 217-225, doi:10.1016/j.cardfail.2014.12.003 (2015).

117 Taylor, M. R. *et al.* Natural history of dilated cardiomyopathy due to lamin A/C gene mutations. *Journal of the American College of Cardiology* **41**, 771-780 (2003).
118 Arbustini, E. *et al.* Autosomal dominant dilated cardiomyopathy with atrioventricular block: a lamin A/C defect-related disease. *Journal of the American College of Cardiology* **39**, 981-990 (2002).
119 van Rijsingen, I. A. *et al.* Risk factors for malignant ventricular arrhythmias in lamin a/c mutation carriers a European cohort study. *Journal of the American College of Cardiology* **59**, 493-500, doi:10.1016/j.jacc.2011.08.078 (2012).
120 van Rijsingen, I. A. *et al.* Lamin A/C mutation is independently associated with an increased risk of arterial and venous thromboembolic complications. *International journal of cardiology* **168**, 472-477, doi:10.1016/j.ijcard.2012.09.118 (2013).
121 Fatkin, D. & Graham, R. M. Molecular mechanisms of inherited cardiomyopathies. *Physiological reviews* **82**, 945-980, doi:10.1152/physrev.00012.2002 (2002).
122 van Rijsingen, I. A. *et al.* Gender-specific differences in major cardiac events and mortality in lamin A/C mutation carriers. *European journal of heart failure* **15**, 376-384, doi:10.1093/eurjhf/hfs191 (2013).
123 Pasotti, M. *et al.* Long-term outcome and risk stratification in dilated cardiolaminopathies. *Journal of the American College of Cardiology* **52**, 1250-1260, doi:10.1016/j.jacc.2008.06.044 (2008).
124 Tesson, F. *et al.* Lamin A/C mutations in dilated cardiomyopathy. *Cardiology journal* **21**, 331-342, doi:10.5603/CJ.a2014.0037 (2014).
125 Pugh, T. J. *et al.* The landscape of genetic variation in dilated cardiomyopathy as surveyed by clinical DNA sequencing. *Genetics in medicine : official journal of the American College of Medical Genetics* **16**, 601-608, doi:10.1038/gim.2013.204 (2014).
126 Zimmerman, R. S. *et al.* A novel custom resequencing array for dilated cardiomyopathy. *Genetics in medicine : official journal of the American College of Medical Genetics* **12**, 268-278, doi:10.1097/GIM.0b013e3181d6f7c0 (2010).
127 Millat, G. *et al.* Clinical and mutational spectrum in a cohort of 105 unrelated patients with dilated cardiomyopathy. *European journal of medical genetics* **54**, e570-575, doi:10.1016/j.ejmg.2011.07.005 (2011).
128 Sebillon, P. *et al.* Expanding the phenotype of LMNA mutations in dilated cardiomyopathy and functional consequences of these mutations. *Journal of medical genetics* **40**, 560-567 (2003).
129 Millat, G. *et al.* Validation of high-resolution DNA melting analysis for mutation scanning of the LMNA gene. *Clinical biochemistry* **42**, 892-898, doi:10.1016/j.clinbiochem.2009.01.016 (2009).
130 Parks, S. B. *et al.* Lamin A/C mutation analysis in a cohort of 324 unrelated patients with idiopathic or familial dilated cardiomyopathy. *American heart journal* **156**, 161-169, doi:10.1016/j.ahj.2008.01.026 (2008).
131 Narula, N. *et al.* Quantitative expression of the mutated lamin A/C gene in patients with cardiolaminopathy. *Journal of the American College of Cardiology* **60**, 1916-1920, doi:10.1016/j.jacc.2012.05.059 (2012).
132 Perez-Serra, A. *et al.* Genetic basis of dilated cardiomyopathy. *International journal of cardiology* **224**, 461-472, doi:10.1016/j.ijcard.2016.09.068 (2016).

133 Forleo, C. *et al.* Clinical and functional characterization of a novel mutation in lamin a/c gene in a multigenerational family with arrhythmogenic cardiac laminopathy. *PloS one* **10**, e0121723 (2015).
134 Haas, J. *et al.* Atlas of the clinical genetics of human dilated cardiomyopathy. *European heart journal* **36**, 1123-1135a, doi:10.1093/eurheartj/ehu301 (2015).
135 Walsh, R. *et al.* Reassessment of Mendelian gene pathogenicity using 7,855 cardiomyopathy cases and 60,706 reference samples. *Genetics in Medicine* **19**, 192 (2017).
136 Ambrosi, P. *et al.* A novel overlapping phenotype characterized by lipodystrophy, mandibular dysplasia, and dilated cardiomyopathy associated with a new mutation in the LMNA gene. *International journal of cardiology* **209**, 317-318 (2016).
137 Kayvanpour, E. *et al.* Genotype-phenotype associations in dilated cardiomyopathy: meta-analysis on more than 8000 individuals. *Clinical Research in Cardiology* **106**, 127-139, doi:10.1007/s00392-016-1033-6 (2017).
138 Hasselberg, N. E. *et al.* Lamin A/C cardiomyopathy: young onset, high penetrance, and frequent need for heart transplantation. *European heart journal* (2017).
139 Nishiuchi, S. *et al.* Gene-Based Risk Stratification for Cardiac Disorders in LMNA Mutation CarriersCLINICAL PERSPECTIVE. *Circulation: Genomic and Precision Medicine* **10**, e001603 (2017).
140 Gerbino, A., Procino, G., Svelto, M. & Carmosino, M. Role of Lamin A/C Gene Mutations in the Signaling Defects Leading to Cardiomyopathies. *Frontiers in physiology* **9**, 1356, doi:10.3389/fphys.2018.01356 (2018).
141 Arimura, T. *et al.* Mouse model carrying H222P-Lmna mutation develops muscular dystrophy and dilated cardiomyopathy similar to human striated muscle laminopathies. *Human molecular genetics* **14**, 155-169, doi:10.1093/hmg/ddi017 (2005).
142 Brull, A., Morales Rodriguez, B., Bonne, G., Muchir, A. & Bertrand, A. T. The Pathogenesis and Therapies of Striated Muscle Laminopathies. *Frontiers in physiology* **9**, 1533, doi:10.3389/fphys.2018.01533 (2018).
143 Scharner, J., Figeac, N., Ellis, J. A. & Zammit, P. S. Ameliorating pathogenesis by removing an exon containing a missense mutation: a potential exon-skipping therapy for laminopathies. *Gene therapy* **22**, 503-515, doi:10.1038/gt.2015.8 (2015).
144 Lee, J. M. *et al.* Modulation of LMNA splicing as a strategy to treat prelamin A diseases. *The Journal of clinical investigation* **126**, 1592-1602, doi:10.1172/jci85908 (2016).
145 Azibani, F. *et al.* Gene Therapy via Trans-Splicing for LMNA-Related Congenital Muscular Dystrophy. *Molecular therapy. Nucleic acids* **10**, 376-386, doi:10.1016/j.omtn.2017.12.012 (2018).
146 Davis, R. J. The mitogen-activated protein kinase signal transduction pathway. *The Journal of biological chemistry* **268**, 14553-14556 (1993).
147 Keshet, Y. & Seger, R. The MAP kinase signaling cascades: a system of hundreds of components regulates a diverse array of physiological functions. *Methods in molecular biology (Clifton, N.J.)* **661**, 3-38, doi:10.1007/978-1-60761-795-2_1 (2010).
148 Muchir, A. *et al.* Activation of MAPK pathways links LMNA mutations to cardiomyopathy in Emery-Dreifuss muscular dystrophy. *The Journal of clinical investigation* **117**, 1282-1293, doi:10.1172/jci29042 (2007).
149 Muchir, A., Wu, W. & Worman, H. J. Reduced expression of A-type lamins and emerin activates extracellular signal-regulated kinase in cultured cells. *Biochimica et biophysica acta* **1792**, 75-81, doi:10.1016/j.bbadis.2008.10.012 (2009).

150 Lammerding, J. *et al.* Lamin A/C deficiency causes defective nuclear mechanics and mechanotransduction. *The Journal of clinical investigation* **113**, 370-378 (2004).
151 Chatzifrangkeskou, M. *et al.* Cofilin-1 phosphorylation catalyzed by ERK1/2 alters cardiac actin dynamics in dilated cardiomyopathy caused by lamin A/C gene mutation. *Human molecular genetics* **27**, 3060-3078, doi:10.1093/hmg/ddy215 (2018).
152 Muchir, A. *et al.* Treatment with selumetinib preserves cardiac function and improves survival in cardiomyopathy caused by mutation in the lamin A/C gene. *Cardiovascular research* **93**, 311-319, doi:10.1093/cvr/cvr301 (2012).
153 Wu, W., Shan, J., Bonne, G., Worman, H. J. & Muchir, A. Pharmacological inhibition of c-Jun N-terminal kinase signaling prevents cardiomyopathy caused by mutation in LMNA gene. *Biochimica et biophysica acta* **1802**, 632-638, doi:10.1016/j.bbadis.2010.04.001 (2010).
154 Wu, W. *et al.* Macrocyclic MEK1/2 inhibitor with efficacy in a mouse model of cardiomyopathy caused by lamin A/C gene mutation. *Bioorganic & medicinal chemistry* **25**, 1004-1013, doi:10.1016/j.bmc.2016.12.014 (2017).
155 Chiarini, F. *et al.* The Cutting Edge: The Role of mTOR Signaling in Laminopathies. *International journal of molecular sciences* **20**, doi:10.3390/ijms20040847 (2019).
156 Choi, J. C. *et al.* Temsirolimus activates autophagy and ameliorates cardiomyopathy caused by lamin A/C gene mutation. *Science translational medicine* **4**, 144ra102, doi:10.1126/scitranslmed.3003875 (2012).
157 DuBose, A. J. *et al.* Everolimus rescues multiple cellular defects in laminopathy-patient fibroblasts. *Proceedings of the National Academy of Sciences of the United States of America* **115**, 4206-4211, doi:10.1073/pnas.1802811115 (2018).
158 Worman, H. J. Inner nuclear membrane and regulation of Smad-mediated signaling. *Biochimica et biophysica acta* **1761**, 626-631, doi:10.1016/j.bbalip.2006.02.010 (2006).
159 Pan, D. *et al.* The integral inner nuclear membrane protein MAN1 physically interacts with the R-Smad proteins to repress signaling by the transforming growth factor-{beta} superfamily of cytokines. *The Journal of biological chemistry* **280**, 15992-16001, doi:10.1074/jbc.M411234200 (2005).
160 Van Berlo, J. H. *et al.* A-type lamins are essential for TGF-beta1 induced PP2A to dephosphorylate transcription factors. *Human molecular genetics* **14**, 2839-2849, doi:10.1093/hmg/ddi316 (2005).
161 Rosenkranz, S. TGF-beta1 and angiotensin networking in cardiac remodeling. *Cardiovascular research* **63**, 423-432, doi:10.1016/j.cardiores.2004.04.030 (2004).
162 Chatzifrangkeskou, M. *et al.* ERK1/2 directly acts on CTGF/CCN2 expression to mediate myocardial fibrosis in cardiomyopathy caused by mutations in the lamin A/C gene. *Human molecular genetics* **25**, 2220-2233, doi:10.1093/hmg/ddw090 (2016).
163 Le Dour, C. *et al.* Decreased WNT/beta-catenin signalling contributes to the pathogenesis of dilated cardiomyopathy caused by mutations in the lamin a/C gene. *Human molecular genetics* **26**, 333-343, doi:10.1093/hmg/ddw389 (2017).
164 Mounkes, L. C., Kozlov, S. V., Rottman, J. N. & Stewart, C. L. Expression of an LMNA-N195K variant of A-type lamins results in cardiac conduction defects and death in mice. *Human molecular genetics* **14**, 2167-2180, doi:10.1093/hmg/ddi221 (2005).
165 Macquart, C. *et al.* Microtubule cytoskeleton regulates connexin 43 localization and cardiac conduction in cardiomyopathy caused by mutation in A-type lamins gene. *Human molecular genetics*, doi:10.1093/hmg/ddy227 (2018).

166 Markiewicz, E. *et al.* The inner nuclear membrane protein emerin regulates beta-catenin activity by restricting its accumulation in the nucleus. *The EMBO journal* **25**, 3275-3285, doi:10.1038/sj.emboj.7601230 (2006).
167 Fagotto, F., Gluck, U. & Gumbiner, B. M. Nuclear localization signal-independent and importin/karyopherin-independent nuclear import of beta-catenin. *Current biology : CB* **8**, 181-190, doi:10.1016/s0960-9822(98)70082-x (1998).
168 Neumann, S. *et al.* Nesprin-2 interacts with {alpha}-catenin and regulates Wnt signaling at the nuclear envelope. *The Journal of biological chemistry* **285**, 34932-34938, doi:10.1074/jbc.M110.119651 (2010).
169 Auguste, G. *et al.* Suppression of Activated FOXO Transcription Factors in the Heart Prolongs Survival in a Mouse Model of Laminopathies. *Circulation research* **122**, 678-692, doi:10.1161/circresaha.117.312052 (2018).
170 Zhang, X., Tang, N., Hadden, T. J. & Rishi, A. K. Akt, FoxO and regulation of apoptosis. *Biochimica et biophysica acta* **1813**, 1978-1986, doi:10.1016/j.bbamcr.2011.03.010 (2011).
171 Ho, C. Y., Jaalouk, D. E., Vartiainen, M. K. & Lammerding, J. Lamin A/C and emerin regulate MKL1-SRF activity by modulating actin dynamics. *Nature* **497**, 507-511, doi:10.1038/nature12105 (2013).
172 Bertrand, A. T. *et al.* Cellular microenvironments reveal defective mechanosensing responses and elevated YAP signaling in LMNA-mutated muscle precursors. *Journal of cell science* **127**, 2873-2884, doi:10.1242/jcs.144907 (2014).
173 Michels, V. V. *et al.* The frequency of familial dilated cardiomyopathy in a series of patients with idiopathic dilated cardiomyopathy. *The New England journal of medicine* **326**, 77-82, doi:10.1056/nejm199201093260201 (1992).
174 McCartan, C., Mason, R., Jayasinghe, S. R. & Griffiths, L. R. Cardiomyopathy classification: ongoing debate in the genomics era. *Biochemistry research international* **2012**, 796926, doi:10.1155/2012/796926 (2012).
175 McNally, E. M., Golbus, J. R. & Puckelwartz, M. J. Genetic mutations and mechanisms in dilated cardiomyopathy. *The Journal of clinical investigation* **123**, 19-26, doi:10.1172/jci62862 (2013).
176 Herman, D. S. *et al.* Truncations of titin causing dilated cardiomyopathy. *The New England journal of medicine* **366**, 619-628, doi:10.1056/NEJMoa1110186 (2012).
177 Hinson, J. T. *et al.* HEART DISEASE. Titin mutations in iPS cells define sarcomere insufficiency as a cause of dilated cardiomyopathy. *Science (New York, N.Y.)* **349**, 982-986, doi:10.1126/science.aaa5458 (2015).
178 Hershberger, R. E. & Siegfried, J. D. Update 2011: clinical and genetic issues in familial dilated cardiomyopathy. *Journal of the American College of Cardiology* **57**, 1641-1649, doi:10.1016/j.jacc.2011.01.015 (2011).
179 Kamisago, M. *et al.* Mutations in sarcomere protein genes as a cause of dilated cardiomyopathy. *The New England journal of medicine* **343**, 1688-1696, doi:10.1056/nejm200012073432304 (2000).
180 Brauch, K. M. *et al.* Mutations in ribonucleic acid binding protein gene cause familial dilated cardiomyopathy. *Journal of the American College of Cardiology* **54**, 930-941, doi:10.1016/j.jacc.2009.05.038 (2009).
181 Haas, J. *et al.* Atlas of the clinical genetics of human dilated cardiomyopathy. *European heart journal* **36**, 1123 (2015).

182 Olson, T. M. *et al.* Sodium channel mutations and susceptibility to heart failure and atrial fibrillation. *Jama* **293**, 447-454, doi:10.1001/jama.293.4.447 (2005).
183 Vatta, M. *et al.* Mutations in Cypher/ZASP in patients with dilated cardiomyopathy and left ventricular non-compaction. *Journal of the American College of Cardiology* **42**, 2014-2027 (2003).
184 Mohapatra, B. *et al.* Mutations in the muscle LIM protein and alpha-actinin-2 genes in dilated cardiomyopathy and endocardial fibroelastosis. *Molecular genetics and metabolism* **80**, 207-215 (2003).
185 Schmitt, J. P. *et al.* Dilated cardiomyopathy and heart failure caused by a mutation in phospholamban. *Science (New York, N.Y.)* **299**, 1410-1413, doi:10.1126/science.1081578 (2003).
186 Taylor, M. R. *et al.* Prevalence of desmin mutations in dilated cardiomyopathy. *Circulation* **115**, 1244-1251, doi:10.1161/circulationaha.106.646778 (2007).
187 Hershberger, R. E., Hedges, D. J. & Morales, A. Dilated cardiomyopathy: the complexity of a diverse genetic architecture. *Nature reviews. Cardiology* **10**, 531-547, doi:10.1038/nrcardio.2013.105 (2013).
188 Brodsky, G. L. *et al.* Lamin A/C gene mutation associated with dilated cardiomyopathy with variable skeletal muscle involvement. *Circulation* **101**, 473-476 (2000).
189 van den Hoogenhof, M. M., Pinto, Y. M. & Creemers, E. E. RNA Splicing: Regulation and Dysregulation in the Heart. *Circulation research* **118**, 454-468, doi:10.1161/circresaha.115.307872 (2016).
190 Yang, J. *et al.* RBM24 is a major regulator of muscle-specific alternative splicing. *Developmental cell* **31**, 87-99, doi:10.1016/j.devcel.2014.08.025 (2014).
191 Liu, J., Kong, X., Zhang, M., Yang, X. & Xu, X. RNA binding protein 24 deletion disrupts global alternative splicing and causes dilated cardiomyopathy. *Protein & cell* **10**, 405-416, doi:10.1007/s13238-018-0578-8 (2019).
192 Gaertner, A., Brodehl, A. & Milting, H. Screening for mutations in human cardiomyopathy-is RBM24 a new but rare disease gene? *Protein & cell* **10**, 393-394, doi:10.1007/s13238-018-0590-z (2019).
193 Ye, J. *et al.* hnRNP U protein is required for normal pre-mRNA splicing and postnatal heart development and function. *Proceedings of the National Academy of Sciences of the United States of America* **112**, E3020-3029, doi:10.1073/pnas.1508461112 (2015).
194 Wei, C. *et al.* Repression of the Central Splicing Regulator RBFox2 Is Functionally Linked to Pressure Overload-Induced Heart Failure. *Cell reports*, doi:10.1016/j.celrep.2015.02.013 (2015).
195 Refaat, M. M. *et al.* Genetic variation in the alternative splicing regulator RBM20 is associated with dilated cardiomyopathy. *Heart rhythm* **9**, 390-396, doi:10.1016/j.hrthm.2011.10.016 (2012).
196 Li, D. *et al.* Identification of novel mutations in RBM20 in patients with dilated cardiomyopathy. *Clinical and translational science* **3**, 90-97, doi:10.1111/j.1752-8062.2010.00198.x (2010).
197 Kong, S. W. *et al.* Heart failure-associated changes in RNA splicing of sarcomere genes. *Circulation. Cardiovascular genetics* **3**, 138-146, doi:10.1161/CIRCGENETICS.109.904698 (2010).

198 Goonasekera, S. A. *et al.* Decreased cardiac L-type Ca(2)(+) channel activity induces hypertrophy and heart failure in mice. *The Journal of clinical investigation* **122**, 280-290, doi:10.1172/JCI58227 (2012).
199 Chen, X. *et al.* L-type Ca2+ channel density and regulation are altered in failing human ventricular myocytes and recover after support with mechanical assist devices. *Circulation research* **91**, 517-524 (2002).
200 Hu, Z. *et al.* Aberrant Splicing Promotes Proteasomal Degradation of L-type CaV1.2 Calcium Channels by Competitive Binding for CaVbeta Subunits in Cardiac Hypertrophy. *Scientific reports* **6**, 35247, doi:10.1038/srep35247 (2016).
201 Herman , D. S. *et al.* Truncations of Titin Causing Dilated Cardiomyopathy. *New England Journal of Medicine* **366**, 619-628, doi:doi:10.1056/NEJMoa1110186 (2012).
202 Parks, S. B. *et al.* Lamin A/C mutation analysis in a cohort of 324 unrelated patients with idiopathic or familial dilated cardiomyopathy. *American heart journal* **156**, 161-169 (2008).
203 Garcia-Pavia, P. *et al.* Desmosomal protein gene mutations in patients with idiopathic dilated cardiomyopathy undergoing cardiac transplantation: a clinicopathological study. *Heart* **97**, 1744-1752, doi:10.1136/hrt.2011.227967 (2011).
204 Obler, D. *et al.* Familial dilated cardiomyopathy secondary to dystrophin splice site mutation. *Journal of cardiac failure* **16**, 194-199, doi:10.1016/j.cardfail.2009.11.009 (2010).
205 Otomo, J. *et al.* Electrophysiological and histopathological characteristics of progressive atrioventricular block accompanied by familial dilated cardiomyopathy caused by a novel mutation of lamin A/C gene. *Journal of cardiovascular electrophysiology* **16**, 137-145 (2005).
206 Blech-Hermoni, Y. & Ladd, A. N. RNA binding proteins in the regulation of heart development. *The international journal of biochemistry & cell biology* **45**, 2467-2478, doi:10.1016/j.biocel.2013.08.008 (2013).
207 Beraldi, R. *et al.* Rbm20-deficient cardiogenesis reveals early disruption of RNA processing and sarcomere remodeling establishing a developmental etiology for dilated cardiomyopathy. *Human molecular genetics* **23**, 3779-3791, doi:10.1093/hmg/ddu091 (2014).
208 Guo, W. *et al.* RBM20, a gene for hereditary cardiomyopathy, regulates titin splicing. *Nature medicine* **18**, 766-773, doi:10.1038/nm.2693 (2012).
209 Long, Jennifer C. & Caceres, Javier F. The SR protein family of splicing factors: master regulators of gene expression. *Biochemical Journal* **417**, 15-27, doi:10.1042/bj20081501 (2009).
210 Ghosh, G. & Adams, J. A. Phosphorylation mechanism and structure of serine-arginine protein kinases. *The FEBS journal* **278**, 587-597, doi:10.1111/j.1742-4658.2010.07992.x (2011).
211 Zhou, Z. & Fu, X. D. Regulation of splicing by SR proteins and SR protein-specific kinases. *Chromosoma* **122**, 191-207, doi:10.1007/s00412-013-0407-z (2013).
212 Maatz, H. *et al.* RNA-binding protein RBM20 represses splicing to orchestrate cardiac pre-mRNA processing. *The Journal of clinical investigation* **124**, 3419-3430, doi:10.1172/jci74523 (2014).
213 Wang, E. T. *et al.* Alternative isoform regulation in human tissue transcriptomes. *Nature* **456**, 470-476,

doi:http://www.nature.com/nature/journal/v456/n7221/suppinfo/nature07509_S1.html (2008).
214 Methawasin, M. *et al.* Experimentally increasing titin compliance in a novel mouse model attenuates the Frank-Starling mechanism but has a beneficial effect on diastole. *Circulation* **129**, 1924-1936, doi:10.1161/CIRCULATIONAHA.113.005610 (2014).
215 Labeit, S. & Kolmerer, B. Titins: giant proteins in charge of muscle ultrastructure and elasticity. *Science* **270**, 293-296 (1995).
216 Helmes, M., Trombitas, K. & Granzier, H. Titin develops restoring force in rat cardiac myocytes. *Circulation research* **79**, 619-626 (1996).
217 Bang, M. L. *et al.* The complete gene sequence of titin, expression of an unusual approximately 700-kDa titin isoform, and its interaction with obscurin identify a novel Z-line to I-band linking system. *Circulation research* **89**, 1065-1072 (2001).
218 Lahmers, S., Wu, Y., Call, D. R., Labeit, S. & Granzier, H. Developmental control of titin isoform expression and passive stiffness in fetal and neonatal myocardium. *Circulation research* **94**, 505-513, doi:10.1161/01.RES.0000115522.52554.86 (2004).
219 Granzier, H. L. & Irving, T. C. Passive tension in cardiac muscle: contribution of collagen, titin, microtubules, and intermediate filaments. *Biophysical journal* **68**, 1027-1044, doi:10.1016/S0006-3495(95)80278-X (1995).
220 Opitz, C. A., Leake, M. C., Makarenko, I., Benes, V. & Linke, W. A. Developmentally regulated switching of titin size alters myofibrillar stiffness in the perinatal heart. *Circulation research* **94**, 967-975, doi:10.1161/01.RES.0000124301.48193.E1 (2004).
221 Warren, C. M., Krzesinski, P. R., Campbell, K. S., Moss, R. L. & Greaser, M. L. Titin isoform changes in rat myocardium during development. *Mechanisms of development* **121**, 1301-1312, doi:http://dx.doi.org/10.1016/j.mod.2004.07.003 (2004).
222 Fukuda, N., Wu, Y., Farman, G., Irving, T. C. & Granzier, H. Titin isoform variance and length dependence of activation in skinned bovine cardiac muscle. *The Journal of physiology* **553**, 147-154, doi:10.1113/jphysiol.2003.049759 (2003).
223 Agarkova, I. & Perriard, J. C. The M-band: an elastic web that crosslinks thick filaments in the center of the sarcomere. *Trends in cell biology* **15**, 477-485, doi:10.1016/j.tcb.2005.07.001 (2005).
224 Obermann, W. M., Gautel, M., Weber, K. & Furst, D. O. Molecular structure of the sarcomeric M band: mapping of titin and myosin binding domains in myomesin and the identification of a potential regulatory phosphorylation site in myomesin. *The EMBO journal* **16**, 211-220, doi:10.1093/emboj/16.2.211 (1997).
225 Agarkova, I., Auerbach, D., Ehler, E. & Perriard, J. C. A novel marker for vertebrate embryonic heart, the EH-myomesin isoform. *The Journal of biological chemistry* **275**, 10256-10264 (2000).
226 Siedner, S. *et al.* Developmental changes in contractility and sarcomeric proteins from the early embryonic to the adult stage in the mouse heart. *The Journal of physiology* **548**, 493-505, doi:10.1113/jphysiol.2002.036509 (2003).
227 Schoenauer, R. *et al.* EH-myomesin splice isoform is a novel marker for dilated cardiomyopathy. *Basic research in cardiology* **106**, 233-247, doi:10.1007/s00395-010-0131-2 (2011).
228 Makarenko, I. *et al.* Passive stiffness changes caused by upregulation of compliant titin isoforms in human dilated cardiomyopathy hearts. *Circulation research* **95**, 708-716, doi:10.1161/01.RES.0000143901.37063.2f (2004).

229 Nagueh, S. F. *et al.* Altered titin expression, myocardial stiffness, and left ventricular function in patients with dilated cardiomyopathy. *Circulation* **110**, 155-162, doi:10.1161/01.CIR.0000135591.37759.AF (2004).
230 Rajan, S. *et al.* Molecular and functional characterization of a novel cardiac-specific human tropomyosin isoform. *Circulation* **121**, 410-418, doi:10.1161/CIRCULATIONAHA.109.889725 (2010).
231 Zhou, Q. *et al.* Ablation of Cypher, a PDZ-LIM domain Z-line protein, causes a severe form of congenital myopathy. *The Journal of cell biology* **155**, 605-612, doi:10.1083/jcb.200107092 (2001).
232 Arimura, T. *et al.* Impaired binding of ZASP/Cypher with phosphoglucomutase 1 is associated with dilated cardiomyopathy. *Cardiovascular research* **83**, 80-88, doi:10.1093/cvr/cvp119 (2009).
233 Gray, C. B. & Heller Brown, J. CaMKIIdelta subtypes: localization and function. *Frontiers in pharmacology* **5**, 15, doi:10.3389/fphar.2014.00015 (2014).
234 Dzhura, I., Wu, Y., Colbran, R. J., Balser, J. R. & Anderson, M. E. Calmodulin kinase determines calcium-dependent facilitation of L-type calcium channels. *Nature cell biology* **2**, 173-177, doi:10.1038/35004052 (2000).
235 Hidalgo, C. G. *et al.* The multifunctional Ca(2+)/calmodulin-dependent protein kinase II delta (CaMKIIdelta) phosphorylates cardiac titin's spring elements. *Journal of molecular and cellular cardiology* **54**, 90-97, doi:10.1016/j.yjmcc.2012.11.012 (2013).
236 Kruger, M. *et al.* Thyroid hormone regulates developmental titin isoform transitions via the phosphatidylinositol-3-kinase/ AKT pathway. *Circulation research* **102**, 439-447, doi:10.1161/circresaha.107.162719 (2008).
237 Wu, Y., Peng, J., Campbell, K. B., Labeit, S. & Granzier, H. Hypothyroidism leads to increased collagen-based stiffness and re-expression of large cardiac titin isoforms with high compliance. *Journal of molecular and cellular cardiology* **42**, 186-195, doi:http://dx.doi.org/10.1016/j.yjmcc.2006.09.017 (2007).
238 Zhu, C., Yin, Z., Tan, B. & Guo, W. Insulin regulates titin pre-mRNA splicing through the PI3K-Akt-mTOR kinase axis in a RBM20-dependent manner. *Biochimica et biophysica acta* **1863**, 2363-2371, doi:10.1016/j.bbadis.2017.06.023 (2017).
239 Stamm, S. Regulation of alternative splicing by reversible protein phosphorylation. *The Journal of biological chemistry* **283**, 1223-1227, doi:10.1074/jbc.R700034200 (2008).
240 Lipp, J. J., Marvin, M. C., Shokat, K. M. & Guthrie, C. SR protein kinases promote splicing of nonconsensus introns. *Nat Struct Mol Biol* **22**, 611-617, doi:10.1038/nsmb.3057 http://www.nature.com/nsmb/journal/v22/n8/abs/nsmb.3057.html#supplementary-information (2015).
241 Zhou, Z. *et al.* The Akt-SRPK-SR axis constitutes a major pathway in transducing EGF signaling to regulate alternative splicing in the nucleus. *Molecular cell* **47**, 422-433, doi:10.1016/j.molcel.2012.05.014 (2012).
242 Zhu, C. *et al.* RBM20 is an essential factor for thyroid hormone-regulated titin isoform transition. *Journal of molecular cell biology* **7**, 88-90, doi:10.1093/jmcb/mjv002 (2015).
243 Zhu, C., Yin, z. & guo, w. Insulin and Angiotensin II Regulate Titin Alternative Splicing via Rbm20. *The FASEB Journal* **29** (2015).
244 Ito, J. *et al.* RBM20 and RBM24 cooperatively promote the expression of short enh splice variants. *FEBS letters* **590**, 2262-2274 (2016).

245 Dauksaite, V. & Gotthardt, M. Molecular basis of titin exon exclusion by RBM20 and the novel titin splice regulator PTB4. *Nucleic acids research* **46**, 5227-5238, doi:10.1093/nar/gky165 (2018).
246 George, C. H. *et al.* Alternative Splicing of Ryanodine Receptors Modulates Cardiomyocyte Ca²⁺ Signaling and Susceptibility to Apoptosis. *Circulation research* **100**, 874 (2007).
247 Tang, Y., Tian, X., Wang, R., Fill, M. & Chen, S. R. W. Abnormal Termination of Ca²⁺ Release Is a Common Defect of RyR2 Mutations Associated With Cardiomyopathies<span hwp:id="article-title-59" class="sub-article-title">Novelty and Significance</span&gt. *Circulation research* **110**, 968 (2012).
248 Holaska, J. M., Rais-Bahrami, S. & Wilson, K. L. Lmo7 is an emerin-binding protein that regulates the transcription of emerin and many other muscle-relevant genes. *Human molecular genetics* **15**, 3459-3472, doi:10.1093/hmg/ddl423 (2006).
249 Ooshio, T. *et al.* Involvement of LMO7 in the association of two cell-cell adhesion molecules, nectin and E-cadherin, through afadin and alpha-actinin in epithelial cells. *The Journal of biological chemistry* **279**, 31365-31373, doi:10.1074/jbc.M401957200 (2004).
250 Huber, A. B., Weinmann, O., Brosamle, C., Oertle, T. & Schwab, M. E. Patterns of Nogo mRNA and protein expression in the developing and adult rat and after CNS lesions. *The Journal of neuroscience : the official journal of the Society for Neuroscience* **22**, 3553-3567, doi:20026323 (2002).
251 Sarkey, J. P. *et al.* Nogo-A knockdown inhibits hypoxia/reoxygenation-induced activation of mitochondrial-dependent apoptosis in cardiomyocytes. *Journal of molecular and cellular cardiology* **50**, 1044-1055, doi:10.1016/j.yjmcc.2011.03.004 (2011).
252 Bullard, T. A. *et al.* Identification of Nogo as a novel indicator of heart failure. *Physiological genomics* **32**, 182-189, doi:10.1152/physiolgenomics.00200.2007 (2008).
253 Gramolini, A. O. *et al.* Comparative proteomics profiling of a phospholamban mutant mouse model of dilated cardiomyopathy reveals progressive intracellular stress responses. *Molecular & cellular proteomics : MCP* **7**, 519-533, doi:10.1074/mcp.M700245-MCP200 (2008).
254 Wells, Q. S. *et al.* Whole exome sequencing identifies a causal RBM20 mutation in a large pedigree with familial dilated cardiomyopathy. *Circ Cardiovasc Genet* **6**, 317-326, doi:10.1161/circgenetics.113.000011 (2013).
255 Rampersaud, E. *et al.* Rare variant mutations identified in pediatric patients with dilated cardiomyopathy. *Progress in pediatric cardiology* **31**, 39-47 (2011).
256 Long, P. A., Evans, J. M. & Olson, T. M. Diagnostic Yield of Whole Exome Sequencing in Pediatric Dilated Cardiomyopathy. *Journal of cardiovascular development and disease* **4**, 11 (2017).
257 Klauke, B. *et al.* High proportion of genetic cases in patients with advanced cardiomyopathy including a novel homozygous Plakophilin 2-gene mutation. *PloS one* **12**, e0189489 (2017).
258 Zhao, Y. *et al.* Targeted next-generation sequencing of candidate genes reveals novel mutations in patients with dilated cardiomyopathy. *International journal of molecular medicine* **36**, 1479-1486, doi:10.3892/ijmm.2015.2361 (2015).

259 Waldmüller, S. *et al.* Targeted 46-gene and clinical exome sequencing for mutations causing cardiomyopathies. *Molecular and cellular probes* **29**, 308-314 (2015).
260 Beqqali, A. *et al.* A mutation in the glutamate-rich region of RNA-binding motif protein 20 causes dilated cardiomyopathy through missplicing of titin and impaired Frank-Starling mechanism. *Cardiovascular research* **112**, 452-463, doi:10.1093/cvr/cvw192 (2016).
261 Panorchan, P., Wirtz, D. & Tseng, Y. Structure-function relationship of biological gels revealed by multiple-particle tracking and differential interference contrast microscopy: the case of human lamin networks. *Phys Rev E Stat Nonlin Soft Matter Phys* **70**, 041906, doi:10.1103/PhysRevE.70.041906 (2004).
262 Frock, R. L. *et al.* Lamin A/C and emerin are critical for skeletal muscle satellite cell differentiation. *Genes Dev* **20**, 486-500, doi:10.1101/gad.1364906 (2006).
263 Bechert, K., Lagos-Quintana, M., Harborth, J., Weber, K. & Osborn, M. Effects of expressing lamin A mutant protein causing Emery-Dreifuss muscular dystrophy and familial partial lipodystrophy in HeLa cells. *Exp Cell Res* **286**, 75-86 (2003).
264 Burke, B., Mounkes, L. C. & Stewart, C. L. The nuclear envelope in muscular dystrophy and cardiovascular diseases. *Traffic* **2**, 675-683 (2001).
265 Taylor, M. R. *et al.* Natural history of dilated cardiomyopathy due to lamin A/C gene mutations. *J Am Coll Cardiol* **41**, 771-780 (2003).
266 Wessely, R., Seidl, S. & Schomig, A. Cardiac involvement in Emery-Dreifuss muscular dystrophy. *Clin Genet* **67**, 220-223, doi:10.1111/j.1399-0004.2004.00395.x (2005).
267 Hutchison, C. J. & Worman, H. J. A-type lamins: guardians of the soma? *Nat Cell Biol* **6**, 1062-1067, doi:10.1038/ncb1104-1062 (2004).
268 Broers, J. L., Hutchison, C. J. & Ramaekers, F. C. Laminopathies. *J Pathol* **204**, 478-488, doi:10.1002/path.1655 (2004).
269 Burke, B. & Stewart, C. L. Life at the edge: the nuclear envelope and human disease. *Nat Rev Mol Cell Biol* **3**, 575-585, doi:10.1038/nrm879 (2002).
270 Sullivan, T. *et al.* Loss of A-type lamin expression compromises nuclear envelope integrity leading to muscular dystrophy. *J Cell Biol* **147**, 913-920 (1999).
271 Lammerding, J. *et al.* Lamin A/C deficiency causes defective nuclear mechanics and mechanotransduction. *J Clin Invest* **113**, 370-378, doi:10.1172/JCI19670 (2004).
272 Broers, J. L. *et al.* Decreased mechanical stiffness in LMNA-/- cells is caused by defective nucleo-cytoskeletal integrity: implications for the development of laminopathies. *Hum Mol Genet* **13**, 2567-2580, doi:10.1093/hmg/ddh295 (2004).
273 Fidzianska, A. & Hausmanowa-Petrusewicz, I. Architectural abnormalities in muscle nuclei. Ultrastructural differences between X-linked and autosomal dominant forms of EDMD. *J Neurol Sci* **210**, 47-51 (2003).
274 Fidzianska, A., Toniolo, D. & Hausmanowa-Petrusewicz, I. Ultrastructural abnormality of sarcolemmal nuclei in Emery-Dreifuss muscular dystrophy (EDMD). *J Neurol Sci* **159**, 88-93 (1998).
275 Nikolova, V. *et al.* Defects in nuclear structure and function promote dilated cardiomyopathy in lamin A/C-deficient mice. *J Clin Invest* **113**, 357-369, doi:10.1172/JCI19448 (2004).
276 Melcon, G. *et al.* Loss of emerin at the nuclear envelope disrupts the Rb1/E2F and MyoD pathways during muscle regeneration. *Human molecular genetics* **15**, 637-651, doi:10.1093/hmg/ddi479 (2006).

277 Crisp, M. *et al.* Coupling of the nucleus and cytoplasm: role of the LINC complex. *J Cell Biol* **172**, 41-53, doi:10.1083/jcb.200509124 (2006).
278 Worman, H. J. & Gundersen, G. G. Here come the SUNs: a nucleocytoskeletal missing link. *Trends Cell Biol* **16**, 67-69, doi:10.1016/j.tcb.2005.12.006 (2006).
279 Mislow, J. M. *et al.* Nesprin-1alpha self-associates and binds directly to emerin and lamin A in vitro. *FEBS Lett* **525**, 135-140 (2002).
280 Zhang, Q. *et al.* Nesprin-2 is a multi-isomeric protein that binds lamin and emerin at the nuclear envelope and forms a subcellular network in skeletal muscle. *J Cell Sci* **118**, 673-687, doi:10.1242/jcs.01642 (2005).
281 Libotte, T. *et al.* Lamin A/C-dependent localization of Nesprin-2, a giant scaffolder at the nuclear envelope. *Mol Biol Cell* **16**, 3411-3424, doi:10.1091/mbc.E04-11-1009 (2005).
282 Folker, E. S., Ostlund, C., Luxton, G. W., Worman, H. J. & Gundersen, G. G. Lamin A variants that cause striated muscle disease are defective in anchoring transmembrane actin-associated nuclear lines for nuclear movement. *Proc Natl Acad Sci U S A* **108**, 131-136, doi:10.1073/pnas.1000824108 (2011).
283 Worman, H. J. & Schirmer, E. C. Nuclear membrane diversity: underlying tissue-specific pathologies in disease? *Curr Opin Cell Biol* **34**, 101-112, doi:10.1016/j.ceb.2015.06.003 (2015).
284 Wu, C. H., Liu, I. J., Lu, R. M. & Wu, H. C. Advancement and applications of peptide phage display technology in biomedical science. *J Biomed Sci* **23**, 8, doi:10.1186/s12929-016-0223-x (2016).
285 Giordano, R. J., Cardo-Vila, M., Lahdenranta, J., Pasqualini, R. & Arap, W. Biopanning and rapid analysis of selective interactive ligands. *Nat Med* **7**, 1249-1253, doi:10.1038/nm1101-1249 (2001).
286 Sullivan, T. *et al.* Loss of A-type lamin expression compromises nuclear envelope integrity leading to muscular dystrophy. *The Journal of cell biology* **147**, 913-920 (1999).
287 R: A Language and Environment for Statistical Computing (R Foundation for Statistical Computing, 2011).
288 Muller, T., Rahmann, S. & Rehmsmeier, M. Non-symmetric score matrices and the detection of homologous transmembrane proteins. *Bioinformatics (Oxford, England)* **17 Suppl 1**, S182-189, doi:10.1093/bioinformatics/17.suppl_1.s182 (2001).
289 Brammer, L. A. *et al.* A target-unrelated peptide in an M13 phage display library traced to an advantageous mutation in the gene II ribosome-binding site. *Anal Biochem* **373**, 88-98, doi:10.1016/j.ab.2007.10.015 (2008).
290 Nguyen, K. T. *et al.* Identification and characterization of mutant clones with enhanced propagation rates from phage-displayed peptide libraries. *Anal Biochem* **462**, 35-43, doi:10.1016/j.ab.2014.06.007 (2014).
291 Kim, D. I. *et al.* Probing nuclear pore complex architecture with proximity-dependent biotinylation. *Proc Natl Acad Sci U S A* **111**, E2453-2461, doi:10.1073/pnas.1406459111 (2014).
292 Clever, M., Funakoshi, T., Mimura, Y., Takagi, M. & Imamoto, N. The nucleoporin ELYS/Mel28 regulates nuclear envelope subdomain formation in HeLa cells. *Nucleus* **3**, 187-199, doi:10.4161/nucl.19595 (2012).
293 Holaska, J. M. & Wilson, K. L. An emerin "proteome": purification of distinct emerin-containing complexes from HeLa cells suggests molecular basis for diverse roles including

gene regulation, mRNA splicing, signaling, mechanosensing, and nuclear architecture. *Biochemistry* **46**, 8897-8908, doi:10.1021/bi602636m (2007).
294 Wilkinson, F. L. *et al.* Emerin interacts in vitro with the splicing-associated factor, YT521-B. *Eur J Biochem* **270**, 2459-2466 (2003).
295 Lattanzi, G. *et al.* Association of emerin with nuclear and cytoplasmic actin is regulated in differentiating myoblasts. *Biochem Biophys Res Commun* **303**, 764-770 (2003).
296 Sakaki, M. *et al.* Interaction between emerin and nuclear lamins. *J Biochem* **129**, 321-327 (2001).
297 Clements, L., Manilal, S., Love, D. R. & Morris, G. E. Direct interaction between emerin and lamin A. *Biochem Biophys Res Commun* **267**, 709-714, doi:10.1006/bbrc.1999.2023 (2000).
298 Kubben, N. *et al.* Identification of differential protein interactors of lamin A and progerin. *Nucleus* **1**, 513-525, doi:10.4161/nucl.1.6.13512 (2010).
299 Hein, M. Y. *et al.* A human interactome in three quantitative dimensions organized by stoichiometries and abundances. *Cell* **163**, 712-723, doi:10.1016/j.cell.2015.09.053 (2015).
300 Castello, A. *et al.* Insights into RNA biology from an atlas of mammalian mRNA-binding proteins. *Cell* **149**, 1393-1406, doi:10.1016/j.cell.2012.04.031 (2012).
301 Rolland, T. *et al.* A proteome-scale map of the human interactome network. *Cell* **159**, 1212-1226, doi:10.1016/j.cell.2014.10.050 (2014).
302 Lee, T. H. *et al.* Vascular endothelial growth factor mediates intracrine survival in human breast carcinoma cells through internally expressed VEGFR1/FLT1. *PLoS Med* **4**, e186, doi:10.1371/journal.pmed.0040186 (2007).
303 Bhattacharya, S. & Ghosh, M. K. HAUSP regulates c-MYC expression via de-ubiquitination of TRRAP. *Cell Oncol (Dordr)* **38**, 265-277, doi:10.1007/s13402-015-0228-6 (2015).
304 Humphries, J. D. *et al.* Proteomic analysis of integrin-associated complexes identifies RCC2 as a dual regulator of Rac1 and Arf6. *Sci Signal* **2**, ra51, doi:10.1126/scisignal.2000396 (2009).
305 Yang, M. & Yuan, Z. M. A novel role of PRR14 in the regulation of skeletal myogenesis. *Cell Death Dis* **6**, e1734, doi:10.1038/cddis.2015.103 (2015).
306 Mislow, J. M., Kim, M. S., Davis, D. B. & McNally, E. M. Myne-1, a spectrin repeat transmembrane protein of the myocyte inner nuclear membrane, interacts with lamin A/C. *J Cell Sci* **115**, 61-70 (2002).
307 Nikolova-Krstevski, V. *et al.* Nesprin-1 and actin contribute to nuclear and cytoskeletal defects in lamin A/C-deficient cardiomyopathy. *J Mol Cell Cardiol* **50**, 479-486, doi:10.1016/j.yjmcc.2010.12.001 (2011).
308 Hakelien, A. M., Delbarre, E., Gaustad, K. G., Buendia, B. & Collas, P. Expression of the myodystrophic R453W mutation of lamin A in C2C12 myoblasts causes promoter-specific and global epigenetic defects. *Exp Cell Res* **314**, 1869-1880, doi:10.1016/j.yexcr.2008.02.018 (2008).
309 Quiros-Gonzalez, I. *et al.* Lamin A is involved in the development of vascular calcification induced by chronic kidney failure and phosphorus load. *Bone* **84**, 160-168, doi:10.1016/j.bone.2016.01.005 (2016).
310 Li, W. *et al.* Decreased bone formation and osteopenia in lamin a/c-deficient mice. *PLoS One* **6**, e19313, doi:10.1371/journal.pone.0019313 (2011).
311 Hartig, S. M., He, B., Long, W., Buehrer, B. M. & Mancini, M. A. Homeostatic levels of SRC-2 and SRC-3 promote early human adipogenesis. *J Cell Biol* **192**, 55-67, doi:10.1083/jcb.201004026 (2011).

312 Kodera, Y. *et al.* Ligand type-specific interactions of peroxisome proliferator-activated receptor gamma with transcriptional coactivators. *J Biol Chem* **275**, 33201-33204, doi:10.1074/jbc.C000517200 (2000).
313 Kim, J. H., Lee, J. N. & Paik, Y. K. Cholesterol biosynthesis from lanosterol. A concerted role for Sp1 and NF-Y-binding sites for sterol-mediated regulation of rat 7-dehydrocholesterol reductase gene expression. *J Biol Chem* **276**, 18153-18160, doi:10.1074/jbc.M101661200 (2001).
314 Lloyd, D. J., Trembath, R. C. & Shackleton, S. A novel interaction between lamin A and SREBP1: implications for partial lipodystrophy and other laminopathies. *Hum Mol Genet* **11**, 769-777 (2002).
315 Rocha, P. P., Scholze, M., Bleiss, W. & Schrewe, H. Med12 is essential for early mouse development and for canonical Wnt and Wnt/PCP signaling. *Development* **137**, 2723-2731, doi:10.1242/dev.053660 (2010).
316 Schiano, C., Casamassimi, A., Vietri, M. T., Rienzo, M. & Napoli, C. The roles of mediator complex in cardiovascular diseases. *Biochim Biophys Acta* **1839**, 444-451, doi:10.1016/j.bbagrm.2014.04.012 (2014).
317 Rondon, A. G., Jimeno, S. & Aguilera, A. The interface between transcription and mRNP export: from THO to THSC/TREX-2. *Biochim Biophys Acta* **1799**, 533-538, doi:10.1016/j.bbagrm.2010.06.002 (2010).
318 Dominguez-Sanchez, M. S., Barroso, S., Gomez-Gonzalez, B., Luna, R. & Aguilera, A. Genome instability and transcription elongation impairment in human cells depleted of THO/TREX. *PLoS Genet* **7**, e1002386, doi:10.1371/journal.pgen.1002386 (2011).
319 Sciarretta, S., Volpe, M. & Sadoshima, J. Mammalian target of rapamycin signaling in cardiac physiology and disease. *Circ Res* **114**, 549-564, doi:10.1161/CIRCRESAHA.114.302022 (2014).
320 Choi, J. C. *et al.* Dual specificity phosphatase 4 mediates cardiomyopathy caused by lamin A/C (LMNA) gene mutation. *The Journal of biological chemistry* **287**, 40513-40524, doi:10.1074/jbc.M112.404541 (2012).
321 Liu, G. H. *et al.* Regulation of myoblast differentiation by the nuclear envelope protein NET39. *Mol Cell Biol* **29**, 5800-5812, doi:10.1128/MCB.00684-09 (2009).
322 van Dijk, J. *et al.* Polyglutamylation is a post-translational modification with a broad range of substrates. *J Biol Chem* **283**, 3915-3922, doi:10.1074/jbc.M705813200 (2008).
323 Kimura, Y. *et al.* Identification of tubulin deglutamylase among Caenorhabditis elegans and mammalian cytosolic carboxypeptidases (CCPs). *J Biol Chem* **285**, 22936-22941, doi:10.1074/jbc.C110.128280 (2010).
324 Berezniuk, I. *et al.* Cytosolic carboxypeptidase 5 removes alpha- and gamma-linked glutamates from tubulin. *J Biol Chem* **288**, 30445-30453, doi:10.1074/jbc.M113.497917 (2013).
325 Hao, Y. H. *et al.* Regulation of WASH-dependent actin polymerization and protein trafficking by ubiquitination. *Cell* **152**, 1051-1064, doi:10.1016/j.cell.2013.01.051 (2013).
326 Ramakrishnan, S. N., Lau, P., Burke, L. J. & Muscat, G. E. Rev-erbbeta regulates the expression of genes involved in lipid absorption in skeletal muscle cells: evidence for cross-talk between orphan nuclear receptors and myokines. *J Biol Chem* **280**, 8651-8659, doi:10.1074/jbc.M413949200 (2005).

327 Ramakrishnan, S. N. *et al.* Rev-erb beta regulates the Srebp-1c promoter and mRNA expression in skeletal muscle cells. *Biochem Biophys Res Commun* **388**, 654-659, doi:10.1016/j.bbrc.2009.08.045 (2009).
328 Park, B. *et al.* Association of Lbc Rho guanine nucleotide exchange factor with alpha-catenin-related protein, alpha-catulin/CTNNAL1, supports serum response factor activation. *J Biol Chem* **277**, 45361-45370, doi:10.1074/jbc.M202447200 (2002).
329 Kreiseder, B. *et al.* alpha-Catulin downregulates E-cadherin and promotes melanoma progression and invasion. *Int J Cancer* **132**, 521-530, doi:10.1002/ijc.27698 (2013).
330 Muralikrishna, B., Chaturvedi, P., Sinha, K. & Parnaik, V. K. Lamin misexpression upregulates three distinct ubiquitin ligase systems that degrade ATR kinase in HeLa cells. *Mol Cell Biochem* **365**, 323-332, doi:10.1007/s11010-012-1272-4 (2012).
331 Maron, B. J. *et al.* Contemporary definitions and classification of the cardiomyopathies: an American Heart Association Scientific Statement from the Council on Clinical Cardiology, Heart Failure and Transplantation Committee; Quality of Care and Outcomes Research and Functional Genomics and Translational Biology Interdisciplinary Working Groups; and Council on Epidemiology and Prevention. *Circulation* **113**, 1807-1816, doi:10.1161/circulationaha.106.174287 (2006).
332 Yancy, C. W. *et al.* 2013 ACCF/AHA Guideline for the Management of Heart Failure: Executive Summary. *A Report of the American College of Cardiology Foundation/American Heart Association Task Force on Practice Guidelines* **128**, 1810-1852, doi:10.1161/CIR.0b013e31829e8807 (2013).
333 Pinto, Y. M. *et al.* Proposal for a revised definition of dilated cardiomyopathy, hypokinetic non-dilated cardiomyopathy, and its implications for clinical practice: a position statement of the ESC working group on myocardial and pericardial diseases. *European heart journal* **37**, 1850-1858, doi:10.1093/eurheartj/ehv727 (2016).
334 McKenna, W. J., Maron, B. J. & Thiene, G. Classification, Epidemiology, and Global Burden of Cardiomyopathies. *Circulation research* **121**, 722-730, doi:10.1161/circresaha.117.309711 (2017).
335 Masarone, D. *et al.* Epidemiology and clinical aspects of genetic cardiomyopathies. *Heart failure clinics* **14**, 119-128 (2018).
336 LeWinter, M. M., Wu, Y., Labeit, S. & Granzier, H. Cardiac titin: structure, functions and role in disease. *Clinica chimica acta* **375**, 1-9 (2007).
337 Gigli, M. *et al.* A Review of the Giant Protein Titin in Clinical Molecular Diagnostics of Cardiomyopathies. *Front Cardiovasc Med* **3**, 21, doi:10.3389/fcvm.2016.00021 (2016).
338 Hidalgo, C. & Granzier, H. Tuning the molecular giant titin through phosphorylation: role in health and disease. *Trends in cardiovascular medicine* **23**, 165-171, doi:10.1016/j.tcm.2012.10.005 (2013).
339 Zerbino, D. R. *et al.* Ensembl 2018. *Nucleic acids research* **46**, D754-d761, doi:10.1093/nar/gkx1098 (2018).
340 Zahr, H. C. & Jaalouk, D. E. Exploring the Crosstalk Between LMNA and Splicing Machinery Gene Mutations in Dilated Cardiomyopathy. *Frontiers in genetics* **9**, 231, doi:10.3389/fgene.2018.00231 (2018).
341 Wyles, S. P. *et al.* Modeling structural and functional deficiencies of RBM20 familial dilated cardiomyopathy using human induced pluripotent stem cells. *Human molecular genetics* **25**, 254-265, doi:10.1093/hmg/ddv468 (2016).

342 Streckfuss-Bomeke, K. *et al.* Severe DCM phenotype of patient harboring RBM20 mutation S635A can be modeled by patient-specific induced pluripotent stem cell-derived cardiomyocytes. *J Mol Cell Cardiol* **113**, 9-21, doi:10.1016/j.yjmcc.2017.09.008 (2017).
343 Li, S., Guo, W., Dewey, C. N. & Greaser, M. L. Rbm20 regulates titin alternative splicing as a splicing repressor. *Nucleic acids research* **41**, 2659-2672, doi:10.1093/nar/gks1362 (2013).
344 Murayama, R. *et al.* Phosphorylation of the RSRSP stretch is critical for splicing regulation by RNA-Binding Motif Protein 20 (RBM20) through nuclear localization. *Scientific reports* **8**, 8970-8970, doi:10.1038/s41598-018-26624-w (2018).
345 Yeakley, J. M. *et al.* Phosphorylation regulates in vivo interaction and molecular targeting of serine/arginine-rich pre-mRNA splicing factors. *The Journal of cell biology* **145**, 447-455, doi:10.1083/jcb.145.3.447 (1999).
346 Watanabe, T., Kimura, A. & Kuroyanagi, H. Alternative Splicing Regulator RBM20 and Cardiomyopathy. *Frontiers in molecular biosciences* **5**, 105, doi:10.3389/fmolb.2018.00105 (2018).
347 Methawasin, M. *et al.* Experimentally increasing titin compliance in a novel mouse model attenuates the Frank-Starling mechanism but has a beneficial effect on diastole. *Circulation* **129**, 1924-1936, doi:10.1161/CIRCULATIONAHA.113.005610 (2014).
348 Mislow, J. M. *et al.* Nesprin-1α self-associates and binds directly to emerin and lamin A in vitro. *FEBS letters* **525**, 135-140 (2002).
349 Rajgor, D. & Shanahan, C. M. Nesprins: from the nuclear envelope and beyond. *Expert reviews in molecular medicine* **15**, e5, doi:10.1017/erm.2013.6 (2013).
350 Rajgor, D., Mellad, J. A., Autore, F., Zhang, Q. & Shanahan, C. M. Multiple novel nesprin-1 and nesprin-2 variants act as versatile tissue-specific intracellular scaffolds. *PLoS One* **7**, e40098, doi:10.1371/journal.pone.0040098 (2012).
351 Zhang, Q. *et al.* Nesprin-1 and-2 are involved in the pathogenesis of Emery–Dreifuss muscular dystrophy and are critical for nuclear envelope integrity. *Human molecular genetics* **16**, 2816-2833 (2007).
352 Puckelwartz, M. J. *et al.* Nesprin-1 mutations in human and murine cardiomyopathy. *Journal of molecular and cellular cardiology* **48**, 600-608 (2010).
353 Chen, Z. *et al.* A novel SYNE1 gene mutation in a Chinese family of Emery-Dreifuss muscular dystrophy-like. *BMC Medical Genetics* **18**, 63, doi:10.1186/s12881-017-0424-5 (2017).
354 Zhou, C. *et al.* Novel nesprin-1 mutations associated with dilated cardiomyopathy cause nuclear envelope disruption and defects in myogenesis. *Human molecular genetics* **26**, 2258-2276, doi:10.1093/hmg/ddx116 (2017).
355 Haskell, G. T. *et al.* Whole Exome Sequencing Identifies Truncating Variants in Nuclear Envelope Genes in Patients With Cardiovascular Disease. *Circulation. Cardiovascular genetics* **10**, doi:10.1161/circgenetics.116.001443 (2017).
356 Marme, A. *et al.* Loss of Drop1 expression already at early tumor stages in a wide range of human carcinomas. *International journal of cancer* **123**, 2048-2056, doi:10.1002/ijc.23763 (2008).
357 Duong, N. T. *et al.* Nesprins: tissue-specific expression of epsilon and other short isoforms. *PLoS One* **9**, e94380, doi:10.1371/journal.pone.0094380 (2014).
358 Rajgor, D. *et al.* Mammalian microtubule P-body dynamics are mediated by nesprin-1. *J Cell Biol* **205**, 457-475, doi:10.1083/jcb.201306076 (2014).

359 Eulalio, A., Behm-Ansmant, I. & Izaurralde, E. P bodies: at the crossroads of post-transcriptional pathways. *Nature reviews. Molecular cell biology* **8**, 9-22, doi:10.1038/nrm2080 (2007).
360 Eulalio, A., Behm-Ansmant, I., Schweizer, D. & Izaurralde, E. P-body formation is a consequence, not the cause, of RNA-mediated gene silencing. *Molecular and cellular biology* **27**, 3970-3981, doi:10.1128/mcb.00128-07 (2007).
361 Rajgor, D., Hanley, J. G. & Shanahan, C. M. Identification of novel nesprin-1 binding partners and cytoplasmic matrin-3 in processing bodies. *Mol Biol Cell* **27**, 3894-3902, doi:10.1091/mbc.E16-06-0346 (2016).
362 Coelho, M. B. *et al.* Nuclear matrix protein Matrin3 regulates alternative splicing and forms overlapping regulatory networks with PTB. *The EMBO journal* **34**, 653-668, doi:10.15252/embj.201489852 (2015).
363 Lorenzi, P. *et al.* RNA-binding proteins RBM20 and PTBP1 regulate the alternative splicing of FHOD3. *The international journal of biochemistry & cell biology* **106**, 74-83, doi:10.1016/j.biocel.2018.11.009 (2019).
364 Ameyar-Zazoua, M. *et al.* Argonaute proteins couple chromatin silencing to alternative splicing. *Nature structural & molecular biology* **19**, 998-1004, doi:10.1038/nsmb.2373 (2012).
365 Zastrow, M. S., Flaherty, D. B., Benian, G. M. & Wilson, K. L. Nuclear titin interacts with A- and B-type lamins in vitro and in vivo. *Journal of cell science* **119**, 239-249, doi:10.1242/jcs.02728 (2006).
366 Bertero, A. *et al.* Dynamics of genome reorganization during human cardiogenesis reveal an RBM20-dependent splicing factory. *Nature communications* **10**, 1538, doi:10.1038/s41467-019-09483-5 (2019).
367 Simon, D. N. & Wilson, K. L. Partners and post-translational modifications of nuclear lamins. *Chromosoma* **122**, 13-31, doi:10.1007/s00412-013-0399-8 (2013).
368 Earle, A. J. *et al.* Mutant lamins cause nuclear envelope rupture and DNA damage in skeletal muscle cells. *bioRxiv*, 364778, doi:10.1101/364778 (2019).
369 Davidson, P. M. & Lammerding, J. Broken nuclei--lamins, nuclear mechanics, and disease. *Trends Cell Biol* **24**, 247-256, doi:10.1016/j.tcb.2013.11.004 (2014).
370 Maggi, L., Carboni, N. & Bernasconi, P. Skeletal Muscle Laminopathies: A Review of Clinical and Molecular Features. *Cells* **5**, doi:10.3390/cells5030033 (2016).
371 Emery, A. E. Emery-Dreifuss muscular dystrophy - a 40 year retrospective. *Neuromuscular disorders : NMD* **10**, 228-232 (2000).
372 Mouilleron, S., Langer, C. A., Guettler, S., McDonald, N. Q. & Treisman, R. Structure of a pentavalent G-actin*MRTF-A complex reveals how G-actin controls nucleocytoplasmic shuttling of a transcriptional coactivator. *Science signaling* **4**, ra40, doi:10.1126/scisignal.2001750 (2011).
373 Yang, L. *et al.* Mutations in LMNA modulate the lamin A--Nesprin-2 interaction and cause LINC complex alterations. *PLoS One* **8**, e71850, doi:10.1371/journal.pone.0071850 (2013).
374 Lammerding, J. *et al.* Abnormal nuclear shape and impaired mechanotransduction in emerin-deficient cells. *J Cell Biol* **170**, 781-791, doi:10.1083/jcb.200502148 (2005).
375 Bione, S. *et al.* Identification of a novel X-linked gene responsible for Emery-Dreifuss muscular dystrophy. *Nature genetics* **8**, 323-327, doi:10.1038/ng1294-323 (1994).

376 Kayvanpour, E. *et al.* Genotype-phenotype associations in dilated cardiomyopathy: meta-analysis on more than 8000 individuals. *Clinical research in cardiology : official journal of the German Cardiac Society*, doi:10.1007/s00392-016-1033-6 (2016).
377 Depreux, F. F. *et al.* Disruption of the lamin A and matrin-3 interaction by myopathic LMNA mutations. *Human molecular genetics* **24**, 4284-4295 (2015).
378 Rajgor, D. *et al.* Lamin A/C controls nuclear matrin-3 levels and localization, but not alternative splicing of cassette exons. *bioRxiv*, 378240, doi:10.1101/378240 (2018).
379 Sedki, D. Insights into the deregulations of Rbm20 in Lamin A/C and emerin related cardiomyopathies. Thesis, American University of Beirut, (2015).
380 Lizcano, J. M. & Alessi, D. R. The insulin signalling pathway. *Current biology* **12**, R236-R238 (2002).
381 Zahr, H. C. & Jaalouk, D. E. Exploring the crosstalk between LMNA and splicing machinery gene mutations in dilated cardiomyopathy. *Frontiers in genetics* **9** (2018).
382 Vaughan, A. *et al.* Both emerin and lamin C depend on lamin A for localization at the nuclear envelope. *Journal of cell science* **114**, 2577-2590 (2001).
383 Sewry, C. A. *et al.* Skeletal muscle pathology in autosomal dominant Emery-Dreifuss muscular dystrophy with lamin A/C mutations. *Neuropathology and applied neurobiology* **27**, 281-290 (2001).
384 Ranade, D., Pradhan, R., Jayakrishnan, M., Hegde, S. & Sengupta, K. Lamin A/C and Emerin depletion impacts chromatin organization and dynamics in the interphase nucleus. *BMC molecular and cell biology* **20**, 11, doi:10.1186/s12860-019-0192-5 (2019).
385 Holt, I. *et al.* Effect of pathogenic mis-sense mutations in lamin A on its interaction with emerin in vivo. *Journal of cell science* **116**, 3027-3035, doi:10.1242/jcs.00599 (2003).
386 Gangemi, F. & Degano, M. Disease-associated mutations in the coil 2B domain of human lamin A/C affect structural properties that mediate dimerization and intermediate filament formation. *Journal of structural biology* **181**, 17-28, doi:10.1016/j.jsb.2012.10.016 (2013).
387 Motsch, I. *et al.* Lamins A and C are differentially dysfunctional in autosomal dominant Emery-Dreifuss muscular dystrophy. *European journal of cell biology* **84**, 765-781, doi:10.1016/j.ejcb.2005.04.004 (2005).
388 Simon, D. N., Zastrow, M. S. & Wilson, K. L. Direct actin binding to A- and B-type lamin tails and actin filament bundling by the lamin A tail. *Nucleus (Austin, Tex.)* **1**, 264-272, doi:10.4161/nucl.1.3.11799 (2010).
389 Louvet, E. & Percipalle, P. Transcriptional control of gene expression by actin and myosin. *International review of cell and molecular biology* **272**, 107-147, doi:10.1016/s1937-6448(08)01603-1 (2009).
390 Yoo, Y., Wu, X. & Guan, J. L. A novel role of the actin-nucleating Arp2/3 complex in the regulation of RNA polymerase II-dependent transcription. *The Journal of biological chemistry* **282**, 7616-7623, doi:10.1074/jbc.M607596200 (2007).
391 Suzuki, H. & Matsuoka, M. hnRNPA1 autoregulates its own mRNA expression to remain non-cytotoxic. *Molecular and cellular biochemistry* **427**, 123-131, doi:10.1007/s11010-016-2904-x (2017).
392 Sun, Y. *et al.* Autoregulation of RBM10 and cross-regulation of RBM10/RBM5 via alternative splicing-coupled nonsense-mediated decay. *Nucleic acids research* **45**, 8524-8540, doi:10.1093/nar/gkx508 (2017).

393 Pervouchine, D. *et al.* Integrative transcriptomic analysis suggests new autoregulatory splicing events coupled with nonsense-mediated mRNA decay. *Nucleic acids research* **47**, 5293-5306, doi:10.1093/nar/gkz193 (2019).
394 Jeong, S. SR Proteins: Binders, Regulators, and Connectors of RNA. *Molecules and cells* **40**, 1-9, doi:10.14348/molcells.2017.2319 (2017).
395 Muchir, A. *et al.* Abnormal p38alpha mitogen-activated protein kinase signaling in dilated cardiomyopathy caused by lamin A/C gene mutation. *Human molecular genetics* **21**, 4325-4333, doi:10.1093/hmg/dds265 (2012).
396 Thapar, R. & Denmon, A. P. Signaling pathways that control mRNA turnover. *Cellular signalling* **25**, 1699-1710, doi:10.1016/j.cellsig.2013.03.026 (2013).
397 Chrestensen, C. A. *et al.* MAPKAP kinase 2 phosphorylates tristetraprolin on in vivo sites including Ser178, a site required for 14-3-3 binding. *The Journal of biological chemistry* **279**, 10176-10184, doi:10.1074/jbc.M310486200 (2004).
398 Briata, P. *et al.* p38-dependent phosphorylation of the mRNA decay-promoting factor KSRP controls the stability of select myogenic transcripts. *Molecular cell* **20**, 891-903, doi:10.1016/j.molcel.2005.10.021 (2005).
399 Shveygert, M., Kaiser, C., Bradrick, S. S. & Gromeier, M. Regulation of eukaryotic initiation factor 4E (eIF4E) phosphorylation by mitogen-activated protein kinase occurs through modulation of Mnk1-eIF4G interaction. *Molecular and cellular biology* **30**, 5160-5167, doi:10.1128/mcb.00448-10 (2010).
400 Esnault, S., Shen, Z. J., Whitesel, E. & Malter, J. S. The peptidyl-prolyl isomerase Pin1 regulates granulocyte-macrophage colony-stimulating factor mRNA stability in T lymphocytes. *Journal of immunology (Baltimore, Md. : 1950)* **177**, 6999-7006, doi:10.4049/jimmunol.177.10.6999 (2006).
401 Briata, P. *et al.* PI3K/AKT signaling determines a dynamic switch between distinct KSRP functions favoring skeletal myogenesis. *Cell death and differentiation* **19**, 478-487, doi:10.1038/cdd.2011.117 (2012).
402 Schmidlin, M. *et al.* The ARE-dependent mRNA-destabilizing activity of BRF1 is regulated by protein kinase B. *The EMBO journal* **23**, 4760-4769, doi:10.1038/sj.emboj.7600477 (2004).
403 Doller, A., Pfeilschifter, J. & Eberhardt, W. Signalling pathways regulating nucleo-cytoplasmic shuttling of the mRNA-binding protein HuR. *Cellular signalling* **20**, 2165-2173, doi:10.1016/j.cellsig.2008.05.007 (2008).
404 Holmes, B. *et al.* mTORC2/AKT/HSF1/HuR constitute a feed-forward loop regulating Rictor expression and tumor growth in glioblastoma. *Oncogene* **37**, 732-743, doi:10.1038/onc.2017.360 (2018).
405 Guo, W. *et al.* Splicing Factor RBM20 Regulates Transcriptional Network of Titin Associated and Calcium Handling Genes in The Heart. *International journal of biological sciences* **14**, 369-380, doi:10.7150/ijbs.24117 (2018).
406 Choi, J. C. *et al.* Elevated dual specificity protein phosphatase 4 in cardiomyopathy caused by lamin A/C gene mutation is primarily ERK1/2-dependent and its depletion improves cardiac function and survival. *Human molecular genetics* **27**, 2290-2305, doi:10.1093/hmg/ddy134 (2018).
407 Bernasconi, P. *et al.* Elevated TGF beta2 serum levels in Emery-Dreifuss Muscular Dystrophy: Implications for myocyte and tenocyte differentiation and fibrogenic processes. *Nucleus (Austin, Tex.)* **9**, 292-304, doi:10.1080/19491034.2018.1467722 (2018).

408 Bertacchini, J. *et al.* The protein kinase Akt/PKB regulates both prelamin A degradation and Lmna gene expression. *FASEB journal : official publication of the Federation of American Societies for Experimental Biology* **27**, 2145-2155, doi:10.1096/fj.12-218214 (2013).
409 Shiojima, I. *et al.* Short-term akt activation in cardiac muscle cells improves contractile function in failing hearts. *The American journal of pathology* **181**, 1969-1976, doi:10.1016/j.ajpath.2012.08.020 (2012).
410 Shiojima, I. *et al.* Disruption of coordinated cardiac hypertrophy and angiogenesis contributes to the transition to heart failure. *The Journal of clinical investigation* **115**, 2108-2118, doi:10.1172/jci24682 (2005).
411 Hakuno, F. *et al.* Constitutive expression of insulin receptor substrate (IRS)-1 inhibits myogenic differentiation through nuclear exclusion of Foxo1 in L6 myoblasts. *PLoS One* **6**, e25655, doi:10.1371/journal.pone.0025655 (2011).
412 Kwon, H. *et al.* A-type lamin-dependent homo-oligomerization for pY19-Caveolin-2 to function as an insulin-response epigenetic regulator. *Biochimica et biophysica acta* **1863**, 2681-2689, doi:10.1016/j.bbamcr.2016.08.011 (2016).
413 Dutta, S., Bhattacharyya, M. & Sengupta, K. Changes in the Nuclear Envelope in Laminopathies. *Advances in experimental medicine and biology* **1112**, 31-38, doi:10.1007/978-981-13-3065-0_3 (2018).
414 von Roretz, C., Beauchamp, P., Di Marco, S. & Gallouzi, I. E. HuR and myogenesis: being in the right place at the right time. *Biochimica et biophysica acta* **1813**, 1663-1667, doi:10.1016/j.bbamcr.2011.01.036 (2011).
415 Grammatikakis, I., Abdelmohsen, K. & Gorospe, M. Posttranslational control of HuR function. *Wiley interdisciplinary reviews. RNA* **8**, doi:10.1002/wrna.1372 (2017).
416 Yu, Y. *et al.* Phosphoproteomic analysis identifies Grb10 as an mTORC1 substrate that negatively regulates insulin signaling. *Science (New York, N.Y.)* **332**, 1322-1326, doi:10.1126/science.1199484 (2011).
417 Kim, H. H. *et al.* Nuclear HuR accumulation through phosphorylation by Cdk1. *Genes & development* **22**, 1804-1815, doi:10.1101/gad.1645808 (2008).